PhD thesis, s960853

Numerical simulations of interface dynamics in microfluidics

Mads Jakob Jensen

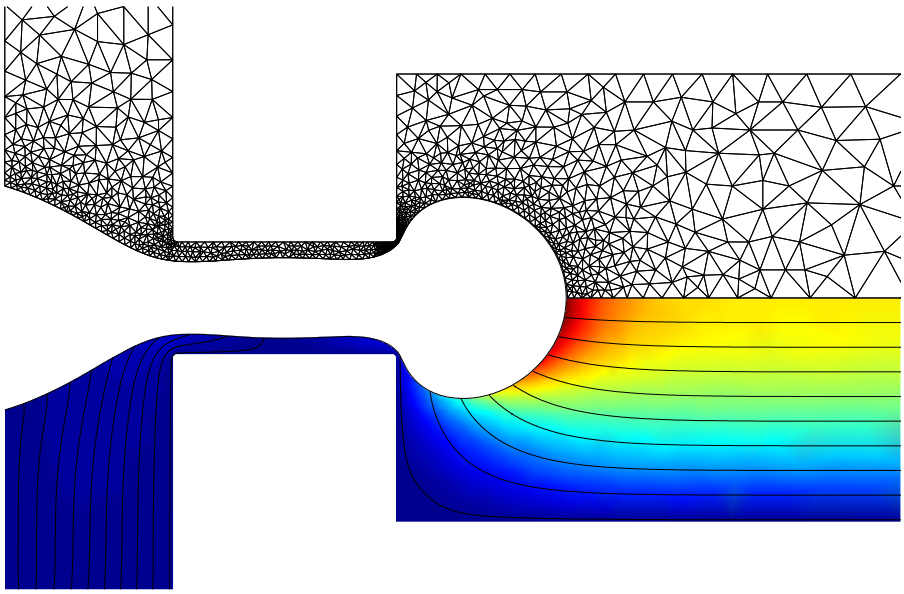

Supervisor: Prof. Henrik Bruus

MIC – Department of Micro and Nanotechnology
Technical University of Denmark

August 31, 2005

Abstract

A short background presentation has been given of the author's work concerned with the quasi static motion of gas bubbles in liquid filled microchannel contractions. This presentation includes a discussion of a first theoretical paper [1] and a presentation of a paper made in collaboration with the experimental group of D. Attinger at the State University of New York, Stony Brook, USA [2]. Hereafter a review is given of the experimental results of Garstecki *et al.* [3, 4, 5], these are concerned with a microfluidic implementation of a flow-focusing device. This study acts as the base and motivation for the consequent work presented in the thesis.

The governing equations for a two-fluid axisymmetric Newtonian Stokes flow problem have then been presented. The dynamic and kinematic boundary condition at the free interface between the two immiscible fluids are given together with a choice for a non-dimensional scaling of the equations. The equations are further reformulated into a somewhat unusual divergence form that is suited for the later numerical implementation in Femlab. A model for a non-Newtonian liquid has been discussed at the end of the theory section.

In a generic framework a direct numerical model for the simulation of a two-phase flow in an axisymmetric geometry has been developed. It is based on an second-order Runge–Kutta time integration scheme and curvature code implemented in Matlab . The governing equations have been solved by using the commercial finite-element program Femlab that interfaces with Matlab through a script language. A detailed description of the code and its inner workings together with a test of the time integration scheme has also been given.

The code has then been validated using three flow problems that have analytical solutions: (1) the surface tension driven coalescence of two viscous liquid cylinders, (2) the steady state shape of a translating gas bubble on a liquid filled capillary, and (3) the problem of a viscous drop in a viscous extensional flow. The code has been validated, has been seen to perform very well, and its flexibility has been demonstrated.

After the numerical testing the code has been applied to a first numerical investigation of the time-dependent dynamics of the creation of gas bubbles in an axisymmetric flow-focusing device. The axisymmetric simulations have shown that the collapse of the gas thread before bubble snap-off is different from recent experimental results by Garstecki *et al.*. We have suggested that the differences are geometrically induced. An extended general scaling law for the volume of the created gas bubbles has further been presented which includes one geometry parameter and surface tension. The numerical results have

confirmed existing experimental results and also the full new scaling. A simple snap-off mechanism has also been implemented and a bubbling sequence of four bubbles has been simulated. Conclusively a flow-focusing system containing a non-Newtonian liquid and a gas has been modelled and some initial new results have been presented; these include a scaling law for the volume of created gas bubbles in this non-linear system.

The PhD thesis work has resulted in the publication of of 2 peer reviewed papers, the submission of 2 papers, and the publication of 6 peer reviewed conference proceedings.

Resumé

Der er kort gjort rede for baggrunden for forfatterens arbejde med luftboblers kvasistatiske bevægelse i indsnævringer i væskefyldte mikrokanaler. Denne indtroduktion omfatter en gennemgang af en grundlæggende teoretisk artikel [1] og fremlæggelse af en artikel udarbejdet i samarbejde med D. Attingers eksperimentalgruppe [2]. Herefter følger en oversigt over Garstecki *et al.*'s eksperimentelle resultater [3, 4, 5] om en microfluidid implementering af et flow-focusing device. Denne undersøgelse er grundlag og begrundelse for det videre arbejde i denne afhandling.

De styrende ligninger for et tovæske aksesymmetrisk Newtonsk Stokes strømningsproblem er opstillet. De dynamiske og kinematiske randbetingelser for en fri overflade mellem to ikke- blandbare væsker formuleres sammen med dimensionsløs skalering af ligninger. Disse er endvidere omformuleret i en noget usædvanlig divergensform, som er tilpasset den numeriske implementering i Femlab. I slutningen af den teoretiske afdeling diskuteres en model for en ikke-Newtonsk væske.

En numerisk model til at simulere to-fase strømninger i aksesymmetriske geometrier er udviklet i generiske rammer. Den bygger på en andenordens Runge–Kutta tidsintegrationsrutine og en krumningskode implementeret i Matlab. De styrende ligninger er løst ved hjælp af det kommercielle finite-element program Femlab, der kommunikerer med Matlab. Der fremlægges ligeledes en detaljeret beskrivelse af koden med detaljer og en test af tidsintegrationsrutinen.

Koden er blevet testet på tre kendte strømningsproblemer: (1) benchmark-problemet med "the surface tension coalescence of two viscous liquid cylinders", (2) den stationære form af en luftboble, der bevæger sig i et væskefyldt kapillarrør og (3) spørgsmålet om en dråbe i en "extensional" strømning. Programmet er godkendt, fungerer fint og kodens fleksibilitet er vist.

Herefter er koden blevet anvendt til en numerisk undersøgelse af den tidsafhængige dynamik ved dannelse af luftbobler i en aksesymmetrisk flow-focusing device. Simuleringerne har vist, at dynamikken lige før bruddet (snap-off) ikke ligner Garstecki *et al.*'s seneste forsøgsresultater. Vi formoder, at forskellene er geometrisk afhængige. Der er yderligere redegjort for en udvidet lov for skalering af boblernes volumen, som omfatter en geometrisk parameter og overfladespænding. Simuleringerne bekræfter de eksisterende eksperimentelle resultater samt vores skaleringslov. En række af fire bobler er også blevet simuleret. Afsluttende er der modelleret et system, som indeholder en ikke-Newtonsk væske og en gas, og der er redegjort for visse helt nye resultater, som omfatter en lov for skaleringen af boblernes volumen i dette ikke-lineære system.

Afhandlingen har resulteret i publikationen af 2 peer-reviewed artikler, i at yderligere 2 artikler er blevet indsendt til publikation, samt at 6 peer-reviewed konference proceedings er blevet publiceret.

Preface

This thesis is submitted in candidacy for the PhD degree from the Technical University of Denmark (DTU). It is based on the work carried out in the Microfluidics Theory and Simulations group (MIFTS), Department for Micro and Nanotechnology (MIC) at DTU from September 2002 to August 2005 under the supervision of Prof. Henrik Bruus. Part of the work was initiated during a stay abroad in the spring of 2004 in the group of Prof. Howard A. Stone at the Division of Engineering and Applied Sciences (DEAS), Harvard University, USA. It has been a privilege to work in the MIFTS group and, hopefully, to contribute to its ripening on the international scientific scene.

I would like to thank Henrik for outstanding supervision, I have benefited enormously from his engagement in the work of his students, and for his profound physical insight. His help and tutoring in article writing has been very enlightening. I have really enjoyed our discussions about physics as well as non-physical topics.

I thank Howard Stone for giving me the opportunity to stay five month in his group at Harvard University and for sharing his great knowledge about fluid dynamics. The bulk part of the work in this thesis was motivated by the fantastic experimental results on the flow-focusing device produced by Piotr Garstecki – I am grateful that he shared his results at an early stage.

I would also like to thank all the members of MIFTS for a very relaxed but very inspiring working environment and for some awesome "moose meetings". A grand "thank you" to my fellow PhD companions and good friends Anders Brask and Lennart Bitsch for their great support. Furthermore, many special thanks to Laurits H. Olesen for his great patience and for sharing his mammoth knowledge of FEMLAB.

Thanks to all former and present employees of MIC and DANCHIP for creating a pleasant and friendly working atmosphere. Finally, I would like to thank all my friends, my parents, my sister, and my girlfriend Karina for being there.

Mads Jakob Jensen
MIC – Department of Micro and Nanotechnology
Technical University of Denmark
Lyngby, August 31, 2005

Contents

List of Figures

List of Tables

List of Symbols

Symbol	Description	Unit
U	Characteristic velocity	m s^{-1}
L	Characteristic length	m
R (or r)	Radius	m
F	Force	N
p (or P)	Pressure	Pa
z	Axial coordinate	m
r	Radial coordinate	m
E_{tot}	Total surface energy	J
P_{clog}	Clogging pressure	Pa
ΔP_b	Pressure across a bubble	Pa
x_{cm}	Center of mass coordinate	m
V	Volume	m^3
p_{gas}	Gas pressure	Pa
Q	Flow rate	m^3 s^{-1}
Q_{out}	Outlet flow-rate	m^3 s^{-1}
Q_{in}	Inlet flow-rate	m^3 s^{-1}
Q_{g}	Gas flow-rate	m^3 s^{-1}
t	Time	s
V_b	Bubble volume	m^3
S	Curve arc length parameter	m
M	Number of boundary points	-
H	Outlet channel radius	m
d	Gas outlet diameter	m
W	Outlet length	m
h_{thr}	Thread radius	m
n	Power law exponent	-
$\boldsymbol{u} = (u, v)$	Velocity field	m s^{-1}
$\boldsymbol{n}$	Surface unit normal	-
$\boldsymbol{t}$	Surface tangent	-
$\boldsymbol{x} = (z, r)$	Position	m
$\boldsymbol{\sigma}$	Stress matrix	Pa=kg m^{-1} s^{-2}

$\boldsymbol{\nabla}$	Nabla or del operator	m^{-1}
$\boldsymbol{\Gamma}$	Flux matrix	(varying)
x_i	Coordinate component	m
u_i	Velocity component	m s^{-1}
σ_{ij}	Full stress tensor	Pa=kg m^{-1} s^{-2}
$\tau_{ij} = \sigma_{ij} + p\delta_{ij}$	Stress tensor	Pa=kg m^{-1} s^{-2}
n_i	Surface normal components	-
$\dot{\gamma}_{ij}$	Rate of strain tensor	s^{-1}
ρ	Density	kg m^{-3}
μ	Dynamic viscosity	Pa s=kg m^{-1} s^{-1}
γ	Surface tension	J m^{-2}
γ_{lg}	Liquid-gas surface tension	J m^{-2}
θ	Contact angle	-
κ	Curvature	m^{-1}
$\dot{\gamma}$	Shear rate	s^{-1}
φ	FEM basis function	-
ζ	Mesh size	-
Ω	Computational domain	-
$\partial\Omega$	Domain boundary	-
ϵ_ρ	Density ratio	-
ϵ_μ	Viscosity ratio	-
ℓ	Distance from bubble tip to outlet	m
η	General viscosity	Ps s
$Re = \rho U L/\mu$	Reynolds number	
$Ca = \mu U/\gamma$	Capillary number	
$\tilde{p}_2 = p_g asL/\mu U$	Dimensionless pressure	

Note: Dimensionless parameters have an added tilde. Take for example the dimensionless axial coordinate $\tilde{z} = z/L$.

Chapter 1

Introduction

In the last decade, great innovations in the microfluidic area have been made. Microfluidics is hydrodynamics in devices with scales less than a millimeter. A great amount of work has been put into the development of different components such as micropumps, microvalves, mixing chambers, and chemical reaction chambers. An integration of these components makes up the so-called "lab-on-a-chip" concept which is one of the driving ideas behind the research. The miniaturization process is revolutionizing the chemical, biochemical, and medical industry. Complete chemical and biological analyzes will be carried out in the lab-on-a-chip systems, also called Micro Total Analysis Systems (μTAS).

The microfluidic systems will most certainly make dramatic changes in the way laboratories work: smaller, cheaper, and fully automated devices will perform faster and more accurate measurements than today. The application prospects are wide. From easy environmental monitoring to medical monitoring of patients in geographically remote areas. The microfluidic field is vast, is in full expansion, and it is the subject of increasing investments from industry. The development and fabrication of integrated microfluidic devices require the use of special geometries and the interplay of many physical effects such as pressure driven flows, electrokinetics, magnetohydrodynamics, multi-phase flows, and capillarity [6]. As a consequence fascinating variants of classical well-studied fluid dynamic problems arise. The involved physics draw on classical theory for viscous flows and capillarity, see for instance Bachelor [7].

In microfluidics, viscous theory is applicable because small characteristic dimensions L and flow velocities U generally define flows with small Reynolds numbers $Re = \rho U L/\mu < 1$, where ρ is density and μ the dynamic viscosity. Moreover, surface tension related effects, associated with the presence of a free interface, introduce a unique type of force that scales directly to length. The capillary number $Ca = \mu U/\gamma$, where γ is the surface tension, defining the viscous stress to interfacial force ratio is generally small at the operating flow regimes. Hence, the surface tension forces dominate most other forces, such as gravity, pressure, and viscous drag. As the surface tension effects are directly related to lengths, the actual geometry of the device is cardinal. Furthermore as the bulk flow is mostly viscous, and therefore linear, the non-linearity of the system is embedded in the curvature of the free surface.

In the history of microfluidics, bubbles have most often been seen as an impediment rather than an asset [8, 9, 1, 2]. The bubbles are introduced into the liquid at the inlets or by electrolysis. Due to the small dimensions, the gas bubbles are prone to get stuck in sensitive places whereby they may clog the flow and completely eliminate the functionality of the microdevice. In recent years, however, the design of microfluidic devices making use of surface tension effects has been initiated. These include micro pumps using bubbles as actuators [10], two fluid pumps [11], devices where drops are used as chemical reactors [12], and devices creating controlled liquid-liquid emulsions [13], especially liquid-gas emulsions [14, 3, 15, 16].

The study of liquid-gas emulsions, and more specifically the generation of bubbles on the micrometer scale in a predefined geometry, makes it possible to investigate a variety of physical phenomena, such as capillarity, dripping, and bubbling processes. The initial studies were mainly experimental and more recently they have been driven by industrial applications of such devices, e.g., drop formation in ink-jet printing [17]. In recent years, studies have been concerned with the so-called flow-focusing configuration [14, 3, 4, 5, 15, 16]. One implementation seen via microfluidic devices allows for the generation of controlled multi-phase flows; this has mainly been investigated experimentally. Many interesting physical phenomena have been described, including flow-rate controlled breakup of gas threads [4], but also the appearance of chaotic behavior as reported in other bubbling devices [3, 5, 18].

Microfluidic devices are already at a stage where further efficient development requires the use of simulation capabilities. Advances in computational fluid dynamics (CFD) enable a better and less expensive design process. An effort in the CFD field should nevertheless be made together with a thorough theoretical study of the given problem and testing of the CFD models. Thus the numerical simulation of drop and bubble formation is also necessary. Modelling of free-surface dynamics includes the use of direct numerical techniques, such as the volume-of-fluid methods [41], tracer methods, and boundary-integral methods [20, 21]. A wide array of analytical and semi-analytical models have also been introduced such as, for example, the thin jet approximation [18, 22, 23, 24, 25].

This thesis is concerned with the numerical and theoretical description of interface dynamics in microfluidics. We shortly present our recently published work treating of the clogging of microchannel contractions by gas bubbles [1, 2]. The bulk of the present work deals with the development of a generic free-surface finite-element model for the simulation of axisymmetric geometries. The numerical model is based on an in-house MATLAB free surface and second order Runge–Kutta time integration scheme that interfaces with the commercial FEMLAB finite-element solver. The validity of the numerical results is assessed through a thorough testing where numerical results are compared with existing analytical results. The main result of the thesis is the presentation of a first numerical analysis of an axisymmetric flow-focusing device. We compare our numerical findings with existing experimental results and further develop on these. As our numerical model is very flexible we modify it and further study the physics of a flow-focusing device where the fluid follows a simple non-Newtonian model. An outline of the thesis is given below and, furthermore, every chapter is introduced by a presentation of necessary background material.

1.1 Outline of the thesis

- **Chap. 2 - Background: bubbles in microchannel contractions**
  We present the background of the work discussed in this thesis; it includes a presentation of a first theoretical paper by the author [1] and a second paper which has recently been submitted [2]. Both papers are concerned with the clogging of microchannels by bubbles.

- **Chap. 3 - Motivation: the flow-focusing device**
  In this chapter, we present how the author, while on a stay abroad at Harvard University, found the inspiration to study the flow-focusing device. Existing literature and experimental results are also presented here.

- **Chap. 4 - The governing equations**
  The governing equations for two-phase stokes flow are here presented together with a description of the necessary boundary conditions at free interfaces. The chapter also shortly presents a simple model for a non-Newtonian liquid.

- **Chap. 5 - Numerics: implementation**
  In this chapter, all the details of the implementation of our free-surface model are given. We focus on describing important numerical tricks used in the code.

- **Chap. 6 - Numerics: validation**
  In this part, we thoroughly test the numerical code on three test cases for which analytical results exist: (1) the benchmark problem of the surface driven coalescence of two infinite liquid cylinders, (2) we use the code to compute the steady state shape of a gas bubble moving in a liquid filled cylindrical capillary, and (3) we simulate the dynamics of a viscous drop in a viscous extensional-flow.

- **Chap. 7 - The flow-focusing device**
  This chapter is the main results chapter where the numerical simulations of the dynamics in an axisymmetric flow-focusing device are presented. The chapter is mainly based on a recently submitted paper [80]. Further details not presented in the paper are also detailed. Finally, the most recent unpublished work concerned with non-Newtonian fluids in the flow-focusing device is discussed.

- **Chap. 8 - Outlook and conclusion**
  We finalize the thesis by discussing possible further development of the code and also further application areas. Concluding remarks are also given here.

1.2 Publications during PhD studies

Peer reviewed research papers

1. *The clogging pressure of bubbles in hydrophilic microchannel contractions*,
   M. J. Jensen, G. Goranovic, and H. Bruus,
   J. Micromech. Microeng. **14**, 876 (2004).

2. *A novel electroosmotic pump design for nonconducting liquids: theoretical analysis of flow rate-pressure characteristics and stability*,
   A. Brask, G. Goranovic, M. J. Jensen, and H. Bruus
   J. Micromech. Microeng. **15**, 883 (2005).

3. *Transient pressure drops of bubbles passing through liquid filled microchannel contractions: an experimental and numerical study*,
   H. Chio, M. J. Jensen, X. Wang, H. Bruus, and D. Attinger
   Submitted to J. Micromech. Microeng., June 2005.

4. *A numerical study of two-phase Stokes flow in an axisymmetric flow-focusing device*,
   M. J. Jensen, H. A. Stone, and H. Bruus,
   Submitted to Physics of Fluids, August 2005.

Peer reviewed conference proceedings

1. *Dynamics of bubbles in microchannels*,
   M. J. Jensen, G. Goranovic, and H. Bruus,
   muTAS-2002, Nara, Japan, November 2002, proc. vol. 2, p. 733-735.

2. *Quasi-static Motion of Bubbles in Microchannel Contractions*,
   M. J. Jensen, G. Goranovic, and H. Bruus,
   NanoTech 2003, San Francisco, USA, February 2003, proc. vol. 1, p. 258-261. [**oral presentation**]

3. *Clogging pressures of bubbles in microchannel contractions: theory and experiments*,
   M. J. Jensen, X. Wang, D. Attinger, and H. Bruus,
   NanoTech 2004, Boston, USA, March 2004.

4. *Numerical and experimental investigation of bubble pinch-off in the flow-focusing device*,
   M. J. Jensen, P. Garstecki, M. Fuerstman, H. Bruus, G. M. Whitesides, and H. A. Stone,
   muTAS-2004, Malmö, Sweden, September 2004, proc. vol. 1, p. 626-628.

5. *Fast packaging of polymeric cantilever chip by micromilling*,
   A. Johansson, G. Perozziello, M. J. Jensen, O. Geschke, and A. Boisen,
   International Conference on Multi-Material Micro Manufacture (4M), Karlsruhe, Germany 2004.

6. *Numerical simulation of two phase flow in the flow-focusing device*,
   M. J. Jensen and H. Bruus,
   Euromech Colloquium 472 on Microfluidics and Transfer, September 6-8, 2005, Grenoble, France. [**oral presentation**]

Chapter 2

Background: bubbles in microchannel contractions

The intention of this chapter is to present the work made in the first part of my PhD studies. It thus provides the reader an insight into my long lasting interest in multi-phase flow problems in microfluidics. The chapter will not go into details, as it is my wish that the most significant part of the present thesis should be concerned with my newly developed code and its applications. The rest of the thesis deals with the development, testing and application of my free surface flow finite-element model.

During my MSc thesis work and especially my PhD studies, I have studied the physics of two-phase flows in microscale geometries (two-phase microfluidics). The studies have mainly been concerned with the numerical and theoretical treatment of quasi stationary systems with liquid-gas interfaces and with numerical simulations of time-dependent free-surface two-phase Stokes-flow problems. The work has mainly focused on the significant

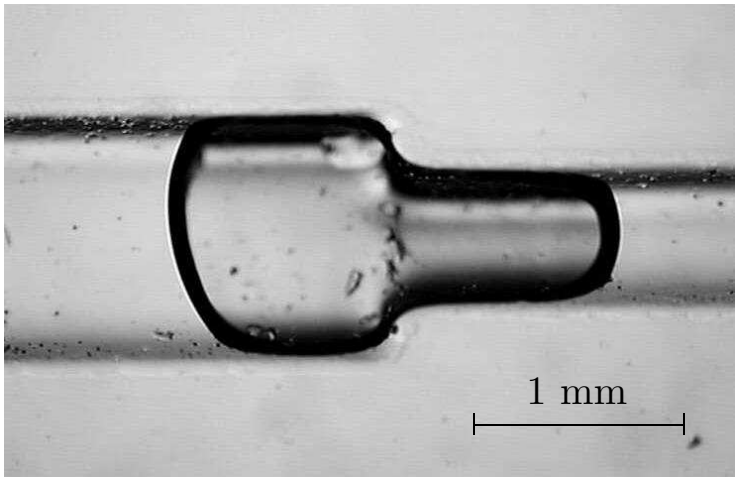

Figure 2.1: Microscope picture of a gas bubble getting stuck in a liquid filled microchannel contraction. The channel was created by laser ablation of a PMMA substrate.

influence geometry has on the dynamics in these microfluidic systems. During my research stay at Harvard university in the spring of 2004 I started developing my own free surface model to model the flow-focusing configuration. The motivation for this part of my work is presented in Chap. 3.

My initial bubble studies were chiefly motivated by the fact that gas bubbles present in microfluidic devices are prone to get stuck at, e.g., channel contractions. Hereby bubbles can clog the main liquid flow and disturb measurements or functionality of the microfluidic system in an uncontrolled manner. The microscope picture in Fig. 2.1 depicts how a gas bubble is stuck in a microchannel contraction. Although these problems related to two phase systems were already identified a decade ago [8, 9] they had not been studied theoretically to a great extent. Using a simple model system of a capillary contracting linearly from a large constant radius R to a small constant radius r we presented such a first study in a paper published in Journal of Micromechanics and Microengineering [1]. The work was inspired by results obtained while writing my MSc thesis [27]. We restricted our analysis to the quasi-stationary motion of a hydrophilic wetting bubble through the contraction. A small summary of the paper and the main results are presented in Sec. 2.1 below. The paper is presented in its full length in Appendix C.

The theoretical results from the paper were presented by my supervisor Henrik Bruus when he was invited to SmallTalk 2003 *The microfluidics, microarrays, and bioMEMS conference and exhibition, San Jose (CA), 13-16 July 2003.* In the audience Associate Prof. Daniel Attinger[1] found the problem very interesting and proposed a collaboration. The group of D. Attinger has a large experimental expertise. We initiated a collaboration and D. Attinger started an experimental study of gas bubbles passing through microchannel contractions in glass capillaries. The culmination of our work was the submission of an experimental and theoretical paper to the Journal of Micromechanics and Microengineering [2] in July of 2005. We give a short review of our work in Sec. 2.1 while the paper is presented in full length in Appendix E.

2.1 Theoretical paper

In the paper *The clogging pressure of bubbles in hydrophilic microchannel contractions* [1] we present a general semi-analytical model for the quasi static motion of a compressible gas bubble through an axisymmetric channel with a contraction of arbitrary shape $r(x)$. A sketch of the physical system with various labels is depicted in Fig. 2.2.

In most cases the total energy E_{tot} of a bubble of surface tension σ increases when it is moved from a wide channel (of radius R) to a narrow channel (of radius r), and the bubble thus tends to clog the flow of the fluid.[2] The so-called clogging pressure P_{clog} is needed to

[1] From the Dept. of Mechanical Engineering, State University of New York at Stony Brook, NY, USA.

[2] All dynamic components of the energy disappear as we are studying a quasi stationary system. As the surface to volume ratio is very large in microfluidics the only energy we need to take into account is the total interfacial energy.

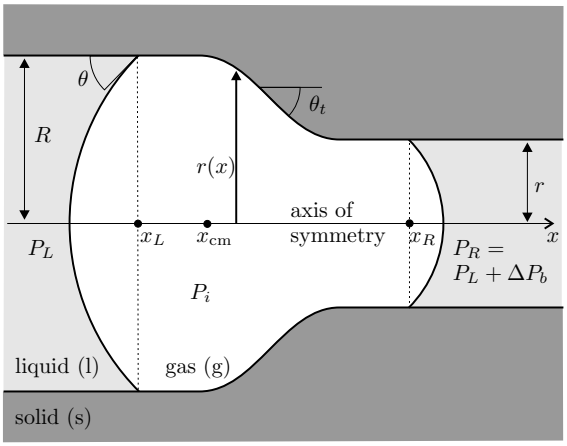

Figure 2.2: Sketch of a bubble with internal pressure P_i, center of mass coordinate x_{cm}, left (right) contact line coordinate x_L (x_R), contact angle $\theta < 90°$, and tapering angle $\theta_t = \arctan[-r'(x)]$. The channel is contracting from constant large radius R to small radius r. The specific channel profile is defined by some function $r(x)$. The pressure left (right) of the bubble is denoted P_L (P_R) and the pressure difference across the bubble is $\Delta P_b = P_R - P_L$.

push the bubble out of or through the contraction. However, in the case of a hydrophilic channel contraction there exists a range of parameters where the bubble gains energy by moving into the narrow part of the channel. Two examples of such situations are given in Figs. 2.3 and 2.4. Respectively five and four snapshots of the bubble are given together with the associated energy curve $E_{\mathrm{tot}}(x_{\mathrm{cm}})$, where x_{cm} is the center of mass coordinate of the bubble. The related force $F = dE_{\mathrm{tot}}/dx_{\mathrm{cm}}$ on the bubble and the pressure drop across the bubble $\Delta P_b(x_{\mathrm{cm}})$ are also depicted.

The most rare behavior is shown in Fig. 2.3, here with a tapering angle of the contraction of $\theta_t = 10°$. In this case the energy $E_{\mathrm{tot}}(x_{\mathrm{cm}})$ decreases monotonically as function of x_{cm} which means that the bubble is sucked through the channel as it gains energy. In the second and more general case illustrated in Fig. 2.4, where $\theta_t = 20°$, an energy barrier appears on the energy curve. In this case the force F takes positive values which means that a pressure needs to be applied at the left of the bubble to push it through the contraction. These two examples of parameters are only two of the many parameters analyzed in the paper.

In the paper we further apply the energy analysis tool to a parametric study of varying geometries. We conclude by giving a set of geometrical design rules for constructing microfluidic channel contractions that reduce or prevent clogging. Most importantly a system should preferably be designed such that gas bubbles cannot span the entire contraction region.

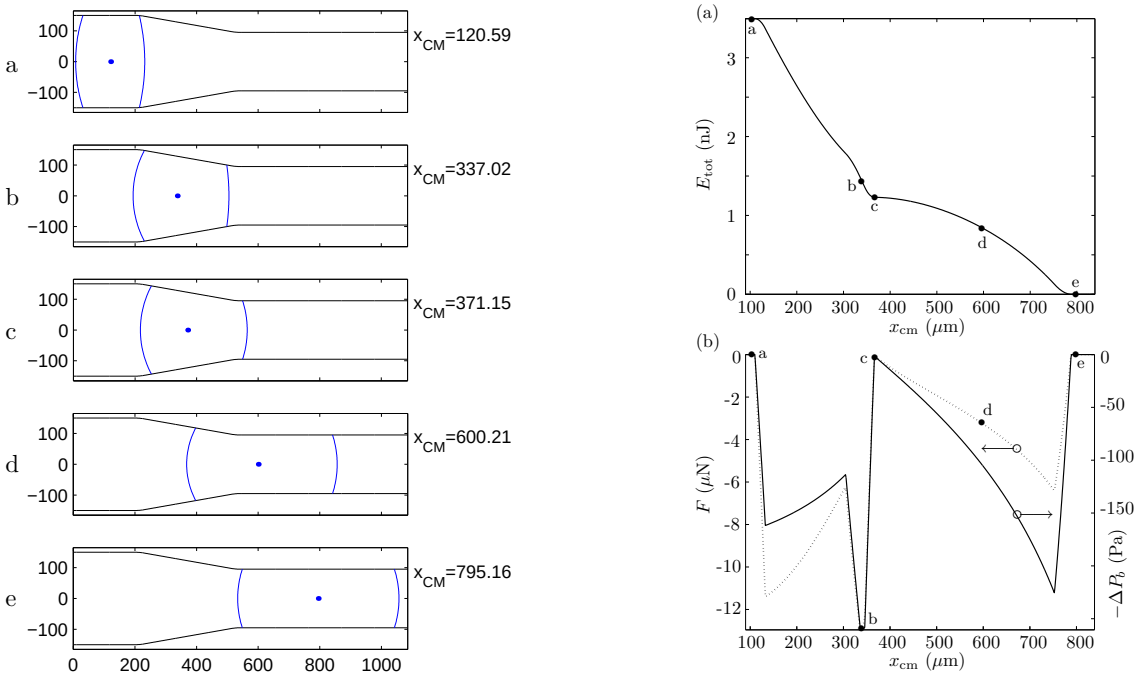

Figure 2.3: Snapshots, energy curve, force curve, and pressure curve for a bubble moving from an $R = 150$ μm to an $R = 100$ μm channel. The contraction is linear and has a tapering angle of $\theta_t = 10°$. The contact angle $\theta = 72°$.

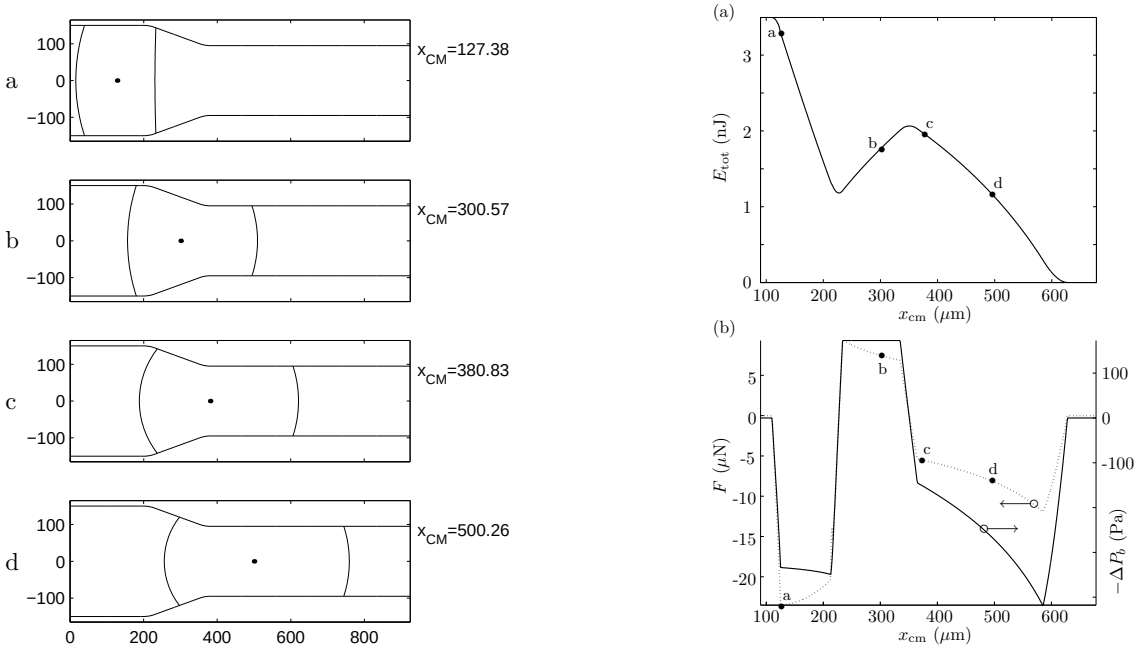

Figure 2.4: Snapshots, energy curve, force curve, and pressure curve for a bubble moving from an $R = 150$ μm to an $R = 100$ μm channel. The contraction is linear and has a tapering angle of $\theta_t = 20°$. The contact angle $\theta = 72°$.

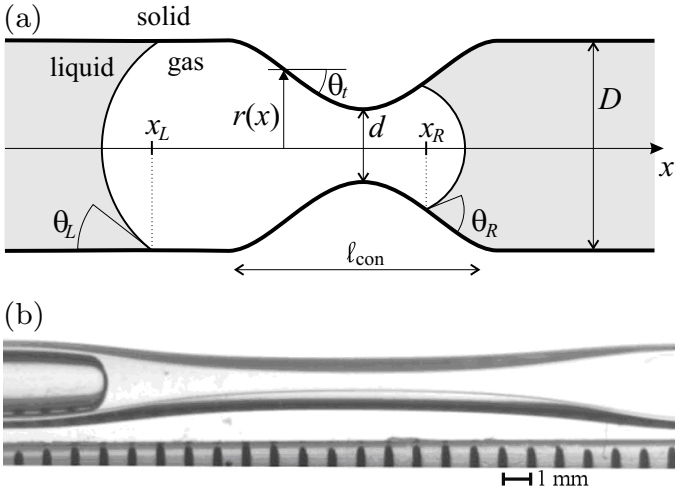

Figure 2.5: (a) Sketch of the gas-liquid-solid system with channel profile $r(x)$, main diameter D, contraction diameter d, left and right contact angles θ_L and θ_R, left and right contact line position x_L and x_R, length of the contraction ℓ_{con}, and local tapering angle θ_t. (b) Photograph of a gas bubble (dark gray) entering from the left into a liquid-filled (white) tube with a 490 μm contraction. The flow rate Q of the liquid is 0.33 μL/s.

2.2 Experimental and numerical paper

In the paper *Transient pressure drops of gas bubbles passing through liquid-filled microchannel contractions: an experimental and numerical study* [2] we compare the theoretical results first presented in our paper [1] with experimental results produced in the group of D. Attinger. The numerical implementation of the theoretical model is modified so that it can handle any tube shape $r(x)$ as well as different advancing and receding contact angles, see Fig. 2.5.

With the experimental set-up, which is depicted in Fig. 2.6, the pressure difference across the bubble was monitored together with the bubble position. The position and motion of the bubble was controlled by the liquid flow rate Q using a syringe pump. Ample details about the experimental setup are found in the paper.

An example of a comparison between the theoretical model and the experimental results is given in Fig. 2.7. The pressure across the bubble ΔP_b is plotted as function of the displaced liquid volume $V_{\text{in}} = Qt$, where t is time. The first peak on the curve corresponds to the passage of the right meniscus through the contraction while the second negative peak corresponds to the passage of the left meniscus. From the figure it is evident that the theory deviates from the experiments at the second passage. In the paper we describe the possible reasons for this discrepancy, they include: drying of deposited wetting liquid films, stick slip motion of contact lines, as well as bubble deformation.

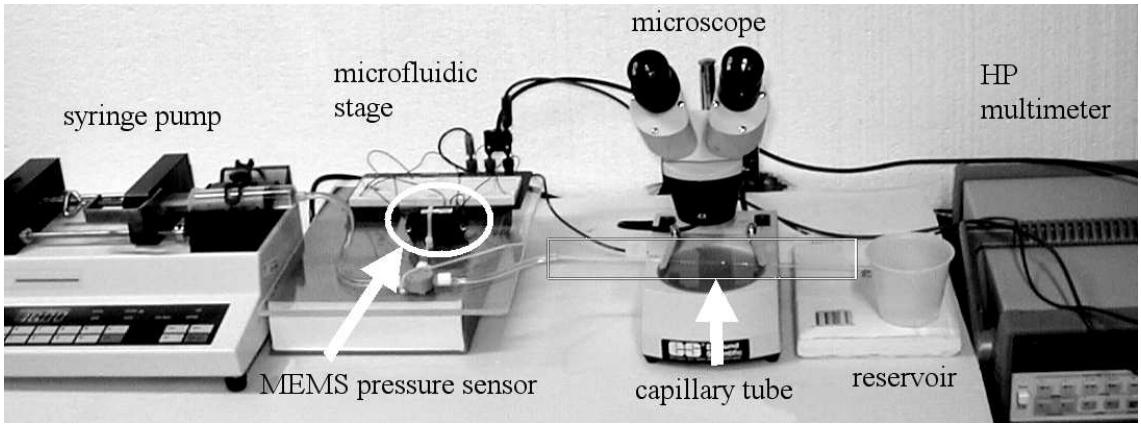

Figure 2.6: Measurement set-up allowing for transient visualization and pressure measurement during the transport of a microbubble in a microchannel.

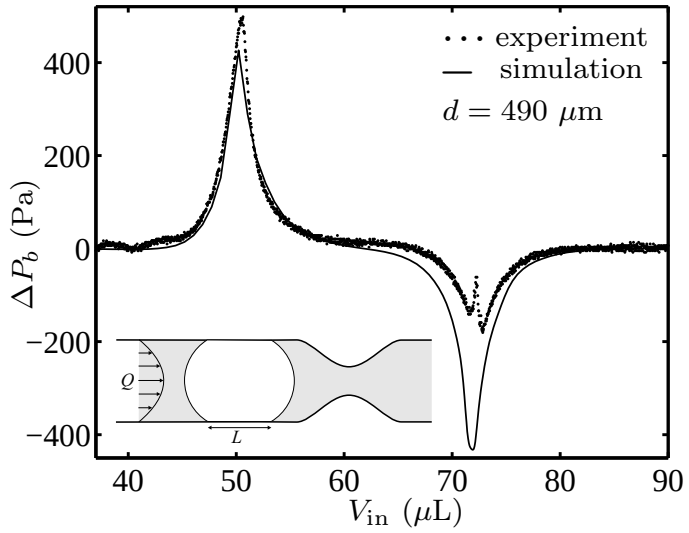

Figure 2.7: Direct measurements with the MEMS pressure sensor (dots) and simulation based on measured shape (full line) of the pressure across a long $L = 8$ mm bubble in tube A7 for $Q = 0.33$ μL/s as a function of displaced liquid volume $V_{\rm in} = Qt$, where t is the time. The observed values of the advancing and receding wetting angle used for the simulations are 10° and 9°, respectively. The inset indicates the bubble length L and the liquid flow rate Q.

Chapter 3

Motivation: the flow-focusing device

In the spring of 2004 and as part of my PhD studies I had the opportunity to have a five month research stay in the group of Prof. H. A. Stone in the Division of Engineering and Applied Sciences (DEAS) at Harvard University. During the first few weeks of the stay I visited several groups at Harvard and got to meet Piotr Garstecki of the Whitesides group who conducted experiments with the so-called flow-focusing configuration on a microfluidic chip. Because of my great interest in geometry dependent two-phase phenomena in microfluidics I got very interested and we started a small collaboration. I had no specific project description for my stay abroad and thus engaged in developing a numerical model for simulating the dynamics of a free interface in an axisymmetric version of the flow-focusing geometry. The model and the numerical results that the code has produced are amply discussed in the rest of this thesis.

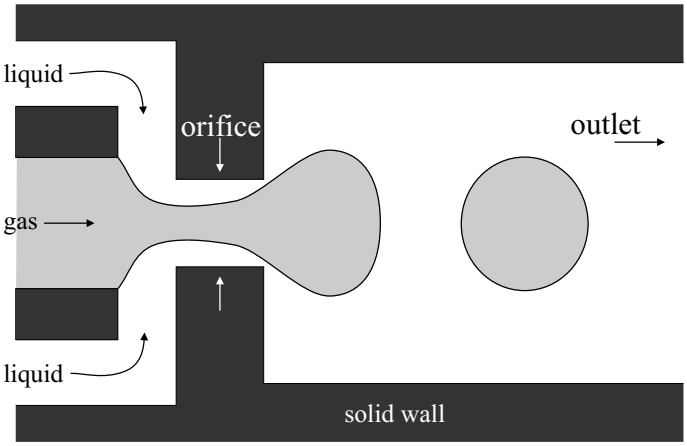

Figure 3.1: Sketch of a flow-focusing device where a gas jet under constant pressure p_{gas} is focused into the orifice region by a liquid flow at flow rate Q_{in}. Bubbles are created periodically when gas volumes snap-off.

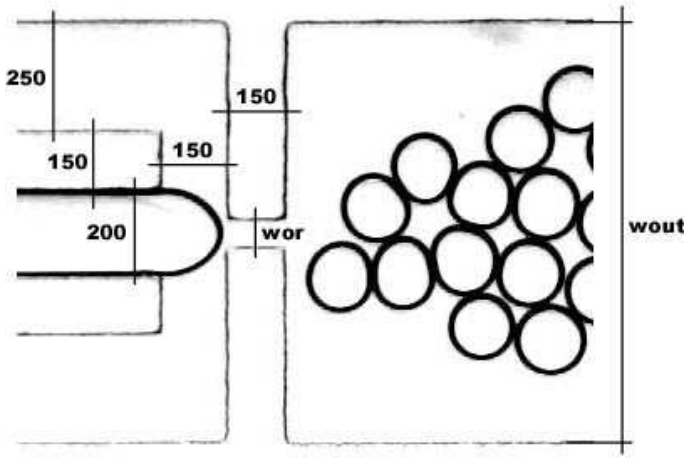

Figure 3.2: Micrograph of a planar microfluidic flow-focusing device the characteristic lengths are given in micrometers. By courtesy of P. Garstecki.

A sketch of a planar flow-focusing configuration is given in Fig. 3.1. A gas thread at constant pressure p_{gas} is focused into the orifice region by a liquid stream with flow rate Q_{in}. Over a wide range of the flow parameters the gas thread breaks periodically and delivers bubbles of nearly constant volume into the outlet channel [14, 3]. The first work reporting the formation of bubbles in a microfluidic flow-focusing like configuration was by Gañán-Calvo and Gordillo [15], they used a technique called capillary flow focusing. The first implementation of a flow-focusing device onto a planer microchannel design was done by Anna *et al.* [14]. For this study the channels were produced using soft lithography which allows for rapid fabrication and on-chip integration of the system. In the more recent extensive studies of the flow-focusing device by Garstecki *et al.* [3, 4, 5] the device is also used on-chip and in a planar microfluidic configuration, see the micrograph of Fig. 3.2. In the recent paper by Utada *et al.* [13] they report using an axisymmetric version of the flow-focusing device.

From an industrial point of view the flow-focusing device is very interesting as it can produce microbubbles of very constant volume and at high bubbling frequencies. The devices have countless applications and are in particular interesting in fundamental medical applications, in on-chip separation procedures, in the production of special foams and many more. An example of such a structured foam produced by a microfluidic flow-focusing device is given in Fig. 3.3. By adding a surfactant to the liquid the bubbles do not coalesce and naturally arrange in a lattice-like structure [3]. Further applications of the flow-focusing configuration include the creation of liquid-liquid emulsions, double emulsions [13], and micro beads.

In the academic world the flow-focusing device is of paramount interest as it enables for the study of a rich variety of hydrodynamic phenomena: (1) In a microfluidic implementation the device allows for the study of breakup in a confined geometry. Garstecki *et al.* describe the flow-rate controlled snap-off mechanism [4], where the dynamics of the

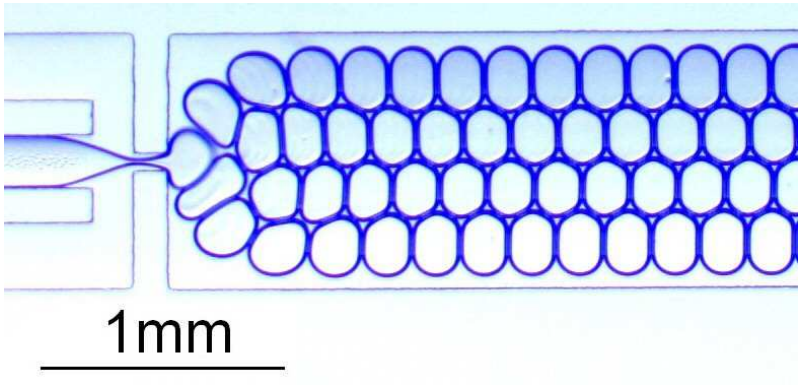

Figure 3.3: Microscope picture of bubbles that have arranged in a lattice like structure in the outlet channel of a planar microfluidic flow-focusing device. By courtesy of P. Garstecki.

breakup of the gas thread are entirely controlled by the liquid flow-rate Q_{in}. The study describe deviations from the classical capillary instability. Moreover, it explains why the volume of the bubbles created in the device V_b scale as $V_b \propto p_{\text{gas}}/\mu Q_{\text{in}}$. We discussed this scaling in detail in Chap. 7 and confirm it by means of numerical simulations. (2) The flow-focusing device further exhibits rich nonlinear behavior when it is bubbling. When monitoring the volume of the bubble V_b as function of the liquid flow-rate Q_{in} Garstecki *et al.* [5] describe period doubling, halving bifurcations, and chaotic behavior. The system is seen to exhibit similarity with the dripping faucet [18].

The diverseness of the dynamics in the two-phase flow of the flow-focusing device greatly motivated my decision to initiate a numerical study. The use of computational fluid dynamics (CFD) enables the analysis of a wide range of parameters and provides a detailed picture of the dynamics. It is the intent of the simulations to help fully understand the experimental results. Especially it is relatively easy to vary geometric parameters when conducting a numerical study whereas it is quite time consuming when performing experiments. As a first step towards modelling the full 3D dynamics corresponding to the experimental results in a planar geometry we chose to model an axisymmetric version of the flow-focusing device. This of course bearing in mind that the difference in geometry most probably will influence on some of the dynamics.

Chapter 4

The governing equations

The cornerstone of any numerical study is the definition a set of governing equations characterizing the physics of the system at hand. In this chapter we will present the basic governing equations of fluid dynamics. The main focus of this chapter will be on formulating the equations in an axisymmetric system of coordinates and on rewriting the equations into a divergence form that is suited for numerical implementation in FEMLAB.

The most general form of the equations is firstly presented and then the axisymmetric formulation for Newtonian fluids is given. We then move on to describing the very important conditions that apply at an interface between two immiscible fluids. Related to that is the description of the curvature of a surface of revolution. Further, we describe the re-scaling of the governing equations to a dimensionless form. The equations are then reformulated in a divergence form for a fluid-fluid system and a liquid-gas system, respectively. Second to last we list the equations for the case of zero Reynolds-number flows and, finally, we present the power-law model for describing a non-Newtonian liquid.

4.1 The equations of motion

The momentum conservation equation for a fluid in the continuum approximation is the Navier–Stokes equation. In an isothermal system the momentum equation in tensor form it is given as

$$\rho\left(\frac{\partial u_i}{\partial t} + u_j\frac{\partial u_i}{\partial x_j}\right) = \frac{\partial \sigma_{ij}}{\partial x_j} \tag{4.1}$$

where i and j run over the spatial dimensions and implicit summation is assumed, ρ is the density of the fluid, σ_{ij} is the full stress tensor, t is time, u_i is a velocity component, and x_i is a spatial variable component. The conservation of mass in the fluid system is given by the continuity equation

$$\frac{\partial \rho}{\partial t} + \frac{\partial(\rho u_i)}{\partial x_i} = 0. \tag{4.2}$$

The momentum Eq. (4.1) and the mass conservation Eq. (4.2) together with a constitutive equation for the stress tensor σ_{ij} form the equations of motion of the fluid. These

three equations together with appropriate boundary conditions (BCs) compose a closed system for finding the flow field (u_i, p, ρ) in the fluid [28, 7, 29, 30, 31]. In the case of an incompressible fluid where the density ρ is constant the continuity Eq. (4.2) reduces to the incompressibility condition

$$\frac{\partial u_i}{\partial x_i} = 0. \tag{4.3}$$

In vector notation Eqs. (4.1) and (4.2) are written as,

$$\rho\left(\frac{\partial \boldsymbol{u}}{\partial t} + (\boldsymbol{u}\cdot\boldsymbol{\nabla})\boldsymbol{u}\right) = \boldsymbol{\nabla}\cdot\boldsymbol{\sigma} \tag{4.4}$$

$$\frac{\partial \rho}{\partial t} + \boldsymbol{\nabla}\cdot(\rho\boldsymbol{u}) = 0 \tag{4.5}$$

where $\boldsymbol{u}$ is the velocity vector and $\boldsymbol{\sigma} = [\sigma_{ij}]$ is the stress matrix. The incompressibility condition Eq. (4.3) is simply $\boldsymbol{\nabla}\cdot\boldsymbol{u} = 0$.

4.2 Axisymmetric equations of motion

In the main part of this thesis we will be studying Newtonian incompressible fluids. Moreover, the systems we investigate are generally axisymmetric, see the (z, r, ϕ) system of coordinates in Fig. 4.1. In the case of flows that have no periodic component in the angular direction ϕ the Navier–Stokes Eq. (4.1) reduces to

$$z\text{-mom.:} \qquad \rho\left[\frac{\partial u}{\partial t} + v\frac{\partial u}{\partial r} + u\frac{\partial u}{\partial z}\right] = -\frac{\partial p}{\partial z} + \mu\left[\frac{1}{r}\frac{\partial}{\partial r}\left(r\frac{\partial u}{\partial r}\right) + \frac{\partial^2 u}{\partial z^2}\right] \tag{4.6}$$

$$r\text{-mom.:} \qquad \rho\left[\frac{\partial v}{\partial t} + v\frac{\partial v}{\partial r} + u\frac{\partial v}{\partial z}\right] = -\frac{\partial p}{\partial r} + \mu\left[\frac{1}{r}\frac{\partial}{\partial r}\left(r\frac{\partial v}{\partial r}\right) + \frac{\partial^2 v}{\partial z^2} - \frac{v}{r^2}\right], \tag{4.7}$$

where z is the axial coordinate, r the radial coordinate, u the axial velocity, v the radial velocity, p the pressure, and μ is the dynamic viscosity [28]. The first equation is the momentum equation in the axial direction and the second in the radial direction. In an axisymmetric system the continuity condition for an incompressible fluid is

$$\frac{1}{r}v + \frac{\partial v}{\partial r} + \frac{\partial u}{\partial z} = 0. \tag{4.8}$$

For the case of an isotropic Newtonian-fluid the constitutive stress tensor components are

$$\sigma_{ij} = \mu\left(\frac{\partial u_i}{\partial x_j} + \frac{\partial u_j}{\partial x_i}\right) - \delta_{ij}p \tag{4.9}$$

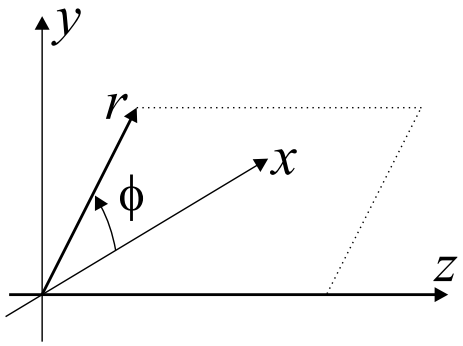

Figure 4.1: Sketch of a cylindrical system of coordinates (z, r, ϕ) and a rectangular system of coordinates (x, y, z). The zr-plane is unchanged in an axisymmetric system.

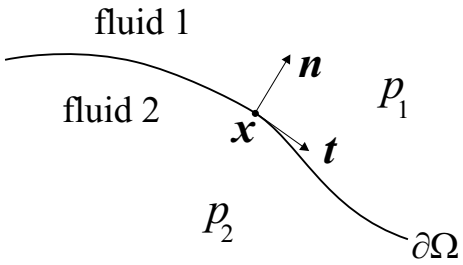

Figure 4.2: Sketch of an free interface $\partial\Omega$ between fluid 1 and fluid 2, of respective pressures p_1 and p_2. The surface normal is $\boldsymbol{n}$ and the surface tangent is $\boldsymbol{t}$ at the interface position is $\boldsymbol{x}$.

and the respective components of the stress tensor $\boldsymbol{\sigma}$ in an axisymmetric system of coordinates are

$$\sigma_{zz} = 2\mu\frac{\partial u}{\partial z} - p, \tag{4.10}$$

$$\sigma_{rr} = 2\mu\frac{\partial v}{\partial r} - p, \tag{4.11}$$

$$\sigma_{zr} = \sigma_{rz} = \mu\left(\frac{\partial u}{\partial r} + \frac{\partial v}{\partial z}\right). \tag{4.12}$$

4.3 Free surface conditions

Consider a system consisting of two immiscible fluids with interface $\partial\Omega$ see Fig. 4.2. The two domains are marked 1 and 2 and have the material properties (μ_1, ρ_1) and (μ_2, ρ_2), respectively. The velocity field is denoted u_i throughout the fluid domains as it is continuous across an interface. The pressure however is not continuous when the interface has a tension. In Fig. 4.2 the pressure is denoted p_1 in domain 1 and so forth. At the location of the free surface between the fluids there is continuity of the stress tensor in the tangential direction, and a discontinuity in the normal direction. The size of the pressure

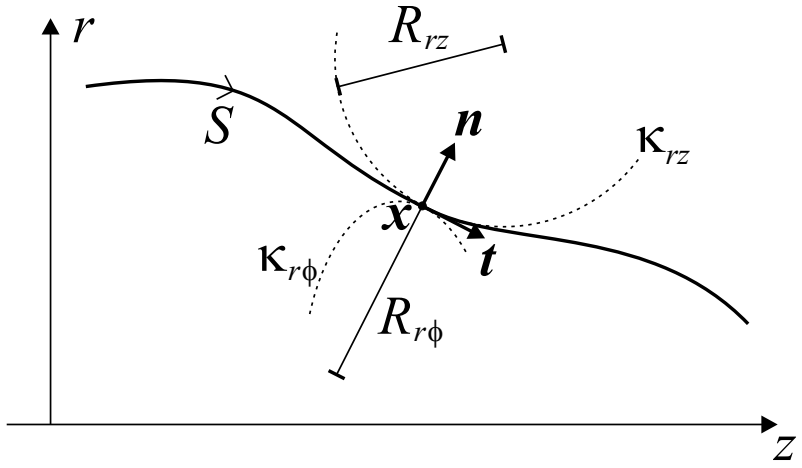

Figure 4.3: Sketch of a meridian curve $\boldsymbol{x}(S)$ to a surface of revolution. The meridian curve is parameterized by S with tangent $\boldsymbol{t}(S)$ and normal $\boldsymbol{n}(S)$. The two principal curvatures of the surface of revolution are $\kappa_{rz} = 1/R_{rz}$ in the rz-plane and $\kappa_{r\phi} = 1/R_{r\phi}$ in a plane with normal $\boldsymbol{t}$, see Fig. 4.1.

discontinuity Δp is prescribed by the Young–Laplace equation,

$$\Delta p = \gamma\kappa, \quad \kappa = \boldsymbol{\nabla}_s \cdot \boldsymbol{n}, \tag{4.13}$$

where γ is the surface tension, κ the mean curvature of the interface (see below), $\boldsymbol{n}$ the unit surface normal, and $\boldsymbol{\nabla}_s$ the gradient operator along $\partial\Omega$. This condition regarding the stress translates to the dynamic boundary condition,

$$n_j\sigma_{2,ij} - n_j\sigma_{1,ij} = \gamma\kappa n_i, \tag{4.14}$$

where the indices i and j run over the spacial dimensions z and r, and $\boldsymbol{n} = (n_1, n_2) = (n_z, n_r)$ is the unit normal at the interface. The expression at the left side of the equal sign is the total resulting force on the interface while the right side tells that the force is normal to the interface and proportional to $\gamma\kappa$.

At the free surface the interface must move at the speed of a fluid element just next to it, i.e., continuity of the velocity field. This condition is the kinematic boundary condition for the free surface,

$$\frac{dx_i}{dt} = u_i \quad x_i \in \partial\Omega, \tag{4.15}$$

where we have taken the total time-derivative. This last condition is often used computationally to update the interface shape.

4.4 The curvature κ

The curvature term κ in Eq. (4.14) is given as the mean of the two principal normal curvatures of a surface. The curvature is also expressed mathematically as the trace of the so-called Weingarten map matrix [27, 32, 33].

In the case of an axisymmetric systems all surfaces are represented by a surfaces of revolution defined by a meridian curve. In Fig. 4.3 the meridian curve is defined by a parametric curve $\boldsymbol{x}(S) = [z(S), r(S)]$. In this case the two main curvatures are in the rz-plane and in the plane spanned by the normal $\boldsymbol{n}(S)$ and the unit normal $\boldsymbol{e}_\phi$. The two components of the curvature are named κ_{rz} and $\kappa_{r\phi}$, respectively. The total curvature κ is hence

$$\kappa = \kappa_{rz} + \kappa_{r\phi}. \tag{4.16}$$

In the following formulation S is not assumed to be the arc length parameter ℓ but any parameter, hence $S = S(\ell)$.

The curvature $\kappa_{rz} = 1/R_{rz}$ is found, by using a fundamental results from the theory of curves [33], as

$$\frac{\partial \boldsymbol{t}}{\partial \ell} = \kappa_{rz}\boldsymbol{n} \quad \Rightarrow \quad \kappa_{rz} = \left|\frac{\partial \boldsymbol{t}}{\partial \ell}\right|, \tag{4.17}$$

where by the chain rule we have

$$\frac{\partial}{\partial \ell} = \frac{\partial}{\partial S}\frac{\partial S}{\partial \ell} = \frac{\partial}{\partial S}(\dot{\boldsymbol{x}} \cdot \dot{\boldsymbol{x}})^{-1/2}, \tag{4.18}$$

and a dot represents differentiation with respect to S. Using these relations the curvature κ_{rz} is found as

$$\kappa_{rz} = \frac{\dot{z}\ddot{r} - \dot{r}\ddot{z}}{(\dot{r}^2 + \dot{z}^2)^{3/2}}. \tag{4.19}$$

The second part of the curvature $\kappa_{r\phi}$ is found by projecting the inverse radius $r(S)^{-1}$ onto the normal $\boldsymbol{n}$ and yields

$$\kappa_{r\phi} = \frac{1}{R_{r\phi}} = \frac{n_r}{r} = \frac{-\dot{z}}{r(\dot{r}^2 + \dot{z}^2)^{1/2}}, \tag{4.20}$$

where $R_{r\phi}$ is defined on Fig. 4.3 and lies in the plane with $\boldsymbol{t}$ as surface normal (spanned by $\boldsymbol{n}$ and $\boldsymbol{e}_\phi$). The two components of the unit normal are

$$(n_z, n_r) = \left(\frac{\dot{r}}{(\dot{r}^2 + \dot{z}^2)^{1/2}}, \frac{-\dot{z}}{(\dot{r}^2 + \dot{z}^2)^{1/2}}\right). \tag{4.21}$$

4.5 Dimensionless form

It is always advantageous to render the governing equations dimensionless. We have re-scale the equations with respect to a characteristic length L and a characteristic velocity U. The specific choice of U and L is discussed and pointed out in every specific problem discussed in this thesis. The pressure is in the following re-scaled with respect to the viscous stress measure $\mu U/L$. A re-scaling of the pressure with the Young–Laplace pressure γ/L is often used in capillary systems[1]. For high Reynolds-number flows the pressure is normally scaled with respect to the the dynamic pressure measure ρU^2.

[1] When the dynamics of the system are governed by the forces at the free interface it is suitable to scale the velocity by γ/μ. This is especially the case when non-controlled capillary instabilities occur. They propagate at the interface at the natural speed $U = \gamma/\mu$, see Refs. [34, 23] for further details.

With the present choice of pressure scaling the re-scaled flow variables are thus given by

$$x_i = L\,\tilde{x}_i, \quad u_i = U\,\tilde{u}_i, \quad t = \tilde{t}\frac{L}{U}, \quad \text{and} \quad p = \tilde{p}\frac{\mu U}{L}. \tag{4.22}$$

where a tilde over a symbol represents a dimensionless quantity. Using this re-scaling we may rewrite the Navier–Stokes Eq. (4.6) and (4.7), and the continuity Eq. (4.8) as

$$Re\left[\frac{\partial\tilde{u}}{\partial\tilde{t}} + \tilde{v}\frac{\partial\tilde{u}}{\partial\tilde{r}} + \tilde{u}\frac{\partial\tilde{u}}{\partial\tilde{z}}\right] = -\frac{\partial\tilde{p}}{\partial\tilde{z}} + \left[\frac{1}{\tilde{r}}\frac{\partial}{\partial\tilde{r}}\left(\tilde{r}\frac{\partial\tilde{u}}{\partial\tilde{r}}\right) + \frac{\partial^2\tilde{u}}{\partial\tilde{z}^2}\right], \tag{4.23}$$

$$Re\left[\frac{\partial\tilde{v}}{\partial\tilde{t}} + \tilde{v}\frac{\partial\tilde{v}}{\partial\tilde{r}} + \tilde{u}\frac{\partial\tilde{v}}{\partial\tilde{z}}\right] = -\frac{\partial\tilde{p}}{\partial\tilde{r}} + \left[\frac{1}{\tilde{r}}\frac{\partial}{\partial\tilde{r}}\left(\tilde{r}\frac{\partial\tilde{v}}{\partial\tilde{r}}\right) + \frac{\partial^2\tilde{v}}{\partial\tilde{z}^2} - \frac{\tilde{v}}{\tilde{r}^2}\right], \tag{4.24}$$

$$\frac{\tilde{v}}{\tilde{r}} + \frac{\partial\tilde{v}}{\partial\tilde{r}} + \frac{\partial\tilde{u}}{\partial\tilde{z}} = 0, \tag{4.25}$$

where Re is the Reynolds number $Re = \rho UL/\mu$. When using the re-scaled version of the governing equations the dynamic boundary condition Eq. (4.14) is rewritten as

$$n_j\tilde{\sigma}_{2,ij} - n_j\tilde{\sigma}_{1,ij} = \frac{1}{Ca}\tilde{\kappa}n_i, \tag{4.26}$$

where $Ca = \mu U/\gamma$ is the capillary number[2], $\tilde{\sigma}_{ij}$ is the dimensionless stress tensor, and the curvature scales as $\kappa = \tilde{\kappa}/L$.

4.6 Divergence form: general case

When the momentum and continuity equations are solved numerically they have to be formulated in a form suitable for implementation with the finite element solver FEMLAB a detailed discussion about this is given in Chap. 5. This reformulation is called a divergence form it is defined as follows

$$d_a\frac{d\tilde{\boldsymbol{U}}_k}{d\tilde{t}} + \tilde{\boldsymbol{\nabla}}\cdot\tilde{\boldsymbol{\Gamma}}_k = \tilde{\boldsymbol{F}}_k, \tag{4.27}$$

where $\tilde{\boldsymbol{U}}_k = (\tilde{u}, \tilde{v}, \tilde{p}_k)$, $\tilde{\boldsymbol{\Gamma}}_k = \tilde{\boldsymbol{\Gamma}}_k(\tilde{z}, \tilde{r}, \tilde{p}_k, \tilde{u}, \tilde{v}, \frac{\partial\tilde{u}}{\partial\tilde{z}}, ...)$, $\tilde{\boldsymbol{F}}_k = \tilde{\boldsymbol{F}}_k(\tilde{z}, \tilde{r}, \tilde{p}_k, \tilde{u}, \tilde{v}, \frac{\partial\tilde{u}}{\partial\tilde{z}}, ...)$, d_a is called the mass parameter, and k is the fluid domain number. In the dimensionless governing equation, Eqs. (4.23) to (4.25), many terms are divided with $\tilde{r}$ and one with $\tilde{r}^2$. Such terms are not suitable for computation as they are very sensitive to the numerical precision near the singularity at $\tilde{r} = 0$. To help correct this the governing equations are multiplied by $\tilde{r}$.

[2]When defining the capillary number and the Reynolds number a clear definition has to be given. Specifically in systems with two fluids it is important which material properties are used. This is further discussed below.

Governing equations: After multiplication with $\tilde{r}$ and some algebra the governing equations in liquid 1 may be reformulated to

$$\begin{bmatrix} \tilde{r}Re\frac{\partial \tilde{u}}{\partial \tilde{t}} \\ \tilde{r}Re\frac{\partial \tilde{v}}{\partial \tilde{t}} \\ 0 \end{bmatrix} + \tilde{\boldsymbol{\nabla}} \cdot \begin{bmatrix} \tilde{r}\left(2\frac{\partial \tilde{u}}{\partial \tilde{z}} - \tilde{p}_1\right) & \tilde{r}\left(\frac{\partial \tilde{u}}{\partial \tilde{r}} + \frac{\partial \tilde{v}}{\partial \tilde{z}}\right) \\ \tilde{r}\left(\frac{\partial \tilde{u}}{\partial \tilde{r}} + \frac{\partial \tilde{v}}{\partial \tilde{z}}\right) & \tilde{r}\left(2\frac{\partial \tilde{v}}{\partial \tilde{r}} - \tilde{p}_1\right) \\ 0 & 0 \end{bmatrix} = \begin{bmatrix} \tilde{r}Re\left(\tilde{v}\frac{\partial \tilde{u}}{\partial \tilde{r}} + \tilde{u}\frac{\partial \tilde{u}}{\partial \tilde{z}}\right) \\ \tilde{r}Re\left(\tilde{v}\frac{\partial \tilde{v}}{\partial \tilde{r}} + \tilde{u}\frac{\partial \tilde{v}}{\partial \tilde{z}}\right) - \tilde{p}_1 + 2\frac{\tilde{v}}{\tilde{r}} \\ \tilde{v} + \tilde{r}\left(\frac{\partial \tilde{v}}{\partial \tilde{r}} + \frac{\partial \tilde{u}}{\partial \tilde{z}}\right) \end{bmatrix} \tag{4.28}$$

and in liquid 2 the system becomes

$$\begin{bmatrix} \tilde{r}\epsilon_\rho Re\frac{\partial \tilde{u}}{\partial t} \\ \tilde{r}\epsilon_\rho Re\frac{\partial \tilde{v}}{\partial t} \\ 0 \end{bmatrix} + \tilde{\boldsymbol{\nabla}} \cdot \begin{bmatrix} \tilde{r}\left(2\epsilon_\mu\frac{\partial \tilde{u}}{\partial \tilde{z}} - \tilde{p}_2\right) & \epsilon_\mu\tilde{r}\left(\frac{\partial \tilde{u}}{\partial \tilde{r}} + \frac{\partial \tilde{v}}{\partial \tilde{z}}\right) \\ \epsilon_\mu\tilde{r}\left(\frac{\partial \tilde{u}}{\partial \tilde{r}} + \frac{\partial \tilde{v}}{\partial \tilde{z}}\right) & \tilde{r}\left(2\epsilon_\mu\frac{\partial \tilde{v}}{\partial \tilde{r}} - \tilde{p}_2\right) \\ 0 & 0 \end{bmatrix} = \begin{bmatrix} \tilde{r}\epsilon_\rho Re\left(\tilde{v}\frac{\partial \tilde{u}}{\partial \tilde{r}} + \tilde{u}\frac{\partial \tilde{u}}{\partial \tilde{z}}\right) \\ \tilde{r}\epsilon_\rho Re\left(\tilde{v}\frac{\partial \tilde{v}}{\partial \tilde{r}} + \tilde{u}\frac{\partial \tilde{v}}{\partial \tilde{z}}\right) - \tilde{p}_2 + 2\epsilon_\mu\frac{\tilde{v}}{\tilde{r}} \\ \tilde{v} + \tilde{r}\left(\frac{\partial \tilde{v}}{\partial \tilde{r}} + \frac{\partial \tilde{u}}{\partial \tilde{z}}\right) \end{bmatrix} \tag{4.29}$$

where $\tilde{\boldsymbol{\nabla}} = \left[\frac{\partial}{\partial \tilde{z}}, \frac{\partial}{\partial \tilde{r}}\right]$. The matrix at the left of the equal sign in Eqs. (4.28) and (4.29) is $\tilde{\boldsymbol{\Gamma}}_k = [\tilde{\Gamma}_{ij}]_k$ and the matrix at the right is $\tilde{\boldsymbol{F}}_k = [\tilde{F}_i]_k$. From Eq. (4.28) it is evident that the four upper elements of $\tilde{\boldsymbol{\Gamma}}$ correspond to $\tilde{r}$ times the Cauchy stress tensor. The dimensionless parameters are defined as

$$Ca = \frac{\mu_1 U}{\gamma}, \quad Re = \frac{UL\rho_1}{\mu_1}, \quad p_k = \tilde{p}_k\frac{\mu_1 U}{L}, \quad \epsilon_\mu = \frac{\mu_2}{\mu_1}, \quad \epsilon_\rho = \frac{\rho_2}{\rho_1}, \tag{4.30}$$

where fluid 1 has been chosen as reference, ϵ_μ is the viscosity ratio, and ϵ_ρ is the density ratio. Note that only the pressure has a domain subscript as it is discontinuous while the velocity field is continuous throughout the fluid.

Boundary condition: At the interface between the two fluids the dynamic boundary condition Eq. 4.14 is rewritten in terms of the Γ matrices,

$$n_j\tilde{\Gamma}_{2,ij} - n_j\tilde{\Gamma}_{1,ij} = r\frac{1}{Ca}\tilde{\kappa}n_i \tag{4.31}$$

where $\tilde{\kappa}$ is the dimensionless curvature. The curvature term $\tilde{\kappa}$ simplifies when it is multiplied by $\tilde{r}$ and yields,

$$\tilde{r}\tilde{\kappa} = \tilde{r}\frac{\dot{z}\ddot{r} - \dot{r}\ddot{z}}{(\dot{r}^2 + \dot{z}^2)^{3/2}} + n_r. \tag{4.32}$$

4.7 Divergence form: liquid-gas system

When the two-fluid system consists of a liquid and a gas the governing Eqs. (4.28) and (4.29) simplify. Compared to the liquid, the shear stress and the viscosity of the gas are negligible and the pressure variations are expected to be small, so we only need to specify a pressure in the gas domains. We thus assume that $\mu_{\text{gas}} \ll \mu_{\text{liquid}}$ which is mainly due to the fact that $\rho_{\text{gas}} \ll \rho_{\text{liquid}}$. So if fluid 2 is the gas we may set $\epsilon_\mu = 0$ and $\epsilon_\rho = 0$. Thus, in fluid 1 according to Eq. (4.28) we have,

$$\begin{aligned}\begin{bmatrix} \tilde{r}Re\frac{\partial \tilde{u}}{\partial \tilde{t}} \\ \tilde{r}Re\frac{\partial \tilde{v}}{\partial \tilde{t}} \\ 0 \end{bmatrix} + \tilde{\boldsymbol{\nabla}} \cdot \begin{bmatrix} \tilde{r}\left(2\frac{\partial \tilde{u}}{\partial \tilde{z}} - \tilde{p}\right) & \tilde{r}\left(\frac{\partial \tilde{u}}{\partial \tilde{r}} + \frac{\partial \tilde{v}}{\partial \tilde{z}}\right) \\ \tilde{r}\left(\frac{\partial \tilde{u}}{\partial \tilde{r}} + \frac{\partial \tilde{v}}{\partial \tilde{z}}\right) & \tilde{r}\left(2\frac{\partial \tilde{v}}{\partial \tilde{r}} - \tilde{p}\right) \\ 0 & 0 \end{bmatrix} \\ = \begin{bmatrix} \tilde{r}Re\left(\tilde{v}\frac{\partial \tilde{u}}{\partial \tilde{r}} + \tilde{u}\frac{\partial \tilde{u}}{\partial \tilde{z}}\right) \\ \tilde{r}Re\left(\tilde{v}\frac{\partial \tilde{v}}{\partial \tilde{r}} + \tilde{u}\frac{\partial \tilde{v}}{\partial \tilde{z}}\right) - \tilde{p} + 2\frac{\tilde{v}}{\tilde{r}} \\ \tilde{v} + \tilde{r}\left(\frac{\partial \tilde{v}}{\partial \tilde{r}} + \frac{\partial \tilde{u}}{\partial \tilde{z}}\right) \end{bmatrix}. \end{aligned} \tag{4.33}$$

Where $\tilde{p}$ is the pressure in the liquid. The only reference to the gas is now through the pressure $\tilde{p}_2$ in Eq. (4.29). After rearranging the terms in the boundary condition the pressure in the gas $\tilde{p}_2$ appears and we have

$$\tilde{\Gamma}_{11}n_1 + \tilde{\Gamma}_{12}n_2 = \tilde{r}\left(\frac{1}{Ca}\,\tilde{\kappa} - \tilde{p}_2\right)n_1 \tag{4.34}$$

$$\tilde{\Gamma}_{21}n_1 + \tilde{\Gamma}_{22}n_2 = \tilde{r}\left(\frac{1}{Ca}\,\tilde{\kappa} - \tilde{p}_2\right)n_2, \tag{4.35}$$

where

$$\tilde{p}_2 = \frac{p_{\text{gas}}L}{\mu U}, \tag{4.36}$$

and p_{gas} is the dimensional pressure in the gas. In practice we may set p_{gas} equal to a constant or make if obey the ideal gas law.

4.8 Stokes-flow

In the problems that are studied in this thesis the flow is generally viscous at has small Reynolds numbers $Re \ll 1$. In practice when implementing the equations numerically we will be assuming that the flow is laminar an set $Re = 0$. This reduces the governing Eqs. (4.28) and (4.29) to the Stokes-flow equations. When $Re = 0$ the nonlinear convective terms disappear as well as the time dependent terms. The governing equations are thus linear in the dependent variables (u, v, p). In a Stokes-flow system involving a free surface the only time dependence is through the kinematic boundary condition Eq. (4.15) at the interface. Moreover, the only nonlinearity is introduced via the curvature term Eq. (4.32) of the dynamic boundary condition Eq. (4.31). Thus even though the governing equations are linear in the dependent variables the dynamics are still nonlinear. The systems that we

will be studying are listed below with governing equations, dynamic boundary conditions, and re-scaled parameters:

Liquid-liquid axisymmetric

$$\tilde{\boldsymbol{\nabla}} \cdot \begin{bmatrix} \tilde{r}\left(2\frac{\partial \tilde{u}}{\partial \tilde{z}} - \tilde{p}_1\right) & \tilde{r}\left(\frac{\partial \tilde{u}}{\partial \tilde{r}} + \frac{\partial \tilde{v}}{\partial \tilde{z}}\right) \\ \tilde{r}\left(\frac{\partial \tilde{u}}{\partial \tilde{r}} + \frac{\partial \tilde{v}}{\partial \tilde{z}}\right) & \tilde{r}\left(2\frac{\partial \tilde{v}}{\partial \tilde{r}} - \tilde{p}_1\right) \\ 0 & 0 \end{bmatrix} = \begin{bmatrix} 0 \\ -\tilde{p}_1 + 2\frac{\tilde{v}}{\tilde{r}} \\ \tilde{v} + \tilde{r}\left(\frac{\partial \tilde{v}}{\partial \tilde{r}} + \frac{\partial \tilde{u}}{\partial \tilde{z}}\right) \end{bmatrix} \tag{4.37}$$

$$\tilde{\boldsymbol{\nabla}} \cdot \begin{bmatrix} \tilde{r}\left(2\epsilon_\mu \frac{\partial \tilde{u}}{\partial \tilde{z}} - \tilde{p}_2\right) & \epsilon_\mu \tilde{r}\left(\frac{\partial \tilde{u}}{\partial \tilde{r}} + \frac{\partial \tilde{v}}{\partial \tilde{z}}\right) \\ \epsilon_\mu \tilde{r}\left(\frac{\partial \tilde{u}}{\partial \tilde{r}} + \frac{\partial \tilde{v}}{\partial \tilde{z}}\right) & \tilde{r}\left(2\epsilon_\mu \frac{\partial \tilde{v}}{\partial \tilde{r}} - \tilde{p}_2\right) \\ 0 & 0 \end{bmatrix} = \begin{bmatrix} 0 \\ -\tilde{p}_2 + 2\epsilon_\mu \frac{\tilde{v}}{\tilde{r}} \\ \tilde{v} + \tilde{r}\left(\frac{\partial \tilde{v}}{\partial \tilde{r}} + \frac{\partial \tilde{u}}{\partial \tilde{z}}\right) \end{bmatrix} \tag{4.38}$$

$$n_j \tilde{\Gamma}_{2,ij} - n_j \tilde{\Gamma}_{1,ij} = \tilde{r} \frac{1}{Ca} \tilde{\kappa} n_i \tag{4.39}$$

$$x_i = \tilde{x}_i L, \quad u_i = \tilde{u}_i U, \quad t = \tilde{t}\frac{L}{U}, \quad p = \tilde{p}\frac{\mu_1 U}{L}, \quad \epsilon_\mu = \frac{\mu_2}{\mu_1}, \quad Ca = \frac{\mu_1 U}{\gamma} \tag{4.40}$$

Liquid-gas axisymmetric

$$\tilde{\boldsymbol{\nabla}} \cdot \begin{bmatrix} \tilde{r}\left(2\frac{\partial \tilde{u}}{\partial \tilde{z}} - \tilde{p}\right) & \tilde{r}\left(\frac{\partial \tilde{u}}{\partial \tilde{r}} + \frac{\partial \tilde{v}}{\partial \tilde{z}}\right) \\ \tilde{r}\left(\frac{\partial \tilde{u}}{\partial \tilde{r}} + \frac{\partial \tilde{v}}{\partial \tilde{z}}\right) & \tilde{r}\left(2\frac{\partial \tilde{v}}{\partial \tilde{r}} - \tilde{p}\right) \\ 0 & 0 \end{bmatrix} = \begin{bmatrix} 0 \\ -\tilde{p} + 2\frac{\tilde{v}}{\tilde{r}} \\ \tilde{v} + \tilde{r}\left(\frac{\partial \tilde{v}}{\partial \tilde{r}} + \frac{\partial \tilde{u}}{\partial \tilde{z}}\right) \end{bmatrix} \tag{4.41}$$

$$n_j \tilde{\Gamma}_{ij} - n_j \tilde{\Gamma}_{ij} = \tilde{r}\left(\frac{1}{Ca}\tilde{\kappa} - \tilde{p}_2\right) n_i \tag{4.42}$$

$$x_i = \tilde{x}_i L, \quad \tilde{u}_i = \tilde{u}_i U, \quad t = \tilde{t}\frac{L}{U}, \quad p = \tilde{p}\frac{\mu U}{L}, \quad Ca = \frac{\mu U}{\gamma}, \quad \tilde{p}_2 = \frac{p_{\text{gas}} L}{\mu U} \tag{4.43}$$

Liquid-gas 2D rectangular

$$\boldsymbol{\nabla} \cdot \begin{bmatrix} \left(2\frac{\partial \tilde{u}}{\partial \tilde{x}} - \tilde{p}\right) & \left(\frac{\partial \tilde{u}}{\partial \tilde{y}} + \frac{\partial \tilde{v}}{\partial \tilde{x}}\right) \\ \left(\frac{\partial \tilde{u}}{\partial \tilde{y}} + \frac{\partial \tilde{v}}{\partial \tilde{x}}\right) & \left(2\frac{\partial \tilde{v}}{\partial \tilde{y}} - \tilde{p}\right) \\ 0 & 0 \end{bmatrix} = \begin{bmatrix} 0 \\ 0 \\ \frac{\partial \tilde{u}}{\partial \tilde{x}} + \frac{\partial \tilde{v}}{\partial \tilde{y}} \end{bmatrix} \tag{4.44}$$

$$n_j\tilde{\Gamma}_{ij} - n_j\tilde{\Gamma}_{ij} = \left(\frac{1}{Ca}\tilde{\kappa} - \tilde{p}_2\right) n_i \tag{4.45}$$

$$x_i = \tilde{x}_i L, \quad u_i = \tilde{u}_i U, \quad t = \tilde{t}\frac{L}{U}, \quad p = \tilde{p}\frac{\mu U}{L}, \quad Ca = \frac{\mu U}{\gamma}, \quad \tilde{p}_2 = \frac{p_{\text{gas}} L}{\mu U} \tag{4.46}$$

4.9 Non-Newtonian liquid: power-law model

The fluid described in the previous sections was treated as a Newtonian fluid, that is, a fluid where there is a linear relation between the stress tensor $\boldsymbol{\tau}$ and the rate of strain tensor $\dot{\boldsymbol{\gamma}}$. The constant of proportionality is the dynamic viscosity μ. The stress tensor $\boldsymbol{\tau}$ is given as

$$\tau_{ij} = \mu\left(\frac{\partial u_i}{\partial x_j} + \frac{\partial u_j}{\partial x_i}\right) \tag{4.47}$$

that is $\boldsymbol{\tau} = \boldsymbol{\sigma} + p\boldsymbol{I}$, see Eq. (4.9). To be specific $\boldsymbol{\sigma}$ is called the total stress tensor while $\boldsymbol{\tau}$ is the stress tensor [36]. The rate of strain tensor is

$$\dot{\gamma}_{ij} = \left(\frac{\partial u_i}{\partial x_j} + \frac{\partial u_j}{\partial x_i}\right). \tag{4.48}$$

In a non-Newtonian fluid the viscosity is not constant. A model for such a fluid is given by the generalized Newtonian fluid where the dynamic viscosity, now denoted η, is a function of the shear rate $\dot{\gamma}$ and we write $\eta = \eta(\dot{\gamma})$. The shear rate is given by

$$\dot{\gamma} = \sqrt{\frac{1}{2}\dot{\gamma}_{ij}\dot{\gamma}_{ij}}. \tag{4.49}$$

One of the most commonly used expressions for $\eta(\dot{\gamma})$ is the so-called power-law model containing two free parameters,

$$\eta = m\dot{\gamma}^{n-1} \tag{4.50}$$

where m has units $\text{Pa}\,\text{s}^n$ and n is dimensionless. When $n = 1$ and $m = \mu$ the Newtonian fluid is recovered. If $n < 1$ the fluid is said to be shear thinning (pseudo elastic) and when $n > 1$ the fluid is shear thickening (dilatant). Further details about this model and any others are found in Ref. [36].

Using the power law model Eq. (4.50) for the viscosity of the liquid the governing equations in dimensionless form for the axisymmetric liquid-gas system are

$$\tilde{\boldsymbol{\nabla}} \cdot \begin{bmatrix} \tilde{r}\left(2\tilde{\eta}\frac{\partial \tilde{u}}{\partial \tilde{z}} - \tilde{p}\right) & \tilde{r}\tilde{\eta}\left(\frac{\partial \tilde{u}}{\partial \tilde{r}} + \frac{\partial \tilde{v}}{\partial \tilde{z}}\right) \\ \tilde{r}\tilde{\eta}\left(\frac{\partial \tilde{u}}{\partial \tilde{r}} + \frac{\partial \tilde{v}}{\partial \tilde{z}}\right) & \tilde{r}\left(2\tilde{\eta}\frac{\partial \tilde{v}}{\partial \tilde{r}} - \tilde{p}\right) \\ 0 & 0 \end{bmatrix} = \begin{bmatrix} 0 \\ -\tilde{p} + 2\tilde{\eta}\frac{\tilde{v}}{\tilde{r}} \\ \tilde{v} + \tilde{r}\left(\frac{\partial \tilde{v}}{\partial \tilde{r}} + \frac{\partial \tilde{u}}{\partial \tilde{z}}\right) \end{bmatrix} \tag{4.51}$$

where

$$\tilde{\eta} = \sqrt{2\left(\frac{\partial \tilde{u}}{\partial \tilde{z}}\right)^2 + \left(\frac{\partial \tilde{v}}{\partial \tilde{z}} + \frac{\partial \tilde{u}}{\partial \tilde{r}}\right)^2 + 2\left(\frac{\partial \tilde{v}}{\partial \tilde{r}}\right)^2}, \tag{4.52}$$

and it is now obvious that Eq. (4.51) is no longer linear in the dependent variables $(\tilde{u}, \tilde{v}, \tilde{p})$ because of $\tilde{\gamma}$. The dynamic boundary conditions is again

$$n_j \tilde{\Gamma}_{ij} - n_j \tilde{\Gamma}_{ij} = \tilde{r} \left(\frac{1}{Ca} \tilde{\kappa} - \tilde{p}_2 \right) n_i. \tag{4.53}$$

The dimensionless parameters, here marked with a star superscript, are as follows

$$x_i = \tilde{x}_i L, \quad u_i = \tilde{u}_i U, \quad t = \tilde{t} \frac{L}{U}, \quad p = \tilde{p}\, m \left(\frac{U}{L} \right)^n, \tag{4.54}$$

$$\tilde{p}_2 = \frac{p_{\text{gas}}}{m} \left(\frac{U}{L} \right)^{-n}, \quad Ca = \frac{Lm}{\gamma} \left(\frac{U}{L} \right)^n, \quad \eta = \tilde{\eta}\, m \left(\frac{U}{L} \right)^{n-1}. \tag{4.55}$$

Note: The tilde on the dimensionless variables are dropped in the following two chapters. They are naturally reintroduced in Chap. 7.

Chapter 5

Numerics: implementation

A considerable part of the work of producing the numerical results presented in this thesis was put in developing the free surface program itself. Even though the basic concepts behind free-surface flow simulations are rather simple, the implementation poses many practical challenges. The main purpose of this chapter is thus twofold: firstly, to describe how the code works and, secondly, to point out and detail all the schemes and numerical tricks developed to make the code reliable and accurate.

Many different methods exist to solve a free surface problem. They rely on either a level-set like approach where the interface is more or less smeared out or on a well defined interface location defined by grid points. The first class include the level-set method [37, 38], the volume-of-fluid VOF methods [27, 39, 19, 40, 41], and free-surface lattice-Boltzman methods [42]. Common for these methods is that the interface is defined through a single valued function $F(\boldsymbol{x}) \in \mathbb{R}$. The last class of methods comprise boundary integral methods [21], finite element (FEM) arbitrary Lagrange–Euler (ALE) methods [43, 44], and the Runge–Kutta specified free interface FEM method we have implemented and present here. Generally said, the first class of methods is relatively faster but the physics at the free interface are not always precisely described while the second class is slower but simulate the full physics at the free interface.

Chiefly our code solves for the full dynamics of an axisymmetric Stokes-flow problem involving a free fluid-fluid interfaces. The numerical solver is based on an in-house MATLAB [45] free surface and second order Runge–Kutta time integration code that interfaces with the commercial FEMLAB FEM solver [46]. The governing equations and the boundary conditions at the free interface were presented in Chap. 4.

This chapter is introduced by a problem formulation and a presentation of the main aspects of the method. This first part is concluded by a program algorithm flow-chart. From this point on every aspect presented in the algorithm flow-chart is discussed separately and in detail: the governing equations and boundary conditions, the meshing, the curvature scheme, and the time integration algorithm.

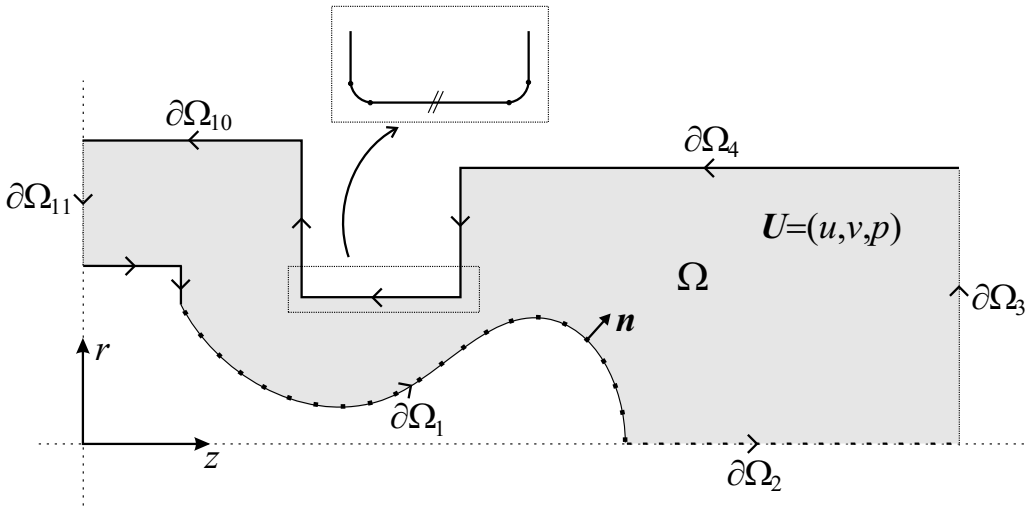

Figure 5.1: Sketch of the flow-focusing device geometry with computational domain Ω. The boundaries are denoted $\partial\Omega_i$, for $i = 1, ..., 13$, the free surface boundary is $\partial Omega_1$. There is rotational symmetry about the z-axis.

5.1 The problem and method

The main goal of the present work is to study the time-dependent dynamics of the two-phase Stokes-flow in an axisymmetric flow-focusing device. We have thus chosen to present the code using the flow-focusing device as a concrete example.

Figure 5.1 depicts the geometry used for the axisymmetric flow-focusing device. We wish to solve the Stokes flow Eq. (4.41) in the computational domain Ω while applying the liquid-gas dynamic boundary condition Eq. (4.42) at the moving boundary $\partial\Omega_1$. The time dependent evolution of the boundary is given by the kinematic boundary condition Eq. (4.15).

As the Stokes flow has zero Reynolds-number $Re = 0$ there is no inertia in the system. This fact reduces the time dependence of the problem such that it is only present in the kinematic boundary condition at the free surface. The problem is hence reduced to a quasi-stationary problem in the following sense: given an interface shape $\boldsymbol{x} = (z(S), r(S))$ we solve for the flow field (u, v, p) and the stress field $\boldsymbol{\sigma}$ in the liquid. If the stress is non-zero at any point on the liquid-gas interface this interface will move according to the velocity data. The problem of evolving the interface in time is thus a question of subsequently solving the flow, computing the interface velocity, and then evolve the interface according to the kinematic boundary condition Eq. (4.15) using a specific time integration scheme (we use a second order Runge–Kutta scheme).

We utilize the commercial FEM program FEMLAB to solve the flow equations. The main idea of the FEM method is to approximate the solution (u, v, p) of the PDE by using a linear combination of basis functions, i.e.,

$$[u(\boldsymbol{x}), v(\boldsymbol{x}), p(\boldsymbol{x})] = \sum_i [u_i\varphi_{i1}(\boldsymbol{x}), v_i\varphi_{i2}(\boldsymbol{x}), p_i\varphi_{i3}(\boldsymbol{x})]\,, \tag{5.1}$$

where φ_{il} are the basis functions, $l = 1, 2, 3$ the dependent variable indic, i the node number, and (u_i, v_i, p_i) are the coefficients to be solved for. The discretization of the problem is introduced by only choosing a finite number of basis functions. In the FEM method the basis functions are chosen such that they have a compact support. The computational domain Ω is divided into a triangular mesh, and a given basis function is now only nonzero on the triangular elements surrounding a given node i. The computation of the coefficients (u_i, v_i, p_i) is done, by FEMLAB, by solving a large matrix problem. In the case where the governing equations are linear in the dependent variables and stationary the FEMLAB linear solver `femlin` is used [81]. Some further details on the FEM method are given in Appendix B.

The FEMLAB program is very flexible and see-through and it interfaces nicely with MATLAB via a scripting language. It is consequently possible to include in-house MATLAB functions into the equation systems solved by FEMLAB , see Secs. 5.2 and 5.4. We have coded the time integration procedure, the interface evolution scheme, and the curvature scheme in MATLAB , while we use FEMLAB to solve for the flow field (u, v, p) and provide the interface velocities at the free surface. To solve the PDEs FEMLAB is feat with information about the geometry and it is given mesh parameters so that it can mesh the computational domain, see Sec. 5.3. This information is also provided by the MATLAB code.

An algorithm flow-chart of the main program is given in Fig. 5.2. I this chart we refer to the following sections for in-dept information about certain schemes and program pieces. The full MATLAB program is found in Appendix A together with relevant subroutines and functions.

5.2 Governing equations and boundary conditions

When interfacing with FEMLAB it is possible to enter the governing equations in two very general forms: (1) using a weak formulation (see Appendix B and Refs. [75, 76] for more details) or (2) using a general PDE formulation or strong form [81]. In the case of the a liquid-gas system discussed here it is straight forward to use the general formulation. A particular PDE is here given on the form

$$d_a \frac{d\boldsymbol{U}}{dt} + \boldsymbol{\nabla} \cdot \boldsymbol{\Gamma} = \boldsymbol{F} \quad \text{in } \Omega, \tag{5.2}$$

in terms of the variable vector $\boldsymbol{U} = (U_1, U_2, U_3) = (u, v, p)$, the flux tensor $\boldsymbol{\Gamma}$, the generalized source term $\boldsymbol{F}$, and d_a is a parameter. Comparing this to the governing Eq. (4.41) we immediately recognize

$$\boldsymbol{\Gamma} = \begin{bmatrix} r\left(2\frac{\partial u}{\partial z} - p\right) & r\left(\frac{\partial u}{\partial r} + \frac{\partial v}{\partial z}\right) \\ r\left(\frac{\partial u}{\partial r} + \frac{\partial v}{\partial z}\right) & r\left(2\frac{\partial v}{\partial r} - p\right) \\ 0 & 0 \end{bmatrix}, \quad \boldsymbol{F} = \begin{bmatrix} 0 \\ -p + 2\frac{v}{r} \\ v + r\left(\frac{\partial v}{\partial r} + \frac{\partial u}{\partial z}\right) \end{bmatrix}, \tag{5.3}$$

and $d_a = 0$ as we have no time dependency here. Again note that $\boldsymbol{\Gamma} = r\boldsymbol{\sigma}$, where $\boldsymbol{\sigma}$ is the Cauchy stress-tensor Eq. (4.9). The above formulation is in the FEMLAB scripting language given as:

set constants
    geometry parameters
    physical parameters
    numerical parameters
    initial interface shape

define FEMLAB *environment*
    curvature user functions ($\star$ Sec. 5.4)
    finite elements (order and shape)
    governing equations ($\star$ Sec. 5.2)
    boundary conditions ($\star$ Sec. 5.2)

start time-loop (while $t < T_{\text{end}}$ & $i < M$)
    set geometry
    mesh ($\star$ Sec. 5.3)
    modify mesh structure: make S_t arc-length ($\star$ Sec. 5.3)
    calculate curvature approximating splines ($\star$ Sec. 5.4)
    solve flow

    start of Runge–Kutta gradient computation
    compute interface normal $\boldsymbol{n}(S_t)$ and velocity $\boldsymbol{u}(S_t)$
    compute δt
    evolve interface (Euler step) $\boldsymbol{x}(S_{t+\delta t/2}) := \boldsymbol{x}(S_t) + (\boldsymbol{u}\cdot\boldsymbol{n})\boldsymbol{n}(S_t)\frac{\delta t}{2}$
    compute interpolating interface splines ($\star$ Sec. 5.3)
    re-mesh ($\star$ Sec. 5.3)
    modify mesh structure: make $S_{t+\delta t/2}$ arc-length
    compute arc-length map $S_{t+\delta t/2} = f(S_t)$ ($\star$ Sec. 5.5)
    calculate curvature approximating splines ($\star$ Sec. 5.4)
    solve flow
    end of Runge–Kutta gradient computation

    compute interface normal $\boldsymbol{n}(S_{t+\delta t/2})$ and velocity $\boldsymbol{u}(S_{t+\delta t/2})$
    evolve interface (Runge–Kutta step) ($\star$ Sec. 5.5)
        $\boldsymbol{x}(S_{t+\delta t}) := \boldsymbol{x}(S_t) + (\boldsymbol{u}\cdot\boldsymbol{n})\boldsymbol{n}(S_{t+\delta t/2})\delta t$, with $S_{t+\delta t/2} = f(S_t)$
    compute interpolating interface splines ($\star$ Sec. 5.3)
    collect and save data
    $i := i + 1$, $t := t + \delta t$
end time-loop (end while)

    post processing and data plot

Figure 5.2: Algorithm flow-chart, passages marked with a star $\star$ are further discussed in the sections below.

```
fem.sdim = {'z' 'r'};
fem.dim = {'u' 'v' 'p'};
fem.shape ={shlag(2,'u') shlag(2,'v') shlag(1,'p')};

fem.form = 'general';
fem.equ.ga = {{{'r*(2*uz-p)' 'r*(ur+vz)'} {'r*(ur+vz)' 'r*(2*vr-p)'} {'0' '0'}}};
fem.equ.f = {{{'0'} {'-p+2*v/r'} {'r*(uz+vr)+v'}}};
```

The matrix $\boldsymbol{\Gamma}$ is entered in `fem.equ.ga` and $\boldsymbol{F}$ in the structure `fem.equ.f`. The field `fem.sdim` defines the shape and order of the basis functions used for u, v, and p, respectively. Finally, the dependent and independent variables are defined in `fem.dim` and `fem.sdim`, respectively.

The boundary conditions corresponding to the general form of Eq. (5.2) are

$$n_j \Gamma_{lj} = G_l + \frac{\partial R_{lm}}{\partial U_l} \mu_m \qquad \text{on } \partial\Omega_m \tag{5.4}$$

$$0 = R_{lm} \qquad \text{on } \partial\Omega_m \tag{5.5}$$

where $l = 1, 2, 3$ is the variable counter, $m = 1, ..., 13$ is the constraint number (the boundary number), $j = 1, 2$ is the space dimension number (z and r), n_j is the outward surface normal component $\boldsymbol{n} = (n_1, n_2) = (n_z, n_r)$, see Fig. 5.1, and $\boldsymbol{\Gamma} = [\Gamma_{lj}]$. The coefficients μ_m are Lagrange multipliers calculated by FEMLAB such that the constraint in Eq. (5.5) is fulfilled. Equation (5.4) is the Neumann condition and Eq. (5.5) is the Dirichlet condition or constraint.

In the flow-focusing device sketched in Fig. 5.1 we are using five different types of boundary conditions: (1) free surface condition on boundary $\partial\Omega_1$, (2) symmetry condition on $\partial\Omega_2$, (3) fixed pressure and straight out on $\partial\Omega_3$, (4) no slip conditions on $\partial\Omega_m$, $m = 4, 5, 6, 7, 8, 9, 10, 12, 13$, and (5) a fixed inlet velocity on $\partial\Omega_{11}$. In terms of the Neumann and Dirichlet conditions formulated in Eqs. (5.4) and (5.5) are as follows.

Free surface dynamic boundary condition:

$$(R_1, R_2, R_3) = (0, 0, 0) \tag{5.6}$$

$$G_1 = \left(r p_2 + \frac{1}{Ca} \kappa(s) \right) n_1 \tag{5.7}$$

$$G_2 = \left(r p_2 + \frac{1}{Ca} \kappa(s) \right) n_2 \tag{5.8}$$

$$G_3 = 0 \tag{5.9}$$

Symmetry ar $r = 0$:

$$(R_1, R_2, R_3) = (v, 0, 0) \tag{5.10}$$

$$\boldsymbol{G} = \boldsymbol{0} \quad \text{as} \quad r = 0 \tag{5.11}$$

Fixed pressure p_0 and $\boldsymbol{u} \cdot \boldsymbol{t} = 0$:

$$(R_1, R_2, R_3) = (0, v, 0) \tag{5.12}$$
$$G_1 = rp_0 n_1 = rp_0 \tag{5.13}$$
$$G_2 = rp_0 n_2 = 0 \quad \text{as} \quad \boldsymbol{n} = (1, 0) \tag{5.14}$$
$$G_3 = 0 \tag{5.15}$$

Fixed inlet velocity:

$$(R_1, R_2, R_3) = (u - U_{\text{in}}(s), v, 0) \tag{5.16}$$
$$\boldsymbol{G} = \boldsymbol{0} \tag{5.17}$$

No slip $\boldsymbol{u} = \boldsymbol{0}$:

$$(R_1, R_2, R_3) = (0, 0, 0) \tag{5.18}$$
$$\boldsymbol{G} = \boldsymbol{0} \tag{5.19}$$

Where the parameter $s \in [0, 1]$ and is defined on every boundary $\partial\Omega_m$ in the specified boundary orientation, see arrows in Fig. 5.1. In FEMLAB scripting language the boundary conditions are simply given as:

```
fem.bnd.ind = {[11] [3] [2] [4:10 12:13] [1]};
fem.bnd.g = {{0 0 0} {0 0 0} {0 0 0} {0 0 0} ...
            {{'(r*p2+1/Ca*(kappa20_rz(s)+kappa20_rt(s)))*nz'} ...
             {'(r*p2+1/Ca*(kappa20_rz(s)+kappa20_rt(s)))*nr'} 0}};
fem.bnd.r = {{{'u-Ui*s*(1-s)'} {'v'} 0} {0 {'v'} 0} {{'v'} 0 0} ...
             {{'u'} {'v'} 0} {0 0 0}};
```

5.3 Meshing and interface representation

In the main program the free interface $\partial\Omega_1$ (see Fig. 5.1) is defined by a number of discrete points (z_i, r_i) with corresponding arc-length parameter S_i, with $i = 1, .., M$, see Fig. 5.3. In the MATLAB program presented in Appendix A these are named `zint`, `rint`, and `S`, respectively. The location of the interface points and corresponding values of S_i are updated every time the domain Ω is meshed, i.e., every time the governing equations are solved. In this way we avoid the classical problems with conglomeration or spreading of the interface points [21].

While developing the code we found that the values of S_i were not corresponding to the correct arc-length values. This gave rise to a great deal of confusion when, e.g., interpolating interface velocities. Fortunately FEMLAB is a very flexible and it is possible to correct the mesh structure by using the FEMLAB `meshenrich` command in a clever way. In a few lines of MATLAB code we extract the new interface locations (z_i, r_i) from the FEMLAB mesh structure `fem.mesh.p` and update the values for S_i in the structure

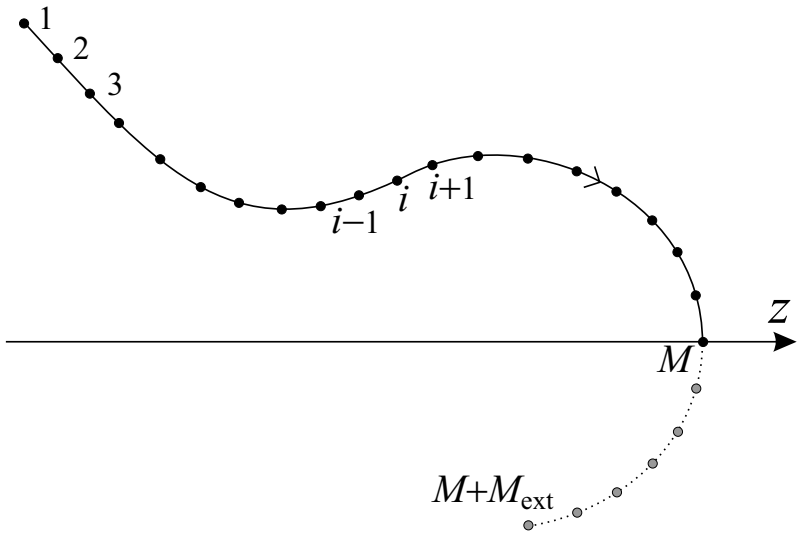

Figure 5.3: Interface represented by $i = 1, ..., M$ points and M_{ext} extra ghost points to ensure symmetry of the interface interpolating splines.

`fem.mesh.e`, the corresponding code lines are:

```
Idex=find(fem.mesh.e(5,:)==2);
Is=fem.mesh.e(1,Idex); Ie=fem.mesh.e(2,Idex); Izr=[Is Ie(end)];
zint=fem.mesh.p(1,Izr);
rint=fem.mesh.p(2,Izr);
dL=sqrt((zint(1:end-1)-zint(2:end)).^2+(rint(1:end-1)-rint(2:end)).^2);
S=[0 dL*triu(ones(length(dL)))]/sum(dL);
mesh_temp.p=fem.mesh.p; mesh_temp.t=fem.mesh.t; mesh_temp.e=fem.mesh.e;
mesh_temp.e(3,Idex)=S(1:end-1); mesh_temp.e(4,Idex)=S(2:end);
fem.mesh=meshenrich(mesh_temp);
```

As the interface is moving the geometry is changing. To communicate the change of the geometry boundary to FEMLAB the geometry is defined in a user defined geometry function `geomfile.m`. As input this file gets a boundary number m and the arc-length parameter S, and as output it provides an (z, r) coordinate. The source code is provided in Appendix A. To provide an (z, r) value for any given S value the interface $(z_i(S_i), r_i(S_i))$ is interpolated by a cubic spline. For that purpose we use the MATLAB build-in `spline.m` function. The spline information is stored in the `ppz` and `ppr` MATLAB structures. When creating the splines M_{ext} extra ghost points are added near the symmetry line $r = 0$ to ensure symmetry of the interface spline, see Fig. 5.3.

The meshing of the computational domain is performed with the FEMLAB meshing algorithm `meshinit`. An example of a mesh is given in Fig. 5.4. Creating a mesh of good quality is paramount for good numerical results and stability. Moreover, the resolution of the mesh near the free interface is crucial for modelling the free-surface dynamics correctly. The spacial resolution of the interface (z_i, r_i) is directly influenced by the mesh quality.

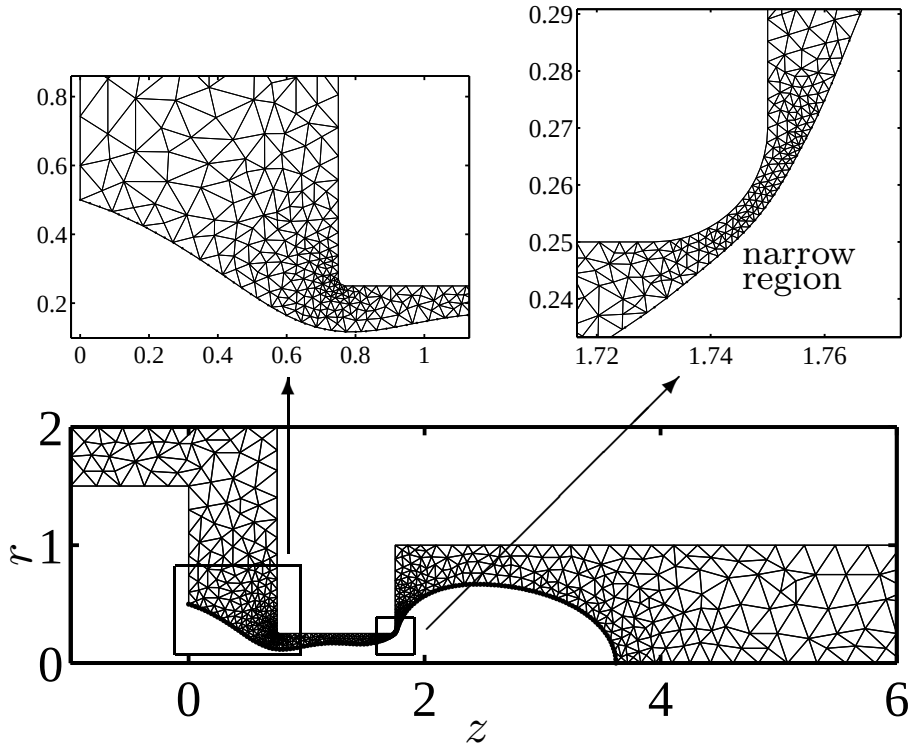

Figure 5.4: Example of a meshing of the computational domain Ω. The insets show zoom of the grid where it is refined. The resolution of a narrow region with hnarrow=4 is also shown.

The typical mesh command is:

```
fem.mesh = meshinit(fem,'Hmaxedg',[1 3 6 8; zeta 0.25 0.004 0.02], ...
        'Hgrad',1.18,'Report','off','Hpntedg',[2; length(S)],'Hnarrow',4, ...
        'Hmax',0.3,'Hcurve',10);
```

In the above piece of code the mesh parameters are the following:

- `Hmaxedg`: is the maximal element size on a given boundary segment. The free-interface mesh-size ζ is a program variable and is called `zeta`. The mesh size on the rounded corners ($\partial\Omega_6$ and $\partial\Omega_8$ in Fig. 5.1) of the orifice region is also set. This ensures reliable results when the gas-jet is exiting the orifice region, as depicted in Fig. 5.4.

- `Hgrad`: is the mesh-element size growth-rate away from a boundary. Typical good values are between 1.15 and 1.2.

- `Hpentedg`: is the number of initial points used in the mesh algorithm to resolve the free interface. It is important for this number to be roughly equal to the number of boundary points M. If it is not the mesh quality decreases drastically near the free surface.

- `Hnarrow`: is the number of elements used to resolve narrow parts on the mesh, see the insert in Fig. 5.3. This parameter is typically set equal to 4.
- `Hmax`: is the overall maximal element size of the grid in the computational domain Ω.
- `Hcurve`: is the curvature resolution parameter. It was found that it is extremely important for this parameter to have a large value (≥ 10). A small value is used to prescribe a large amount of resolution for curved boundaries. However, as we are using interpolating splines to describe the free interface small un-physical wiggles may appear. These errors grow significantly if the wiggles "get caught" by the mesh algorithm. The resolution of the interface is thus controlled lonely by the interface mesh size ζ.

5.4 Curvature scheme

In the way we have implemented the free surface model the curvature κ enters the dynamic boundary condition explicitly.[1] The curvature is very important as it is the only term responsible for the nonlinearity of the system, see Sec. 4.4;

$$\kappa = \frac{\dot{z}\ddot{r} - \dot{r}\ddot{z}}{(\dot{r}^2 + \dot{z}^2)^{3/2}} - \frac{\dot{z}}{r(\dot{r}^2 + \dot{z}^2)^{1/2}}, \tag{5.20}$$

where a dot represents differentiation with respect to S and $\kappa = \kappa(S)$. Because second order derivatives of the interface shape $(z(S), r(S))$ enter the curvature expression one should be very careful when treating it numerically as it is very sensitive to numerical noise. In Fig. 5.5 this is exemplified by showing that only a slight move of an interface point changes the curvature of the interpolating spline. The key to avoiding this is to use an approximating cubic spline to determine the curvature. One of the foremost elements in our code is the decoupling of the curvature approximating splines from the boundary interpolating splines.

Within FEMLAB the curvature enters as $\kappa(S)$ and has to be defined for all S on the free boundary. This is mainly due to the way FEMLAB numerically handles integration by using Gauss quadrature. In the program we have defining two functions `kappa20_rz.m` and `kappa20_rt.m` corresponding to the two contributions $\kappa_{rz}(S)$ and $\kappa_{r\phi}(S)$ with input S and the curvature as output. These enter in the expression for the boundary condition.

As mentioned the curvature computation is based upon cubic approximating splines. For that purpose we used the `spaps.m` smoothing spline function from the MATLAB splines library. This function produces a piecewise cubic spline $f \in C_2$ of, e.g., the z coordinate $z = f_z(S)$. The spline f_z minimizes the roughness measure

$$F\left(\frac{d^3 f_z}{dS^3}\right) = \int_0^1 \left|\frac{d^3 f_z}{dS^3}\right|^2 \mathrm{d}S \tag{5.21}$$

[1] In Appendix B we shortly describe how it is possible to project the curvature onto the FEM basis functions. In this way it is not necessary to include it explicitly. This method is not as numerically stable as the one we use but mathematically it is very neat.

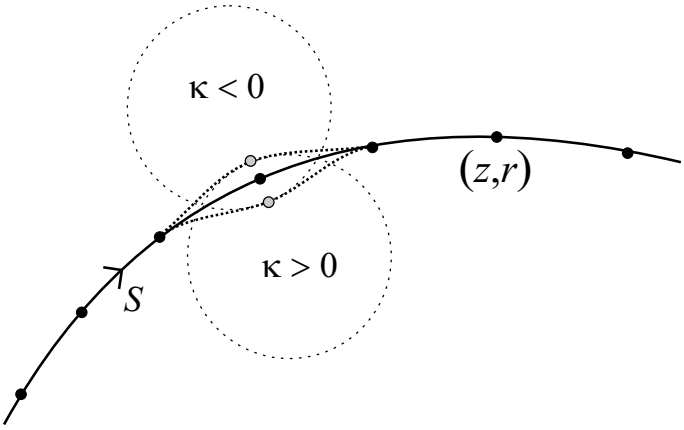

Figure 5.5: Sketch of a boundary with boundary mesh points. If one of these points is moves slightly the curvature of the interpolating spline changes drastically.

over all piecewise C_3 functions $f_z \in C_2$ for which the error

$$E(f_z) = \sum_i w_i |z_i - f_z(S_i)|^2 < tol_{\rm sp}, \tag{5.22}$$

where w_i are weights and $tol_{\rm sp}$ is the overall tolerance. Now, because f is C_2 the differentiations in Eq. (5.20) are done exactly on f. The curvature $\kappa(S)$ becomes smooth because small numerical errors in the interface position (z_i, r_i) are filtered out, see example in Fig. 5.6. We typically use $tol_{\rm sp} = 10^{-7}$, we have $w_1 = w_M = 100$, and $w_i = 1$ for $i \neq 1, M$. The computation of the splines f_z, f_r, and their derivatives is done in the function `kappadata20.m` presented in Appendix A.

5.5 Time integration scheme

As mentioned earlier the time dependency in the problem boils down to the kinematic boundary condition Eq. (4.15) at the free interface,

$$\frac{d\boldsymbol{x}(S)}{dt} = \boldsymbol{u}(\boldsymbol{x}(S), t) \quad \text{for} \quad \boldsymbol{x} \in \partial\Omega, \tag{5.23}$$

where the velocity $\boldsymbol{u}$ is provided by the FEMLAB solution of the Stokes-flow problem and S is the arc-length parameter re-scaled with the total interface length. The presence of the the curvature Eq. (5.20) in the dynamic boundary condition introduce terms that have a large number of spatial derivatives. If Eq. (5.23) is solved by an explicit time integration method strong time stability-constraints are introduced [60, 62]. These constraints are generally time dependent and become more severe due to point clustering on the free interface [60]. Such constraints are referred to as stiffness. To avoid these problems our free interface is re-meshed at every solution step and we have chosen to solve the first order ordinary differential (ODE) Eq. (5.23) by using a second order Runge–Kutta scheme [63].

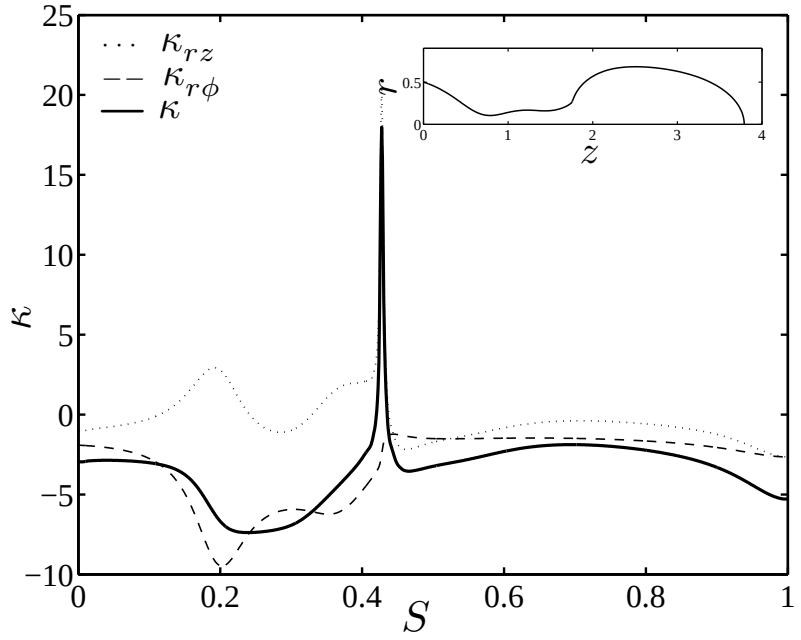

Figure 5.6: Example of the curvature results obtained with the approximating splines $\kappa(S) = \kappa_{rz} + \kappa_{r\phi}$ for the interface shape shown in the inset.

The algorithm is extended such that the problem of the free interface changing length over time is taken into account. Moreover, as we are not interested in the tangential movement $(\boldsymbol{u}\cdot\boldsymbol{t})\boldsymbol{t}$ of the interface points along the interface [21, 60] we use the classical reformulation of Eq. (5.23) to

$$\frac{d\boldsymbol{x}(S)}{dt} = (\boldsymbol{u}\cdot\boldsymbol{n})\boldsymbol{n} = F(\boldsymbol{x}(S),t) \quad \text{for} \quad \boldsymbol{x}\in\partial\Omega, \tag{5.24}$$

where $\boldsymbol{u}$ and $\boldsymbol{n}$ are functions of $\boldsymbol{x}(S)$ and t.

In a classical Runge–Kutta scheme an ODE $dy/dt = F(t,y)$ is discretized by

$$\begin{aligned} k_1 &= \frac{\Delta t}{2}F(t,y(t)) \\ k_2 &= \Delta t\, F(t+\frac{\Delta t}{2}, y_t + k_1) \\ y(t+\Delta t) &= y(t) + k_2 + O(\Delta t^3) \end{aligned} \tag{5.25}$$

where Δt is the discrete time step and the method is second order in time t. We have taken this method and extended it to Eq. (5.24) to include a mapping $S(t+\Delta t/2) = f(S(t))$

because our interface stretches and thus changes in time, $S = S(t)$. In this way we have

$$\begin{aligned} \boldsymbol{k}_1 &= \frac{\Delta t}{2}(\boldsymbol{u}\cdot\boldsymbol{n})\boldsymbol{n}\Big|_{\boldsymbol{x}(S(t))} \\ \boldsymbol{k}_2 &= \Delta t\,(\boldsymbol{u}\cdot\boldsymbol{n})\boldsymbol{n}\Big|_{\boldsymbol{x}(S(t+\frac{\Delta t}{2}))+\boldsymbol{k}_1} \quad \text{with} \quad S(t+\frac{\Delta t}{2}) = f(S(t)) \\ \boldsymbol{x}(t+\Delta t) &= \boldsymbol{x}(t) + \boldsymbol{k}_2 + O(\Delta t^3), \end{aligned} \tag{5.26}$$

the mapping f is a spline made on basis of the values $S_i(t)$ and $S_i(t+\Delta t/2)$. The value of the solution variables are interpolated on the boundary by using the `postinterp` FEMLAB function. At every time time step Δt is chosen so that,

$$\Delta t = \delta_t \min_i \left[\frac{\zeta_i}{\boldsymbol{u}\cdot\boldsymbol{n}_i}\right] \tag{5.27}$$

where $\delta_t < 1$ and ζ_i is the local mesh size at the site i.

To validate the time integration scheme a series of numerical test were performed. Figure 5.7 shows a comparison of six different time integration set-ups, the code was run for $Ca = 0.5$ and $p_2 = 90$ until the snap-off point.[2] The reference interface shape (marked with stars) was obtained by implementing a simple Euler first order scheme and running it with very small time steps $\delta_t = 0.003$. Secondly, an Adams predictor-corrector method [62] was implemented and run for $\delta_t = 0.3$: the method is seen to fall close to the reference but it was computationally quite heavy as it is based on an iterative method. Thirdly, the Runge–Kutta algorithm was implemented without the mapping $S(t + \Delta t/2) = f(S(t))$ and run for both $tol_{\mathrm{SP}} = 10^{-4}$ and 10^{-6}: clearly this was a bad idea and the results fall far from both the reference and the Adams curves. Finally, the full Runge–Kutta scheme with mapping was run for two FEM configurations. The numbers in brackets refer to the odder of the basis functions used for u, v, and p respectively. The results clearly shows that the method is reliable. Most importantly of all the computational cost is very low compared to the other methods. Less than 200 times steps where used for the Runge–Kutta methods (solving twice every time step), about 250 for the Adams method (solving 3 to 6 times every time step), and 3800 time steps were used for the Euler method. Clearly the time integration scheme that we have implemented seems very reliable. Moreover, the test shows the importance of the mapping f that handles the problems associated with the interface elongating and the shifting of the interface points $\boldsymbol{x}_i$. In the next Chap. 6 we present a validation of the code by numerically studying three problems that have analytical solutions.

[2] Results and discussions about snap-off and bubble generation are presented in Chap. 7.

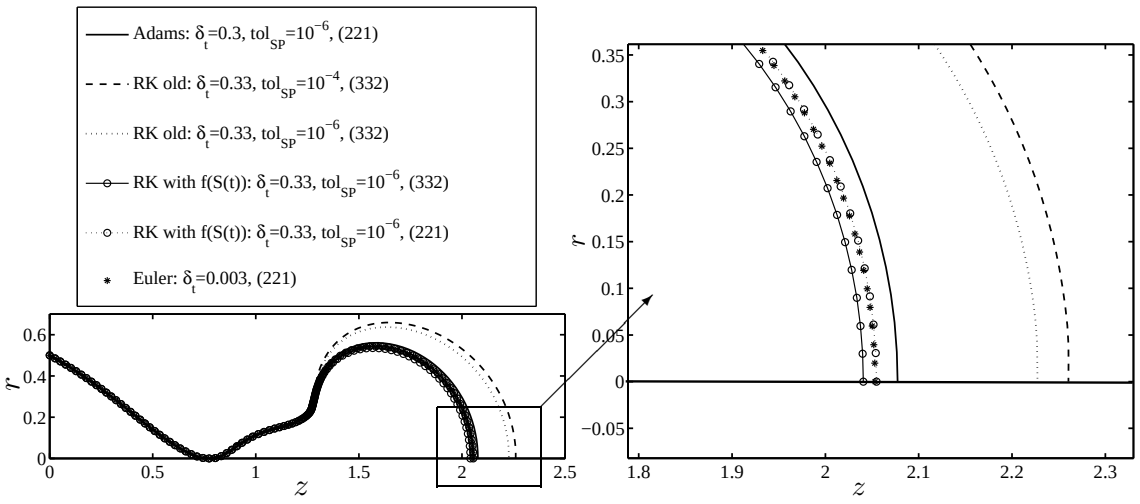

Figure 5.7: Comparison of four different time integration schemes: (1) First order Euler (stars), (2) Adams predictor-corrector scheme (full line), (3) Runge–Kutta (RK) without mapping f (doted lines), and (4) full Ringe–Kutta with mapping (lines with open circles).

Chapter 6

Numerics: validation

To assess the validity of the code described in Chap. 5 we have performed a series of numerical tests. A description of the tests and their results are presented in this chapter. The code is implemented for both 2D rectangular geometries and for 2D axisymmetric geometries. Both types of problems are tested and analyzed in this chapter.

Firstly, the code is tested on a standard benchmark problem: the surface tension driven Stokes-flow coalescence of two infinitely long parallel cylinders of unit radius. Secondly the steady state shape of gas bubbles in a cylindrical capillary tubes is studied, and thirdly the viscous drop in extensional flow problem is treated. Some further examples a then shortly presented and, finally, conclusions are drawn.

6.1 Coalescence of liquid cylinders

To validate the code described in Chap. 5 it has been applied to a standard 2D benchmark problem: the surface tension driven Stokes-flow coalescence of two infinitely long parallel liquid cylinders of radius one. This problem is set in a 2D rectangular geometry. The main advantage using this problem is that an exact analytical solution is known for this problem [47, 48, 49, 50, 51]. As we do not use the full axisymmetric model we are mainly testing the time scheme and parts of the curvature scheme. The volume conservation properties of the code are verified along with mesh dependency and convergence rate.

6.1.1 Problem set-up and analytical solution

When testing a numerical scheme or a new code it is always very convenient to compare the numerical results to known analytical solution. As we are working with Stokes-flow problems the work of R. W. Hopper is of paramount interest as his papers [47, 48, 49, 50] describe exact analytical solutions for a number of surface-tension driven 2D Stokes-flow problems in simply-connected geometries.

Figure 6.1 depicts a cross section view of two infinitely long liquid cylinders in contact at $(x, y) = (0, 0)$. The system reduces to a 2D problem because of the translational symmetry. The governing equations for the 2D flow are given in Eqs. (4.44) and (4.45). Note that

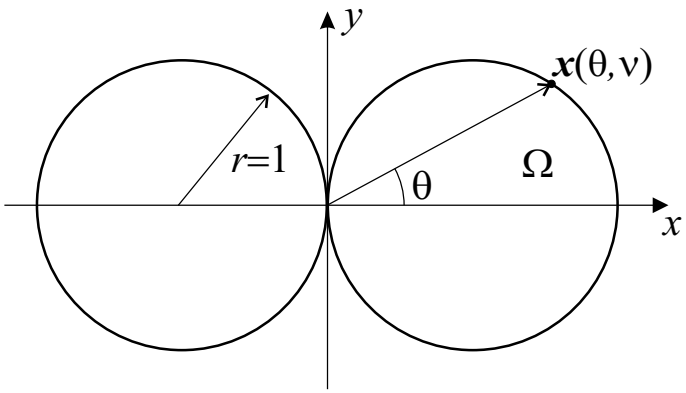

Figure 6.1: Cross-section view of two infinite cylinders of radius $r = 1$ touching at $(x, y) = (0.0)$. The closed curve describing the shape is given by $\boldsymbol{x}(\theta, \nu)$.

this may be physically unrealistic as the possibility of instabilities in the third dimension are removed. Nevertheless the problem is perfectly fitted for conducting numerical tests. As we assume the cylinders are suspended in zero-gravity surface-tension forces are the only driving the system, and they are thus pivotal in the analysis.

To solve the free-surface problem analytically Hopper used a time dependent conformal mapping from the domain Ω depicted in Fig. 6.1 to the unit circle. In the formulation of Hopper the cylinders had a radius of $1/\sqrt{2}$, details of the method are found in Ref. [47]. For the case of cylinders of radius $r = 1$ the location $\boldsymbol{x} = (x, y)$ of the free surface is given in Ref. [51] and is,

$$x(\theta, \nu) = \frac{(1-\nu^2)(1-\nu)\sqrt{2}\cos\theta}{(1-2\nu\cos 2\theta+\nu^2)\sqrt{1+\nu^2}} \tag{6.1}$$

$$y(\theta, \nu) = \frac{(1-\nu^2)(1+\nu)\sqrt{2}\sin\theta}{(1-2\nu\cos 2\theta+\nu^2)\sqrt{1+\nu^2}}, \tag{6.2}$$

where θ is the angle defined in Fig. 6.1 and ν is a decreasing function of time t, with $0 \leq \nu(t) \leq 1$. The liquid opening appearing where the two cylinders are coalescing is called the neck, from Eq. (6.2) the neck height H_{neck} is fond as

$$H_{\text{neck}} = y(\frac{\pi}{2}, \nu) = \frac{(1-\nu)\sqrt{2}}{\sqrt{1+\nu^2}}. \tag{6.3}$$

This height is an important observable that is easily compared to the numerical results. The time t is given as

$$t(\nu) = \frac{\pi}{\sqrt{2}} \int_\nu^1 \frac{dk}{k\sqrt{1+k^2}K(k)}, \tag{6.4}$$

where $K(k)$ is the complete elliptic integral of the first kind,

$$K(k) = \int_0^{\frac{\pi}{2}} \frac{ds}{\sqrt{1-k^2\sin^2 s}}. \tag{6.5}$$

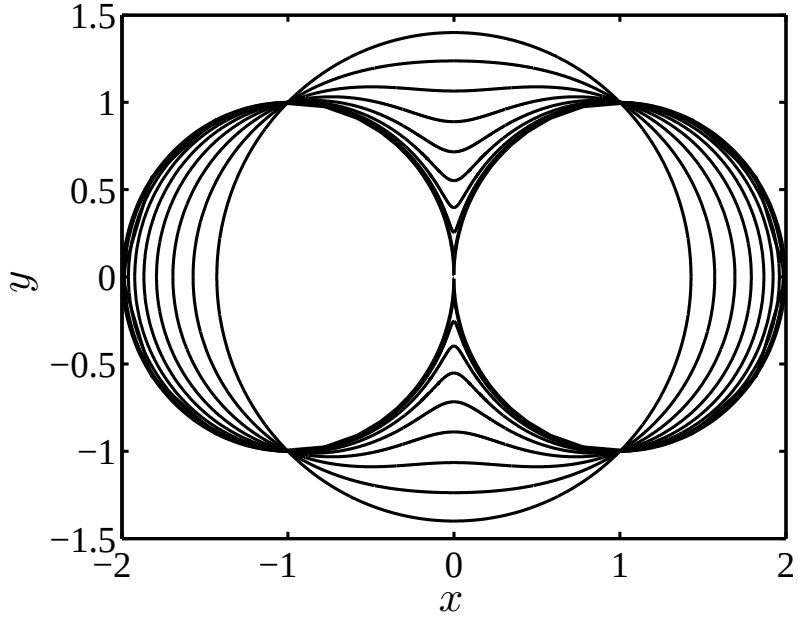

Figure 6.2: Evolution of the shape of two coalescing infinite liquid cylinders. The shapes are obtained using the analytical solution Eqs. (6.1) and (6.2).

The evolution of the shape of the two coalescing cylinders is depicted in Fig. 6.2. The shapes have been calculated using Eqs. (6.1) and (6.2). The elliptic integral is evaluated using the MATLAB function `ellipke.m` and the integral of Eq. (6.4) is evaluated using a simple trapeze formula.

6.1.2 Numerical results

The system of the two liquid cylinders has three symmetries (a) the translational symmetry, (b) a symmetry about the x-axis, and (c) a symmetry about the y-axis. In the simulations we utilize all the symmetries, such that the computational domain is reduced to the upper right quadrant. An example of the computational domain with mesh is depicted in Fig. 6.3.

As initial condition for the shape of the interface we used the curve generated by Eqs. (6.1) and (6.2) at a small time $t > 0$. The five different sets of mesh parameters used to test the program are seen in Table. 6.1. The code ran until $t = 11$ at which point the shape is virtually constant and the neck height assumes a constant value $H_{\text{neck}} = \sqrt{2}$.

A zoom of the region near the neck of the two coalescing cylinders is seen in Fig. 6.4. The figure shows the interface with interface mesh points and the velocity field for three different times.

In Fig. 6.5 the neck height H_{neck} is plotted as function of time t. The analytical result from Eq. (6.3) are depicted together with the numerical results obtained with the five different mesh parameter sets given in Table. 6.1. For all the simulations the initial neck height was $H_{\text{neck}} = 0.2$ corresponding to time $t = 0.16$. The computation time ranged

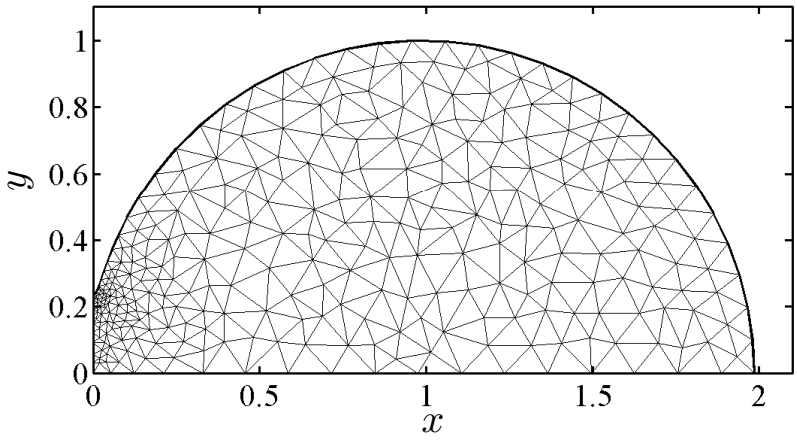

Figure 6.3: Example of a mesh used for the simulations. The mesh is refined around the interface at the neck where the curvature is large, near $(x, y) = (0, 0.2)$.

mesh nr.	δ_t	tol_{SP}	ζ	ζ_{vtx}	*Hcurve*	# elements
1	0.33	10^{-7}	0.05	0.005	0.1	1062
2	0.5	10^{-7}	0.05	0.005	0.1	1062
3	0.5	10^{-7}	0.05	0.05	0.2	953
4	0.5	10^{-7}	0.1	0.1	0.2	752
5	0.5	10^{-7}	0.1	0.1	10	399

Table 6.1: Table of the mesh parameters used for the numerical tests includes: the time-step parameter δ_t, the curvature spline-tolerance parameter tol_{SP}, the free interface mesh size ζ, the mesh size at the neck vertex ζ_{vtx}, the FEMLAB mesh curvature parameter *Hcurve*, and the number of triangular mesh elements.

from 60 min for mesh 1 to 15 min for mesh 5. From the graph it is seen that the numerical and analytical solutions are nearly identical. For the finer grids 1 and 2 the error was less than 0.1%. There are no significant differences due to the choice of δ_t. For grids 3 and 4 the initial evolution is in good agreement but discrepancies are noted for $t > 2.5$. For larger times wiggles in the interface splines (`ppx` and `ppy`, see Sec. 5.3) are caught by the FEMLAB mesh routine as `Hcurve` is small. These wiggles are discussed in detail in Sec. 5.3 of Chap. 5. It is worth noticing that mesh 5 does not produce these wiggles as `Hcurve` is set equal to 10 and thus does not influence the meshing. Finally it is also interesting to note that all five mesh produce nearly equally good results for small times. At small times the curvature in the neck region is large and one could expect a coarser mesh to be less good. As the curvature scheme of this code utilizes approximating splines and symmetry points the curvature of the neck region is nicely represented even for few interface points.

The area conservation properties of the code are also investigated. In Fig. 6.6 the relative variation in area $|A(t) - A_0|/A_0$, where A_0 is the area at time $t = 0$, is plotted as function of time. For meshes 1 and 2 the error is very small and constant while for meshes 3, 4 and 5 the error is a factor 4 larger but still less than 0.1%, which is very small.

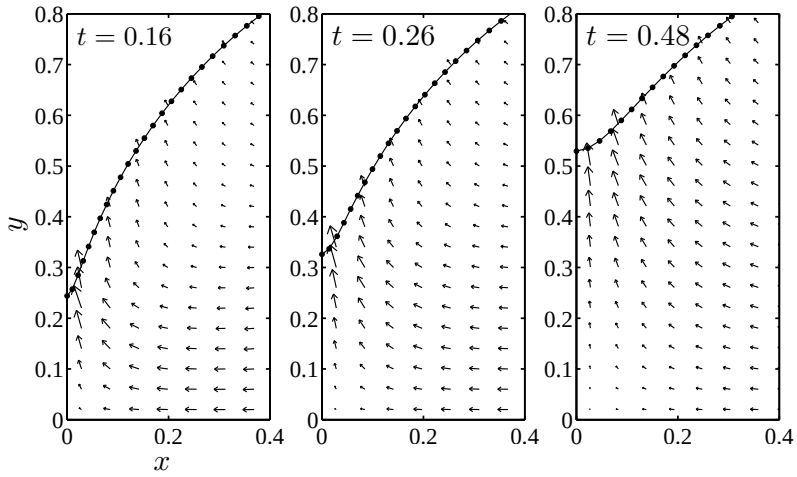

Figure 6.4: Zoom near the neck region showing the interface with mesh points and the velocity field for three different times $t = 0.16$, 0.26, and 0.48.

The results are very good and gives great confidence in the performance of the code. Especially the time stepping algorithm and the curvature algorithm seem very reliable. These ensure correct dynamics at the free surface and in turn ensures good area/volume conservation properties of the code.

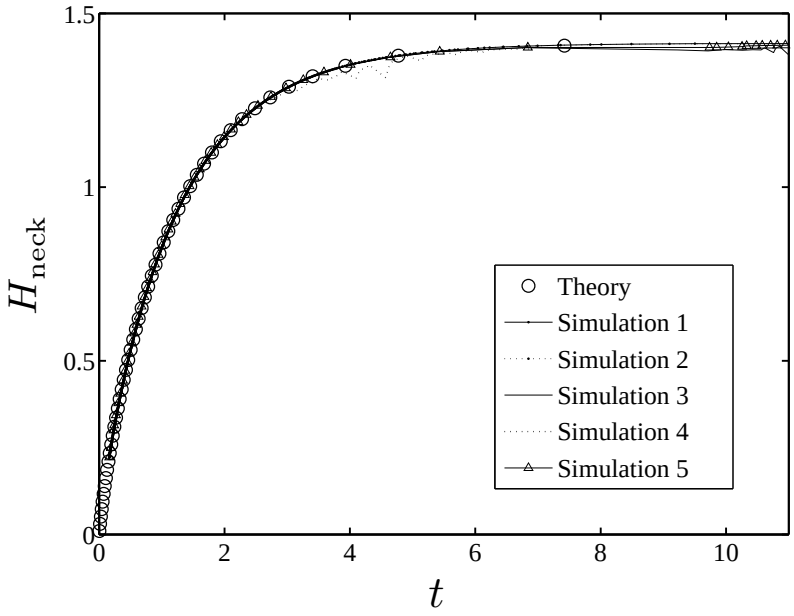

Figure 6.5: The neck height H_{neck} plotted as function of time. The circles represent the analytical results from Eq. (6.3) and the lines are simulation results with the different mesh parameters given in Table. 6.1.

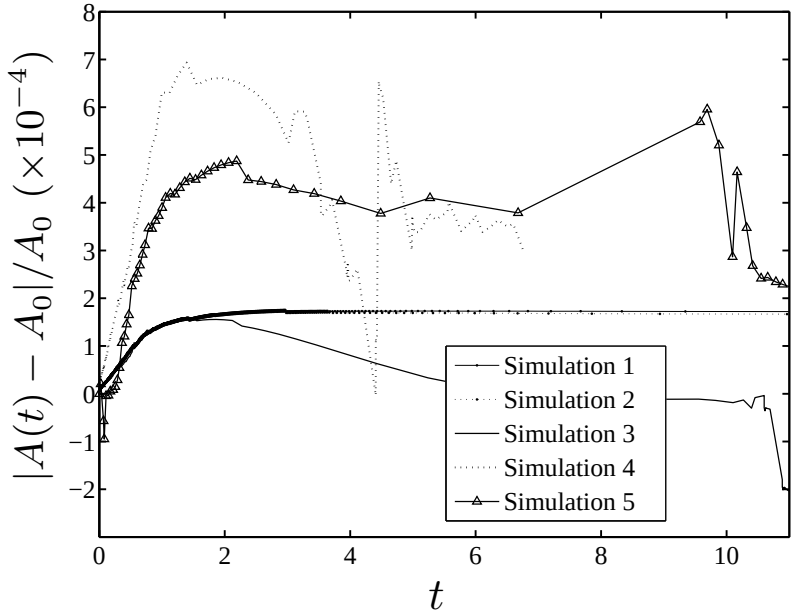

Figure 6.6: The relative variation in area $|A(t) - A_0|/A_0$, where A_0 is the area at time $t = 0$, plotted as function of time.

6.2 Bubble translating steadily in a capillary tube

The main application of the code is with axisymmetric systems, specifically the axisymmetric flow-focusing device studied in detail in the later Chap. 7. As a simple test of the axisymmetric version of the code we will numerically study the steady-state shape of a long non-wetting gas-bubble translating in a cylindrical capillary filled with liquid. The first theoretical treatment of a bubble moving steadily at velocity V in a circular capillary tube was done by Bretherton in his classical work from 1960 [52]. His analysis is limited to infinitely long bubbles and is an asymptotic result for low capillary numbers $Ca = \mu V/\gamma$, where γ is the liquid-gas interfacial-tension and μ the dynamic viscosity of the liquid. Later in 1983 Parker and Homsy [53] formalized Bretherton's approach by using perturbation and asymptotic matching theory. Work on bubbles of finite length was done by Schwartz *et al.* (1986) [54], and by Ratulowski and Chang [55] in 1989. The latter work introduced a very cunning arc-length representation of the liquid-gas interface enabling the treatment of bubbles of arbitrary size. The theoretical results where compared to experiments and were seen to be valid for $Ca < 0.1$. The previously mentioned studies utilize Stokes flow with appropriate boundary conditions. These are no-slip at solid walls and the use of the Young-Laplace equation on the bubble interface to describe the discontinuity in the normal stress.

6.2.1 Theoretical results

We will now shortly present some of the theoretical results obtained in Refs. [52, 53, 54, 55]. Consider a bubble of length L moving at speed V in a long cylindrical capillary of radius R filled with liquid. The bubble is driven by the liquid flow, which far from the bubble is simple poiseuille flow. The mean velocity of the liquid is $U = U_{\max}/2$, where $U_{\max}$ is the maximal velocity. The thickness of the liquid film around the bubble is denoted h_0, see Fig. 6.7(a).

In deriving the expressions presented here the governing equations were re-scaled slightly differently from the ones we present in Chap. 4. In this numerical test the governing equations and the BC at the interface are

$$0 = -\boldsymbol{\nabla} p + Ca\nabla^2 \boldsymbol{u} \tag{6.6}$$

$$0 = \boldsymbol{\nabla} \cdot \boldsymbol{u} \tag{6.7}$$

$$\boldsymbol{\sigma} \cdot \boldsymbol{n} = (p_2 - \kappa)\boldsymbol{n} \quad \text{at} \quad \partial\Omega_{\text{bubble}}, \tag{6.8}$$

where we have re-scaled the velocity with V, lengths with R, and the pressure with γ/R, see also Fig. 6.7(a). Using this scaling and the governing equations Eq. (6.6) and (6.7) Bretherton [52] found the thickness h_0 of the wetting film to be given by

$$h_0 = 0.643(3Ca)^{2/3}, \tag{6.9}$$

where the pre-factor of 0.643 is found by fitting numerical data.[1] The speed of the bubble exceeds the mean velocity of the liquid by an amount wV, where the relation between V

[1] In this example we assume that the bubble is non-wetting. We are not interested in the problems

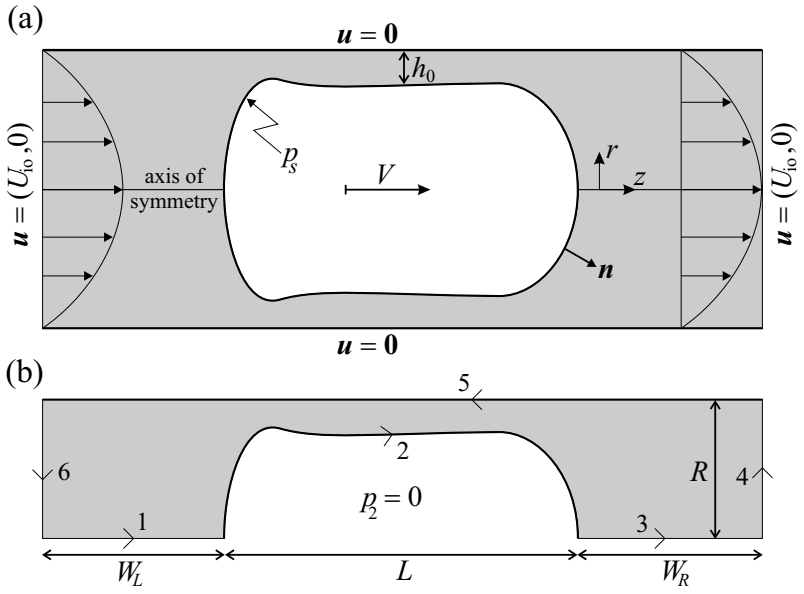

Figure 6.7: Sketch of a system comprising a gas bubble translating at speed V in a capillary tube. (a) the physical system with the wetting film thickness h_0, the velocity BCs at the inlet and outlet, the no-slip condition at the tube wall, the pressure p_s at the surface of the bubble found by applying Eq. (6.8), and the surface normal $\boldsymbol{n}$. (b) Sketch of the computational domain including bubble length L, channel re-scaled radius $R = 1$, and the boundary orientations and numbers.

and U is

$$U = (1 - w)V, \quad w = 1.29(3Ca)^{2/3}, \tag{6.10}$$

It has been shown numerically that Eq. (6.10) is valid for bubbles of volume $V_b > 0.95V_c$, where $V_c = 4/3\pi R^3$ is a critical bubble volume [56]. Finally, the pressure drop across the bubble Δp_b is given by

$$\Delta p_b = 9.40Ca^{2/3} - 12.6Ca^{0.95}. \tag{6.11}$$

The last term in this expression is a correction to the original Bretherton formula $\Delta p_b = 9.40Ca^{2/3}$. The correction corresponds to the next-order correction one would expect from an asymptotic analysis [55]. Note that the pressure drop is independent of the bubble length. This results from the zero shear stress condition at the liquid-gas interface. The pressure drop is only function of the curvature of the bubble front and rear, respectively.

6.2.2 Model set-up

The axisymmetric version of the code, described in Chap. 5, is applied to the problem of finding the steady state shape of a gas bubble in a capillary. The code is here utilized in a slightly different way than in the previous example. As we wish to find the steady state

arising when the wetting film becomes very thin, i.e., with dynamic contact angles [34, 35], film drying [57], non-hydrodynamic forces etc. Note that forces such as long-range van der Waals typically become important for length scales less than about 10 to 100 nm [56].

shape of the interface we are not simulating actual dynamics of the gas bubble but rather using the code to find the minimal energy configuration of the system.

We initiate the code with a bubble shaped like a cylinder with two hemispherical caps. The code is then ran by succeedingly advancing one time step and then moving the bubble back to the initial location. By employing this strategy we evolve the initial shape to a steady state shape. The convergence to the steady state shape is easily assessed by monitoring one of several parameters as, e.g., the bubble length L, the interface length L_{int}, the difference between rear and front interface velocity Δu, or simply the shape of the bubble interface $\boldsymbol{x}_{\text{int}}$.

In Fig. 6.7(a) all the physical boundary conditions of the system are depicted. On the solid walls the no-slip condition is applied $\boldsymbol{u} = \boldsymbol{0}$. At the inlet and outlet of the capillary identical velocity BCs are applied, i.e.,

$$\boldsymbol{u} = (U_{\text{io}}, 0) \quad \text{with} \quad U_{\text{io}} = 2(1-r)(1+r), \tag{6.12}$$

as $r \in [0,1]$, this yields a mean liquid velocity $U = 1$. By applying these inlet and outlet boundary conditions we force the bubble to be incompressible because of volume conservation of the incompressible liquid, condition given in Eq. (6.7). The pressure in the system is defined on the bubble surface through the stress BC Eq. (6.8). The pressure p_2 in the gas depicted on Fig. 6.7(b) only serves as zero point and is set equal to zero.

Figure 6.7(b) depicts the computational domain used in the simulations. At $r = 0$ on boundaries 1 and 3 we obviously apply symmetry conditions. The length of the distance at the left and right of the bubble W_L and W_R, respectively, are chosen such that $W_L = 6R = 6$ and $W_R = 6R = 6$. This ensures that the bubble shape is not influenced by boundary effects.

6.2.3 Numerical results

The aim of this test is mainly to test the time-step algorithm for volume conservation properties and the coupling to the mass conservation properties of the FEMLAB solver.

Single parameter run

In this first example we have chosen a given set of parameters namely (a) the physical parameters $L = 6$, $W_L = W_R = 6$, and $Ca = 6.5 \times 10^{-2}$, and (b) the numerical parameters $\zeta = 0.03$, $\delta_t = 0.33$, and $tol_{\text{SP}} = 10^{-7}$.

The evolution of the interface from the initial cylinder with hemispherical caps (dotted line) to the steady state shape (bold full line) is depicted in Fig. 6.8. The steady state shape has the characteristic bump of just at the rear just before the end cap [52, 55]. The convergence to the steady state shape was achieved in 450 time steps (corresponding to 3.5 h of calculation time) and was assessed by the parameters depicted in Fig. 6.9. Figure 6.9(a) shows the thickness of the wetting layer h_0 together with the Bretherton limit of Eq. (6.9). As expected they do not agree as the Bretherton theory only is valid for $Ca \ll 1$. In Fig. 6.9(b) the excess speed parameter w is ploted as function of time, again, together with the Bretherton limit of Eq. (6.10). The graphs in Fig. 6.9(c) show

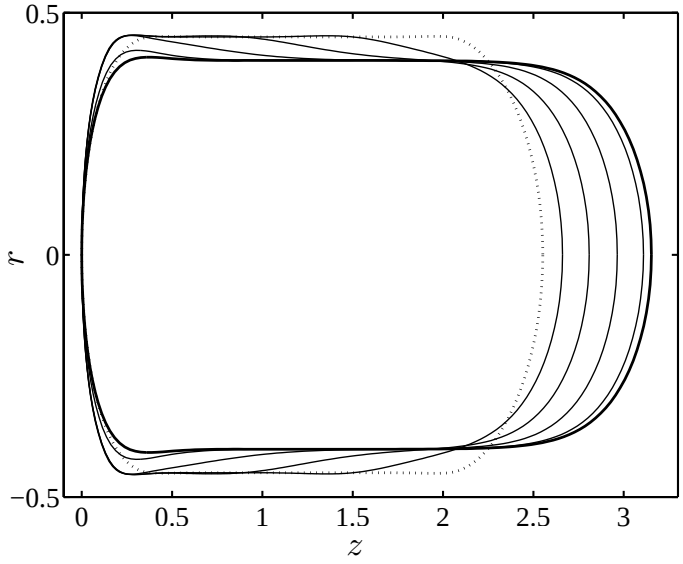

Figure 6.8: Evolution of the interface from the initial shape of a cylinder with hemispherical caps (dotted line) to the final steady state shape (bold full line). The aspect ratio of the axis is 1 to 4 such that the details of the shape near the wall are more pronounced.

the relative change in bubble volume $(V_b - V_0)/V_0$, where V_0 is the initial volume at $t = 0$, and in (d) the normal velocity $\boldsymbol{u} \cdot \boldsymbol{n}$ of the interface at the symmetry axis $r = 0$ at the front and rear of the bubble, respectively. It is seen that h_0, w, and the relative volume error converge to a constant value, while the normal velocities also are seen to become identical and equal to the bubble speed V. It is also very interesting to note that the change in bubble volume is less than 0.1 %. The very small change may be due to drift in the time-step algorithm or in the fact that FEMLAB may not be fulfilling the volume conservation Eq. (6.7) exactly.

Small parametric run

The previous example is now extended to include four values of the capillary number namely $Ca = 6.5 \times 10^{-2}$, 3.7×10^{-2}, 1.7×10^{-2}, and 9.0×10^{-3}. All the other parameters are unchanged. The steady state shapes of of the four bubbles are depicted in Fig. 6.10. For decreasing Ca, that is for increasing surface tension, the bubbles fill the channel more.

In Fig. 6.11 the simulated values of h_0, w, and Δp (circles) are compared to the theoretical results of Eqs. (6.9) to (6.11) (lines). In Fig. 6.11(c) the original Bretherton model is depicted together with the extended result of Eq. (6.11). From the three graphs it is evident that the theory diverge from the simulated "exact" results for larger values of the capillary number. This trend is consistent with the results from Ref. [55]. Note that the pressure drop Δp fits well with the extended theory for a larger range of Ca numbers.

While performing the simulations to obtain the results discussed above we noted that the time step parameter δ_t (see Sec. 5.5) had to be decreased, for decreasing values of the capillary number, to avoid heavy wiggling of the interface. This observation is consistent

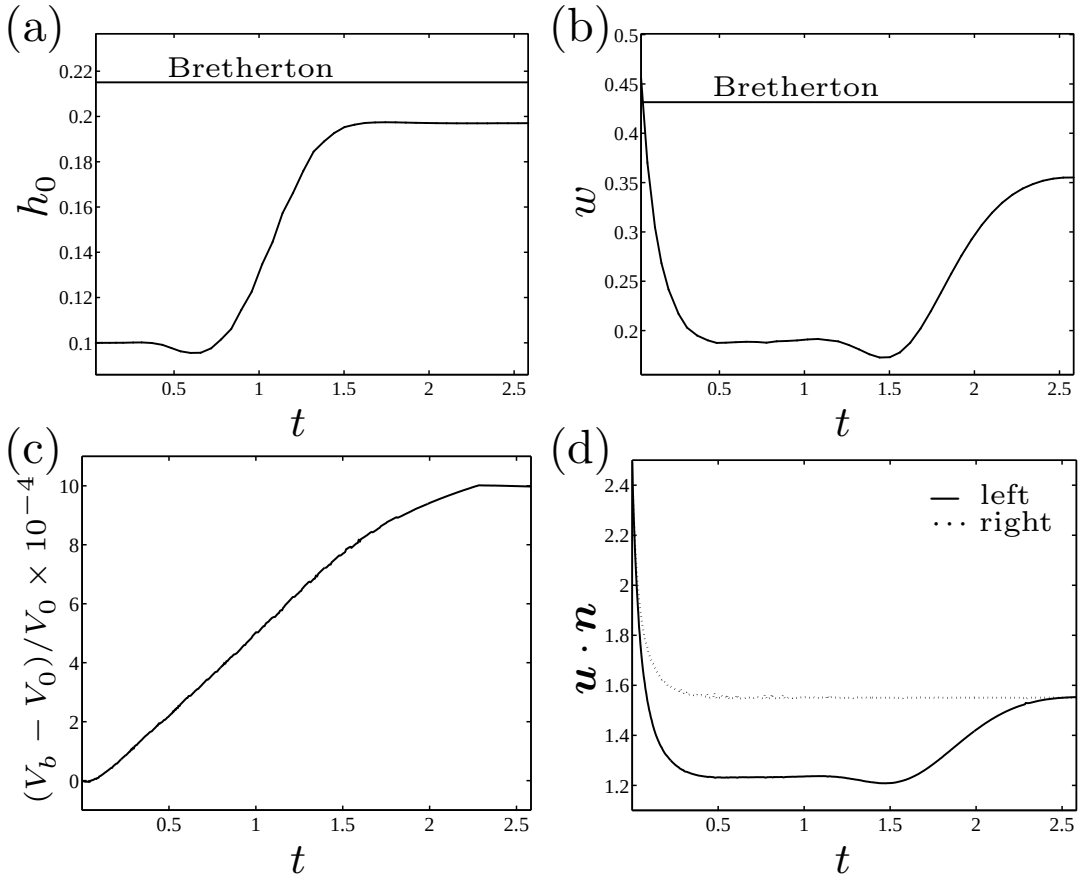

Figure 6.9: The convergence towards steady state is assessed by (a) the thickness of the wetting layer h_0, the Bretherton limit of Eq. (6.9) is also depicted, (b) the excess speed parameter w, Bretherton limit of Eq. (6.10) also depicted, (c) the relative change in bubble volume $(V_b - V_0)/V_0$, where V_0 is the initial volume at $t = 0$, and (d) the normal velocity of the interface at the symmetry axis $r = 0$ at the front and rear of the bubble, respectively.

with existing numerical schemes. Rider *et al.* [19] introduce a maximally allowed time step $\delta t_\gamma \propto h_{\min}^{3/2}/\gamma$, where $h_{\min}$ is the minimal resolution of the interface and γ is the surface tension. This factor is related to the oscillation period of capillary waves and is derived from the dispersion relation of capillary waves [28, 31]. When wiggles where observed, especially in the interface velocities, the time step was decreased and the wiggles disappeared.

The shapes of two small bubbles have been calculated for $Ca = 9.0 \times 10^{-3}$ and 6.5×10^{-2}, their shapes are depicted in Fig. 6.12. In this case the volumes of the bubbles V_b are less than the critical volume mentioned earlier: $V_b = 0.45$ and $V_c = 0.52$. The thickness h_0 and the parameter w are still relatively close to the Bretherton results, within 10%, while pressure drop across the bubble Δp compares very well to the theoretical result of Eq. (6.11).

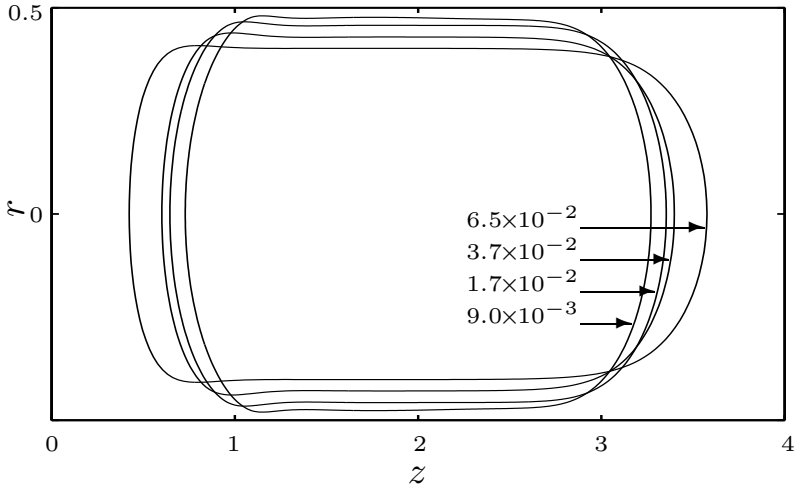

Figure 6.10: Steady state shapes of a bubble for four different values of the capillary number.

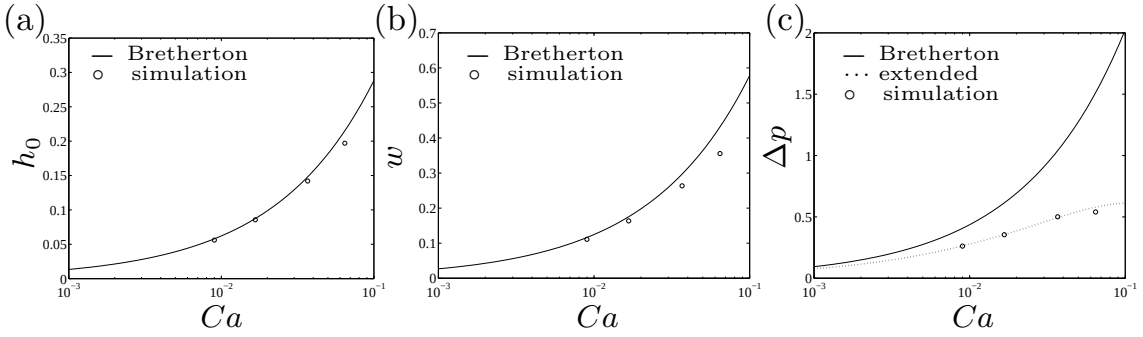

Figure 6.11: Comparison of theoretical and numerical results of (a) the wetting film thickness h_0, (b) the excess speed parameter w, and (c) the pressure drop across the bubble Δp.

This test further confirm the very good qualities of the code. Particulary the volume conservation properties and the time-step algorithm show their reliability. If the code had to be ran for even smaller values of the capillary number δ_t would have had to be decreased even further and the simulations would have become very time consuming. In practice it is possible to numerically include so-called hyper viscosity terms that dampen the capillary waves. This ensures that the time steps may be chosen large and the computation time thus remain reasonable [27].

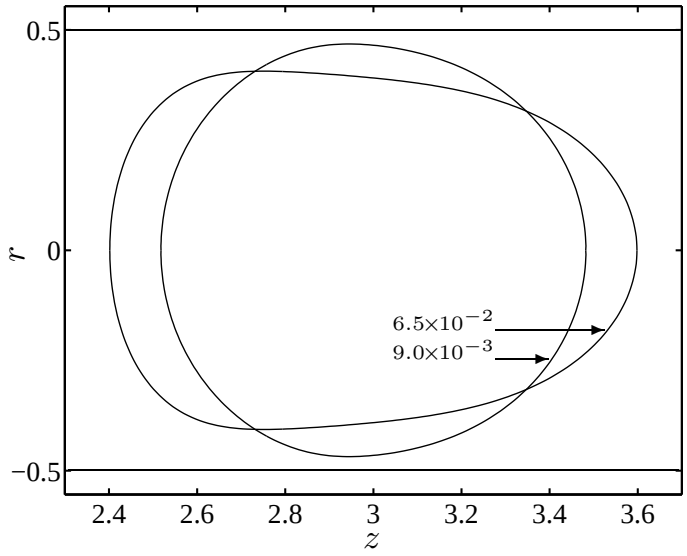

Figure 6.12: Steady state shapes of a small bubble for two different values of the capillary number, $Ca = 6.5 \times 10^{-2}$ and $Ca = 9.0 \times 10^{-3}$.

6.3 Viscous drop in extensional viscous flow

As a final numerical test we will study the steady deformation of a neutrally-buoyant viscous-drop in a viscous extensional-flow. To this purpose the code has been extended to include two fluids of different viscosities. The governing equations of this system are given in Sec. 4.8. The system has two free parameters: (1) the viscosity ratio ϵ_μ between the drop and the external fluid, and (2) the capillary number Ca (both defined below).

The subject of deformation of drops in viscous flows was initially studied by G. I. Taylor and traces back to 1932 [58, 65, 66]. A very good review of the subject is given by Stone in Ref. [67]. Acrivos [68, 69] give a summary of theoretical results for long slender drops in his paper from 1978. More recently two papers compare experimental and theoretical results and also discuss breakup of the drops [70, 71]. The introduction of simple non-Newtonian fluids obeying the power-law is discussed in Ref. [72]. Generally the deformation problem has been the subject of many numerical and experimental studies for varying external flow properties and complexities [67].

The present test more has the nature of a small study or example than that of an actual numerical test-case. This is mainly due to the fact that theoretical results for this system only exists for specific limits in the parameter space. We explore these limits to some extend but do also present more qualitative results for parameters with values in intermediate ranges. Firstly, we shortly present the theory and the model set-up and secondly we present the numerical results.

6.3.1 Theory

A drop placed in a simple axisymmetric extensional flow is depicted in Fig. 6.13. The external forcing extensional flow is given by,

$$\boldsymbol{u} = U_{\text{ext}} = \left(Gz, -\frac{1}{2}Gr \right) \tag{6.13}$$

where G is the shear rate. The ratio between the viscosity of the drop μ_2 and the viscosity of the external fluid μ_1 is denoted $\epsilon_\mu = \mu_2/\mu_1$. The capillary number of the system is defined as $Ca = \mu_1 U/\gamma$ with $U = aG$, where γ is the interfacial tension and a is the radius of the initial spherical drop of same constant volume. In the following all lengths are rendered dimensionless with a, pressures with $\mu_1 G$, and velocities with $U = aG$. As a measure of the deformation of the drop is given by either

$$d_f = \frac{L - R_0}{L + R_0} \qquad \text{for small deformations} \tag{6.14}$$

$$D_f = \frac{L}{a} \qquad \text{for large deformations.} \tag{6.15}$$

The capillary number Ca and the viscosity ratio ϵ_μ are the two free parameters of the present system. The problem now consists of determining the final steady shape of an initial spherical drop of dimensionless radius 1. It is important to note that for many choices of the free parameters Ca and ϵ_μ the drop is unstable and will elongate to a point

where it will eventually break-up. There are two regimes where theoretical results exist these are the small and the large deformation regimes:

The small deformation regime

The work with small deformations of a drop in extensional flow was pioneered by G. I. Taylor. In this regime the drop only deforms slightly from spherical and the domain perturbation method may be applied [71]. In our case this regime exist for $Ca \ll 1$ and for all values of ϵ_μ. In this regime it was first demonstrated by Taylor that the deformation d_f is linear in Ca for a given ϵ_μ.

The large deformation regime

This regime exist when the drop is very elongated and has a small slenderness ratio R_0/L. In this regime a theory exist when the viscosity ratio is small actually when $(5\epsilon_\mu)^{1/2} \ll 1$, see Refs. [68, 71]. In this large deformation regime a so-called deformation relation exists,

$$f = 20^{-1/2} \frac{g^{1/2}}{1 + \frac{4}{5} g^3}, \tag{6.16}$$

where $g = L\epsilon_\mu^{1/3}$ is the re-scaled steady state length of the bubble and $f = Ca\, \epsilon_\mu^{1/6}$ is a measure of the flow strength.

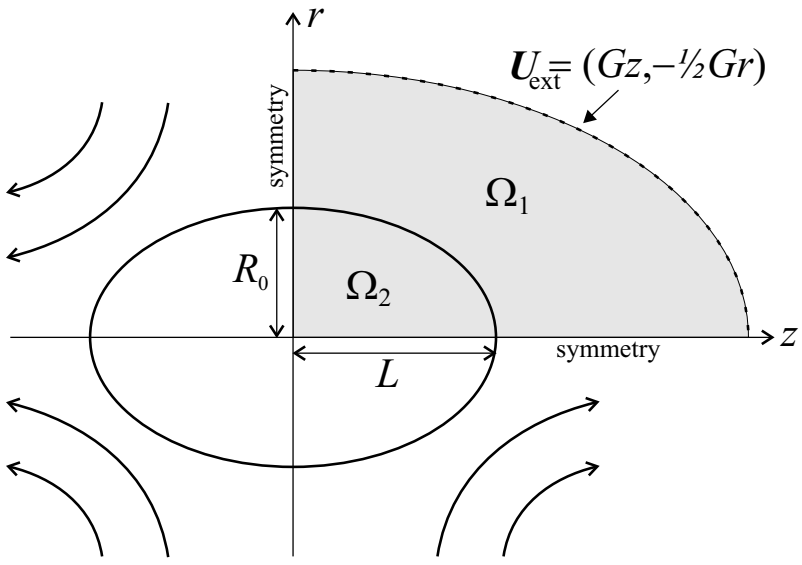

Figure 6.13: Sketch of the drop in an extensional flow. The drop length is L and the radius at $z = 0$ is R_0. The light gray area represents the total computational domain $\Omega = \Omega_1 \cap \Omega_2$, where we have used all possible symmetries. The outer dottel line represents the boundary where we impose the extensional flow condition $\boldsymbol{u} = U_{\text{ext}} = (Gz, -1/2\, Gr)$. The arrows illustrate the nature of the extensional flow.

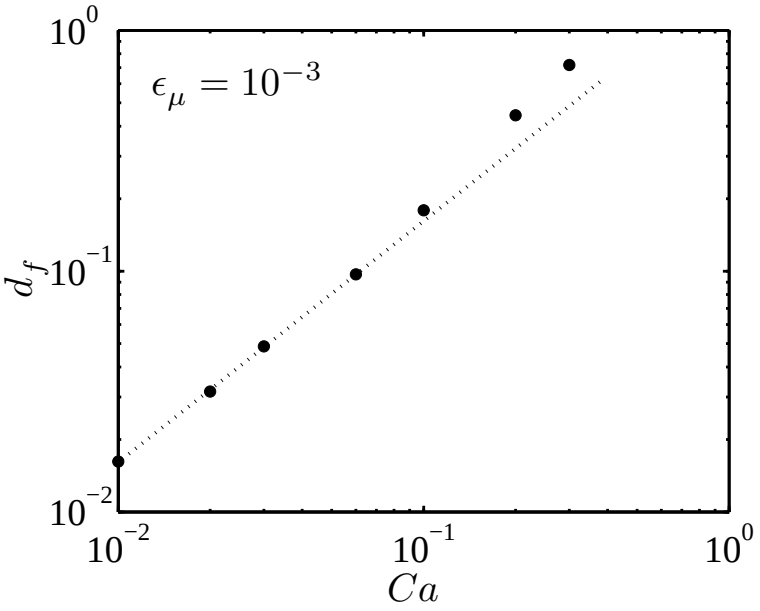

Figure 6.14: Double logarithmic plot of the small deformation parameter d_f as function of the capillary number Ca, for $\epsilon_\mu = 10^{-3}$. The numerical data-points deviate from the linear behavior for increasing values of Ca.

6.3.2 Model set-up

Numerically the computational domain $\Omega = \Omega_1 \cap \Omega_2$ is reduced using symmetry about the z and r-axis, see Fig. 6.13. At the boundary between liquid 1 and 2 the free surface boundary condition is applied, see Eq. (4.39). At the outer boundary of Ω_1 the velocity boundary condition given in Eq. (6.13) is applied. To ensure that no numerical drift occurs in the pressure the pressure is fixed at $(z, r) = (0, 0)$ such that $p(0, 0) = 0$.

6.3.3 Numerical results

To assess the convergence the drop shape to a steady state shape the deformation parameter d_f and the interface velocity at $r = 0$ and $z = 0$ where monitored. This strategy resembles the one employed for the bubble in capillary problem discussed above. Results for the large and the small deformation regimes are here discussed separately.

Small deformation regime

In Fig. 6.14 the small deformation parameter d_f of Eq. (6.14) is plotted as function of the capillary number Ca, for constant $\epsilon_\mu = 10^{-3}$. It is seen that the relation is linear for small values of Ca as predicted by Taylor [65]. For $Ca > 0.1$ the numerical data points are seen to deviate from the linear relation.

Moreover, for two constant values of the capillary number the deformation d_f is plotted as function of the viscosity ration ϵ_μ, see Fig. 6.15. From comparing the two figures

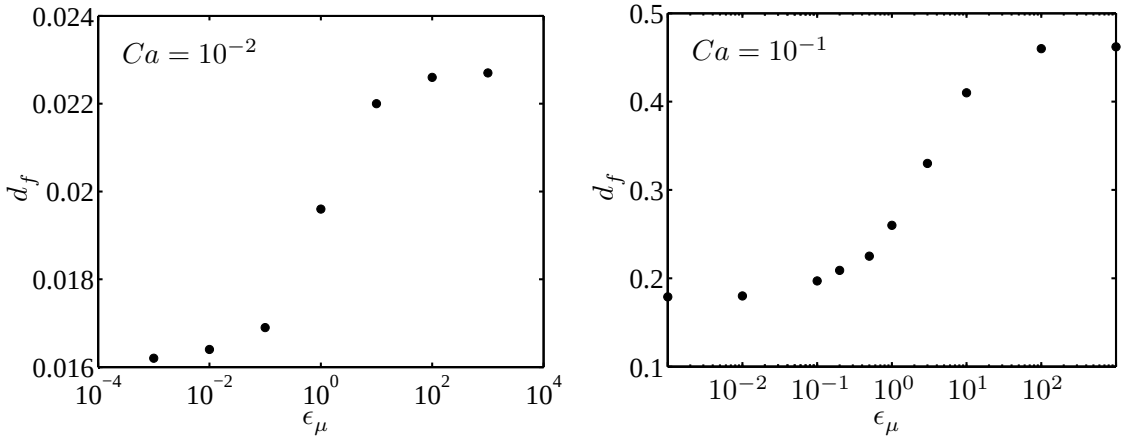

Figure 6.15: The small deformation parameter d_f as function of the viscosity ratio ϵ_μ for two values of the capillary number $Ca = 10^{-2}$ and 10^{-1}.

($Ca = 10^{-2}$ and $Ca = 10^{-1}$) it is seen that the generic behavior is the same: for small and large values of ϵ_μ the deformation is constant and a transition occurs around $\epsilon_\mu = 10^0$. In Ref. [65] Taylor shows that the small deformation parameter follows the relation $d_f = Ca(19\epsilon_\mu + 16)/(16\epsilon_\mu + 16)$. This relation does not correspond to the extensional flow given in Eq. (6.13) but to a flow given by $\boldsymbol{u} = (Gz, -Gr)$. Anyhow, this relation produces the same behavior for d_f as the one depicted in Fig. 6.15.

Large deformation regime

In the large deformation regime the re-scaled length g is related to the re-scaled flow strength f through Eq. (6.16). This relation is depicted in Fig. 6.16 together with labelled numerical results corresponding to the parameters given in Table 6.2. In the figure the solid line represents stable steady state solutions solutions while the line with added crosses represents the unstable branch of the solutions that, hence, have no physical relevance [68]. This means that for a given maximal value of f named $f_{\max}$ given by the two free flow-parameters the drop will be unstable and break-up. This is obviously only valid in the large deformation regime discussed above.

In Table 6.2 the parameters $(5\epsilon_\mu)^{1/2}$ and R_0/L are given. It is seen that points 3, 6, 7, and 10 are those closest to the large deformation regime. The points 3, 6, and 7 are seen to follow the deformation curve relatively well while point 10 is spot on. Point 10 also fulfilling the large deformation criterion best.

In all of the above simulations the relative deviation in the volume of the bubble was less that 0.01%. This is mainly due to the fact that the incompressibility condition is enforced in the drop and outside the drop. The only small drift may be due to the time stepping algorithm or to small errors in the curvature scheme. The computation time and the fineness of the grid varied very much depending on what flow parameters where chosen. For small values of Ca a fine grid and small time-steps are typically needed. But this also depends on the viscosity ratio and hence the amount of viscous damping in the

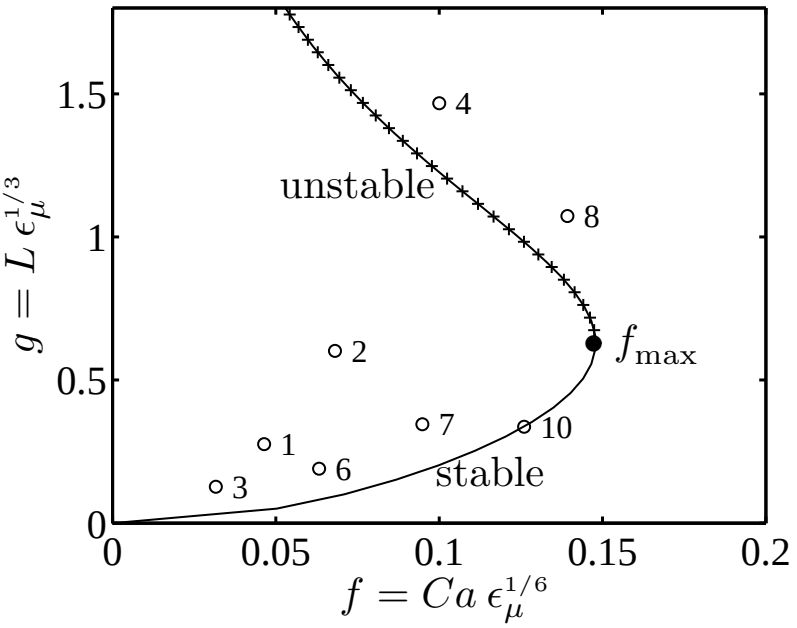

Figure 6.16: Representation of the deformation curve Eq. (6.16) together with numerical data points given in Table 6.2. The solid line represents stable solutions and the line with crosses represents unstable steady state solution. $f_{\max}$ is the maximal value of f for which stable steady state solutions exist.

system.

Intermediate range

Finally we present two figures one of a drop in the intermediate range between large and small deformations and one of a bubble doomed to break up. Firstly, Fig. 6.17 represents the steady state shape for the drop with parameter set # 4 from Table 6.2. The vector plot represents the normalized velocity field and the gray scale plot the pressure field (light gray is low pressure and dark gray is hight pressure). Here it is, e.g., interesting to note the recirculation inside the drop. Secondly, the evolution of the shape of an unstable drop is depicted in Fig. 6.18, where $Ca = 0.5$ and $\epsilon_\mu = 10$. The shape of the drop is still evolving but the simulation was terminated after about 100 min of computation time.

6.4 Concluding remarks outlook

From the results obtained in the three test cases it is evident that the code is reliable and produces correct numerical results. The coupling between time-step algorithm, curvature algorithm and the FEMLAB solver works perfectly.

The code has also shown that it is very versatile and easy to use. It was easily modified to suit the different geometries and physical systems relevant for the three tests. The flexibility of the code certainly lies in the way FEMLAB and MATLAB communicates.

#	Ca	ϵ_μ	$(5\epsilon_\mu)^{1/2}$	R_0/L	f	g
1	10^{-1}	10^{-2}	0.2236	0.6893	0.0464	0.2760
2	10^{-1}	10^{-1}	0.7071	0.6760	0.0681	0.6019
3	10^{-1}	10^{-3}	0.0707	0.6986	0.0316	0.1269
4	10^{-1}	10^{0}	2.2361	0.5567	0.1000	1.4671
5	10^{-1}	10^{1}	7.0711	0.0205	0.1468	20.169
6	2×10^{-1}	10^{-3}	0.0707	0.3842	0.0632	0.1901
7	3×10^{-1}	10^{-3}	0.0707	0.1640	0.0949	0.3457
8	3×10^{-1}	10^{-2}	0.2236	0.0901	0.1392	1.0734
9	3×10^{-1}	10^{-1}	0.7071	0.0716	0.2044	2.4452
10	5×10^{-1}	3×10^{-4}	0.0358	0.1001	0.1260	0.3365
11	10^{0}	10^{-2}	0.2236	0.1402	0.4642	0.8094

Table 6.2: Numerical data obtained for different combinations of the two free parameters: the capillary number Ca and the viscosity ratio ϵ_μ. The data points are plotted together in Fig. 6.16.

Regarding the geometry the very clever geometry function `geomfile` is to be praised, as it is very easy to change geometries or simply build new ones from scratch.

In the case of all three test cases it would have been possible to include many interesting figures and plots depicting a large variety of flow parameters and variables. However, as it was mainly the scope of this chapter to assess the validity of the code we mainly restricted the results to those that could be compared with the theoretical results.

Outlook

In the case of the bubbles in the capillary tube it would have been relatively easy to include: several consecutive bubbles, two different liquids, or liquids having non-Newtonian behavior (see Sec. 4.9 and the final results in Chap. 7). Moreover it could have been very interesting to include a convection diffusion equation at the interface to model the dynamics of surfactants. A system involving many bubbles is analyzed and presented in the main results chapter. The flow-focusing device produces a series of four gas bubbles which compress due to large viscous drag and numerically exaggerated compressibility. Regarding the drops in extensional flow the introduction of a non-Newtonian fluid in the drop could have been compared to the theoretical results of Favelukis *et al.* [72].

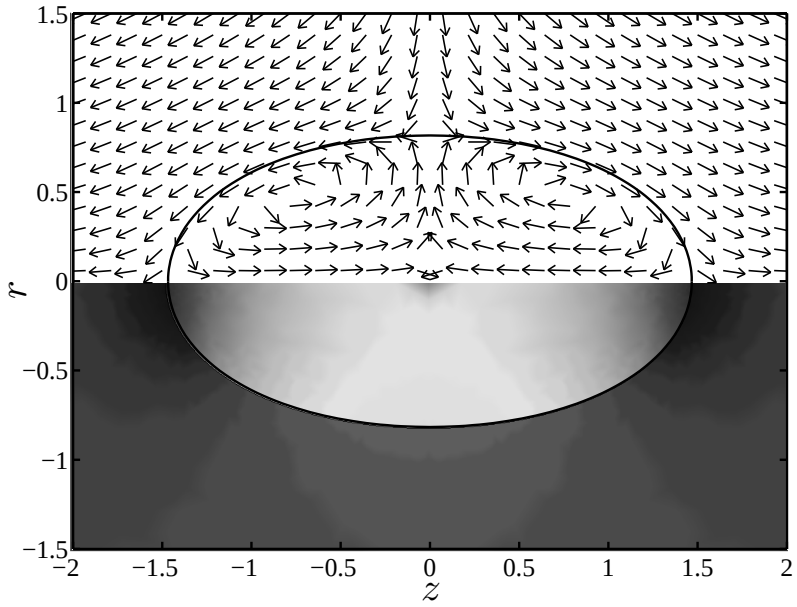

Figure 6.17: The vector plot represents the normalized velocity field and the gray scale plot the pressure field (light gray is low pressure and dark gray is hight pressure). The drop has reached a steady state shape with the parameter set # 4 in Table 6.2.

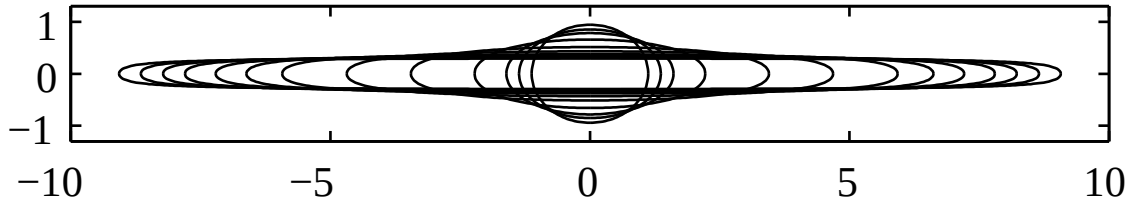

Figure 6.18: Evolution of the shape of a drop for $Ca = 0.5$ and $\epsilon_\mu = 10$.

Chapter 7

The flow-focusing device

This chapter contains the main results of this thesis. Using the code described in the previous chapter we present a first in depth numerical study of an axisymmetric flow-focusing device. The results are presented by the inclusion of our most recent paper *A numerical study of two-phase Stokes flow in an axisymmetric flow-focusing device* [80], submitted to Physics of Fluids in August.

In the following we have firstly inserted the article in its full length. Secondly, additional information not given in the article is presented and, finally, in the last section we present the new results regarding non-Newtonian liquids in the flow-focusing device.

7.1 Paper by Jensen *et al.* 2005

A numerical study of two-phase Stokes flow in an axisymmetric flow-focusing device

Mads Jakob Jensen*, Howard A. Stone**, and Henrik Bruus*

* MIC - Department of Micro and Nanotechnology, DTU Bldg. 345 East, Technical University of Denmark, DK-2800 Kongens Lyngby, Denmark

** Division of Engineering and Applied Sciences (DEAS), Harvard University, 308 Pierce Hall, Cambridge, MA 02138, USA

Abstract

In this paper we present a numerical investigation of the time-dependent dynamics of the creation of gas bubbles in an axisymmetric flow-focusing device. The liquid motion is treated as a Stokes flow, and using a generic framework we implement a second-order time-integration scheme and a free-surface model in Matlab which interfaces with the finite-element software Femlab. We derive scaling laws for the volume of a created bubble and for the gas flow rate, and confirm them numerically. Our results also confirm existing experimental results by Garstecki *et al.*, Phys. Rev. Lett. **94**, 164501 (2005), and predict a scaling yet to be observed: the bubble volume scales with with the outlet channel radius to

the power 4 and the surface tension. Our axisymmetric simulations further show that the collapse of the gas thread before bubble snap-off is different from the recent experimental results. We suggest that this difference is caused by differences in geometry between experiments and the simulations.
PACS numbers: 47.55.Dz, 47.60.+i, 68.03.Cd

7.1.1 Introduction

Studying the generation of bubbles and drops on the micrometer scale in a predefined geometry makes it possible to investigate a variety of physical phenomena, such as capillarity, dripping, and bubbling processes. The initial work on this topic has mainly been experimental and often it has been driven by industrial applications of such devices, e.g., drop formation in ink-jet printing [17]. To better understand experimental results, and possibly aid design of microfluidic devices for controlling multiphase flow, numerical modelling of drop and bubble formation is also necessary. Modelling the free-surface dynamics includes the use of direct numerical techniques such as the volume of fluid methods, tracer methods, and boundary-integral methods [20, 21, 73, 74]. A wide variety of analytical and semi-analytical models have also been introduced such as, for example, the thin jet approximation [18, 22, 23, 24, 25].

In recent years studies have been concerned with the so-called flow-focusing configuration [14, 3, 4, 5, 15, 16]. One implementation possible with microfluidic devices allows for the generation of controlled multi-phase flows; this has mainly been investigated experimentally. Many interesting physical phenomena have been described, including flow-rate controlled breakup of gas threads [4], but also the appearance of chaotic behavior as reported in other bubbling devices [3, 5, 18].

In this paper, which is inspired by the experimental work of Garstecki *et al.* [3, 4], we present a numerical study of a microfluidic flow-focusing device. The study is restricted to the Stokes flow regime (low Reynolds number) in axisymmetric geometries [13]. We derive a scaling law for the volume of created bubbles, which is in agreement with those observed experimentally. We also predict a new scaling: the bubble volume is linearly proportional to the liquid-gas surface tension an effect hitherto not observed in the experimentally realized geometry. Finally, we observe compressibility of gas bubbles in our system. Nevertheless, it is important to note that we do not produce a direct verification of experimental results as our axisymmetric geometry is different from the planar one used in experiments.

To simulate the free-surface dynamics, we have implemented a second-order Runge–Kutta time algorithm in Matlab [45] coupled to the commercial finite-element program Femlab [46] to solve the incompressible Stokes flow equations for the velocity and pressure fields. This approach enables us to account for the full geometry of a device including walls, inlets, and free liquid-gas interfaces. At the location of a free surface, the normal and tangential stress conditions are enforced including the Young–Laplace pressure jump associated with a curved interface. We describe the governing equations and the numerical model in Sec. 7.1.2, we discuss the results in Sec. 7.1.3, and finally conclude in Sec. 7.1.4.

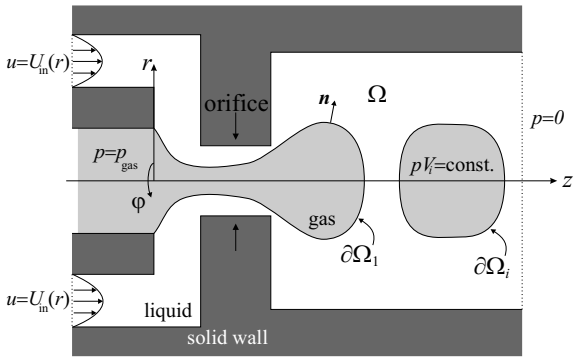

Figure 7.1: Sketch of the axisymmetric flow-focusing device with liquid domain Ω (white), rigid boundaries (dark gray), gas bubbles (light gray), liquid-gas interfaces $\partial\Omega_i$, interface normal $\boldsymbol{n}$, pressure in the gas p_{gas}, and the inlet velocity $u = U_{\text{in}}(r)$ of the liquid. The azimuthal angle φ is depicted to emphasize the axisymmetric geometry.

7.1.2 The model and numerical formulation

The system

The axisymmetric flow-focusing device is depicted schematically in Fig. 7.1. A gas thread (light gray) under constant pressure p_{gas} is focused into an orifice (dark gray) by a liquid stream (white). It is natural to use cylindrical (z, r, φ) coordinates, whereby the liquid flow-rate at the inlet is

$$Q_{\text{in}} = \int_{\partial\Omega_{\text{in}}} \boldsymbol{u} \cdot \boldsymbol{n} dA = 2\pi \int_{\Delta r} U_{\text{in}}(r) r dr \tag{7.1}$$

where $\partial\Omega_{\text{in}}$ is the inlet boundary, $\boldsymbol{u} = U_{\text{in}}(r)\boldsymbol{e}_z$ is the flow profile at the inlet, $\boldsymbol{n} = \boldsymbol{e}_z$ is the surface normal, and Δr is the width of the inlet in the radial direction r. As the system is axisymmetric about the z-axis the liquid is focusing the gas thread uniformly from all sides, i.e., for all $\varphi \in [0, 2\pi[$. Over a large range of flow parameters the gas thread breaks periodically and bubble snap-off occurs. The bubbles flow downstream into the outlet.

The sketch in Fig. 7.1 also shows the boundary conditions: (a) at the liquid inlet the fluid velocity $U_{\text{in}}(r)$ is specified, see Eq. (7.1), (b) at the outlet the pressure is set to zero, (c) on all solid walls we assume no slip $\boldsymbol{u} = \boldsymbol{0}$, (d) at the liquid-gas interfaces $\partial\Omega_i$ the full stress condition is fulfilled, including the Young–Laplace pressure jump associated with a curved interface, and (e) at the line $r = 0$ a symmetry condition is applied.

Governing equations

Compared to the liquid, the shear stress and the viscosity of the gas are negligible and the pressure variations are expected to be small, so we only need to specify a pressure in the gas domains. Moreover, we assume that the gas is an isothermal ideal gas that does not exchange molecules with the surroundings. In the gas thread the pressure is constant p_{gas} and in the isolated ith bubble we set the pressure p_i according to

$$p_i V_i = p_{\text{gas}} V_{\text{snap}} = \text{constant}, \tag{7.2}$$

where V_i is the volume of bubble i and V_{snap} is the volume of a bubble at snap-off.

As the liquid involved in this system is Newtonian the flow field satisfies the Navier–Stokes equation

$$\rho\left(\frac{\partial \boldsymbol{u}}{\partial t} + (\boldsymbol{u}\cdot\boldsymbol{\nabla})\boldsymbol{u}\right) = \boldsymbol{\nabla}\cdot\boldsymbol{\sigma}, \tag{7.3}$$

where t is time, $\boldsymbol{u} = u\boldsymbol{e}_z + v\boldsymbol{e}_r$ the velocity field, ρ the constant density, and $\boldsymbol{\sigma}$ the Cauchy stress tensor. A Newtonian fluid in an axisymmetric system is effectively a 2D system and the four components of the stress tensor are

$$\sigma_{ij} = \mu\left(\frac{\partial u_i}{\partial x_j} + \frac{\partial u_j}{\partial x_i}\right) - p\delta_{ij}. \tag{7.4}$$

where $(x_1, x_2) = (z, r)$, p is the pressure, and μ is the dynamic viscosity of the fluid. Apart from the momentum equation given in Eq. (7.3) and the constitutive stress tensor, the continuity equation is needed,

$$\boldsymbol{\nabla}\cdot\boldsymbol{u} = 0. \tag{7.5}$$

To make parametric studies of physical variables in a dimensionless setup we introduce the dimensional length d and the velocity U, the values of which will be discussed later. Using this we now re-scale time, pressure, position, and velocity and obtain the following expressions

$$\boldsymbol{x} = \tilde{\boldsymbol{x}}d \tag{7.6a}$$
$$\boldsymbol{u} = \tilde{\boldsymbol{u}}\,U \tag{7.6b}$$
$$t = \tilde{t}\,\frac{d}{U} \tag{7.6c}$$
$$p = \tilde{p}\,\frac{\mu U}{d}, \tag{7.6d}$$

as well as the Reynolds number Re given by

$$Re \equiv \frac{\rho U d}{\mu}. \tag{7.7}$$

The tilde is used to identify non-dimensional parameters $\tilde{t}$, $\tilde{p}$, $\tilde{\boldsymbol{u}}$, and $\tilde{\boldsymbol{x}}$. Introducing the re-scaling Eq. (7.6) of the flow parameters it is possible to reformulate Eqs. (7.3), (7.4), and (7.5) into a divergence form. Using the axisymmetric form of the governing equations and some algebra yields

$$\begin{bmatrix} \tilde{r}\,Re\frac{\partial\tilde{u}}{\partial\tilde{t}} \\ \tilde{r}\,Re\frac{\partial\tilde{v}}{\partial\tilde{t}} \\ 0 \end{bmatrix} + \boldsymbol{\nabla}\cdot\underbrace{\begin{bmatrix} \tilde{r}\left(2\frac{\partial\tilde{u}}{\partial\tilde{z}} - \tilde{p}\right) & \tilde{r}\left(\frac{\partial\tilde{u}}{\partial\tilde{r}} + \frac{\partial\tilde{v}}{\partial\tilde{z}}\right) \\ \tilde{r}\left(\frac{\partial\tilde{u}}{\partial\tilde{r}} + \frac{\partial\tilde{v}}{\partial\tilde{z}}\right) & \tilde{r}\left(2\frac{\partial\tilde{v}}{\partial\tilde{r}} - \tilde{p}\right) \\ 0 & 0 \end{bmatrix}}_{\boldsymbol{\Gamma}} = \begin{bmatrix} \tilde{r}\,Re\left(\tilde{v}\frac{\partial\tilde{u}}{\partial\tilde{r}} + \tilde{u}\frac{\partial\tilde{u}}{\partial\tilde{z}}\right) \\ \tilde{r}\,Re\left(\tilde{v}\frac{\partial\tilde{v}}{\partial\tilde{r}} + \tilde{u}\frac{\partial\tilde{v}}{\partial\tilde{z}}\right) - \tilde{p} + 2\frac{\tilde{v}}{\tilde{r}} \\ \tilde{v} + \tilde{r}\left(\frac{\partial\tilde{v}}{\partial\tilde{r}} + \frac{\partial\tilde{u}}{\partial\tilde{z}}\right) \end{bmatrix}, \tag{7.8}$$

where $\boldsymbol{\nabla} = (\frac{\partial}{\partial\tilde{z}}, \frac{\partial}{\partial\tilde{r}})$. The first two rows in the system represent the momentum equations and the third row is the incompressibility condition. Note that the matrix denoted $\boldsymbol{\Gamma}$ at the

left of the equal sign contains $\tilde{r}$ times the Cauchy stress tensor. Rewriting the governing equations into the somewhat unusual form of Eq. (7.8) is beneficial for the numerical implementation of the governing equations into Femlab as discussed in the next section.

At the location of the free interface $\partial\Omega_i$ (see Fig. 7.1) the stress is continuous in the tangential direction but exhibits a discontinuity in the normal direction $\boldsymbol{n}$ given by the Young-Laplace pressure. Thus at the free interface the stress condition is

$$\boldsymbol{n} \cdot \boldsymbol{\sigma} = (2\gamma_{\mathrm{lg}}\kappa - p_{\mathrm{gas}})\boldsymbol{n}. \tag{7.9}$$

where, γ_{lg} is the surface tension of the liquid-gas interface, and κ is the mean curvature of the surface. At the free surface, the interface must move at the speed of a fluid particle just next to it, which is the kinematic boundary condition

$$\frac{d\boldsymbol{x}}{dt} = \boldsymbol{u}(\boldsymbol{x})\big|_{\boldsymbol{x}\in\partial\Omega_i}, \tag{7.10}$$

where we take the total time derivative.

To simplify our treatment we only study the Stokes flow regime and we may hence set $Re = 0$ in Eq. (7.8). In this limit the time-dependent problem reduces to a quasi-stationary problem in the following sense. Given an interface shape we solve for the velocity field $\boldsymbol{u}$ and the stress field $\boldsymbol{\sigma}$ in the liquid. If the stress is non-zero at any point on the liquid-gas interface this interface will move. Mathematically the time dependence only enters through the kinematic boundary condition Eq. (7.10) at this free surface. The flow is thus implicitly a function of the interface shape. Although we are in the $Re = 0$ limit, nonlinearity is nevertheless introduced to the dynamics of the problem by the curvature of the free interface appearing in the dynamic boundary condition Eq. (7.9) [60].

In the following the length scale d introduced in Eq. (7.6) is set equal to the gas inlet diameter depicted in Fig. 7.2. The velocity scale U for the liquid is chosen when there is no gas flow as $Q_{\mathrm{in}}/A_{\mathrm{or}}$, where $A_{\mathrm{or}} = \pi(\alpha d/2)^2$ is the area of the orifice cross section. In terms of these scales the dimensionless inlet velocity is given as

$$\tilde{U}_{\mathrm{in}}(s) = \frac{3\alpha^2}{\left(\frac{d_{\mathrm{in}}}{d}\right)^2 + 3\frac{d_{\mathrm{in}}}{d}} s(1-s), \tag{7.11}$$

where $s \in [0;1[$ is a curve parameter on the inlet boundary. The dimensionless pressure $\tilde{p}_2$ in the gas and the capillary number Ca are defined as

$$Ca \equiv \frac{\mu U}{\gamma_{\mathrm{lg}}}, \tag{7.12}$$

$$\tilde{p}_2 \equiv \frac{p_{\mathrm{gas}} d}{\mu U}. \tag{7.13}$$

Typical parameter values for the various physical quantities are listed in Table 7.1. In terms of the re-scaled variables and parameters, the dynamic boundary condition Eq. (7.9)

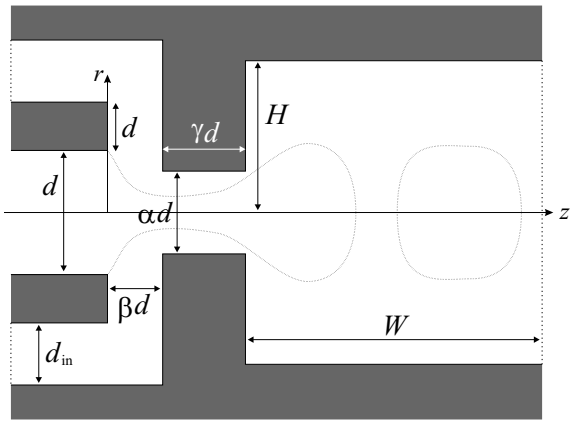

Figure 7.2: Sketch of the axisymmetric flow-focusing device with all relevant lengths shown. Most important are the gas inlet diameter d, the orifice diameter αd, the distance from the orifice to the gas inlet βd, and the length of the orifice γd.

in component form is

$$\Gamma_{11} n_1 + \Gamma_{12} n_2 = \tilde{r} \left(\frac{1}{Ca} \tilde{\kappa} - \tilde{p}_2 \right) n_1 \tag{7.14a}$$

$$\Gamma_{21} n_1 + \Gamma_{22} n_2 = \tilde{r} \left(\frac{1}{Ca} \tilde{\kappa} - \tilde{p}_2 \right) n_2 \tag{7.14b}$$

where $\tilde{\kappa}$ is the dimensionless curvature and Γ_{ij} are the components of the modified Cauchy stress matrix in Eq. (7.8).

The liquid-gas interface is represented as a parametric curve $\tilde{\boldsymbol{x}}(S) = (\tilde{z}(S), \tilde{r}(S))$, where S is the arc-length parameter scaled by the total length of the given interface. The dimensionless curvature $\tilde{\kappa}$ of the interface is given by the non-linear expression

$$\tilde{r}\tilde{\kappa} = \tilde{r} \frac{\dot{z}\ddot{r} - \dot{r}\ddot{z}}{(\dot{r}^2 + \dot{z}^2)^{3/2}} - \frac{\dot{z}}{(\dot{r}^2 + \dot{z}^2)^{1/2}}, \tag{7.15}$$

where a dot is the derivative with respect to S, and we have multiplied with $\tilde{r}$. The last term in the expression is equal to the r-component n_2 of the surface normal and is related to the curvature in the azimuthal direction.

Numerical method

As mentioned above the Stokes problem effectively reduces to a quasi-stationary problem, where at any given time the flow field (u, v, p) is a function of the shape of the liquid-gas interface. This fact is utilized for the numerical treatment of the problem. The problem is solved numerically by using the commercial finite-element program Femlab together with a Matlab code that we have developed comprising the time evolution and numerical schemes for representing the curvature of the interface. The method is inspired by the boundary-integral method [21, 20] and classical finite-element methods [75, 76]. At every

parameter	typical value
d	200 μm
Q_{in}	0.05 μL/s
p_{gas}	5 - 100 kPa
μ	1 - 10 mPas
γ_{lg}	30 and 73 mJ/m^2
U	2 mm/s
Re	0.02 - 0.2
Ca	10^{-3}-10^{-1}

Table 7.1: Typical physical parameter values used in experiments where the flow-focusing device is planar [3, 4].

time step we begin with a given position of the liquid-gas interface and solve for the flow field, then based on the new velocity information at the interface the position of the liquid-gas interface is updated.

To evolve the interface in time we use a second-order Runge–Kutta time step algorithm. This algorithm is extended such that the elongation of the free interface is taken into account. The interface is given by the curve $\boldsymbol{x}(S)$ which is described by a cubic spline that interpolates all the mesh points on the interface. Points on the boundary are only moved normal to the interface such that Eq. (7.10) is transformed to

$$\frac{d\boldsymbol{x}(S)}{dt} = (\boldsymbol{u}\cdot\boldsymbol{n})\boldsymbol{n}\big|_{\boldsymbol{x}\in\partial\Omega_i}, \tag{7.16}$$

where $\boldsymbol{n}$ is the surface normal. Whenever the interface is evolved the finite-element mesh is regenerated to find a new solution of the fields, and as a consequence the boundary points shift from one time step to the next. Hence, to determine the correct Runge–Kutta gradient $(\boldsymbol{u}\cdot\boldsymbol{n})\boldsymbol{n}$, we have introduced a mapping $S = f(S')$, which ensures that the correct gradients, found at time $t + \Delta t/2$, are used at the original interface points at time t to evolve the interface to the next time $t + \Delta t$; see the sketch in Fig. 7.3. Moreover, the mapping also handles the problem of the interface changing length [62].

The form of Eq. (7.8) and the dynamic boundary condition Eqs. (7.14a) and (7.14b) are suited for direct use in Femlab. At each new time step the system is re-meshed, a new curve parameter S is found, and the flow equations with the correct boundary conditions are solved in Femlab. The number of points used to track the interface varies from 30, initially, up to 400 at snap-off. The number increases when narrow liquid regions appear that need to be well resolved. The curvature κ of the interface is found by using an approximating least square cubic spline. This ensures the curvature to be smooth and it eliminates numerical noise introduced by the Femlab meshing algorithm. Moreover, the time step Δt is determined such that no boundary point is moved more than a third of the local mesh size.

A series of tests were performed to verify the time evolution algorithm and the code in general. The time evolution algorithm was compared with a simple Euler method, where the time step was chosen to ensure stability [60, 62, 61]. The solutions were identical but

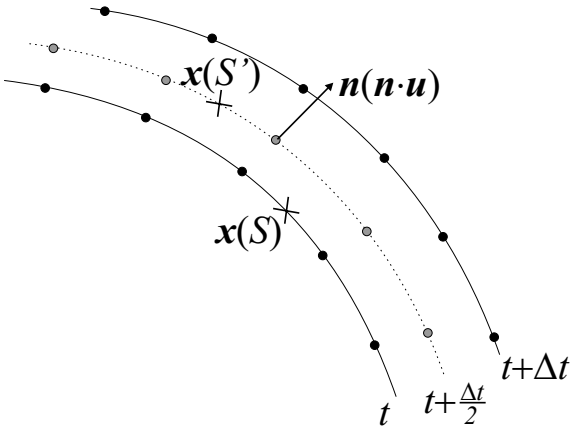

Figure 7.3: Schematic representation of an interface segment with associated grid points. The interface is represented by a curve $\boldsymbol{x}(S)$ at time t and $\boldsymbol{x}(S') = \boldsymbol{x}(f^{-1}(S))$ at the intermediate time $t + \Delta t/2$. The gradient $\boldsymbol{n}(\boldsymbol{n} \cdot \boldsymbol{u})$ of the interface position $\boldsymbol{x}(S)$ used to evolve the interface to time $t + \Delta t$ is derived at the intermediate time, according to a Runge–Kutta scheme.

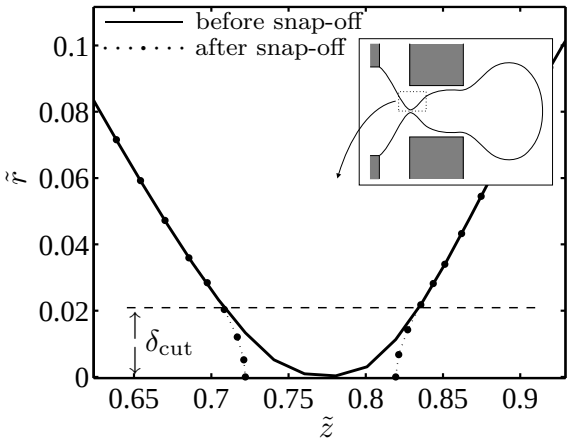

Figure 7.4: The shape $\tilde{r}(\tilde{z})$ of the bubble just before snap-off (solid line) and the new shape after snap-off (dotted line and black points). The length scale δ_{cut} (dashed line) determines where to cut the initial shape.

our method was ten times faster. The code was also tested for stability regarding mesh size and the choice of basis functions. Finally, the code was tested on three specific problems and performed very well in all three cases: (1) a drop in an extensional flow [67, 77, 71], (2) the coalescence of two cylindrically shaped liquid bodies [47], and (3) the steady-state shape of a gas bubble translating in a liquid-filled capillary [52].

Snap-off mechanism

When a bubble snap-off occurs, the curve representing the shape of the gas thread (solid line in Fig. 7.4) has to be divided into two curves (dotted line in Fig. 7.4). In this model

we define a length scale δ_{cut} (marked by the dashed line in Fig. 7.4) that determines where to cut the original shape. The curve is cut at the nearest interface grid point and a cubic spline with vertical tangent at $r = 0$ caps the gas-jet and the new bubble. The spatial resolution of the dynamics near the breakup are restricted by the mesh size h_m, hence we have chosen $\delta_{\text{cut}} > 2h_m$. This method might seem crude however the specific shape near the breaking point does not influence the overall dynamics of the system. Just after the snap-off discontinuities are registered in the liquid pressure at the orifice region as the breakup event is a singular event in itself.

7.1.3 Results and discussion

The time-dependent dynamics of the liquid-gas system evolving in the flow-focusing device sketched in Fig. 7.1 are controlled by many parameters. In the following we have restricted our analysis to the dependence on four parameters: (1) the pressure of the gas thread, (2) the inlet liquid flow-rate $Q_{\text{in}} = A_{\text{or}}U$, (3) one geometry component namely the outlet channel radius H, see Fig. 7.2, and (4) the liquid-gas interfacial tension γ_{lg} characterized by the capillary number Ca. The rest of the geometry parameters depicted in Fig. 7.2 are constant and set to $(\alpha, \beta, \gamma, d_{\text{in}}/d, W/d) = (0.5, 1.5, 2, 1, 15)$. An important parameter to control and observe experimentally is the volume V_b of the created bubbles. The bubble volume is also the focus of our analysis as it is straightforward to determine numerically.

We begin by studying various aspects of the creation of the first bubble in a bubbling sequence and show how V_b scales with the four parameters analyzed. Finally, we study a sequence of four bubbles in a specific geometry. Our results on the axisymmetric geometry are compared to experimental findings on the planar geometry given in Refs. [3, 4].

Bubble growth morphology

The snapshots depicted in Fig. 7.5(a)-(e) represent the creation of a typical bubble. Panel (a) shows the initial insertion of the gas thread into the orifice, (b) the exit from the orifice region of the bursting head of the gas thread, (c) the blocking of the inlet liquid flow as the bubble inflates into the outlet channel, (d) appearance of a clear collapse region and collapse of the gas thread, and finally (e) the snap-off event where the thread radius vanishes $\tilde{h}_{\text{thr}} = 0$. In this case the flow and geometry parameters are $(\tilde{p}_2, Ca, H/d) = (350, 0.1, 1)$, and the total time simulated is $\tilde{t} = 1.0$. The time-dependent distance from the tip of the bursting head of the gas thread to the outlet, where $\tilde{p} = 0$, is denoted $\ell = \ell(t)$, while W is the constant length of the outlet region, see Fig. 7.5(c). The length $\tilde{h}_{\text{thr}} = h_{\text{thr}}/d$ is the dimensionless minimal diameter of the gas thread and is located at $\tilde{z} = z_{\text{thr}}/d$. The volume V_b of a bubble at snap-off is simply calculated as

$$V_b = \pi \int_{z=z_{\text{thr}}}^{z_{\max}} r^2(z) dz, \tag{7.17}$$

where $z_{\max}$ is the z-coordinate of the front of the gas-thread and $r(z)$ is a representation of the interface curve. We will mainly be concerned with bubbles of relatively large volume, for which snap-off occurs when $\ell < W$. For some choice of parameters small bubbles may

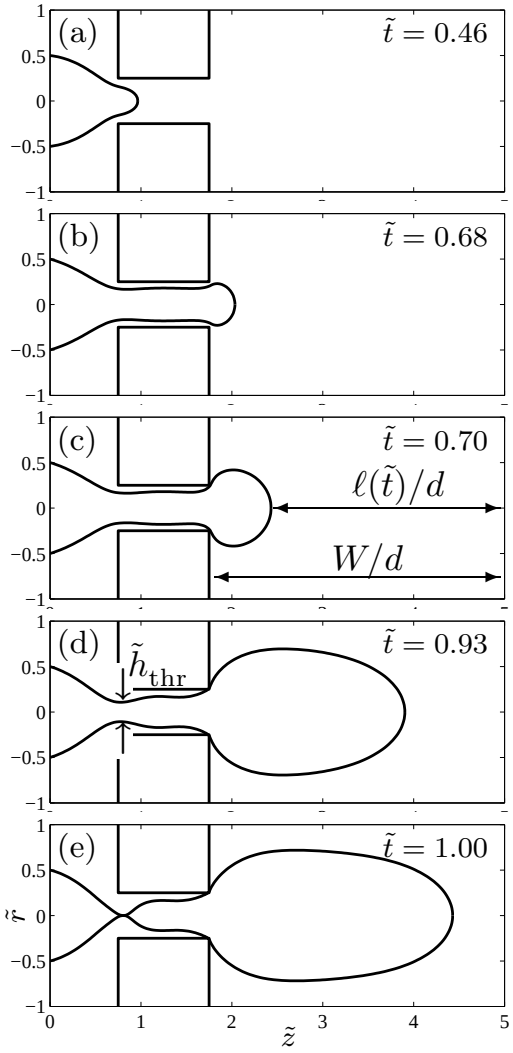

Figure 7.5: A sequence of five snapshots from the simulations representing the creation of a bubble: (a) the initial insertion of the gas thread into the orifice, (b) the exit of the gas thread from the orifice region, (c) the blocking of the inlet liquid flow to the outlet, (d) the controlled collapse of the gas thread, and finally (e) the snap-off event where $\tilde{h}_{\rm thr} = 0$. The length $\ell(\tilde{t})$ is measured from the tip of the bursting head of the gas thread to the outlet where $\tilde{p} = 0$, W is the length of the outlet region, and $\tilde{h}_{\rm thr} = h_{\rm thr}/d$ is the minimal dimensionless diameter of the gas thread. The simulations made for $(\tilde{p}_2, Ca, H/d) = (350, 0.1, 1)$.

snap-off when they are still in the orifice, i.e., when $\ell > W$. At the time of snap-off $z_{\rm thr}$ is generally located at the left end of the orifice.

Bubble growth time τ

The time it takes a bubble to grow is denoted τ. It is defined as the time between the onset of the gas-thread collapse Fig. 7.5(c), when the emerging bubble blocks the liquid

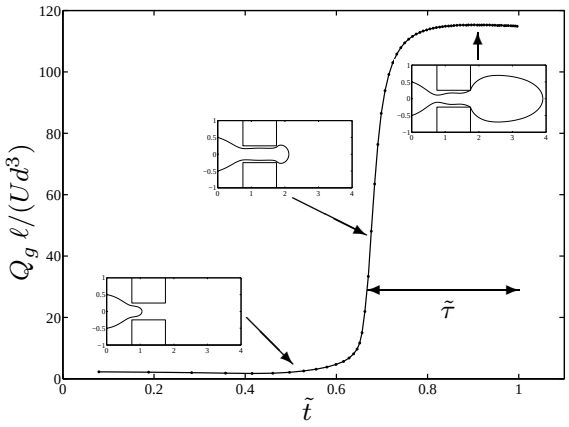

Figure 7.6: Plot of $Q_g\ell/(Ud^4)$ as function of time for $Ca = 0.1$, $\tilde{p}_2 = 350$, and $H/d = 1$. The gas dimensionless flow-rate is found numerically and calculated as $\tilde{Q}_g = d\tilde{V}_g/d\tilde{t}$, where $\tilde{V}_g$ is the volume of the gas.

flow, and the snap-off of the bubble Fig. 7.5(e). When the blocking of the orifice sets in the liquid flow fills the orifice volume $V_{\text{or}} = A_{\text{or}}\gamma d$ at the rate Q_{in}, squeezes the gas thread, and induces the collapse leading to bubble snap-off. As described in Ref. [4], for a fixed orifice geometry and surface tension, the bubble growth time τ therefore scales as

$$\tau \propto \frac{V_{\text{or}}}{Q_{\text{in}}} \propto \frac{1}{U}, \tag{7.18}$$

Numerically we found that the dimensionless time $\tilde{\tau}$ was constant ~ 0.3, and hence that $\tau \propto d/U$. For a constant geometry the numerics confirmed the linear dependence.

Gas flow rate Q_g

The gas flow-rate Q_g is not set explicitly but it can be determined as follows. When the emerging gas bubble begins to block the orifice, it interrupts the liquid flow from the inlet to the outlet. The liquid flow-rate Q_{out} at the outlet is therefore, by volume conservation, equal to the flow-rate Q_g of the gas. Assuming the liquid flow in the outlet region to be a Poiseuille flow, we obtain

$$Q_g = Q_{\text{out}} = \frac{\pi}{8}\frac{1}{\mu}GH^4 \propto GH^4, \tag{7.19}$$

where G is the pressure gradient. A good approximation for G is given by the pressure drop from the tip of the thread to the outlet divided by the distance ℓ, see Fig. 7.5(c). As the emerging bubble blocks the liquid flow the pressure in front of it is approximately $p_{\text{gas}} - \gamma_{\text{lg}}\kappa$, where $\kappa \equiv 2/R$. If we furthermore assume that the bubbles being created are big, i.e., of size comparable to H, we have,

$$G \approx \frac{1}{\ell}\left(p_{\text{gas}} - \frac{2\gamma_{\text{lg}}}{H}\right), \tag{7.20}$$

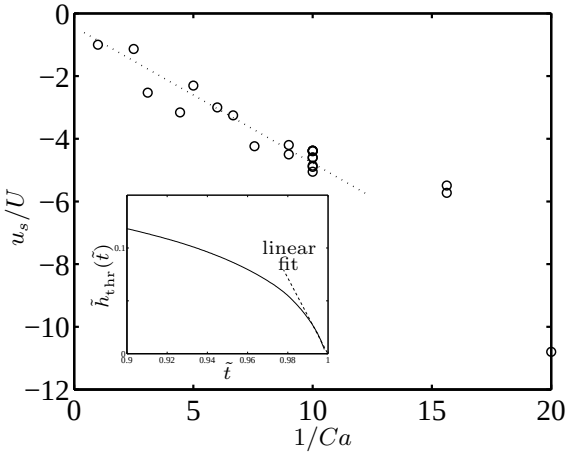

Figure 7.7: Collapse speed u_s/U at snap-off of the gas thread as function of Ca. The inset depicts $\tilde{h}_{\rm thr}(\tilde{t})$ corresponding to the evolution from Fig. 7.5(d) to (e). The dashed line corresponds to the linear fit made to determine u_s/U.

where the radius of curvature $R \approx H$ because of the axisymmetric nature of the geometry studied. Combining Eqs. (7.19) and (7.20) leads to

$$Q_g \ell \propto H^4 \left(p_{\rm gas} - \frac{2\gamma_{\rm lg}}{H} \right). \tag{7.21}$$

Consequently, for constant geometry, gas pressure, and surface tension we expect $Q_g \ell$ to be constant. To verify this expression numerically, the length ℓ is found as the difference between W and the position of the gas front, and Q_g is found as dV_g/dt where V_g is the volume of the gas. The dimensionless quantity $Q_g \ell/(Ud^4)$ is plotted as function of dimensionless time $\tilde{t}$ in Fig. 7.6, where we see that $Q_g \ell$ indeed is constant for $\tilde{t} > 0.7$ after the gas bubble begins to block the orifice. From Fig. 7.6 it is also seen how $\tilde{\tau}$ was determined numerically as $Q_g \ell(\tilde{t})$ changes abruptly when the blocking of the orifice is initiated.

Gas thread collapse speed u_s

The collapse speed of the gas thread just before snap-off is defined as

$$u_s \equiv \left. \frac{dh_{\rm thr}}{dt} \right|_{t=t_0}, \tag{7.22}$$

where t_0 is the time of snap-off. Figure 7.7 shows u_s/U as function of $1/Ca$. The insert in Fig. 7.7 shows the dimensionless thread thickness as function of time $\tilde{h}_{\rm thr}(\tilde{t})$, which corresponds to the evolution from Fig. 7.5(d) to (e). The collapse speed u_s/U is determined by a linear fit to the curve $\tilde{h}_{\rm thr}(\tilde{t})$ near its intersection with the $\tilde{t}$-axis. The spread in the calculated values around the linear fit is due to uncertainties in the linear fit to $\tilde{h}_{\rm thr}(\tilde{t})$. Even though $h_{\rm thr}(t)$ does not have a significant linear regime u_s it is interesting to find

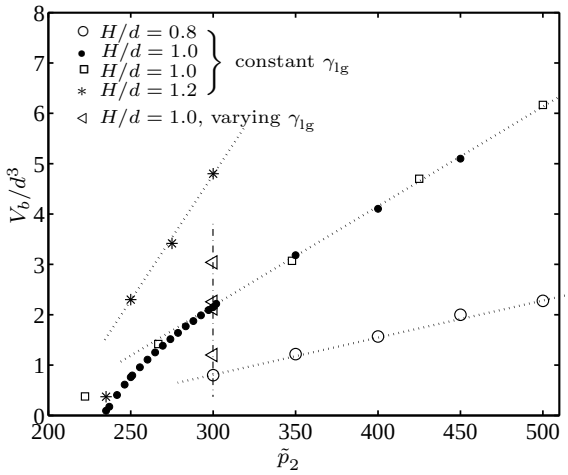

Figure 7.8: The dimensionless volume of the first bubble as function of the parameter $\tilde{p}_2$, for three values of the outlet channel radius $H/d = 0.8$, 1.0, and 1.2 for constant surface tension γ_{lg}. Moreover, the triangles show a variation of the capillary number Ca, i.e., a change in the surface tension for fixed H/d, p_{gas}, and Q_{in}, see Fig. 7.10 for further details.

that u_s/U depends linearly on $1/Ca$, for $Ca > 0.1$. This means that $u_s \propto \gamma_{\mathrm{lg}}/\mu$. Studies of breakup of viscous threads (see Refs. [23, 24, 25, 26]) show that just before snap-off the thread thickness $h_{\mathrm{thr}} \propto (t_0 - t)\,\gamma_{\mathrm{lg}}/\mu$, this seems to agree with our numerical findings.

In the experimental work of Garstecki *et al.* [3, 4] $h_{\mathrm{thr}}(t)$ had a large linear region near t_0 (that is $h_{\mathrm{thr}}(t) \propto (t_0 - t)$). Numerically we do not have this large linear region. We speculate that this disagreement is due to the anisotropic confinement of the gas thread in the planar geometry of the experiments versus the axisymmetric confinement in our model. This most probably influence the dynamics of the collapse differently [78].

Bubble volume V_b

The volume of a bubble at snap-off is given by V_b in Eq. (7.17). It is proportional to the time τ that the gas thread stays open times the flow-rate Q_g of the gas. Combining Eqs. (7.18), (7.19) and (7.20) and having ℓ nearly constant leads to

$$V_b \propto \frac{H^4}{\mu Q_{\mathrm{in}}} \left(p_{\mathrm{gas}} - \frac{2\gamma_{\mathrm{lg}}}{H} \right). \tag{7.23}$$

For the experimental results, presented in Refs. [3, 4], it was determined that for a fixed geometry and surface tension the volume of the bubbles is proportional to the ratio $p_{\mathrm{gas}}/\mu Q_{\mathrm{in}}$. This scaling is directly given by Eq. (7.23) for constant geometry. We also confirm this scaling with our numerical results shown in Fig. 7.8, where for $H/d = 0.8$, 1, and 1.2 (fixed geometry) the dimensionless volume V_b/d^3 of the bubble at snap-off is seen to scale as $\tilde{p}_2 \propto p_{\mathrm{gas}}/\mu Q_{\mathrm{in}}$. Note that there is a deviation from this scaling for small bubbles that do not emerge from the orifice before snap-off, i.e., when $\ell > W$ and our assumptions do not hold.

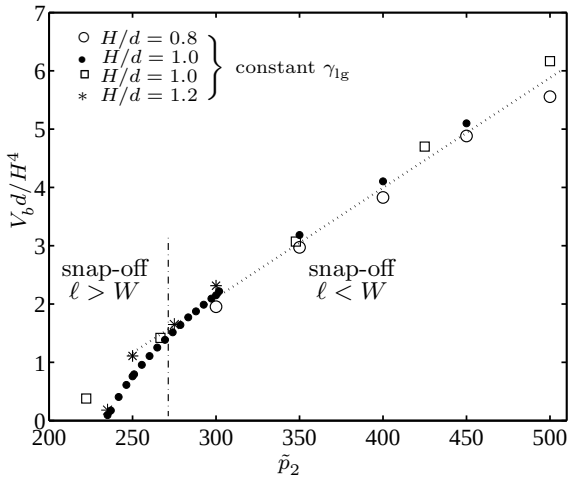

Figure 7.9: Plot of the volume V_b/d^3 scaled with the outlet channel radius $(H/d)^4$ as function of $\tilde{p}_2$ for constant surface tension $\gamma_{\rm lg}$. Note that the three lines sketched in Fig. 7.8 now merge as predicted by Eq. (7.23). The vertical dashed line indicates the transition from bubbles snap-off when $\ell > W$ and $\ell < W$.

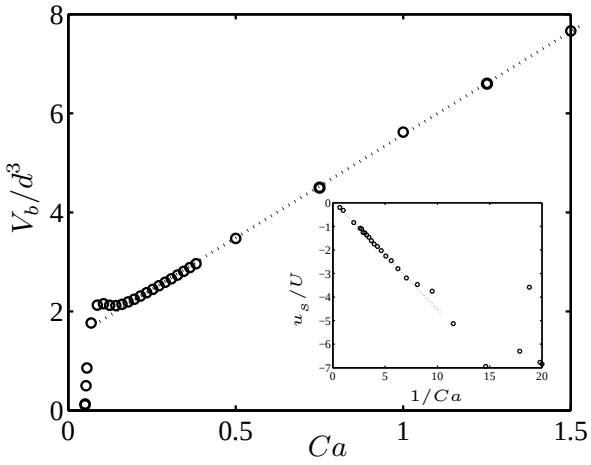

Figure 7.10: The volume V_b of the first bubble as function of the capillary number Ca for constant pressure $\tilde{p}_2 = 300$ and radius $H/d = 1$. The inset show the collapse speed u_s/U as function of $1/Ca$.

In Fig. 7.9 we have depicted $V_b d/H^4$ as function of $\tilde{p}_2$ and see that they fall on one line, hence that $V_b \propto p_{\rm gas} H^4/\mu Q_{\rm in}$. This scaling also follows directly from our general expression Eq. (7.23).

Finally, we study the scaling of the bubble volume as function of the capillary number Ca for constant dimensionless pressure $\tilde{p}_2$. In Fig. 7.10 the volume V_b/d^3 is plotted as function of Ca for $\tilde{p}_2 = 300$ and $H/d = 1$, meaning that we plot it as function of $p_{\rm gas} d/300\gamma_{\rm lg}$. We note a linear relation for values of Ca larger than some critical value

$Ca^* \approx 0.1$. In this regime we have $V_b \propto \mu U/\gamma_{\rm lg}$ or after multiplication by the constant dimensionless pressure $V_b \propto p_{\rm gas} d/\gamma_{\rm lg}$ for $p_{\rm gas} d/\gamma_{\rm lg} > 30$. This last critical value relates to wether a bubble is large $\ell < W$ os small $\ell > W$ when it snap-off, see Fig. 7.5. When the gas pressure cannot overcome the Young–Laplace pressure in the orifice the bubble snap-off occurs for $\ell > (W + \gamma d)$ and we have $p_{\rm gas} < 2\gamma_{\rm lg}/(\alpha d/2)$ yielding $p_{\rm gas} d/\gamma_{\rm lg} < 8$. Values of $p_{\rm gas} d/\gamma_{\rm lg}$ between 8 and 30 correspond to the situation where the gas front is in the orifice or just left of it when bubble snap-off occurs.

The inset in Fig. 7.10 represents the velocity u_s/U as function of $1/Ca$ for the same parameters. From the figure it is seen that $u_s/U \propto 1/Ca$. For $Ca < Ca^*$ the linearity in $1/Ca$ is not clear, this scattering of the data points could be due to numerical noise.

Multi-bubble sequence

In this section we describe a system where four bubbles are created in a sequence. There are three snap-off events and the simulation ends just before the fourth bubble snaps off. The parameters for this model are: $Ca = 0.1$, $\tilde{p}_2 = 320$, $W/d = 15$, $H/d = 0.6$, $(\alpha, \beta, \gamma) = (0.5, 1.5, 2)$. The total computation time for the simulation was one week on an Intel Pentium 4, 3.2 GHz with 1 GB of RAM.

Snapshots of the bubble shape at selected times $\tilde{t}$ are depicted in Fig. 7.11. The size of the bubbles are measured in terms of $\tilde{p}V/d^3$, which is constant for each of the four bubbles and has the value 80.8, 232.7, 208.1, and 195.3, respectively. The data indicates that the system exhibits a transient behavior before reaching a stable period-one bubbling. The snapshots at Fig. 7.11(b), (d), (f), and (h) are taken just before a bubble snap-off occurs. It is clearly seen how a preceding bubble shrinks when a new bubble is about to be released. As discussed earlier a bubble blocks the liquid flow out of the orifice before it snap-off. The blocking occurs on a short time-scale leading to an immediate pressure increase in the liquid in front. The pressure in the liquid in front of the bubble equals the pressure $\tilde{p}_2$ in the bubble minus the curvature contribution, see Eq. (7.20). The preceding bubbles can not escape because of the large viscous drag in the Stokes-flow regime. This results in a very pronounced compression of the preceding bubbles. The compression is seen graphically in Fig. 7.11: the first bubble is, e.g., seen to shrink from figure (c) to (d) and then enlarge from (d) to (e).

The volumes V_b/d^3 of the three released bubbles are plotted as function of time in Fig. 7.12(a). From the graph it is seen how preceding bubbles are compressed when a new bubble is released. The bubbles are released at the times marked by the vertical doted lines. These correspond to the events shown in Figs. 7.11(b), (d), and (f). In Fig. 7.12(b) the mean pressure on a bubble

$$\langle \tilde{p}_i \rangle = \int_{\partial\Omega_i} \boldsymbol{n} \cdot \boldsymbol{\sigma} \cdot \boldsymbol{n} dA \left(\int_{\partial\Omega_i} dA \right)^{-1} \tag{7.24}$$

is depicted as function of time. We clearly see how the volume of a bubble increases as the pressure around it decreases and vice versa. In our model the compressibility of the the bubbles is further enhanced as we have a relatively short outlet channel and because the reference pressure at the outlet is zero. In experiments where the outlet channel is

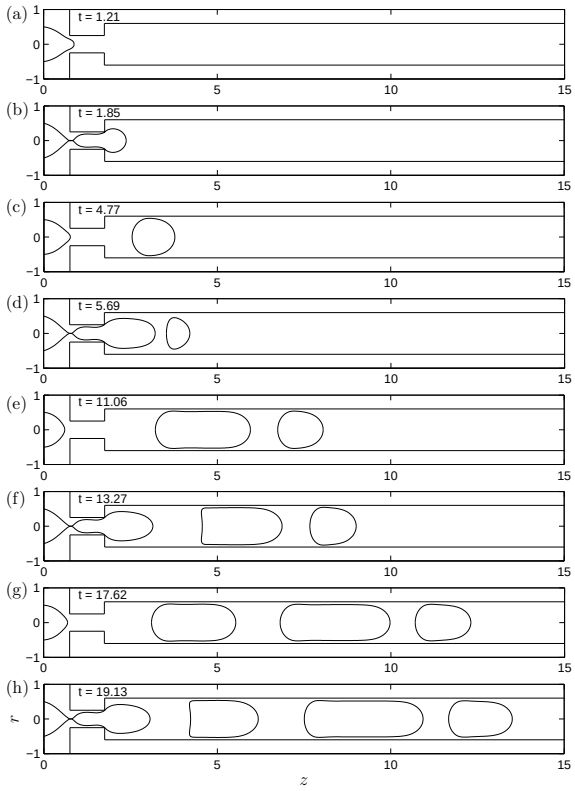

Figure 7.11: A sequence showing the generation of the first four bubbles. The bubble shapes are depicted at different selected times $\tilde{t}$. Snapshots (b), (d), (f), and (h) are taken just before a bubble snap-off event.

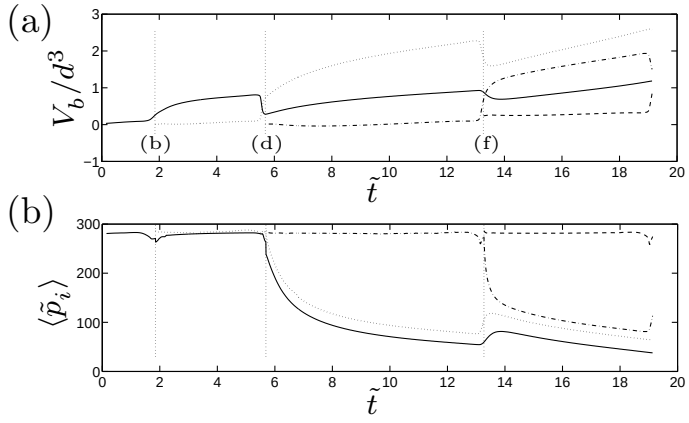

Figure 7.12: (a) The volume V_b/d^3 of the four bubbles as function of time $\tilde{t}$ and (b) the mean pressure $\langle \tilde{p}_i \rangle$ on the bubble surface as function of time. In all the bubbles $\tilde{p}V/d^3$ is constant. The vertical doted lines represent the snapshots (b), (d), and (f) from Fig. 7.11.

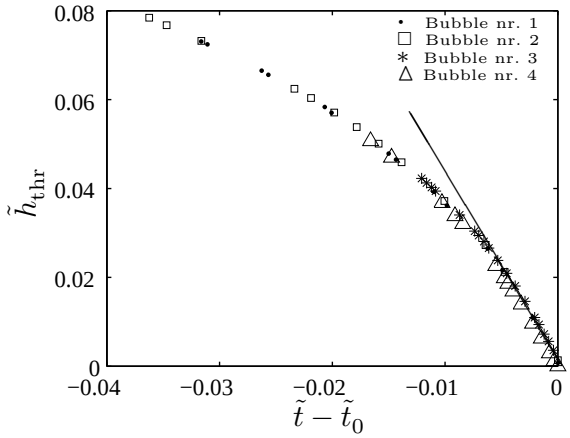

Figure 7.13: The gas thread thickness $\tilde{h}_{\rm thr}$ as a function of the time $\tilde{t} - \tilde{t}_0$. The evolution for the four bubbles are identical. The full line represents the region where the gradient $dh_{\rm thr}/dt$ is determined, just before snap-off.

very long compared to a typical bubble length the compressibility effects are not very pronounced.[1] The bubbles are however seen to expand as they travel far in the outlet [79].

In Fig. 7.13 the gas thread thickness $\tilde{h}_{\rm thr}$ is plotted as function of the time $\tilde{t} - \tilde{t}_0$. We see that for all four bubbles $\tilde{h}_{\rm thr}(\tilde{t})$ has the same shape and hence the same collapse speed $dh_{\rm thr}/dt$. This indicates that the snap-off event is local and not influenced by the hydrodynamic interactions of bubbles further downstream. This results is supported by experimental results [4], in terms of the so-called flow-rate controlled breakup of the gas-thread: the collapse velocity of the liquid thread is only a function of $Q_{\rm in}$ for a given orifice geometry.

7.1.4 Conclusion

In this work we have performed a numerical study of the dynamics of bubble formation in an axisymmetric flow-focusing device in the Stokes-flow limit. For this purpose a generic numerical model for solving free-surface flows in an axisymmetric geometry was developed. The model is based on a second-order Runge–Kutta time integration algorithm and free surface scheme implemented in Matlab which are coupled to the commercial finite element solver Femlab.

The analysis of the flow-focusing device was restricted to four parameters: the inlet liquid flow-rate $Q_{\rm in}$, the gas pressure $p_{\rm gas}$, the outlet channel radius H, and the liquid-gas surface tension $\gamma_{\rm lg}$. Based on these parameters we derive scaling laws for the volume V_b of a created bubble and for the gas flow-rate Q_g. By physical analysis and numerical simulation we have shown that the bubble growth time τ scales proportionally to the

[1] If L_b is the length of a bubble then the pressure drop along its length is $\Delta p_b \approx (p_{\rm gas} - p_{\rm out})L_b/W$, where $p_{\rm out}$ is the pressure at the outlet. The relative change in the bubble volume over the length L_b will be $p_{\rm gas}/(p_{\rm gas} - \Delta p_b)$, using Eq. (7.2). Compressibility effects are hence pronounced if $\Delta p_b/p_{\rm gas}$ is large, i.e., if L_b/W is large or if $p_{\rm gas}$ and $p_{\rm out}$ are lowered by the same amount.

inverse liquid flow rate $1/Q_{\text{in}}$.

The collapse speed u_s of the gas thread immediately prior to the snap-off event was found to be proportional to the ratio γ_{lg}/μ. This scaling was not observed experimentally [3, 4] but is supported by other studies of the breakup of viscous axisymmetric threads. The behavior of the thread thickness as function of time $h_{\text{thr}}(t)$ deviates from the experimental data. We speculate that this difference in the collapse dynamics is due to the difference in geometry of the devices. In the experiments the gas thread is confined anisotropically while it is confined equally from all sides in our axisymmetric model. In the experimental work [4] the collapse region of the gas thread was seen to extend from the gas inlet to the right of the orifice. In our axisymmetric model the collapse region is localized to an area just left of the orifice, see Fig. 7.5(d) and (e). In the simulated geometry the thread can minimize surface area (energy) in two dimensions simultaneously as it is not restricted by a top and bottom lid as in the planar case [78].

The above mentioned scaling law for the bubble volume is presented in Eq. (7.23). For a constant geometry it reduces to the scaling law $V_b \propto p_{\text{gas}}/\mu Q_{\text{in}}$ described by Garstecki *et al.* [3, 4]. We confirm this law by means of simulations for various constant values of H. For a varying outlet channel radius our extended scaling law also predicts an H^4 dependence namely $V_b \propto H^4 p_{\text{gas}}/\mu Q_{\text{in}}$. We confirm this dependence by means of the numerical results presented in Fig. 7.9. Our numerical investigation further reveals that critical values exist for the dimensionless product $\tilde{p}_2 Ca$ determining where the bubble is located when snap-off occurs. These values are determined by the ratio between the Young–Laplace pressure and the gas pressure.

Using a simple mechanism to account for the snap-off we model a sequence of four consecutive bubbles and show that the flow-focusing device does not produce bubbles of constant volume straight away. The results suggests that there is a certain transient behavior before reaching steady state. Bubbles that are located upstream of the orifice influence the pressure drop in the outlet channel. The pressure gradient along the outlet channel is an important factor in the scaling of the bubble volume. Bubbles of constant volume may hence only be created when a constant pressure drop exists in the outlet. This could for example be the case if the outlet region is large compared to the bubbles or if large bubbles are filling the entire outlet region, just as happens in experiments [3].

In the multi bubble sequence we confirm that the collapse speed of the gas thread is not influenced by hydrodynamic interactions of bubbles downstream of the snap-off event. Finally, we see a large compression of the created free gas bubbles in the Stokes-flow regime. The effect is amplified due to the numerical set-up but it is also seen experimentally, however, much less pronounced.

The numerical model we have implemented is versatile, and consequently the work presented in this paper facilitates the study of other features in flow-focusing devices. This could include other geometries of the orifice, liquid-liquid systems, or even non-Newtonian fluids. Results from such studies would be very useful when designing future experiments.

Acknowledgements

We would like to thank Piotr Garstecki for many inspiring discussions and for sharing his experimental results with us at an early stage. H. A. Stone thanks the Harvard MRSEC COMR-02/3805 and F. Jousse and colleagues at Unilever for support.

7.2 Further details for the paper

Flow field in the flow-focusing device

Figure 7.14 illustrates how the liquid flow is blocked when the gas bubble emerges at the right of the orifice. The figure depicts a sequence of six blowups of the orifice region with stream lines entering from the inlet (white lines) and the velocity magnitude $|\boldsymbol{u}|$ in the background contour plot. On every view graph the dimensionless time $\tilde{t}$, the dimensionless liquid flow rate $\tilde{Q}_{\text{or}}$ (through the orifice in a plane at $\tilde{z} = 1.75$), the dimensionless outlet flow rate $\tilde{Q}_{\text{out}}$, and the gas flow rate $\tilde{Q}_g$ are indicated. In all the situations the inlet dimensionless flow-rate is $\tilde{Q}_{\text{in}} = 0.196$ due to the chosen scaling.

The stream lines very elegantly illustrate how the liquid flow is blocked by the emerging gas thread for $\tilde{t} > 0.7$ until snap-off at $\tilde{t}_0 = 1.00$. The numerically integrated data for $\tilde{Q}_{\text{or}}$ supports the graphics. Stream lines that end on the free interface corresponds to areas where the gas thread is compressed by the liquid flow. Notice also that $\tilde{Q}_g + \tilde{Q}_{\text{in}} = \tilde{Q}_{\text{out}}$ as expected from continuity.

The shape of $h_{\text{thr}}(t)$

In the results discussed in the paper it is mentioned that $h_{\text{thr}}(t)$ could not generally be approximated by $(t_0 - t)^\alpha$ with some constant α. In Fig. 7.15 we have, in a double logarithmic plot, depicted h_{thr} as function of $t_0 - t$ and the different symbols correspond to different realizations. From the figure it is evident that the value of α, the slope of the graphs, is not generally well defined. The linear behavior $h_{\text{thr}} \propto (t_0 - t)$ suggested from theoretical studies is only true for times $t_0 - t < 10^{-2}$. The dynamics for relatively large times t are most probably more complicated than first supposed. For times close to t_0 we find the results predicted by viscous theory, i.e., that $u_s \propto \gamma/\mu$. Unfortunately the author had not enough time to study this most interesting problem in more detail. Such a study would, among other things, include an increased temporal and spatial resolution of the problem.

7.3 Non-Newtonian liquid and gas system

For typical flow parameters in microfluidics the rate of strain $\dot{\gamma}$ can be relatively large $10^3 - 10^4$ s^{-1}. These values are sufficient to cause non-Newtonian rheological effects in suspensions [6]. Because of these considerations and because of the flexibility of implementing complicated physics in Femlab we have chosen to study the dynamics in a

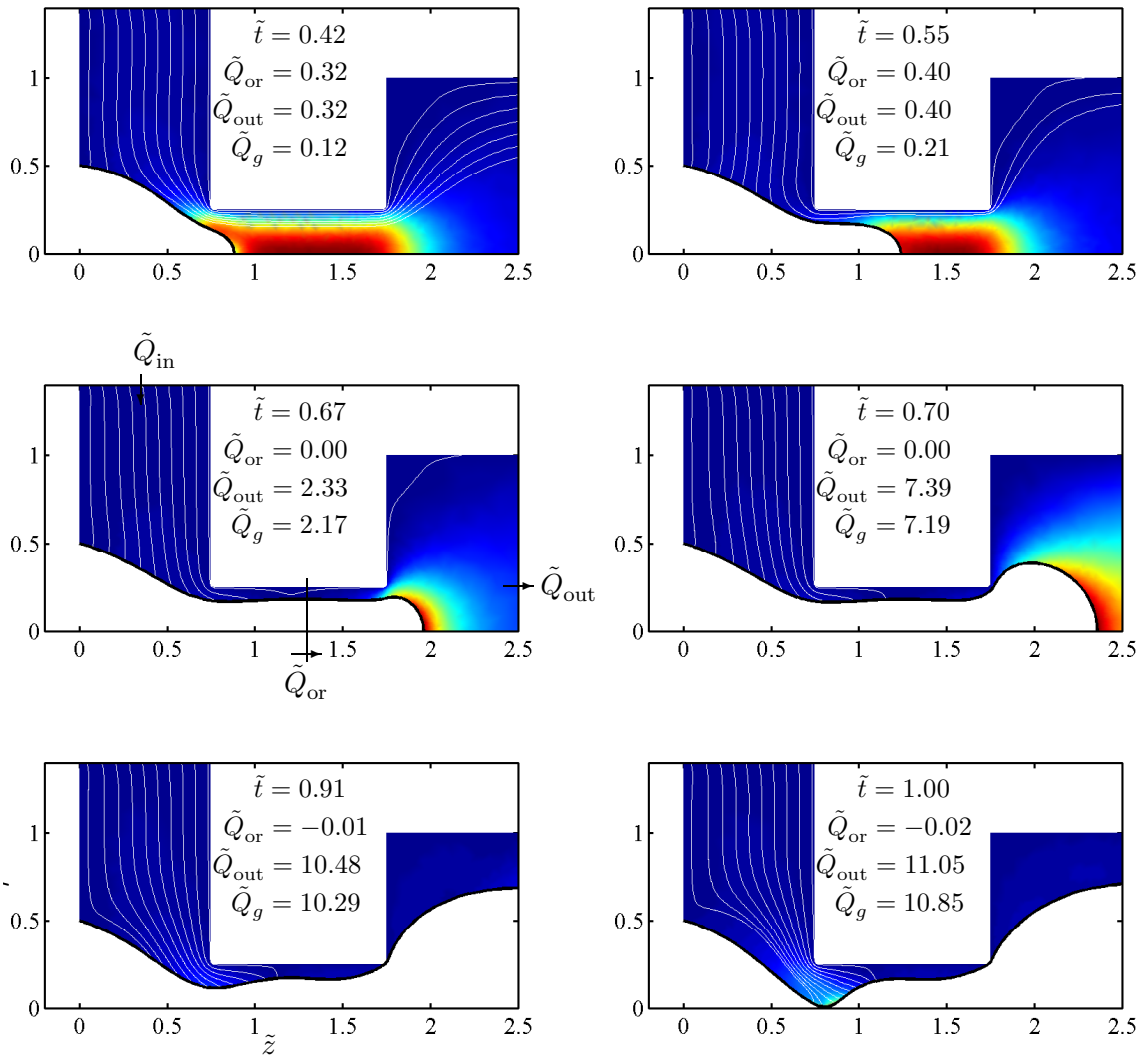

Figure 7.14: A sequence of of six blowups of the orifice region with stream lines from the inlet (white lines) and the velocity magnitude $|\boldsymbol{u}|$ as contour plot in the background. The dimensionless times $\tilde{t}$ are added together with different flow rates.

flow-focusing device where the liquid has non-Newtonian properties. No experimental results have been published about this matter to our knowledge.

The model

The governing equations for a liquid-gas system where the liquid viscosity follows the power-law model

$$\eta = m\dot{\gamma}^{n-1} \tag{7.25}$$

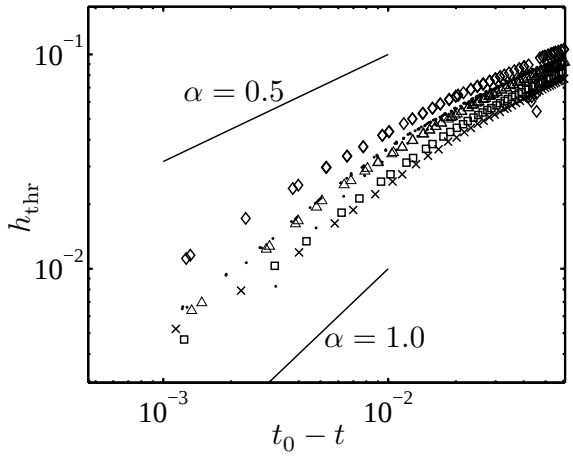

Figure 7.15: A double logarithmic plot of the gas thread thickness h_{thr} as function of time. The different symbols correspond to values of ϵ_u varying from 0.5 to 1.8. The two solid lines correspond to a slope of 1 and 0.5 respectively.

are presented in Sec. 4.9. The studied flow-focusing geometry is the same as the one presented in the paper presented above as well as the geometry described in Chap. 5. The new flow model introduces an additional nonlinearity to the free surface system through the dependent variables (u, v, p), specifically through the strain dependent viscosity $\tilde{\eta}$. This requires the use of an iterative method to solve for the flow field at every time step. In FEMLAB we utilize the nonlinear solver `femnlin` which is based on a damped Newton iterative method [81]. This added non-linearity increases the computation time at every time step. The model also includes one extra dimensionless parameter namely the exponent n defining the degree of "non-Newtoniannes" of the system. These last two facts have restricted the number of parameters n, Ca, $\tilde{p}_2$, and geometry that we have studied, the specific choices are discussed below.

Bubbles in non-Newtonian liquids

For the values of $n = 0.9$, 0.8, and 1.3 studied the system did not directly show any highly nonlinear behavior through the morphology of the interface. In Fig. 7.16 we depict the shape of two bubbles with the same volume $V_b/d^3 = 2.45$. One is created for $n = 0.8$ (shear thinning, full line) and the other for $n = 1.3$ (shear thickening, dashed line). The shape of the shear thinning bubble is slightly more rounded than the one of the shear thickening. It is difficult to compare the shapes as the flow parameters are different for the two bubbles.

A more general morphological study of the bubbles would require far more parameters analyzed. The final shapes of the bubbles at snap-off in Fig. 7.16 were determined after approximately 14 hours of computation on an Intel Pentium 4, 3.2 GHz machine with 1 GB of RAM.

The evolution of the gas thread thickness $\tilde{h}_{\mathrm{thr}}$ is depicted in Fig. 7.17 both in a double logarithmic and a linear plot. It is interesting to note how the slope and behavior near

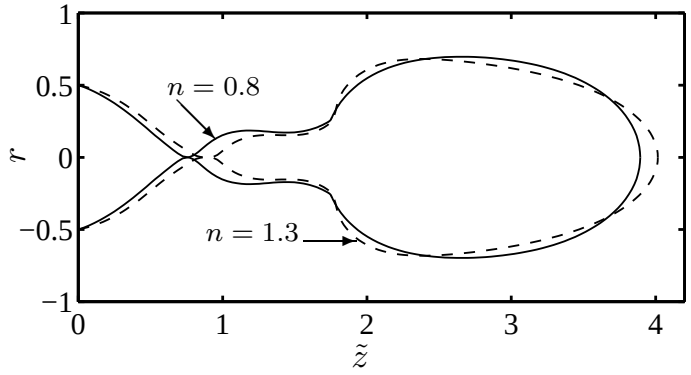

Figure 7.16: Shape of two bubbles for different parameter values: (1) $n = 0.8$, $Ca = 0.16$, $\tilde{p}_2 = 190$ and (2) $n = 1.3$, $Ca = 0.1$, $\tilde{p}_2 = 1020$.

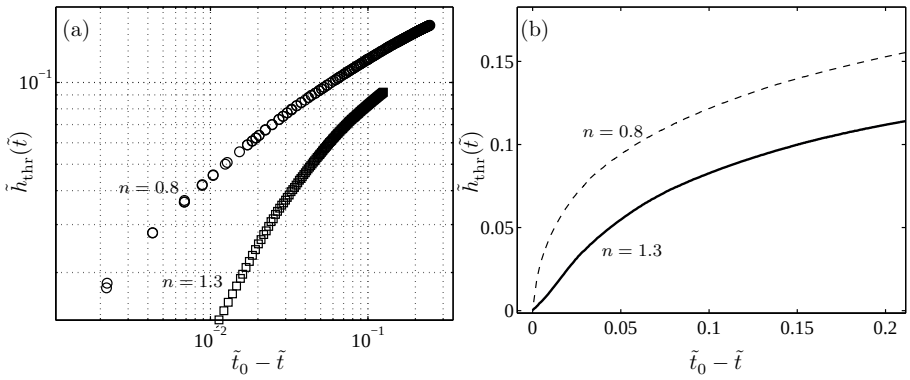

Figure 7.17: Evolution of the gas-thread thickness as function of $\tilde{t}_0 - \tilde{t}$ in (a) a double logarithmic plot and (b) a normal linear plot.

t_0 differs for the two exponents n. For large values of n the effective viscosity η is large meaning that the the collapse speed u_s is small if we assume that the proportionality $u_s \propto \gamma_{\mathrm{lg}}/\eta$ holds. This is supported by the slope of the two graphs near $\tilde{t} = \tilde{t}_0$.

Scaling of the bubble volume V_b

In the paper presented above we argued that the volume of a bubble was equal to the time the gas thread stayed open τ times the gas flow-rate Q_g. This flow rate was found by using volume conservation such that $Q_g = Q_{\mathrm{out}}$. The liquid flow-rate Q_{out} at the outlet was in turn found by assuming simple Poiseuille flow with a driving pressure gradient given by the Young–Laplace pressure at the front of the bubble.

In the present non-Newtonian model we again assume that $\tau \propto 1/Q_{\mathrm{in}}$. This seems reasonable as this time is determined only by the volume V_{or} of the orifice (here fixed) and the flow rate of the supplied liquid Q_{in}. The steady state flow rate of a liquid obeying the

power law model is in a cylinder of radius H given analytically as,

$$Q = \frac{\pi H^3}{1/n+3}\left(\frac{\Delta p H}{2m\ell}\right)^{1/n}, \tag{7.26}$$

where $\Delta p/\ell$ is the pressure gradient [36]. We have following the arguments given in the paper that $\Delta p \approx p_{\text{gas}} - 2\gamma_{\text{lg}}/H$ which for the created bubble volume scaling yields

$$V_b \propto \frac{H^3}{Q_{\text{in}}(1/n+3)}\left[\frac{H}{m}\left(p_{\text{gas}} - \frac{2\gamma_{\text{lg}}}{H}\right)\right]^{1/n}, \tag{7.27}$$

this equation is general and is applicable if snap-off occurs when the bubble front is at the right of the orifice, i.e., $\ell < W$ in the notation of the paper. The dimensionless parameters determining the physics of the system are,

$$\tilde{p}_2 = \frac{p_{\text{gas}}}{m}\left(\frac{U}{d}\right)^{-n}, \tag{7.28}$$

$$Ca = \frac{d\,m}{\gamma_{\text{lg}}}\left(\frac{U}{d}\right)^{n}, \tag{7.29}$$

the geometry factor H/d, and the power law exponent n.

Results

In order to verify the scaling law Eq. (7.27) for the volume of a created bubble we present two figures that are based on 310 hours of computation. As mentioned the computational cost is very large in this non-Newtonian system.

In the first Fig. 7.18 we depicted the dimensionless bubble volume V_b/d^3 as function of the dimensionless quantity $Ca^{-1/n}$ which is proportional to $1/U \times (\gamma_{\text{lg}}/m)^{1/n}$. From the figure it is evident that the dimensionless volume scales linearly with $Ca^{-1/n}$ for both choices of exponent n. This linear behavior also follows from the scaling law Eq. (7.27) which predicts that for a constant geometry V_b is linear in $1/Q_{\text{in}} \times (\gamma_{\text{lg}}/m)^{1/n}$. Even though this result is only based on a few data points the scaling law seems to be correct.

Finally in Fig. 7.19 we have depicted the dimensionless bubble volume V_b/d^3 as function of the dimensionless parameter $\tilde{p}^{1/n}$ for a constant choice of the capillary number $Ca = 0.1$. This means that we actually depict V_b/d^3 as function of $(10p_{\text{gas}}d/\gamma_{\text{lg}})^{1/n}$ which is a measure of the ratio between the surface tension forces and the gas pressure. The scaling law includes the term $(p_{\text{gas}} - 2\gamma_{\text{lg}}/H)^{1/n}$ that connects the gas pressure to the surface-tension related Young–Laplace pressure. Hence, if one of those terms is dominant we expect a linear behavior of V_b/d^3. In Fig. 7.19 we see that for large values of $\tilde{p}^{1/n}$ where the gas pressure is dominant the bubble volume seems to scales linearly (more point would make it more clear). For small values of $\tilde{p}^{1/n}$ surface tension is dominant and bubbles snap off when $\ell > W$, see Fig. 7.5(c). The dimensionless collapse speed u_s/U of the gas thread prior to snap-off was found to be constant ~ -1.1. This finding is consistent with the results from the paper and the fact that the capillary number is constant.

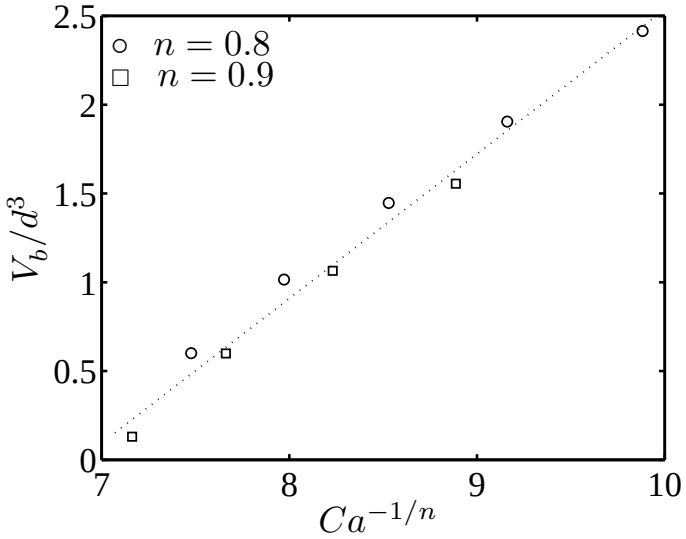

Figure 7.18: Dimensionless volume V_b/d^3 of a created bubble as function of the dimensionless quantity $Ca^(-1/n)$, for $n = 0.8$ and $n = 0.9$, shear thinning.

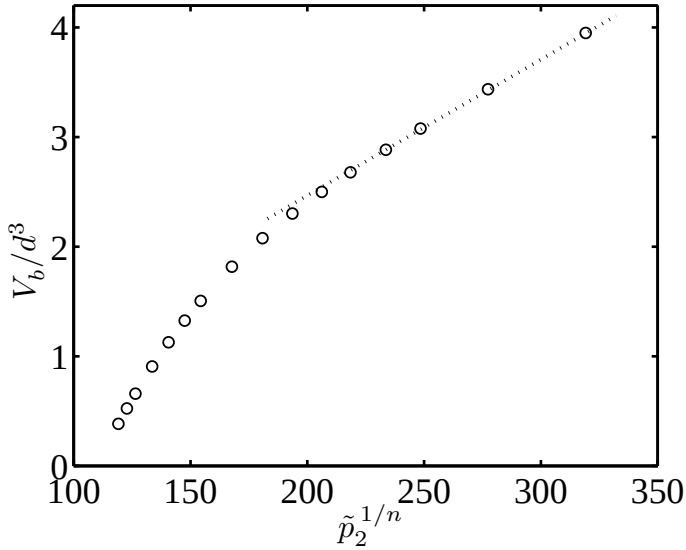

Figure 7.19: Dimensionless volume V_b/d^3 of a created bubble as function of the dimensionless quantity $\tilde{p}^(1/n)$ for constant capillary number $Ca = 0.1$ and exponent $n = 1.3$, shear thickening.

Chapter 8

Conclusion and outlook

Conclusion

In the present thesis, we have been concerned with the numerical and theoretical study of multi phase flows in microfluidic devices and especially the case of liquid-gas systems. The work can roughly be divided into the study of bubbles in microchannel contractions and the study of the bubbling dynamics in a flow-focusing device.

We have shortly presented two of our papers concerned with the passage of gas bubbles through microchannel contractions. The first paper is purely theoretical and presents a simplified physical model. It enables us to calculate the forces and pressures needed to push a bubble through a contraction, of arbitrary shape, very accurately without losing the essential physics of the problem. The model enabled us to formulate geometrical design rules for microchannel contractions to reduce or prevent clogging. The second paper was made in collaboration with the experimental group of D. Attinger at the State Univeristy of New York, Stony Brook, USA. They measured the pressure needed to push gas bubbles through different axisymmetric micro contractions in liquid filled capillaries. The results were compared to our model predictions and we found good agrement. We further present possible explanations for the discrepancies which are mostly dynamic in nature.

A survey of the microfluidic flow-focusing device was then presented and used for motivation for the subsequent study. The main goal of the work presented in this thesis was to numerically study the full free-surface dynamics of the bubbling process in the special flow-focusing geometry. The study was initiated while on a five month research stay in the group of Prof. Howard A. Stone at Harvard university. Computational fluid dynamics is an important tool in microfuidics as it provides detailed information when theoretical models and experimental results are unavailable or difficult to obtain.

We have developed a generic numerical model for solving free-surface Stokes flows in an axisymmetric geometry. The model is based on a second-order Runge–Kutta time-integration algorithm and a free-surface scheme implemented in MATLAB which are coupled to the commercial finite-element solver FEMLAB. The model also comprises a mapping handling problems related to surface elongation as well as an automatic re-meshing and redistribution of interface points. The numerical code was then applied to three test cases

and the results discussed in detail. From the results it was evident that the code is reliable and produces correct numerical results. The coupling between the time integration algorithm, the curvature algorithm, and the FEMLAB solver works perfectly. Moreover, the code is seen to be very versatile and was easily modified to suit the different geometries and physics of the three test systems. The development and thorough testing of a new numerical code are necessary and time consuming.

The model was then utilized to study the two-phase dynamics in an axisymmetric flow-focusing device. Based on a simple physical model we present a general scaling law for the volume V_b of the created bubbles that depends on four parameters: the inlet liquid flow-rate Q_{in}, the gas pressure p_{gas}, the outlet channel radius H, and the liquid-gas surface tension γ_{lg}. By physical analysis and numerical simulation we have shown that the bubble growth time τ scales proportionally to the inverse liquid flow rate $1/Q_{\text{in}}$.

The collapse speed u_s of the gas thread immediately prior to the snap-off event was found to be proportional to the ratio γ_{lg}/μ. This scaling was not observed experimentally by Garstecki *et al.* [3, 4] but is supported by other studies of the breakup of viscous axisymmetric threads. The behavior of the thread thickness as function of time $h_{\text{thr}}(t)$ deviates from the experimental data. We speculate that this difference in the collapse dynamics is due to the difference in geometry of the devices. In the experiments the gas thread is confined anisotropically while it is confined equally from all sides in our axisymmetric model. In the simulated geometry the thread can minimize surface area (energy) in two dimensions simultaneously as it is not restricted by a top and bottom lid as in the planar case.

The above mentioned scaling law for the bubble volume is presented in Eq. (7.23). For a constant geometry it reduces to the scaling law $V_b \propto p_{\text{gas}}/\mu Q_{\text{in}}$ described by Garstecki *et al.* We confirm this law by means of simulations for various constant values of H. For a varying outlet channel radius our extended scaling law also predicts an H^4 dependence namely $V_b \propto H^4 p_{\text{gas}}/\mu Q_{\text{in}}$. This dependence is also confirmed by means of the simulations. Our numerical investigation further reveals that a critical values exist for the dimensionless product $\tilde{p}_2 Ca$ determining where the bubble is located when snap-off occurs. This value is determined by the ratio between the surface tension related Young–Laplace pressure and the gas pressure.

Using a simple mechanism to account for the snap-off we model a sequence of four consecutive bubbles and show that the flow-focusing device does not produce bubbles of constant volume straight away. The results suggests that there is a certain transient behavior before reaching steady state. Bubbles of constant volume are only created when a constant pressure drop exists in the outlet. This could for example be the case if the outlet region is large compared to the bubbles or if large bubbles are filling the entire outlet region, just as happens in experiments.

Using the flexibility of defining the governing equations in FEMLAB we chose as a last model to study the dynamics in a flow-focusing device where the liquid has non-Newtonian properties. We chose for simplicity to model the rheological properties of the fluid according to the power-law model. This model introduces the exponent n as an extra free parameter in the system. Based upon simple physical assumptions we derive a scaling law for the volume V_b of the created bubbles Eq. (7.27). As the power-law model introduces

nonlinearities into the governing equations the computational times were very long. The scaling law was partially confirmed by a restricted number of simulations corresponding to 310 hours of computational time. This study that includes rheological effects produces all new results that have not yet tested experimentally.

Outlook

The code that I have developed is very flexible and generic and allows for the inclusion of many interesting physical phenomena such as the studied non-Newtonian effects. It would also be possible to for example include transport of surfactant at the liquid interface or to include heat transport. The flexibility of the code was proven when it was used to verify the stability and shape of a liquid-liquid interface in a novel design for a electro-osmotic micro pump. The work is presented in the paper: *A novel electroosmotic pump design for nonconducting liquids: theoretical analysis of flow rate-pressure characteristics and stability* by A. Brask, G. Goranovic, M. J. Jensen, and H. Bruus [11] (it is presented in its full length in Appendix D).

It would further be interesting to use the code to study the effect the orifice geometry has on the bubbling dynamics in the flow-focusing device. Moreover, a study of the effects of confinement of the gas thread would be very useful and enlightening. This last study would require the implementation of a full 3D free-surface model.

Bibliography

[1] M. J. Jensen, G. Goranović, and H. Bruus, J. Micromech. Microeng. **14**, 876 (2004).

[2] H. Chio, M. J. Jensen, X. Wang, H. Bruus, and D. Attinger, *Transient pressure drops of gas bubbles passing through liquid-filled microchannel contractions: an experimental and numerical study*, submitted to J. Micromech. Microeng., July 2005.

[3] P. Garstecki, I. Gitlin, W. DiLuzio, E. Kumacheva, H. A. Stone, and G. M. Whitesides, Appl. Phys. Lett. **85**, 2649 (2004).

[4] P. Garstecki, H. A. Stone, and G. M. Whitesides, Phys. Rev. Lett. **94**, 164501 (2005).

[5] P. Garstecki, M. J. Fuerstman, and G. M. Whitesides, Phys. Rev. Lett. **94**, 234502 (2005).

[6] H. A. Stone, A. D. Stroock, and A. Ajdari, Annu. Rev. Fluid Mech. **3**6, 381 (2004).

[7] G. K. Batchelor, *An Introduction to Fluid Dynamics*, Cambridge Univeristy Press, 2000.

[8] P. Gravesen, J. Branebjerg, and O. S. Jensen, J. Micromech. Microeng. **3**, 168 (1993).

[9] M. Elwenspoek, T. S. Kannerubj, R. Miyake, and J. H. J. Fluitman, J. Micromech. Microeng. **4**, 227 (1994).

[10] J. Tsai, L. Lin, Sensors and Actuators A **97-98**, 665 (2002).

[11] A. Brask, G. Goranović, M. J. Jensen, and H. Bruus, J. Micromech. Microeng. **15**, 883 (2005).

[12] T. S. Sammarco and M. A. Burns, AiChE J **45**, 350 (1999).

[13] A. S. Utada, E. Lorenceau, D. R. Link, P. D. Kaplan, H. A. Stone, and D. A. Weitz, Science **308**, 537 (2005).

[14] S. L. Anna, N. Bontoux, and H. A. Stone, App. Phys. Lett. **82**, 364 (2003).

[15] A. M. Gañán-Calvo and J. M. Gordillo, Phys. Rev. Lett. **87**, 274501 (2001).

[16] A. M. Gañán-Calvo, Phys. Rev. E **69**, 027301 (2004).

[17] T. W. Shield, D. B. Bogy, and F. E. Talke, IBM J. Res. Dev. **31**, 96 (1987)

[18] B. Ambravaneswaran, S. D. Phillips, and O. A. Basaran, Phys. Rev. Lett. **85**, 5332 (2000).

[19] W. J. Rider, D. B. Kothe, S. J. Masso, J. H. Cerutti and J. I. Hochstein, *Accurate Sloution Algorithms for Incompressible Multiphase Flows*, AIAA, Paper 95-0699 (1995).

[20] D. F. Zhang and H. A. Stone, Phys. Fluids **9**, 2234 (1997).

[21] C. Pozrikidis, *Boundary Integral and Singularity Methods for Linearized Viscous Flows*, Cambridge University Press, Cambridge, England, (1992).

[22] A. U. Chen, P. K. Notz, and O. A. Basaran, Phys. Rev. Lett. **88**, 174501 (2002)

[23] J. Eggers, Rev. Mod. Phys. **69**, 865 (1997).

[24] I. Cohen, M. P. Brenner, J. Eggers, and S. R. Nagel, Phys. Rev. Lett. **83**, 1147 (1999).

[25] M.P. Brenner, J. Eggers, K. Joseph, S. Nagel, and X. D. Shi, Phys. Fluids **9**, 1573 (1997).

[26] J. R. Lister and H. A. Stone, Phys. Fluids **10**, 2758 (1998).

[27] M. J. Jensen, *Bubbles in Microchannels*, MSc thesis, Mikroelektronic Centret - MIC, Technical University of Denmark, 2002.

[28] L. D. Landau and E. M. Lifshits, *Fluid Mechanics*, Butterworth and Heinemann, 2003.

[29] J. Fredsøe, *Hydrodynamik*, Den private ingeniør forening, DTU, 3. udgave, maj 1994.

[30] A. W. Adamson and A. P. Gast, *Physical Chemistry of Surfaces*, John Wiley and Sons, Inc., Sixth Edition, 1997.

[31] R. F. Probstein, *Physiochemical Hydrodynamics, An Introduction*, John Wiley and Sons, Inc., Second Edition, 1994.

[32] D. J. Struik, *Lectures on Classical Differential Geometry*, Dover Publications, Inc., 1988.

[33] R. S. Millman and G. D. Parker, *Elements of Differential Geometry*, Prentice Hall, 1977.

[34] P.–G. de Gennes, F. Brochard-Wyart, and D. Quere, *Capillarity and Wetting Phenomena: Drops, Bubbles, Pearls, Waves* Springer, 2003.

[35] P.–G. de Gennes, Rev. Mod. Phys. **57**, 827 (1985).

[36] R. B. Bird, R. C. Armstrong, and O. Hassager, *Dynamics of Polymeric Liquids, Volume 1, Fluid Mechanics*, John Wiley and Sons, 1987.

[37] M. Heller, *Dynamics of finite-sized partivles in microfluidic systems*, MSc thesis, MIC-Department of Micro and Nanotechnology, Technical University of Denmark, 2005.

[38] Y. C. Chang, T. Y. Hou, B. Merriman, and S. Osher, J. of Comput. Phys. **124**, 449 (1996).

[39] C. W. Hirt, B. D. Nichols and N. C. Romero, *SOLA-VOF, A Sloution Algorithm for Transient Fluid Flow with Multiple Free Boundaries*, Los Alamos Scientific Laboratory, 1980.

[40] W. J. Rider, D. B. Kothe, S. J. Mosso, J. S. Brock and J. I. Hochstein, *Volume Tracking of Interfaces Having Surface Tension in Two and Three Dimensions*, AIAA, Paper 96-0859 (1996).

[41] W. J. Rider and D. B. Kothe, *Comments on Modelling Interfacial Flows with Volume-Of-Fluid Methods*, Los Alamos National Laboratory, 1995.

[42] S. Chen and G. D. Doolen, Annu. Rev. Fluid Mech. **30**, 329 (1998).

[43] C. V. Hirt, A. A. Amsden, and J. L. Cook, J. Comput. Phys. **14**, 227 (1974).

[44] L. H. Olesen, *Eulerian, Lagrangian, or other reference frames*, internal MIFTS communication note (2005).

[45] `www.matlab.com`

[46] `www.comsol.com`

[47] R. W. Hopper, J. Fluid Mech. **213**, 349 (1990).

[48] R. W. Hopper, J. Fluid Mech. **230**, 355 (1991).

[49] R. W. Hopper, J. Fluid Mech. **243**, 171 (1992).

[50] R. W. Hopper, J. Am. Ceram. Soc. **76**, 2947 (1993).

[51] G. A. L. van de Vorst, *Modelling and Numerical Simulation of Viscous Sintering*, PhD thesis, Eindhoven Univeristy of Technology, 1994.

[52] F. P. Bretherton, J. Fluid Mech. **10**, 166 (1961).

[53] C.–W. Park and G. W. Homsy, J. Fluid Mech. **139**, 291 (1984).

[54] L. W. Schwartz, H. M. Princen, and A. D. Kiss, J. Fluid Mech. **172**, 259 (1986).

[55] J. Ratulowski and H.–C. Chang, Phys. Fluids A **1**, 1642 (1989).

[56] H. J. Stark and M. Manga, Transport Porous Med. **40**, 201 (2000).

[57] C. Redon, F. Brochart-Wyart, and F. Rondelez , Phys. Rev. Lett. **66**, 715 (1991).

[58] G. I. Taylor, Proc. R. Soc. London Ser. A **138**, 41 (1932).

[59] L. H. Olesen, *Computational Fluid Dynamics in Microfluidic Systems*, MSc thesis, Mikroelektronic Centret - MIC, Technical University of Denmark, 2003.

[60] T. Y. Hou, J. S. Lowengrub, and M. J. Shelley, J. Comput. Phys. **114**, 312 (1994).

[61] P. Bach and O. Hassager, J. Fluid Mech. **152**, 173 (1985).

[62] J. R. Cash and S. Semnani, ACM Transactions on Mathematical Software **19**, 63 (1993).

[63] Numerical Recipes in C, `www.nr.com`.

[64] R. V. Roy and L. W. Schwartz, J. Fluid Mech. **391**, 293 (1999).

[65] G. I. Taylor, Proc. R. Soc. London Ser. A **146**, 501 (1934).

[66] G. I. Taylor, Proc. Int. Congr. Appl. Mech., 11th, Munich, pp. 790-96 (1964).

[67] H. A. Stone, Annu. Rev. Fluid Mech. **26**, 65 (1994).

[68] A. Acrivos and T. S. Lo, J. Fluid Mech. **86**, 641 (1978).

[69] A. Acrivos, Ann. N. Y. Acad. Sci. **404**, 1 (1983).

[70] H. A. Stone, B. J. Bentley, and L. G. Leal, J. Fluid Mech. **173**, 131 (1986).

[71] B. J. Bentley and L. G. Leal, J. Fluid Mech. **167**, 241 (1986).

[72] M. Favelukis, O. M. Lavrenteva, and A. Nir, J. Non-Newtonian Fluid Mech. **125**, 49 (2005).

[73] M. Muradoglu and H. A. Stone, Phys. Fluids **17**, 73305 (2005).

[74] T. M. Tsai and M. J. Miksis, J. Fluid Mech. **274**, 197 (1994).

[75] J. N. Reddy and D. K. Gartlink, *The Finite Element Method in Heat Transfer and Fluid Dynamics*, CRC Press, Second Edition, 2000.

[76] R. D. Cook, D. S. Malkus, M. E. Plesha, and R. J. Will, *Concepts and Applications of Finite Element Analysis*, John Wiley and Sons, Inc., Fourth Edition, 2002.

[77] Y. Navot, Phys. Fluids **11**, 990 (1999).

[78] Y. Son, N. S. Martys, J. G. Hagedorn, and K. B. Migler, Macromolecules **36**, 5825 (2003).

[79] P. Garstecki, private communication.

[80] M. J. Jensen, H. A. Stone, and H. Bruus *A numerical study of two-phase Stokes flow in an axisymmetric flow-focusing device*, submitted to Phys. Fluids, August 2005.

[81] FEMLAB Manuals, by Comsol AB (2004).

Appendix A

Source code and program variables

A.1 Main program

```
%%%%%%%%%%%%%%%%%%%%%%%%%%%%%%%%%%%%%%%%%%%%%%%%%%%%%%%%%%%%%%%%%%%%%%%%%%%%%%%
% FEMLAB Model for zero Re interface evolution
% Mads J. Jensen
% MIC - Department of Micro and Nanotechnology, DTU
% DEAS - Division of Engineering and Applied Sciences, Harvard
%
% Verion 20: 2.order Runge Kutta.
%%%%%%%%%%%%%%%%%%%%%%%%%%%%%%%%%%%%%%%%%%%%%%%%%%%%%%%%%%%%%%%%%%%%%%%%%%%%%%%
clear all;
close all;
tic;
cd('C:\Documents and Settings\mjj\My Documents\FEMLAB ff-model');

%%%%%%%%% Parameters %%%%%%%%%
global d H Hfac W L ppz ppr alpha beta gamma sp_z sp_r sp_dz sp_dr sp_ddz sp_ddr

%Geometry parameters
d=0.5; H=2; Hfac=0.5; W=15; di=H-3*d; alpha=0.5; beta=1.5; gamma=2;

%Physical parameters scaling
Re=0; Ca=1.5; p2=300;
Ui=6*(alpha*d)^2/(di^2+6*d*di); %ui(s)=Ui*s*(1-s), yielding Uo=1
Tend=100; %End time

%Changing U (\propto Q)
X=1; Re=Re*X; Ca=Ca*X; p2=p2/X;

% Numerical parameters
Ndat=27;     %datafile number
name='pA';   %datafile name
M=5000;      %maximal number of timesteps
dM=10;       %save data every dM steps
save_data=1; %save data (yes (1) or no (0))
Mext=10;     %extra symmetry points
tol_sp=1e-7; %smoothing spline tolerence
delta=0.33;  %timestep size dt=delta*dT
zeta=0.03;   %Hmax on interface
```

```
% Initial drop shape and data
i=1; isave=1; time=0; disp('-------------------------------------');
S=linspace(0,1,35); %initial S
zint=d*sin(pi/2*S); %initial z
rint=d*cos(pi/2*S); %initial r

%load('data-pA24-011','zint','rint','S','time','dt','L_front','i','isave','Re','Ca','p2',...
   'L_front','L_int','h_thr','z_thr','V_bub','delta','zeta','tol_sp');
   isave=isave+1; i=i+1; L=zint(end);

%%%%% PDE system and parameters %%%%%
fem.const = {'Re' Re 'Ca' Ca 'p2' p2 'Ui' Ui};
fem.functions{1}.type = 'inline';
fem.functions{1}.name='kappa20_rz(s)';
fem.functions{2}.type = 'inline';
fem.functions{2}.name = 'kappa20_rt(s)';

fem.sdim = {'z' 'r'};
fem.dim = {'u' 'v' 'p'};
fem.shape ={shlag(2,'u') shlag(2,'v') shlag(1,'p')};
%fem.sshape = 3;
fem.gporder = 5;

fem.form = 'general';
fem.equ.ga = {{{'r*(2*uz-p)' 'r*(ur+vz)'} {'r*(ur+vz)' 'r*(2*vr-p)'} {'0' '0'}}};
fem.equ.f = {{{'0'} {'-p+2*v/r'} {'r*(uz+vr)+v'}}};

%%%%% PDE boundary conditions %%%%%
fem.bnd.ind = {[12] [4] [3] [1 5:11 13] [2]};
fem.bnd.g = {{0 0 0} {0 0 0}  {0 0 0}  {0 0 0} ...
   {{'(r*p2+1/Ca*(kappa20_rz(s)+kappa20_rt(s)))*nz'}...
   {'(r*p2+1/Ca*(kappa20_rz(s)+kappa20_rt(s)))*nr'} 0}};
fem.bnd.r = {{{'u-Ui*s*(1-s)'} {'v'} 0} {0 {'v'} 0} {{'v'} 0 0} {{'u'} {'v'} 0} {0 0 0}};

%Initializing
h_thr(1)=1; L=zint(end);
ppz=spline([S 1+(1-S(end-1:-1:end-Mext))],[zint zint(end-1:-1:end-Mext)]);
ppr=spline([S 1+(1-S(end-1:-1:end-Mext))],[rint -rint(end-1:-1:end-Mext)]);

%%%%% Caclulations loop %%%%%
while time(end)<Tend & i<=M & L(end)<=0.95*W & h_thr(end)>0
   % Geometry, Meshing
   L=zint(end); d=rint(1);
   fem.geom = 'geom20cur';
   fem.mesh = meshinit(fem,'Hmaxedg',[1 2 3 7 9; 0.2 zeta 0.25 0.004 0.02],...
       'Hgrad',1.18,'Report','off','Hpntedg',[2; length(S)],'Hnarrow',3,...
       'Hmax',0.3,'Hcurve',10);

   % Modifying mesh
   Idex=find(fem.mesh.e(5,:)==2);
   Is=fem.mesh.e(1,Idex); Ie=fem.mesh.e(2,Idex); Izr=[Is Ie(end)];
   zint=fem.mesh.p(1,Izr);
   rint=fem.mesh.p(2,Izr);
   dL=sqrt((zint(1:end-1)-zint(2:end)).^2+(rint(1:end-1)-rint(2:end)).^2);
   S=[0 dL*triu(ones(length(dL)))]/sum(dL);
   mesh_temp.p=fem.mesh.p; mesh_temp.t=fem.mesh.t; mesh_temp.e=fem.mesh.e;
   mesh_temp.e(3,Idex)=S(1:end-1); mesh_temp.e(4,Idex)=S(2:end);
   fem.mesh=meshenrich(mesh_temp);
   [sp_z,sp_r,sp_dz,sp_dr,sp_ddz,sp_ddr]=kappadata20(S,zint,rint,Mext,tol_sp);
```

```
% Solving
fem = femdiff(fem);
fem.xmesh = meshextend(fem);
fem.sol = femlin(fem,'Report','off');

%%%%%%%%%%%%%%%%%%%%%%%%%%%%%%%%%%%%%%
% Start Runge-Kutta time step
S_temp=S;
nz=-spval(sp_dr,S)./sqrt(spval(sp_dz,S).^2+spval(sp_dr,S).^2); nz(end)=1;
nr=spval(sp_dz,S)./sqrt(spval(sp_dz,S).^2+spval(sp_dr,S).^2); nr(end)=0;
un=nz.*postinterp(fem,'u',S,'Dom',2)+nr.*postinterp(fem,'v',S,'Dom',2); un(1)=0;

% Time step size dt
dt(i)=delta*min(dL./abs(un(2:end)));
% Making RK step
zint_temp=zint+un.*nz*dt(i)/2; zint_temp(1)=0;
rint_temp=rint+un.*nr*dt(i)/2; rint_temp(end)=0;
dL=sqrt((zint_temp(1:end-1)-zint_temp(2:end)).^2+...
       (rint_temp(1:end-1)-rint_temp(2:end)).^2);
S=[0 dL*triu(ones(length(dL)))]/sum(dL);
pp_SS=pchip(S_temp,S);
ppz=spline([S 1+(1-S(end-1:-1:end-Mext))],[zint_temp zint_temp(end-1:-1:end-Mext)]);
ppr=spline([S 1+(1-S(end-1:-1:end-Mext))],[rint_temp -rint_temp(end-1:-1:end-Mext)]);

% Geometry, Meshing
L=zint_temp(end); d=rint_temp(1);
fem.geom = 'geom20cur';
fem.mesh = meshinit(fem,'Hmaxedg',[1 2 3 7 9; 0.2 zeta 0.25 0.004 0.02],...
    'Hgrad',1.18,'Report','off','Hpntedg',[2; length(S)],'Hnarrow',3,...
    'Hmax',0.3,'Hcurve',10);

% Modifying mesh
Idex=find(fem.mesh.e(5,:)==2);
Is=fem.mesh.e(1,Idex); Ie=fem.mesh.e(2,Idex); Izr=[Is Ie(end)];
zint_temp=fem.mesh.p(1,Izr);
rint_temp=fem.mesh.p(2,Izr);
dL=sqrt((zint_temp(1:end-1)-zint_temp(2:end)).^2+...
       (rint_temp(1:end-1)-rint_temp(2:end)).^2);
S=[0 dL*triu(ones(length(dL)))]/sum(dL);
mesh_temp.p=fem.mesh.p; mesh_temp.t=fem.mesh.t; mesh_temp.e=fem.mesh.e;
mesh_temp.e(3,Idex)=S(1:end-1); mesh_temp.e(4,Idex)=S(2:end);
fem.mesh=meshenrich(mesh_temp);
[sp_z,sp_r,sp_dz,sp_dr,sp_ddz,sp_ddr]=kappadata20(S,zint_temp,rint_temp,Mext,tol_sp);

% Solving
fem = femdiff(fem);
fem.xmesh = meshextend(fem);
fem.sol = femlin(fem,'Report','off');

% End Runge-Kutta timestep: dt/2
%%%%%%%%%%%%%%%%%%%%%%%%%%%%%%%%%%%%%%
```

```
   S=S_temp; S_RK=ppval(pp_SS,S);
   % Evolving interface with gradiaent evaluated at dt/2
   nz=-spval(sp_dr,S_RK)./sqrt(spval(sp_dz,S_RK).^2+spval(sp_dr,S_RK).^2); nz(end)=1;
   nr=spval(sp_dz,S_RK)./sqrt(spval(sp_dz,S_RK).^2+spval(sp_dr,S_RK).^2); nr(end)=0;
   un=nz.*postinterp(fem,'u',S_RK,'Dom',2)+nr.*postinterp(fem,'v',S_RK,'Dom',2); un(1)=0;
   zint=zint+un.*nz*dt(i); zint(1)=0;
   rint=rint+un.*nr*dt(i); rint(end)=0;
   ppz=spline([S 1+(1-S(end-1:-1:end-Mext))],[zint zint(end-1:-1:end-Mext)]);
   ppr=spline([S 1+(1-S(end-1:-1:end-Mext))],[rint -rint(end-1:-1:end-Mext)]);

   %Data collected/updated at each timestep
   L_front(i)=zint(end); time(i)=sum(dt(1:i)); L_int(i)=postint(fem,'1','Edim',1,'Dl',2);

   I=find(kappa20_rz(S(2:end-1))>0);
   if isempty(I)==0
      rkn=rint(I); zkn=zint(I); [h_thr(i),I]=min(rkn); z_thr(i)=zkn(I);
      I_m=find(zint==z_thr(i)); un_thr(i)=un(I_m);
      V_bub(i)=pi*0.5*sum(diff(zint(I_m:end)).*(rint(I_m:end-1).^2+rint(I_m+1:end).^2));
   else
       h_thr(i)=1; z_thr(i)=0; V_bub(i)=0; un_thr(i)=0;
   end

   disp(sprintf('Time t=%0.2d, i=%0.5g, dt=%0.2d, h_thr=%0.2d',time(i),i,dt(i),h_thr(i)));
   disp(L);
   if find(i==[0:dM:M]) & save_data==1; % Saving data in file
       txt=sprintf(['data-' name '%0.2d-%0.3d'],Ndat,isave);
       save(txt,'zint','rint','S','time','dt','L_front','i','isave',...
           'Re','Ca','p2','L_front','L_int','h_thr','z_thr','V_bub','un_thr',...
           'alpha','beta','gamma','X','delta','zeta','tol_sp','Hfac');
       isave=isave+1;
       disp(txt);
   end
   i=i+1;
   % Freeing memory
   fem.xmesh=0; flgc;
   % Exiting time loop:
   clear halt; halt;
end

%Save last data
i=i-1;
txt=sprintf(['data-' name '%0.2d-%0.3d'],Ndat,isave);
save(txt,'zint','rint','S','time','dt','L_front','i','isave',...
   'Re','Ca','p2','L_front','L_int','h_thr','z_thr','V_bub','un_thr',...
   'alpha','beta','gamma','X','delta','zeta','tol_sp','Hfac');

Tsim=toc;
disp('-------------------------------------');
disp(sprintf('Total computation time %0.4g min',Tsim/60));
disp(sprintf('Re=%0.5g, Ca=%0.5g, p_2=%0.3d, and X=%0.5g',Re,Ca,p2,X));
disp('-------------------------------------');
```

```
%%%%%%%%%%%%%%%%%%%%%%%%%%%%%%%%%%%%%%%%%%%%%%%%%%%%%%%%%%%%%%%%%%%%%%%%
%%%%%%%%%%%%%% Post Processing and Plots %%%%%%%%%%%%%%%%%%%%%%%%%%%%%%%%
%%%%%%%%%%%%%%%%%%%%%%%%%%%%%%%%%%%%%%%%%%%%%%%%%%%%%%%%%%%%%%%%%%%%%%%%
fem.xmesh = meshextend(fem);

figure(1)
subplot(2,2,1);
postplot(fem,'tridata','p','arrowdata',{'u' 'v'},'trirefine',1,...
   'arrowyspacing',25,'arrowxspacing',35,'arrowcolor','k',...
   'arrowstyle','normalized','arrowscale',1); axis image;
xlabel('z'); ylabel('r');

subplot(2,2,2)
data=postinterp(fem,'-nz*u-nr*v',S,'Dom',2);
plot(S,data,'.-'); xlabel('S'); ylabel('Normal velocity: u_n=u\cdotn');

subplot(2,2,3)
plot(S,kappa20_rz(S)+kappa20_rt(S),'k.-'); hold on;
plot(S,kappa20_rz(S),'r.-'); plot(S,kappa20_rt(S),'g.-');
xlabel('S'); ylabel('r \cdot curvature');
legend('\kappa','\kappa_{rz}','\kappa_{r\theta}',1)

subplot(2,2,4) plot(time,L_front,'.-');
xlabel('Time: t'); ylabel('Position of front: L');
```

A.2 Additional functions

kappa20_rz.m

```
function kappa20_rz=kappa20_rz(s)
global sp_r sp_dz sp_dr sp_ddz sp_ddr

kappa20_rz=spval(sp_r,s).*(spval(sp_dz,s).*spval(sp_ddr,s)-spval(sp_dr,s).*...
spval(sp_ddz,s))./(spval(sp_dz,s).^2+spval(sp_dr,s).^2).^(3/2);
```

kappa20_rt.m

```
function kappa20_rt=kappa20_rt(s)
global sp_r sp_dz sp_dr

kappa20_rt=-spval(sp_dz,s)./(spval(sp_dz,s).^2+spval(sp_dr,s).^2).^(1/2);
```

kappadata20.m

```
function[sp_z,sp_r,sp_dz,sp_dr,sp_ddz,sp_ddr]=kappadata20(s,z,r,Mext,tol)

M=length(s); wz=ones(1,M+Mext); wz([1 M-8 M-4 M M+4 M+8])=100;
wr=ones(1,M+Mext); wr([1 M-8 M-4 M M+4 M+8])=100;
sp_z=spaps([s1+(1-s(end-1:-1:end-Mext))],[z z(end-1:-1:end-Mext)],tol,wz,3);
sp_r=spaps([s 1+(1-s(end-1:-1:end-Mext))],[r-r(end-1:-1:end-Mext)],tol,wr,3);
sp_dz=fnder(sp_z,1);
sp_ddz=fnder(sp_z,2);
sp_dr=fnder(sp_r,1);
sp_ddr=fnder(sp_r,2);
```

geom20cur.m

```
function [z,r]=geom20cur(bs,s)
global d H Hfac W L ppz ppr alpha beta gamma
cdel=0.02; nbs=13;

if nargin==0
    z=nbs; return
end

dl=[0 0 0 0 0 0 0 0 0 0 0 0 0;
    1 1 1 1 1 1 1 1 1 1 1 1 1;
    1 1 1 1 1 1 1 1 1 1 1 1 1;
    0 0 0 0 0 0 0 0 0 0 0 0 0];

if nargin==1
    z=dl(:,bs); return
end

z=zeros(size(s)); r=zeros(size(s)); [m,n]=size(bs);
if m==1 & n==1
   bs=bs*ones(size(s));
elseif m~=size(s,1) | n~=size(s,2)
   error('bs must be scaler or of same size as s');
end

%Boundary segment indices
I1=find(bs==1); I2=find(bs==2); I3=find(bs==3); I4=find(bs==4);
I5=find(bs==5); I6=find(bs==6); I7=find(bs==7); I8=find(bs==8);
I9=find(bs==9); I10=find(bs==10); I11=find(bs==11); I12=find(bs==12); I13=find(bs==13);

%Boundary coordinates
z(I1)=0;
r(I1)=3*d*(1-s(I1))+d*s(I1);
z(I2)=ppval(ppz,s(I2));
r(I2)=ppval(ppr,s(I2));
z(I3)=L*(1-s(I3))+W*s(I3);
r(I3)=0;
z(I4)=W;
r(I4)=Hfac*H*s(I4);
z(I5)=W*(1-s(I5))+(beta+gamma)*d*s(I5);
r(I5)=Hfac*H;
z(I6)=(beta+gamma)*d;
r(I6)=Hfac*H*(1-s(I6))+(alpha*d+cdel)*s(I6);
z(I7)=(beta+gamma)*d-cdel + cdel*cos(pi/2*s(I7));
r(I7)=(alpha*d+cdel) - cdel*sin(pi/2*s(I7));
z(I8)=((beta+gamma)*d-cdel)*(1-s(I8))+(beta*d+cdel)*s(I8);
r(I8)=alpha*d;
z(I9)=(beta*d+cdel) + cdel*cos(pi/2*s(I9)+pi/2);
r(I9)=alpha*d+cdel - cdel*sin(pi/2*s(I9)+pi/2);
z(I10)=beta*d;
r(I10)=(alpha*d+cdel)*(1-s(I10))+H*s(I10);
z(I11)=beta*d*(1-s(I11))-1*s(I11);
r(I11)=H;
z(I12)=-1;
r(I12)=H*(1-s(I12))+3*d*s(I12);
z(I13)=-1*(1-s(I13));
r(I13)=3*d;
```

A.3 Program variables description

The most important variables found in the source code above are here list and describe.

Constants

`Ca`:	capillary number Ca
`p2`:	gas pressure $\tilde{p}_2$
`X`:	scaling of flow rate (corresponds to ϵ_u)
`zeta`:	mesh size on moving boundary
`zeta_vtx`:	mesh size at the bubble tip vertex
`tol_sp`:	approximating spline tolerance
`Mext`:	additional ghost symmetry points M_{ext}

Program variables

`zint`:	interface points z-coordinates
`rint`:	interface points r-coordinates
`S`:	interface points arc length parameter
`ppz`:	interface z-coordinates interpolating spline
`ppr`:	interface r-coordinates interpolating spline
`dL`:	distance between interface points $\lvert\boldsymbol{x}_i - \boldsymbol{x}_{i+1}\rvert$
`sp_z`:	approximating spline for $z(S)$
`sp_dz`:	approximating spline for $\dot{z}(S)$
`sp_ddz`:	approximating spline for $\ddot{z}(S)$
`sp_r`:	approximating spline for $r(S)$
`sp_dr`:	approximating spline for $\dot{r}(S)$
`sp_ddr`:	approximating spline for $\ddot{r}(S)$
`nz`:	surface normal z-component $n_z(S)$
`nr`:	surface normal r-component $n_r(S)$
`un`:	interface normal velocity $\boldsymbol{u} \cdot \boldsymbol{n}(S)$
`dt`:	time step Δt
`time`:	time t
`L_int`:	total interface length
`h_thr`:	gas thread thickness h_{thr}
`V_bub`:	emerging bubble volume $V_b = 2\pi \int_{z_{\text{thr}}}^{z_{\max}} r(z) r dz$

Femlab structures

`fem.const`:	constant used in femlab
`fem.function`:	identifies user defined MATLAB functions
`fem.sdim`:	independent variables (z, r)
`fem.dim`:	dependent variables (u, v, p)
`fem.shape`:	finite element shapes
`fem.form`:	form of the governing equations
`fem.equ.ga`:	contains $\boldsymbol{\Gamma}$ from the governing equation
`fem.equ.f`:	contains $\boldsymbol{F}$ from the governing equation
`fem.bnd.g`:	contains G from the BC
`fem.bnd.r`:	contains R from the BC
`fem.mesh`:	contains mesh information created with the `meshinit` function
`fem.sol`:	contains the solution solved with `femlin`

Appendix B

More Femlab and FEM

B.1 Finite element analysis

When solving a PDE with the finite element method the solution field $(u(\boldsymbol{x}), v(\boldsymbol{x}), p(\boldsymbol{x}))$ is approximated by a linear combination of a finite number of basis functions

$$[u(\boldsymbol{x}), v(\boldsymbol{x}), p(\boldsymbol{x})] = \sum_i [u_i \varphi_{i1}(\boldsymbol{x}), v_i \varphi_{i2}(\boldsymbol{x}), p_i \varphi_{i3}(\boldsymbol{x})] \,. \tag{B.1}$$

where (u_i, v_i, p_i) are the coefficients solved for. The basis functions φ_{il}, $l = 1, 2, 3$ have a compact support, i.e., they are only nonzero on the mesh elements in the immediate neighborhood of the mesh node i, see Fig. B.1. The steady state PDE we wish to solve is given on the strong form

$$\partial_j \Gamma_{ljk} = F_{lk} \quad \text{in } \Omega_k, \tag{B.2}$$

where we use the Einstein summation rule, ∂_j means partial differentiation with respect to independent variable j, k is the domain number and $\mathbf{\Gamma}_k = [\Gamma_{lj}]_k$ as in Chap. 5. The

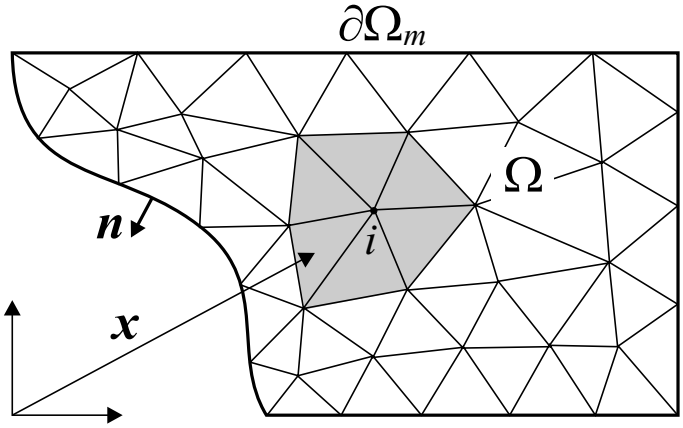

Figure B.1: Sketch of a computational domain Ω with boundary $\partial\Omega = \bigcup_m \partial\Omega_m$. The domain is divided into a triangular mesh. A basis function φ_i has the compact support marked in gray.

boundary conditions are

$$-n_j\Gamma_{lj} = G_l + \frac{\partial R_m}{\partial U_l}\mu_m \qquad \text{on } \partial\Omega_m \tag{B.3}$$

$$0 = R_m \qquad \text{on } \partial\Omega_m. \tag{B.4}$$

where $j = 1, 2$ is the independent variable (dimension z and r), l is the dependent variable counter, m is the boundary number, $\boldsymbol{U} = (u, v, p_k)$ is the dependent variable field, k is the domain number, and $\boldsymbol{n} = (n_1, n_2)$ is the outward normal. It is however only possible to satisfy this equation using infinitely many basis functions. To remedy this issue Eq. (B.2) is multiplied by the basis function φ_{il} and is integrated over the entire domain Ω_k,

$$\int_{\Omega_k} \varphi_{il}\partial_j\Gamma_{ljk}\,\mathrm{d}A = \int_{\Omega_k} \varphi_{il}F_{lk}\,\mathrm{d}A, \tag{B.5}$$

this form is known as the weak form of Eq. (B.2) because we solve the problem only on average. Partial integration of Eq. (B.5) further yields

$$-\int_{\Omega_k} \partial_j\varphi_{il}\Gamma_{ljk}\,\mathrm{d}A + \int_{\partial\Omega} \varphi_{il}(n_j\Gamma_{ljk})\,\mathrm{d}\ell = \int_{\Omega_k} \varphi_{il}F_{lk}\,\mathrm{d}A, \tag{B.6}$$

where we identify the boundary integral as the Neumann condition of Eq. (B.3). We may thus rewrite as

$$-\int_{\partial\Omega_m} \varphi_{il}\left[G_l + \frac{\partial R_m}{\partial U_l}\mu_m\right]\,\mathrm{d}\ell = \int_{\Omega_k} \left[\partial_j\varphi_{il}\Gamma_{ljk} + \varphi_{il}F_{lk}\right]\,\mathrm{d}A. \tag{B.7}$$

If the BC is a Dirichlet condition $0 = R_m$ it is fulfilled by choosing the Lagrange multiplier μ_m accordingly. When solving a PDE by the FEM method Eq. (B.7), which now includes all BCs, transforms to a large algebraic matrix system. Note that for a given i the integrals are only nonzero on the support of φ_{il} and are typically computed using a Gauss quadrature scheme. Ample details are found in Refs. [75, 76, 59].

B.2 Two fluids implementation: weak form

In the case of a system containing two fluids ($k = 1, 2$) the governing Eqs. (4.37) and (4.38), and the boundary conditions Eq. (4.39) are implemented in the weak from. This system was studied in the numerical test case of the viscous drop in viscous extensional flow, Sec. 6.3. For such a two domain system the equation corresponding to Eq. (B.6) is

$$-\int_{\Omega_k} \partial_j\varphi_{il}\Gamma_{ljk}\,\mathrm{d}A + \int_{\partial\Omega} \varphi_{il}n_j(\Gamma_{lj1} - \Gamma_{lj2})\,\mathrm{d}\ell = \int_{\Omega_k} \varphi_{il}F_{lk}\,\mathrm{d}A, \quad k = 1, 2 \tag{B.8}$$

where k is the indic of the domain and the line integral includes both terms Γ_{ljk} only on a boundary $\partial\Omega = \Omega_1 \cap \Omega_2$. On such a fluid-fluid boundary we have

$$\int_{\partial\Omega} \varphi_{il}n_j(\Gamma_{lj1} - \Gamma_{lj2})\,\mathrm{d}\ell = \int_{\partial\Omega} \varphi_{il}\frac{1}{Ca}(r\kappa)n_j\,\mathrm{d}\ell \tag{B.9}$$

when using Eq. (4.39) and $\boldsymbol{n}$ is the normal pointing from domain 1 into domain 2. In the FEMLAB script language the basis functions are referred to with the variable name followed by `_test`. The area integrals are defined in the `fem.eq.weak` fields and the boundary integrals are entered directly in the `fem.bnd.weak` field. The governing equations and BCs are as follows:

```
%%%%% PDE system and parameters %%%%%
fem.const = {'Re' Re 'Ca' Ca 'e_mu' e_mu 'e_rho' e_rho 'G' G};
fem.functions{1}.type = 'inline';
fem.functions{1}.name = 'kappa2L_rz(s)';
fem.functions{2}.type = 'inline';
fem.functions{2}.name = 'kappa2L_rt(s)';

fem.sdim = {'z' 'r'};
fem.dim = {'u' 'v' 'p1' 'p2'};
fem.shape = {shlag(2,'u') shlag(2,'v') shlag(1,'p1') shlag(1,'p2')};
fem.sshape = 3;
fem.gporder = 5;

fem.form = 'weak';
fem.equ.expr = {'G1zz' 'r*(2*uz-p1)' 'G1rr' 'r*(2*vr-p1)'...
                'G1zr' 'r*(ur+vz)' 'G2zz' 'r*(e_mu*2*uz-p2)'...
                'G2rr' 'r*(e_mu*2*vr-p2)' 'G2zr' 'r*e_mu*(ur+vz)'...
                'F1' '-p1+2*v/r' 'F2' '-p2+e_mu*2*v/r'...
                'cont' 'r*(uz+vr)+v' 'p' {'p1' 'p2'}};
fem.equ.shape = {[1 2 3] [1 2 4]};
fem.equ.weak{1} = {'uz_test*G1zz+ur_test*G1zr+vz_test*G1zr+...
                    vr_test*G1rr+v_test*F1+p1_test*cont'};
fem.equ.weak{2} = {'uz_test*G2zz+ur_test*G2zr+vz_test*G2zr+...
                    vr_test*G2rr+v_test*F2+p2_test*cont'};

%%%%% PDE boundary conditions %%%%%
fem.bnd.ind = {[1] [2] [3] [4] [5] [6]};
fem.bnd.shape = {[1 2 3] [1 2 3] [1 2 3 4] [1 2 3] [1 2 4] [1 2 4]};
fem.bnd.constr = {{'u-G*z' 'v+0.5*G*r' 0 0} {'u' 0 0 0} {0 0 0 0}...
                  {'v' 0 0 0} {'u' 0 0 0} {'v' 0 0 0}};
fem.bnd.weak = {0 0 '-1/Ca*(kappa2L_rz(s)+kappa2L_rt(s))*(nz*u_test+nr*v_test)' 0 0 0};
fem.pnt.ind = {[3 5] [2 4] [1]};
fem.pnt.shape = {[1 2 3] [1 2 3 4] [1 2 4]};
fem.pnt.constr = {{0 0 0 0} {0 0 0 0} {0 0 0 'p2'}};
```

B.3 Curvature projection onto test function

When implementing the weak form of Eq. (B.9) in the code the curvature term $r\kappa$ was added as a user defined function, see Sec. XXX. It is however possible to implement the term using the weak formulation and the definition Eq. (4.17). This concept was first thought off by fellow PhD student and FEM guru Laurits H. Olesen. As in Eq. (B.9) we

have

$$\begin{aligned}
&\int_{\partial\Omega} \varphi_{il} n_j (\Gamma_{lj1} - \Gamma_{lj2}) \, \mathrm{d}\ell = \int_{\partial\Omega} \varphi_{il} \frac{1}{Ca} (r\kappa) n_j \, \mathrm{d}\ell \\
=&\int_{\partial\Omega} \varphi_{il} \frac{1}{Ca} (r\kappa) n_j \, \mathrm{d}\ell = \frac{1}{Ca} \int_{\partial\Omega} \varphi_{il} r \left(\frac{\partial t_j}{\partial \ell} + \kappa_{r\phi} \right) \, \mathrm{d}\ell \\
=&\frac{1}{Ca} \left[[t_j \varphi_{il} r]_{\min(\ell)}^{\max(\ell)} - \int_{\partial\Omega} t_j \frac{\partial r \varphi_{il}}{\partial \ell} \, \mathrm{d}\ell + \int_{\partial\Omega} \varphi_{il} n_2 \, \mathrm{d}\ell \right]
\end{aligned} \tag{B.10}$$

here we have used classical the result from 2D differential geometry $\partial \mathbf{t}/\partial \ell = \kappa_{rz}$ Eq. (4.17) and the fact that $r\kappa_{r\phi} = n_2$ Eq. (4.20). Note that Eq. (B.10) is only true for $l = 1, 2$ as $\Gamma_{j3k} = 0$. In the last step we have used integration by parts. The interface tangent is $\boldsymbol{t} = (t_1, t_2)$ and ℓ is the arc-length parameter. The first term in the last equation is zero when $r = 0$ at the symmetry z-axis and it has no influence at the symmetry line defined by the r-axis because of the Dirichlet constraints enforced here, see Fig. 6.13. Moreover, we have

$$\frac{\partial r \varphi_{il}}{\partial \ell} = t_2 \varphi_{il} + r \frac{\partial \varphi_{il}}{\partial \ell} \tag{B.11}$$

as $\partial \boldsymbol{x}/\partial \ell = \boldsymbol{t}$. Inserting Eq. (B.11) into Eq. (B.10) yields

$$\frac{1}{Ca} \left[\int_{\partial\Omega} t_j \left(t_2 \varphi_{il} + r \frac{\partial \varphi_{il}}{\partial \ell} \right) \, \mathrm{d}\ell + \int_{\partial\Omega} \varphi_{il} n_2 \, \mathrm{d}\ell \right] \tag{B.12}$$

where

$$\frac{\partial \varphi_{il}}{\partial \ell} = \boldsymbol{t} \cdot \nabla \varphi_{il} = t_1 \frac{\partial \varphi_{il}}{\partial z} + t_2 \frac{\partial \varphi_{il}}{\partial r}. \tag{B.13}$$

All in all this transformation may seem to complicate the problem more than simplifying it. Nonetheless, it is now possible to express the BC at the free surface in terms of the test functions φ_{il}, the surface normal, and the surface tangent. These quantities are all available internally to FEMLAB . The curvature which includes higher order derivatives of the interface shape has, by this method, been projected onto the test functions. The weak form of the boundary conditions and the governing equations are in FEMLAB script language given as:

```
%%%%% PDE system and parameters %%%%%
fem.const = {'Re' Re 'Ca' Ca 'e_mu' e_mu 'e_rho' e_rho 'G' G};
fem.sdim = {'z' 'r'};
fem.dim = {'u' 'v' 'p1' 'p2'};
fem.shape = {shlag(3,'u') shlag(3,'v') shlag(2,'p1') shlag(2,'p2')};

fem.form = 'weak';
fem.equ.expr = {'G1zz' 'r*(2*uz-p1)' 'G1rr'
                'r*(2*vr-p1)' 'G1zr' 'r*(ur+vz)'...
                'G2zz' 'r*(e_mu*2*uz-p2)' 'G2rr' 'r*(e_mu*2*vr-p2)'...
                'G2zr' 'r*e_mu*(ur+vz)' 'F1' '-p1+2*v/r'...
                'F2' '-p2+e_mu*2*v/r' 'cont' 'r*(uz+vr)+v' 'p' {'p1' 'p2'}};
fem.equ.shape = {[1 2 3] [1 2 4]};
fem.equ.weak{1} = {'uz_test*G1zz+ur_test*G1zr+vz_test*G1zr+vr_test*G1rr+...
                    v_test*F1+p1_test*cont'};
fem.equ.weak{2} = {'uz_test*G2zz+ur_test*G2zr+vz_test*G2zr+vr_test*G2rr+...
                    v_test*F2+p2_test*cont'};

%%%%% PDE boundary conditions %%%%%
fem.bnd.ind = {[1] [2] [3] [4] [5] [6]};
fem.bnd.expr = {'phi_u' '(tr*u_test+r*(tz*uz_test+tr*ur_test))*nz' ...
                'phi_v' '(tr*v_test+r*(tz*vz_test+tr*vr_test))*nr'};
fem.bnd.shape = {[1 2 3] [1 2 3] [1 2 3 4] [1 2 3] [1 2 4] [1 2 4]};
fem.bnd.constr = {{'u-G*z' 'v+0.5*G*r' 0 0} {'u' 0 0 0} {0 0 0 0}...
                  {'v' 0 0 0} {'u' 0 0 0} {'v' 0 0 0}};
fem.bnd.weak = {0 0 ['1/Ca*(tz*tr*u_test+r*uTz_test + tr*tr*v_test+r*vTr_test)' '+' ...
                     '1/Ca*nr*(nz*u_test+nr*v_test)'] 0 0 0};
fem.pnt.ind = {[3 5] [2 4] [1]};
fem.pnt.shape = {[1 2 3] [1 2 3 4] [1 2 4]};
fem.pnt.constr = {{0 0 0 0} {0 0 0 0} {0 0 0 'p2'}};
```

The implementation of the free interface boundary condition in this "projection" formulation was mostly a small FEM experiment. One result obtained for the drop in extensional flow, with $Ca = 0.1$ and $\epsilon_\mu = 10^{-3}$, is compared with the standard method in Fig. B.2. The circles are the projection results and the line the standard results. Steady state was reached after 250 and 80 time steps, respectively, as the time step parameter δ_t had to be chosen three times smaller to ensure stability in the projection method. Anyhow, the two solutions were in quite good agreement

For simulations of systems with large capillary numbers the projection method agreed with the standard method but a lot of numerical noise was introduced for longer runs (large times t). In the case of small capillary numbers the projection method was unstable and noisy even for short times. The problem most certainly lies with un-physical amplification of interface wiggles. The comparison was done with the same grid and time stepping parameters.

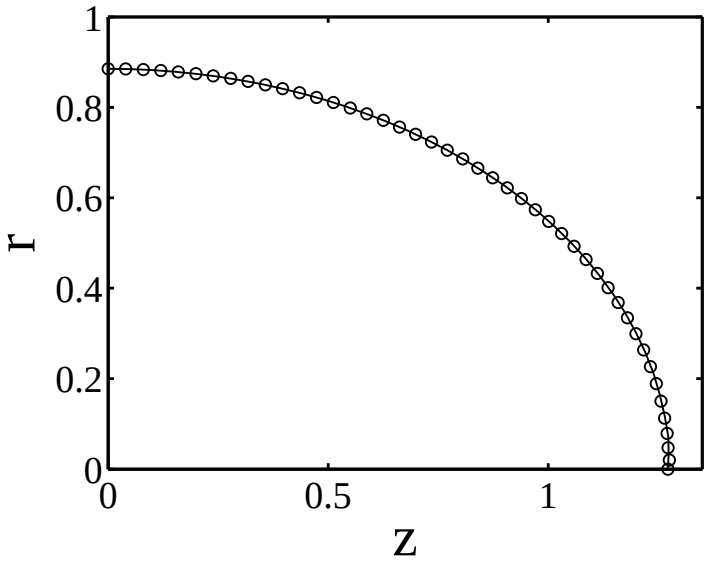

Figure B.2: Comparison of the projection (circles) and the standard (full line) method to handle the curvature at the free interface.

Appendix C

Paper published in J. Micromech. Microeng., 2004

Title
The clogging pressure of bubbles in hydrophilic microchannel contractions

Authors
Mads Jakob Jensen, Goran Goranović, and Henrik Bruus

Reference
J. Micromech. Microeng. **14**, 876 (2004).

INSTITUTE OF PHYSICS PUBLISHING JOURNAL OF MICROMECHANICS AND MICROENGINEERING

J. Micromech. Microeng. **14** (2004) 876–883 PII: S0960-1317(04)72206-8

The clogging pressure of bubbles in hydrophilic microchannel contractions

Mads Jakob Jensen, Goran Goranović and Henrik Bruus

MIC—Department of Micro and Nanotechnology, Technical University of Denmark, Oersteds Plads, Bldg. 345 East, DK-2800 Kgs. Lyngby, Denmark

E-mail: mjj@mic.dtu.dk

Received 19 November 2003
Published 13 May 2004
Online at stacks.iop.org/JMM/14/876
DOI: 10.1088/0960-1317/14/7/006

Abstract

We present a theoretical and numerical study of the quasi-static motion of large wetting bubbles in microfluidic channels with contractions. In most cases the energy of a bubble increases when it is moved from a wide channel to a narrow one, and the bubble thus tends to clog the flow of the fluid. A certain pressure, the so-called clogging pressure, is needed to push the bubbles out of the contraction. However, we show that in the case of a hydrophilic channel contraction there exists a range of parameter values where the bubble actually gains energy by moving into the narrow part. For these specific cases we analyze how the clogging pressure depends on channel geometry, surface tension and contact angle. Based on our analysis we establish design rules for minimizing the clogging pressure of microchannel contractions.

1. Introduction

Many microfluidic networks on modern lab-on-a-chip devices contain channel contractions. These tend to become problematic if, as is often the case, gas bubbles are introduced into the liquid at the inlets or by electrochemical processes. Due to the small channel dimensions gas bubbles can easily be large enough to span the entire channel cross-section. Such 'large' bubbles are prone to get stuck at the channel contraction, whereby they can clog the flow and disturb measurements or functionality of the system in an uncontrolled manner. To clear the clogged channel an external pressure, the so-called clogging pressure, has to be applied to push the clogging bubble out of the system. Although already identified nearly a decade ago [1, 2], this important problem in microfluidic systems has not been studied theoretically to a wide extent, a situation we would like to amend with this paper. The present work is a substantial extension of a preliminary and specialized study presented at the NanoTech 2003 conference [3], now including an analysis of the bubble energies in general cases, inclusion of compressibility effects and the use of different parameter values.

A complete analysis of the motion of a large bubble through a microchannel contraction involves many different physical effects, some which are not completely understood. Any comprehensive analysis would at least require detailed modeling of the liquid–gas, liquid–solid and solid–gas interfaces as well as the dynamics in the bulk fluids. But also more complicated processes near the contact lines need to be addressed, e.g. wetting [4–6], contact line pinning and hysteresis [4, 7], dynamic contact angles and contact lines [8–10] and static and dynamic friction [11–13]. It should be stressed that many of these surface effects are hard to control precisely, therefore dynamical systems where the lubrication assumption is used are also widely analyzed [14, 15].

In this work, however, we will restrict our analysis to quasi-static motion of bubbles. By this we mean that the velocity of the bubble is nearly zero and that the entire model system remains arbitrarily close to equilibrium for all bubble positions. All dynamic aspects are thus neglected, and basically the model involves only the free energy of the internal interfaces of the system and external pressures. This is motivated by the fact that it is difficult to experimentally control surface related properties. We thus only study geometry related effects. We also choose to work only with axisymmetric channels of smooth (but otherwise arbitrary) contraction geometries free from any sharp corners and other singularities. With these simplifications the forces or pressures needed to push a bubble through the system can be calculated accurately without losing the essential physics of

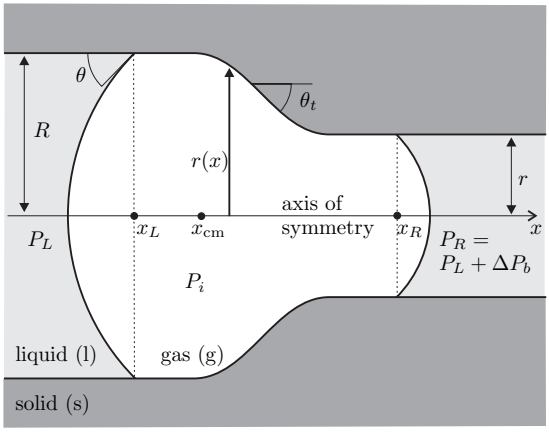

Figure 1. A bubble with internal pressure P_i and center of mass x_cm in a hydrophilic axisymmetric channel. The left (right) contact line has the coordinate x_L (x_R) and contact angle θ. The channel is contracting from a straight part of radius R to one of radius r. The specific channel profile is defined by some function $r(x)$. Throughout this paper we have chosen $r(x)$ to be a sloped straight line joined to the straight parts by two circle arcs. The tapering angle θ_t is given by $\tan\theta_\mathrm{t} = -r'(x)$. The pressure left (right) of the bubble is denoted as P_L (P_R) and the pressure difference across the bubble is ΔP_b.

the problem. This in turn enables us to formulate design rules for microchannel contractions to prevent or reduce clogging. To our knowledge similar analyses have only been made on channels of constant cross-sections [16] and for the special case of sudden contractions [17].

2. The model and basic physical assumptions

Consider a hydrophilic microfluidic channel or capillary, such as the one depicted in figure 1, which is axisymmetric about the x axis with a position dependent channel radius $r(x)$. The channel is filled with a liquid. A large bubble of some other fluid (we think mainly of a gas such as air) is present in the liquid. By large we mean that the volume of the bubble is larger than the volume $V_\mathrm{sph}^\mathrm{max}$ of the largest inscribed sphere that can be placed anywhere in the microchannel. A large bubble divides the liquid into two disconnected parts, left and right of the bubble. The bubble itself consists of a bulk part in direct contact with the walls of the channel and of two menisci, in contact with the liquid, capping the ends of the bubble.

The bubble is assumed to be in quasi-static equilibrium. In that case it is relatively simple to combine mass conservation with geometric constraints to determine, as a function of the bubble position, the pressure drops over the two menisci needed to maintain this equilibrium. We define our central concept, the clogging pressure, as the maximum of the position dependent pressure drop across the bubble, i.e. the minimal external pressure that must be supplied to push the bubble through the microchannel.

2.1. The Young and Young–Laplace equations

Our model system consists of a solid channel containing a liquid and one large gas bubble. Therefore, the essential physical parameters are the three surface tensions (surface free energy per area) σ_lg, σ_sl and σ_sg for the liquid–gas, solid–liquid and solid–gas interfaces, respectively. In equilibrium the contact angle θ is determined by the surface tensions through the Young equation [18, 19]

$$\sigma_\mathrm{sg} - \sigma_\mathrm{sl} = \sigma_\mathrm{lg}\cos\theta. \tag{1}$$

In the following the contact angle is taken as the equilibrium angle or rather as an average contact angle. Because contact angle hysteresis is very sensitive to surface effects, we do not address these questions in this work.

To sustain a curved interface with the main radii of curvature R_1^c and R_2^c between a gas of pressure P_g and a liquid of pressure P_l, the pressure difference $\Delta P = P_\mathrm{g} - P_\mathrm{l}$ must obey the Young–Laplace equation [20]

$$\Delta P = \sigma_\mathrm{lg}\left(\frac{1}{R_1^\mathrm{c}} + \frac{1}{R_2^\mathrm{c}}\right) = 2\sigma_\mathrm{lg}\,\frac{\cos\theta}{r}, \tag{2}$$

where the last equation is applicable for a constant circular cross-section of radius r. We use the standard convention that these radii are taken as positive if the interface is concave when seen from the gas.

2.2. Isothermal motion and compressibility

In the rest of the paper we consider a 'large' bubble having the initial position '1' in the widest part of the channel. The initial volume is $V_1 = \gamma V_\mathrm{sph}^\mathrm{max}$, where $\gamma > 1$ and $V_\mathrm{sph}^\mathrm{max} = 4\pi r_1^3/3$, and the corresponding internal pressure is $P_{\mathrm{i},1}$. At a later stage the bubble is moved to a position '2', where the volume is V_2 and the internal pressure is $P_{\mathrm{i},2}$. In the quasi-static case the bubble motion is isothermal and hence the compressibility condition applies,

$$P_{\mathrm{i},1}V_1 = P_{\mathrm{i},2}V_2. \tag{3}$$

The pressure P_i within the bubble is given as the external pressure P_0 plus the pressure change ΔP across the curved interface, given by equation (2).

The most extreme compression is obtained by pressing a large bubble, which floats without geometrical constraints in a bulk liquid of pressure P_0, into a narrow circular channel of radius r. Combining equations (2) and (3) yields

$$\frac{V_1}{V_2} = \frac{P_{\mathrm{i},2}}{P_{\mathrm{i},1}} \approx \frac{P_{\mathrm{i},2}}{P_0} = 1 + \frac{2\sigma_\mathrm{lg}\cos\theta}{r\,P_0}. \tag{4}$$

For example, moving a large spherical air bubble in water ($\sigma_\mathrm{lg} = 0.0725\,\mathrm{J\,m^{-2}}$) at the ambient pressure $P_0 = 10^5\,\mathrm{Pa}$ into a channel of radius $r = 25\,\mu\mathrm{m}$ leads to $V_1/V_2 \approx 1.06$, i.e. a volume compression of 6%. Moving, as in section 6, a bubble from a $300\,\mu\mathrm{m}$ to a $190\,\mu\mathrm{m}$ wide channel yields a compression of about 0.2%.

In the case of laser ablated microchannels in plastic chips, compressibility effects are negligible as the smallest dimensions typically are greater than $100\,\mu\mathrm{m}$. However, for silicon based micro- or nanofluidic devices, compressibility may play a significant role.

2.3. Quasi-static motion and geometry

For a bubble positioned in a microchannel contraction, the total internal energy E_tot is the sum of the surface free energy, gravitational energy, kinetic energy and frictional energy. We regard the surrounding pressures as external energy. By our definition quasi-static motion of an incompressible bubble

implies that the kinetic energy is zero and friction is also zero because of hydrostatic and thermodynamic equilibrium. Finally, we treat channels of characteristic dimensions $2r$ less than $300\,\mu$m, which is significantly smaller than the capillary length of water, $\Delta_c = \sqrt{\sigma_{\rm lg}/\rho_{\rm l} g} \approx 2700\,\mu$m, where $\rho_{\rm l} = 10^3$ kg m^{-3} and $g = 9.82$ m/s^2. So the gravitational energy can also be neglected, which ensures that the menisci may be approximated by spherical caps.

The total internal energy $E_{\rm tot}$ of the microchannel containing a quasi-statically moving bubble is given only by the surface free energy, i.e. the sum of interfacial energies σ_i times interfacial areas A_i,

$$E_{\rm tot} = \sum_i \sigma_i A_i = \sigma_{\rm lg} A_{\rm lg} + \sigma_{\rm sg} A_{\rm sg} + \sigma_{\rm sl} A_{\rm sl}. \tag{5}$$

The pressure-related applied external force F needed to balance the bubble is given by the gradient of the total internal energy with respect to the center of mass coordinate of the bubble $x_{\rm cm}$. Hence

$$F = \frac{{\rm d}E_{\rm tot}}{{\rm d}x_{\rm cm}}, \tag{6}$$

which thus depends on the bubble position $x_{\rm cm}$ and, through the areas A_i, on the geometry of the channel.

2.4. The clogging pressure

The Young–Laplace pressure drops (cf equation (2)) at the menisci are given by,

$$\Delta P_{\rm L} = P_{\rm i} - P_{\rm L}, \tag{7a}$$

$$\Delta P_{\rm R} = P_{\rm i} - P_{\rm R}. \tag{7b}$$

The total pressure drop $\Delta P_{\rm b}(x_{\rm cm})$ over the bubble as a function of its center of mass $x_{\rm cm}$ is given by

$$\Delta P_{\rm b}(x_{\rm cm}) = P_{\rm R} - P_{\rm L} = \Delta P_{\rm L}(x_{\rm cm}) - \Delta P_{\rm R}(x_{\rm cm}). \tag{8}$$

The clogging pressure $P_{\rm clog}$ is defined as the maximal position dependent pressure drop across the bubble,

$$P_{\rm clog} = \max\{-\Delta P_{\rm b}(x_{\rm cm})\}. \tag{9}$$

The clogging pressure expresses the minimal amount by which the left-hand-side pressure $P_{\rm L}$ must exceed the right-hand-side pressure $P_{\rm R}$ to push the bubble through the contraction quasi-statically from left to right.

3. General energy considerations for axisymmetric microchannels

Consider a bubble placed in a cylindrical channel of radius R. We want to determine the change in energy resulting from moving it into a smaller channel of radius $r < R$, e.g. by moving it from left to right in the channel depicted in figure 1. Intuitively, we would expect the energy to increase as a result of the movement. In most cases this intuition is correct; however, we shall see that in some cases the system gains energy by the move, solely due to geometric conditions.

The bubble has the initial volume $V_1 = \gamma V_{\rm sph}^{\rm max}$, where $\gamma > 1$ and $V_{\rm sph}^{\rm max} = 4\pi R^3/3$. With this constraint the bubble is forced to touch the walls regardless of its position. According to equations (2) and (7*b*) the internal pressure of the bubble is

$$P_{\rm i,1} = P_{\rm R} + 2\sigma_{\rm lg}\frac{\cos\theta}{R}. \tag{10}$$

The volume of the bubble is the sum of two spherical cap volumes and the volume of a cylinder of initial length L. Once the length L is known, the relevant interfacial areas $A_{\rm lg}$ and $A_{\rm sg}$ may be found.

The gas bubble is now moved to the cylindrical channel of radius r, and according to equations (2), (3) and (7*b*) the pressure $P_{\rm i,2}$ and volume V_2 are

$$P_{\rm i,2} = P_{\rm R} + 2\sigma_{\rm lg}\frac{\cos\theta}{r}, \tag{11}$$

$$V_2 = \frac{P_{\rm i,1}}{P_{\rm i,2}}\,V_1. \tag{12}$$

By solving equation (12) it is straightforward to find the change in total free surface energy,

$$\Delta E_{\rm tot} = E_{\rm tot,2} - E_{\rm tot,1} = \sigma_{\rm lg}(A_{\rm lg,2} - A_{\rm lg,1}) + \sigma_{\rm lg} 2\pi\cos\theta(rl - RL), \tag{13}$$

where l is the length of the bubble in the channel of radius $r < R$ (situation 2). In equation (13) the Young relation (1) has been used to eliminate the solid–liquid and solid–gas interfacial energies.

Based on equation (13) we can analyze the energy change when moving the bubble from the wide channel of radius R to the narrow channel of radius r. First we give the limiting values of $\Delta E_{\rm tot}$. In the limit $r/R \to 1$ we obviously get $\Delta E_{\rm tot} \to 0$. In the opposite limit, $r/R \to 0$, the compressibility of the bubble results in convergence of $\Delta E_{\rm tot}$,

$$\lim_{\frac{r}{R}\to 0} \Delta E_{\rm tot} = \frac{\pi R^3}{3}\left(4\gamma R P_{\rm R} - \sigma_{\rm lg}\,\frac{4 + \sin(3\theta) - 3\tan\theta}{\cos^2\theta}\right). \tag{14}$$

To discuss $\Delta E_{\rm tot}$ for general values of r/R we use a numerical example: an air bubble in a water filled PMMA channel for which we have the parameter values $P_{\rm R} = 10^5$ Pa, $\sigma_{\rm lg} = 72.5$ mJ and $\theta = 72^\circ$. The radius ratio r/R and the volume parameter γ are then varied.

In figure 2 the energy $\Delta E_{\rm tot}$ (equation (13)) is plotted as a function of the ratio r/R for given values of γ. The figure shows that for large values of γ, i.e. large bubbles, it requires energy ($\Delta E_{\rm tot} > 0$) to move the bubble from the wide to the narrow channel. However, there exists a critical value $\gamma_{\rm c} \approx 4.75$ below which the system can gain energy by moving the bubble, if the radius ratio r/R is not too small. This behavior is generic for a bubble in a contracting channel, but the specific shape of the curve and the optimal minimum depend on the material parameters and the external pressure $P_{\rm R}$.

The critical value $\gamma_{\rm c}$, above which energy gain is impossible, is given by $\partial\Delta E_{\rm tot}/\partial(r/R) = 0$ at $r/R = 1$,

$$\gamma_{\rm c} = \frac{(3 - \cos(3\theta) + 2\sin\theta)(2\sigma_{\rm lg}\cos\theta + RP_0)}{2RP_{\rm R}\cos\theta(1 + \sin\theta)}. \tag{15}$$

Figure 3 depicts the energy $\Delta E_{\rm tot}$ as a function of the ratio r/R for $\gamma = 1$ and $\gamma = 3$, and for five values of the wide channel radius, $R = 100$, 150, 200, 250 and $300\,\mu$m.

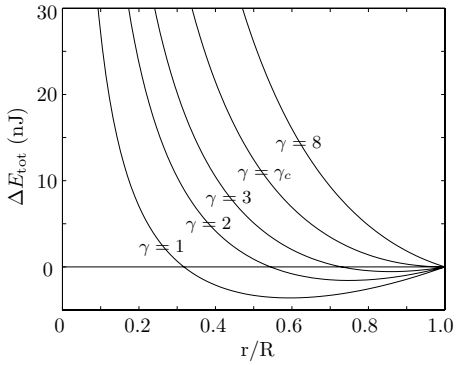

Figure 2. Plot of the energy change $\Delta E_{\rm tot}$ as a function of the ratio r/R. The bubble is moved from a wide channel of radius $R = 150\,\mu$m to a narrow channel of radius r. Five curves are shown corresponding to the volume ratio $\gamma = 1, 2, 3, \gamma_c$ and 8, respectively. $\gamma_c \approx 4.75$. For 'small' volumes $1 \leqslant \gamma < \gamma_c$ the system can gain energy by moving the bubble to the narrow channel, if the width of the latter is not too small. For $\gamma > \gamma_c$ the movement requires energy in all cases.

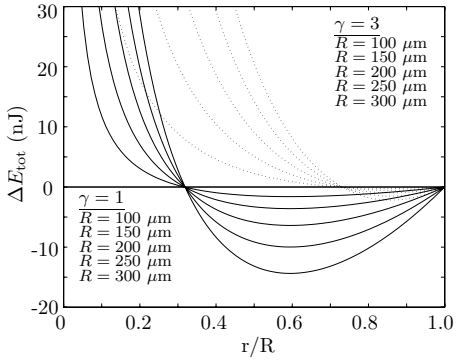

Figure 3. The energy $\Delta E_{\rm tot}$ as a function of the ratio r/R for different values of the wide channel radius, $R = 100, 150, 200, 250$ and $300\,\mu$m. The plain curves correspond to the smallest bubble for $\gamma = 1$ and the dotted curves correspond to a larger bubble with $\gamma = 3$.

From equation (13) it may be seen that $\min\{\Delta E_{\rm tot}\} \propto R^2$ as the area is proportional to R^2 and L is proportional to R. Deviations from this proportionality arise for small values of R because of compressibility. For $\gamma = 1$ in figure 3 we find $\max\{-\Delta E_{\rm tot}\} = kR^2$ with $k = 0.159\,\mathrm{J\,m^{-2}}$. This proportionality is illustrated as the energy at a given r/R point is increased by a factor 4 when R is doubled, e.g. from $R = 150\,\mu$m to $R = 300\,\mu$m.

The previous calculations clearly show that for some geometries it is favorable to place the bubble in the narrow rather than in the wide part of the channel. In the following we shall address the question of whether for such geometries the bubble will move spontaneously or it must cross an energy barrier to arrive at the low-energy state in the narrow channel.

4. Analytical results for contractions with energy gain

Combining the geometry defined in figure 1 with equations (2) and (8), the central expression of our analysis is easily derived,

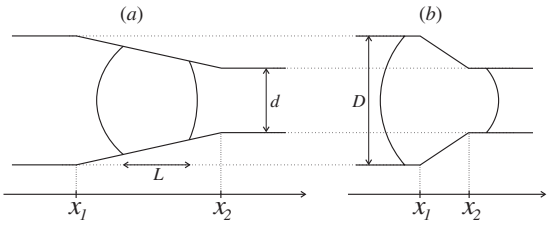

Figure 4. Two generic situations for a bubble of length $L = x_{\rm R} - x_{\rm L}$ near a microchannel contraction of length $x_2 - x_1$. (*a*) The contraction is long enough to contain the entire bubble, i.e. $x_{\rm R} - x_{\rm L} < x_2 - x_1$. (*b*) The contraction is so short that the bubble can span it completely, i.e. $x_{\rm R} - x_{\rm L} > x_2 - x_1$, which is a class β_4 bubble.

$$\Delta P_{\rm b} = 2\sigma_{\rm lg}\left(\frac{\cos[\theta - \theta_{\rm t}(x_{\rm L})]}{r(x_{\rm L})} - \frac{\cos[\theta + \theta_{\rm t}(x_{\rm R})]}{r(x_{\rm R})}\right). \quad (16)$$

From the discussion in section 2.4 it follows that if $\Delta P_{\rm b} < 0$ then the contraction causes bubble clogging, whereas for $\Delta P_{\rm b} > 0$ the bubble tends to move spontaneously through the contraction toward the narrow part.

Based on equation (16) a number of design rules may be established specifying the geometric features that may prevent or decrease clogging. Consider a bubble that starts out in the wide straight section left of the contraction, where it has a length $L_0 = x_{\rm R} - x_{\rm L}$. The pressure drop $\Delta P_{\rm b}$ is zero to begin with, but depending on the shape of the contraction, such as the two examples shown in figure 4, $\Delta P_{\rm b}$ changes as the bubble advances quasi-statically through the contraction.

The first part of any contraction can always be approximated by a circle with an arc angle which is the local tapering angle $\theta_{\rm t}$. As the right contact line $x_{\rm R}$ just enters the contraction, equation (16) can be expanded to first order in $\theta_{\rm t}$ yielding

$$\Delta P_{\rm b} \approx \frac{2\sigma_{\rm lg}\sin\theta}{R}\,\theta_{\rm t} > 0. \quad (17)$$

Thus initially the bubble tends to move spontaneously into the contraction. The physical reason for this is that the local tapering angle allows the meniscus to flatten a little, which reduces the costly gas–liquid interface energy.

Once the bubble moves inside the contraction defined in figure 1, a complicated interplay between the initial bubble length L_0, the contact angle θ, the channel radii $r(x_{\rm L})$ and $r(x_{\rm R})$ at the contact lines and the local tapering angle $\theta_{\rm t}(x)$ decides whether bubble clogging occurs or not. We classify our systems into two main classes:

Class α comprises all cases where no clogging occurs, i.e. where the bubble can move spontaneously through the contraction without applying an external pressure.

Class β contains all cases with clogging, i.e. where $\Delta P_{\rm b} < 0$ at some point or, equivalently, where $P_{\rm clog} > 0$.

For class β four sub-classes can be identified depending on where the bubble is when $\Delta P_{\rm b}$ becomes negative and clogging occurs. This bubble position is classified by the position of the contact lines $x_{\rm L}$ and $x_{\rm R}$ relative to the beginning x_1 and the end x_2 of the contraction region (see figures 1 and 4):

$$\begin{array}{lrcl}
\text{class } \beta_1: & x_{\rm L} < x_1 & \text{and} & x_1 < x_{\rm R} < x_2, \\
\text{class } \beta_2: & x_1 < x_{\rm L} < x_2 & \text{and} & x_1 < x_{\rm R} < x_2, \\
\text{class } \beta_3: & x_1 < x_{\rm L} < x_2 & \text{and} & x_2 < x_{\rm R}, \\
\text{class } \beta_4: & x_{\rm L} < x_1 & \text{and} & x_2 < x_{\rm R}.
\end{array} \quad (18)$$

Table 1. Physical parameters for air bubbles in water flowing through PMMA microchannels.

Parameter values	Reference
$\sigma_{lg} = 72.5 \times 10^{-3}\,\mathrm{J\,m^{-2}}$	[21]
$\sigma_{sg} = 38.9 \times 10^{-3}\,\mathrm{J\,m^{-2}}$	[21]
$\sigma_{sl} = 16.5 \times 10^{-3}\,\mathrm{J\,m^{-2}}$	[21]
$\theta = 72^{\circ}$	[18]

A detailed analysis of equation (16) yields important relations for some of the clogging classes.

A β_2 clogging only occurs if the bubble can move entirely within the tapered region as shown in figure 4(*a*), and if at some point it has a length $L = x_L - x_R$ such that

$$L > \frac{r(x_L)}{\tan\theta_t}\left[1 - \frac{\cos(\theta - \theta_t)}{\cos(\theta + \theta_t)}\right]. \tag{19}$$

In β_4 where the bubble in fact spans the entire contraction as sketched in figure 4(*b*), there is always clogging and the clogging pressure is maximal. The value for ΔP_b is negative and independent of the shape of the contraction. From equation (16) we get

$$\Delta P_b = 2\sigma_{lg}\cos\theta\left(\frac{1}{R} - \frac{1}{r}\right) < 0. \tag{20}$$

The nonclogging class α will in general occur if the bubble is small enough. According to the class β_4 analysis a necessary (but not sufficient) condition for avoiding clogging is that the bubble is small enough to be completely contained in the contraction region. An analysis of the β_2 and β_3 classes shows that it should also be short enough to avoid clogging while the left meniscus is still in the tapered region. The β_1 class furthermore puts upper limits on tapering angles that allow for clog-free flow. Examples from class α and β_4 are treated further by detailed numerical analysis in sections 5.2 and 5.3.

5. Numerical simulations

To illustrate the analysis given above a detailed simulation is made in the following. The aim is to minimize the clogging pressure ΔP_b with respect to a given parameter. We are limiting our analysis so that the variation comprises only one parameter: the tapering angle θ_t.

5.1. The numerical algorithm

In order to find the force and clogging pressure acting on a large bubble for a given geometry, a semianalytical model of the contracting channel is implemented in MatLab. A numerical Romberg integration scheme is used together with a Newton solver to determine the location of the right and left contacts line (x_R and x_L) for a given position of the center of mass coordinate x_{cm}. The respective interface areas A_i are then found. For a specific geometry defined through $r(x)$, the maximal force is found through equations (5) and (6) and the pressure drop ΔP_b is found through equation (16). The heaviest calculation ran for approximately 4 h on a standard PC.

To be specific we use the geometry defined in figure 1 and take PMMA as the solid material, water as the liquid and air as the gas. This configuration has the physical parameters given in table 1.

5.2. A specific system without clogging, class α

The first example is the system with a bubble placed in a relatively gentle contraction depicted in figure 5. The total length of the channel is 1000 μm. The wide straight channel to the left has a radius $R = 150$ μm and length 200 μm. The contraction has a length $x_2 - x_1 = 350$ μm and circle arc lengths of 30 μm, which results in a tapering angle $\theta_t = 10^{\circ}$. The narrow straight channel to the left has a radius $r = 95$ μm and length 500 μm. The bubble starts out in the wide channel to the left. It has a relative volume of $\gamma = 1.02$ (cf section 3) and an initial length $L_0 = 180$ μm.

Figure 5 shows the bubble at five different positions (*a*)–(*e*). As the bubble advances through the channel it is seen how its length $x_R - x_L$ changes and how the curvatures of the menisci vary. The black dots inside the bubble indicate the center of mass x_{cm}.

In figure 6(*a*) the total internal energy of the system is plotted as a function of center of mass position x_{cm}. The zero point of the energy is chosen as the energy of the system when the entire bubble is positioned completely within the narrow part of the channel. The five positions (*a*)–(*e*) in figure 5 are also marked here.

It is seen that the energy decreases monotonically. This means that without a negative external pressure holding it back, it would move spontaneously through the channel from the left to the right. As long as the bubble moves completely within the wide part of the channel, the energy is constant (about 4 nJ). Then as the right edge enters the contraction, position (*a*), the energy drops rapidly in accordance with the pressure drop equation (17). This trend continues as the entire bubble moves inside the contraction, as is the case in position (*b*). The energy continues to drop, but now less rapidly, as the right edge of the bubble enters the narrow channel, see position (*c*). However, as the left bubble edge approaches the narrow channel, the energy drop picks up again, see position (*d*). Finally, the bubble moves completely inside the narrow section and the energy becomes zero (per definition), see position (*e*).

In figure 6(*b*) the corresponding balancing external force F from equation (6), and the clogging pressure across the bubble $-\Delta P_b$, equation (16), are plotted as functions of x_{cm}. The balancing external force is seen to be negative, which means that to maintain the bubble at quasi-static equilibrium, it is necessary to hold it back. Without this force, the bubble would of course, as mentioned above, move spontaneously toward the narrow segment. At position (*c*) where the right edge of the bubble enters the narrow channel, both force and pressure reach local maxima, but even here they are both negative. No clogging occurs in this system, and it therefore belongs to class α as defined in section 4.

5.3. A specific channel with clogging, class β_4

The second example is nearly the same as the first. Only the length of the contraction region has been reduced from 350 μm to 180 μm. This leads to an increase of the tapering angle from 10° to $\theta_t = 20^{\circ}$. In figure 7 four positions (*a*)–(*d*) of the large bubble are depicted. Note that since $\theta + \theta_t = 92^{\circ}$, the right meniscus in the tapered section of the channel in panel (*a*) is nearly flat. In fact it has a slight inward bend.

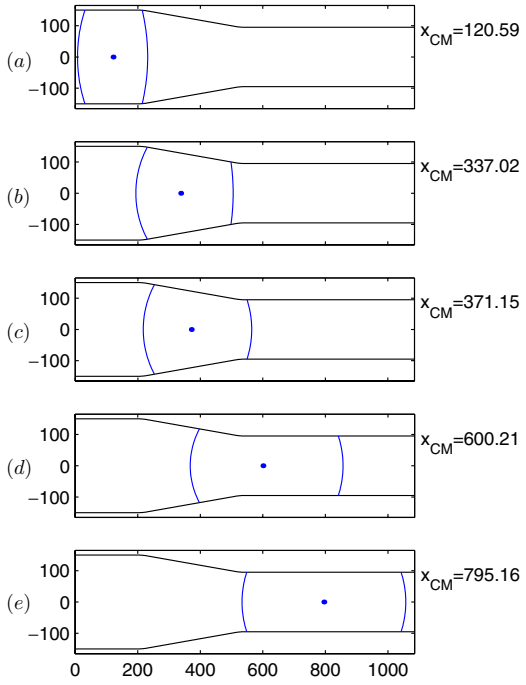

Figure 5. Five positions (*a*)–(*e*) of a large bubble with $\gamma = 1.02$ inside a 1000 μm long hydrophilic channel with a tapering angle $\theta_t = 10^\circ$. The black dots indicate x_{cm}. The contact angle is $\theta = 72^\circ$.

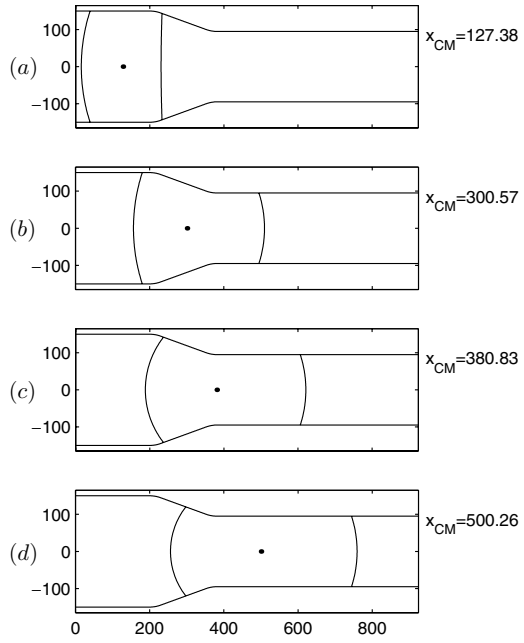

Figure 7. Four positions (*a*)–(*d*) of a bubble with $\gamma = 1.02$ inside a 1000 μm long hydrophilic channel with the tapering angle $\theta_t = 20^\circ$. The black dots indicate x_{cm}. The contact angle is $\theta = 72^\circ$.

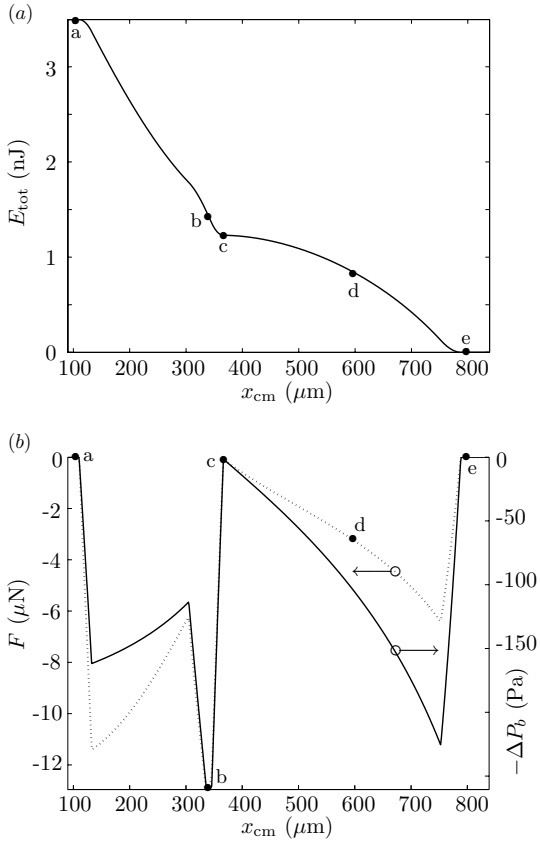

Figure 6. (*a*) A plot of the total internal energy E_{tot} versus the center of mass coordinate x_{cm} for the same bubble as in figure 5. (*b*) The balancing external force F and the pressure drop across the bubble ΔP_b versus x_{cm}. The five dots correspond to the five bubble positions in figure 5. Note that $-\Delta P_b < 0$ for all positions, i.e. no clogging occurs (a class α system).

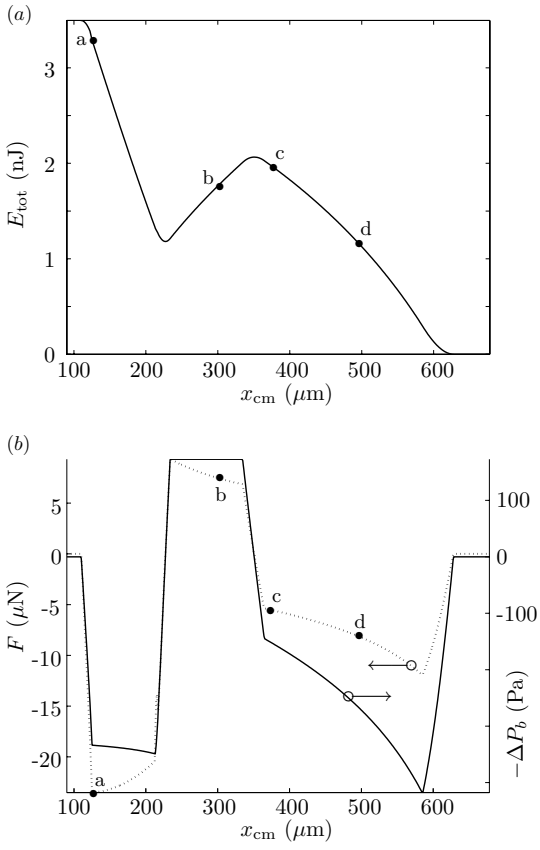

Figure 8. (*a*) A plot of the total internal energy E_{tot} versus the center of mass coordinate x_{cm} for the same bubble as in figure 7. (*b*) The balancing external force F and the pressure drop across the bubble ΔP_b versus x_{cm}. The four dots correspond to the four bubble positions in figure 7. Note that $-\Delta P_b > 0$ for x_{cm} around 300 μm, i.e. clogging occurs (a class β system).

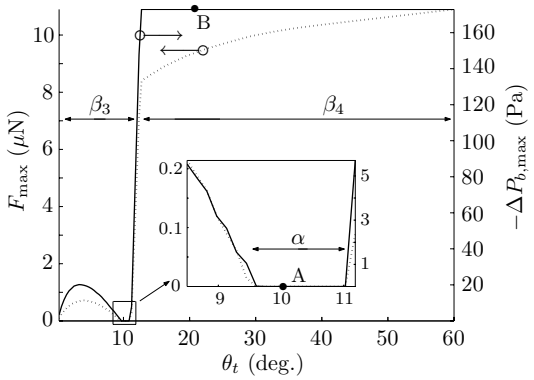

Figure 9. The maximal balancing force $F_{\max}$ and clogging pressure $P_{\text{clog}} = -\Delta P_{\text{b,max}}$ plotted as functions of the tapering angle θ_{t}. Detailed figures illustrating the situation for $\theta_{\text{t}} = 10^\circ$ (marked A) are given in figures 6(*a*) and (*b*), and for $\theta_{\text{t}} = 20^\circ$ (marked B) in figures 8(*a*) and (*b*). The β_3, β_4 and α classes are described in section 4. The maximal clogging pressure occurs in class β_4. It is found by equation (20) to be $P_{\text{clog}} = 173$ Pa.

In figure 8(*a*) the energy is shown as a function of x_{cm}. The four positions (*a*)–(*d*) are also marked. We immediately note a qualitative difference between this graph and that in figure 6(*a*). The energy no longer drops monotonically but exhibits a marked increase between positions (*b*) and (*c*). This corresponds to the case where the bubble spans the entire contraction, i.e. the left bubble edge is still in the wide channel segment when the right edge enters the narrow segment.

This effect is of course also visible in figure 8(*b*) where the balancing external force F and the clogging pressure $-\Delta P_{\text{b}}$ are plotted as functions of x_{cm}. Around position (*b*) both F and $-\Delta P_{\text{b}}$ become positive, which means that external pressure forces need to be applied to move the bubble through the system. Using equation (20) the clogging pressure is found to be 173 Pa. Without this external force the bubble would tend to move backwards out of the channel, i.e. the system is clogging, and in fact it is an example of class β_4 clogging.

5.4. Clogging pressure versus tapering angle $\boldsymbol{\theta_t}$

The previous two examples showed the behavior for a particular channel contraction from $R = 150\,\mu$m to $r = 95\,\mu$m with tapering angles $\theta_{\text{t}} = 10^\circ$ and 20°, respectively. We now extend this analysis to the entire interval $0^\circ < \theta_{\text{t}} < 60^\circ$. For each tapering angle we calculate the maximal external force F and the clogging pressure P_{clog}. The result is shown in figure 9.

The graph clearly shows that some tapering angles ease the passage of bubbles. For the geometrical configuration defined by $R = 150\,\mu$m, $r = 95\,\mu$m and $C = 30\,\mu$m a small window, the interval $9.5^\circ < \theta_{\text{t}} < 11^\circ$, with optimal tapering angles can be identified. In this window $P_{\text{clog}} < 0$ corresponding to the clogging-free class α behavior.

For angles greater than about 11° the maximal force is seen to increase dramatically. This transition corresponds to a configuration where the bubble can span the entire contraction region, i.e. class β_4. We clearly see that once the bubble is able to span the entire contraction, the specific geometry of the contraction (in this case the tapering angle) plays no role. We get the same clogging pressure, $P_{\text{clog}} = 173$ Pa.

Finally, we note, that class β_3 behavior sets in for small tapering angles below 9.5°. A small clogging pressure is observed, less than 30 Pa.

6. Conclusion

The effects of geometry on the quasi-static motion of large bubbles through a hydrophilic microchannel (capillary) contraction are modeled. The simplicity of the model leads to a good physical understanding of bubble clogging. We have shown that in most cases it requires energy to move a bubble from a wide to a narrow channel. However, we have also found that certain bubble sizes and specific channel geometries lead to a gain in energy.

We have specifically studied the contractions where such an energy gain is achieved. Using the central equation for the pressure drop ΔP_{b} across the bubble, equation (16), we analyzed a specific contracting axisymmetric hydrophilic channel, and we identified four different classes, denoted as β_1 to β_4, leading to bubble clogging, and one clogging-free class denoted as α. The details of the analysis are quite complicated due to the large number of parameters: the tapering angle θ_{t}, the contact angle θ, the initial bubble length L_0, the radii R and r of the wide and narrow channel segments, etc. However, one general trend is clear. The tendency for clogging increases as the bubbles become larger.

Based on our analysis, some important design rules can be established for making microchannel contractions with minimal or even vanishing clogging pressures. These rules only apply for channel contractions where the energy is lowest in the narrow part.

First, if the typical size L_0 of the bubbles present in the microfluidic system is known, it is important to design contractions which are larger than L_0. The highest clogging pressures occur namely for bubbles spanning the entire contraction, the so-called β_4 class.

Second, the combined effect of the tapering angle and contact angle has to be taken into account to make sure that L_0 is shorter than the critical length leading to clogging of class β_2 being entirely within the tapered region.

Third (not presented here), to smoothen out and lower any unavoidable positive clogging pressure, it helps to make the curved parts of the contraction as large as possible, thus decreasing their curvature.

The method of analyzing the bubble clogging problem in microchannels presented in this paper is very general. It is straightforward to extend it to other geometries (such as nonmonotonic contractions) and to hydrophobic microchannels. With the presented design rules at hand it is possible to design a system that may filter or sort bubbles of different volumes—one simply places contractions with different tapering angles in properly arranged series. A comparable system designed to sort bubbles is presented in [17]. The model may also be extended to include wetting layers as used in [16], and it may be used to model two phase flows in porous media as in [22, 23]. Some of the dynamical effects such as those briefly mentioned in the introduction may be included as well.

Acknowledgments

This work is partly supported by the Danish Technical Research Council, μTAS Frame Program Grant no 26-00-0220.

References

[1] Gravesen P, Branebjerg J and Søndergård Jensen O 1993 *J. Micromech. Microeng.* **3** 168
[2] Elwenspoek M, Kannerubj T S, Miyake R and Fluitman J H J 1994 *J. Micromech. Microeng.* **4** 227
[3] Jensen M J, Goranović G and Bruus H 2003 *Proc. NanoTech 2003* (*San Francisco, USA, Feb. 2003*) vol 1 258–61
[4] de Gennes P G 1985 *Rev. Mod. Phys.* **57** 827
[5] Brochard-Wyart F and de Gennes P G 1992 *Adv. Colloid Interface Sci.* **39** 1
[6] Stoev K, Ramé E, Leonhardt T and Garoff S 1998 *Phys. Fluids* **10** 1793
[7] Raphaël E and de Gennes P G 1989 *J. Chem. Phys.* **90** 7577
[8] Dussan E B, Ramé V E and Garoff S 1991 *J. Fluid Mech.* **230** 97
[9] de Gennes P G, Hua X and Levinson P 1990 *J. Fluid Mech.* **212** 55
[10] Pismen L M and Rubinstein B Y 2001 *Langmuir* **17** 5265
[11] Tenan M A, Hackwood S and Beni G 1982 *J. Appl. Phys.* **53** 6687
[12] Parlange J-Y 1983 *J. Appl. Phys.* **54** 6744
[13] Schwartz A M, Rader C A and Huey E 1964 *Adv. Chem. Ser.* vol 43 ed R F Gould (Washington, DC: American Chemical Society) p 250
[14] Bretherton F P 1961 *J. Fluid Mech.* **10** 97
[15] Ratulowski J and Chang H -C 1989 *Phys. Fluids* A **1** 97
[16] Bico J and Quéré D 2002 *J. Fluid Mech.* **467** 101
[17] Tordeux C and Fournier J -B 2002 *Europhys. Lett.* **60** 875
[18] Adamson A W and Gast A P 1997 *Physical Chemistry of Surfaces* 6th edn (New York: Wiley)
[19] Probstein R F 1994 *Physiochemical Hydrodynamics: An Introduction* 2nd edn (New York: Wiley)
[20] Batchelor G K 2000 *An Introduction to Fluid Dynamics* (Cambridge: Cambridge University Press)
[21] Jańczuk B, Bialopiotrowicz T and Zdziennicka A 1999 *J. Colloid Interface Sci.* **211** 96
[22] Zha F F, Fane A G, Fall C J D and Schofield R W 1992 *J. Membr. Sci.* **75** 69
[23] Bear J 1998 *Dynamics of Fluids in Porous Media* (New York: Dover)

Appendix D

Paper published in J. Micromech. Microeng., 2005

Title
A novel electroosmotic pump design for nonconducting liquids:
theoretical analysis of flow rate-pressure characteristics and stability

Authors
Anders Brask, Goran Goranović, Mads Jakob Jensen, and Henrik Bruus

Reference
J. Micromech. Microeng. **15**, 883 (2005).

INSTITUTE OF PHYSICS PUBLISHING JOURNAL OF MICROMECHANICS AND MICROENGINEERING
J. Micromech. Microeng. **15** (2005) 883–891 doi:10.1088/0960-1317/15/4/029

A novel electro-osmotic pump design for nonconducting liquids: theoretical analysis of flow rate–pressure characteristics and stability

Anders Brask, Goran Goranović, Mads Jakob Jensen and Henrik Bruus

MIC—Department of Micro and Nanotechnology, Technical University of Denmark, Oersteds Plads, Bldg. 345 East, DK-2800 Kgs. Lyngby, Denmark

E-mail: abr@mic.dtu.dk

Received 30 November 2004, in final form 26 January 2005
Published 11 March 2005
Online at stacks.iop.org/JMM/15/883

Abstract
We present the design and theoretical analysis of a novel electro-osmotic (EO) pump for pumping nonconducting liquids. Such liquids cannot be pumped by conventional EO pumps. The novel type of pump, which we term the two-liquid viscous EO pump, is designed to use a thin layer of conducting pumping liquid driven by electro-osmosis to drag a nonconducting working liquid by viscous forces. Based on computational fluid dynamics, our analysis predicts a characteristic flow rate of the order nL/s/V and a pressure capability of the pump in the hPa/V range depending on, of course, achievable geometries and surface chemistry. The stability of the pump is analyzed in terms of the three instability mechanisms that result from shear-flow effects, electrohydrodynamic interactions and capillary effects. Our linear stability analysis shows that the interface is stabilized by the applied electric field and by the small dimensions of the micropump.

1. Introduction

Electro-osmotic (EO) pumps are suitable for microfluidic applications due to their integrability and compatibility with conventional microtechnology, and moreover they can produce a pulse-free flow without containing any moving parts [1–3]. In EO pumps a liquid is pumped by applying an electric field to the Debye layer. This is formed by the ions in the liquid due to electric screening of the immobile charges on the walls of the pump. In order for such a Debye layer to form, the liquid needs to have significant electrical conductivity, i.e., a sufficiently high concentration of dissociated ions. Nonpolar liquids with very low conductivity ($<10^{-6}$ S m^{-1}), such as oil, cannot form the necessary double layer and therefore cannot be pumped in this way [4]. However, as analyzed below, this problem is circumvented in our design by introducing a conducting secondary liquid. By presenting our design and the theoretical analysis of it, we hope to inspire experimental groups to test our ideas and fabricate a device.

The paper is organized in the following way. In section 2, we introduce the general concept of the pump and its novel features. In sections 3 and 4, we turn to a particular, realizable pump geometry and analyze it in terms of flow rate–pressure (Q–p) characteristics by means of CFD simulations and equivalent circuit theory. Then, in section 5, we assess the stability of the pump by performing a linear stability analysis of the two-liquid interface. Finally, we draw conclusions in section 6.

2. General concept

There are two main types of inline EO pumping schemes in use today. In direct EO pumping, [5, 6], electrodes are in direct contact with a conducting buffer. The buffer enables both the driving force in an electric field, and, due to the charge separation at the walls of a channel, also a bulk-liquid motion, the actual electro-osmotic flow.

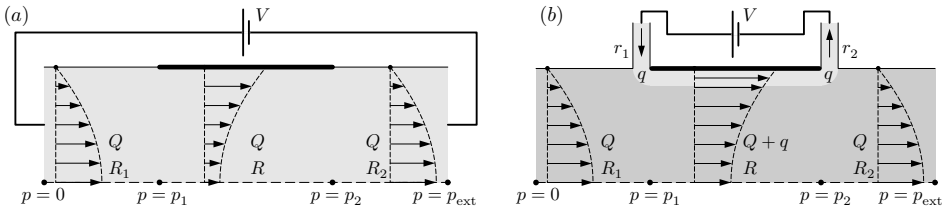

Figure 1. (*a*) The top half of a symmetric channel containing a conducting liquid (light gray), where the EO mobility on the top wall changes step-wise from zero (thin line) in the first section to α_{eo} (thick line) in the middle section and back to zero (thin line) in the last section. The pressure drops and hydraulic resistances in the three sections are $0 - p_1$ and R_1, $p_1 - p_2$ and R, and $p_2 - p_{ext}$ and R_2, respectively. The flow profile is shown in each of the sections. (*b*) A nonconducting working liquid (dark gray) of flow rate Q flowing through the three-section channel of panel (*a*), but in addition a conducting pumping liquid (light gray) of flow rate q enters and exits from two side-channels with hydraulic resistances r_1 and r_2. In both panels are shown the applied voltage V that generates the EO flow. The symmetry plane is indicated by the dashed horizontal line in the bottom.

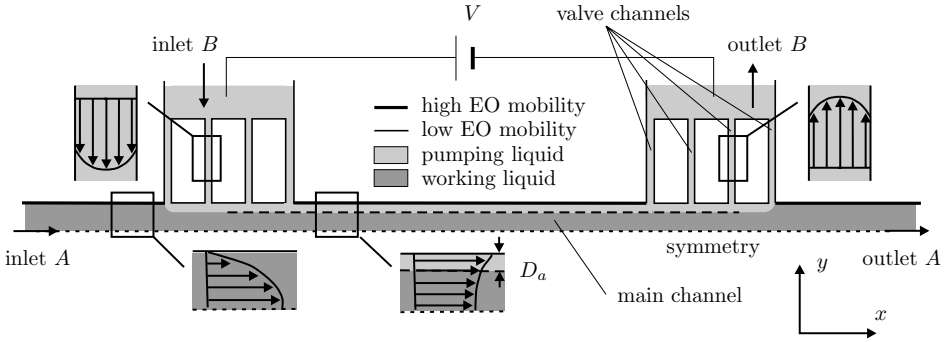

Figure 2. Top view of a possible design of the two-liquid viscous pump. The nonconducting working liquid (dark gray) is being dragged by the EO-driven pumping liquid (light gray) that flows along the edge of the main channel. The pump is mirror-symmetric around the central vertical plane, and only one half is shown. The following specific parameters are chosen to predict the performance of the pump. The displayed microchannels are all 40 μm deep. The main channel where the working liquid flows is 150 μm long and 10 μm wide. The narrow valve channels are 1 μm wide and 42 μm long. The un-coated walls are marked as the thick edges of the main channel. Coated walls are marked with thin edges. In inlet *A* and outlet *A* the flow is parabolic, while in the valves and in the main channel it is a superposition of parabolic and an EO-induced plug flow.

In the so-called indirect EO pumping the liquid in which the electrodes are separated by some barriers from the liquid where the EO flow takes place. The barriers allow ions but not bulk liquid to pass from the electrode chamber to the EO flow region. The barriers between the two regions can be achieved in several ways. (*i*) A channel filled with a conducting gel with a large hydrodynamic resistance [2]. (*ii*) An ion-exchange membrane allowing only positive or negative ions to pass [3]. (*iii*) A nanometer-sized gap (to allow for the Debye layer overlap) in which bulk EO flow can be suppressed allowing practically only flow of ions [7]. Common for these separation methods is that they are based on the Donnan exclusion principle.

Our novel two-liquid viscous pump can be regarded as a hybrid of the two types of EO pumping. There is still a direct contact between the driving and the bulk layers but they now originate from two different liquids. EO flow is used indirectly as it drives layers of conducting secondary liquids, introduced from some side-channels, to pump a nonconducting liquid through the main channel by viscous forces, see figure 1. Such an arrangement, resembling a conveyor belt, allows the pump to be conveniently positioned anywhere within a microfluidic circuit. To our knowledge it is the only EO pumping mechanism that enables inline pumping of nonconducting liquids. In the following subsections we highlight general principles for the operation of the pump: pressure valves, under-pressure induced by spatial variations in EO mobility and optimized potential drop. These principles are sketched in figure 2.

2.1. Ideal EO flow and pressure valves

In the case of an infinitely thin Debye layer the EO flow rate in a rectangular microchannel of length L, height D, and width a is given by

$$Q_{eo} = u_{eo} Da = \alpha_{eo} V_{eff} \frac{Da}{L} \propto a. \tag{1}$$

Here u_{eo} is the electro-osmotic velocity, α_{eo} is the electro-osmotic mobility and V_{eff} is the electric potential drop inside the channel. We refer to this situation as ideal EO flow. The associated EO pressure p_{eo} is given by

$$\Delta p_{eo} = Q_{eo} R_{hyd} = \alpha_{eo} V_{eff} \frac{aD}{L} R_{hyd}. \tag{2}$$

For high aspect ratios $D \gg a$, the hydraulic resistance is

$$R_{hyd} = \frac{12\mu L}{a^3 D} \frac{1}{1 - 0.63\frac{a}{D}}, \tag{3}$$

where μ is the dynamic viscosity. The pressure-driven flow rate Q_p through the channel is given by

$$Q_p = \frac{\Delta p}{R_{hyd}} \propto a^3, \tag{4}$$

where Δp is the pressure drop along the channel.

From equations (1) and (4) it follows that the pressure-driven flow will be negligible compared to the EO flow for small values of a. This can be used to obtain a kind of pressure valves in the two-liquid viscous pump: if narrow channels are placed on the sides of the main channel, their large hydraulic resistance prevents a significant loss of the pressure from the pump into the sides, while at the same time allows the driving EO flow to pass through them. The pressure valves offer two additional advantages. The electrode reservoirs separated by the valves can be exposed to atmospheric pressure. Thus bubble formation from electrolysis will not enter the pump and cause problems. Furthermore, this allows for placing the pump anywhere in a fluidic network.

2.2. *Under-pressure due to changes in EO flow rate*

In order for a nonconducting liquid to enter the pump an under-pressure needs to be induced at the entrance of the pump. This can be achieved by allowing for spatial variation in the EO flow rate Q_{eo}. Mass conservation ensures that the total flow rate $Q = Q_{\mathrm{eo}} + Q_{\mathrm{p}}$ is constant, so a change in Q_{eo} implies a change in Q_{p} and hence a change in pressure. The change in Q_{eo} can be obtained either by variations in the EO mobility or by variations in the channel width a large enough to induce a varying degree of the Debye layer overlap. In this paper we will focus on the first method.

The EO flow given in equation (1) corresponds to a constant EO mobility, in which case no under-pressure is generated inside the channel. If, however, the EO mobility is allowed to change along the channel, a more complex pressure field is obtained. To simplify the discussion without loosing the main physics, we study the three-section channel shown in figure 1(*a*), where the EO mobility changes from zero to α_{eo} and back to zero. It is the inhomogeneity of the EO mobility that is important, not its specific functional form. The hydraulic resistances of the three sections are R_1, R and R_2, respectively. The pressure changes from 0 to p_1, from p_1 to p_2, and from p_2 to p_{ext} along the first, second and third section, respectively. Thus the EO pump is set up to work against an external backpressure p_{ext}. The expressions for the total constant flow rate Q in each of the three sections are

$$Q = \frac{(0 - p_1)}{R_1} = \frac{(p_1 - p_2)}{R} + Q_{\mathrm{eo}} = \frac{(p_2 - p_{\mathrm{ext}})}{R_2}. \tag{5}$$

By straightforward algebra this yields

$$Q = \frac{RQ_{\mathrm{eo}} - p_{\mathrm{ext}}}{R_1 + R + R_2}, \tag{6}$$

$$p_1 = \frac{R_1}{R_1 + R + R_2}(p_{\mathrm{ext}} - RQ_{\mathrm{eo}}), \tag{7}$$

implying that a positive flow rate will be induced once RQ_{eo} is larger than the backpressure p_{ext}. Moreover, an under-pressure p_1 is induced over the first section of the pump, which ensures that liquid is sucked into the pump.

In figure 1(*b*) this principle of generating an under-pressure is applied to the two-liquid viscous pump. We study the case of immiscible liquids with a stable interface pinned at the corners of the side-channels. In this case the individual flow rates of the pumping and working liquids are constant. For the sake of simplicity we neglect the curvature effects due to surface tension and postpone this study until sections 4.1 and 5.

The nonconducting working liquid (dark gray) enters the first section of the large, three-section main channel of the hydraulic resistance R_1 and leaves the section of the hydraulic resistance R_2 with the same flow rate Q given by

$$\frac{1}{R_1}(0 - p_1) = Q, \qquad \frac{1}{R_2}(p_2 - p_{\mathrm{ext}}) = Q. \tag{8}$$

The conducting pumping liquid (light gray) enters with the flow rate q through the inlet side-channel having the hydraulic resistance r_1, and exits with the same flow rate q through the outlet side-channel having the hydraulic resistance r_2. Since we are neglecting the Young–Laplace pressure drops from the curved interfaces the pressures p_1 and p_2 are as above, and the flow rate q is seen to be

$$\frac{1}{r_1}(0 - p_1) = q, \qquad \frac{1}{r_2}(p_2 - 0) = q. \tag{9}$$

In the active part of the pump, the middle section with the hydraulic resistance R, the expression for the total flow rate is simplified, if we assume that the two liquids have the same viscosity (this assumption is easily relaxed in numerical simulations):

$$\frac{1}{R}(p_1 - p_2) + Q_{\mathrm{eo}} = Q + q. \tag{10}$$

The expressions for Q, p_1 and q become

$$Q = \frac{RQ_{\mathrm{eo}} - p_{\mathrm{ext}}}{R_1 + \left(1 + \frac{R_1}{r_1}\right)R + R_2}, \tag{11}$$

$$p_1 = -R_1 Q, \tag{12}$$

$$q = \frac{R_1}{r_1}Q. \tag{13}$$

Like for the simple channel equation (6), a positive flow rate Q appears once $RQ_{\mathrm{eo}} > p_{\mathrm{ext}}$, and in this case an under-pressure p_1 is generated thus making it possible to suck the nonconducting working liquid into the EO pump. A simulation of the induced under-pressure in the regions below the pressure valves is shown in section 4. In the limit of very high resistance of the side-channel, $r_1 \gg R_1$, equation (11) reduces to equation (6). Note, that because we have neglected the Young–Laplace pressure drops, and assumed a stable interface, the external pressure is fixed to be $p_{\mathrm{ext}} = [R_1(r_2/r_1) - R_2]Q$. Once the full dynamics of the free interface is introduced, the interfaces will adjust its shape to a given p_{ext}, see section 4.1.

As mentioned, a favorable under-pressure can also be achieved for constant EO mobility by reducing the cross section of the valve region compared to the main channel if the reduction is so large that the Debye layer overlap occurs. The overlap will reduce the EO velocity in the valves and change the flow profile from a plug-like to a parabolic-like one [8]. Since typically the Debye layers are 1–100 nm wide, the pressure valves in this case consist of nanochannels. Depending on the fabrication techniques, the nanochannels can be realized as channels with very high aspect ratio [9], very shallow channels [4], or as parts of nanoporous frits [10].

Regardless of the pump realization, the flow profiles will have some common characteristics. Due to the induced pressures the valve regions and the inlet/outlet regions of the

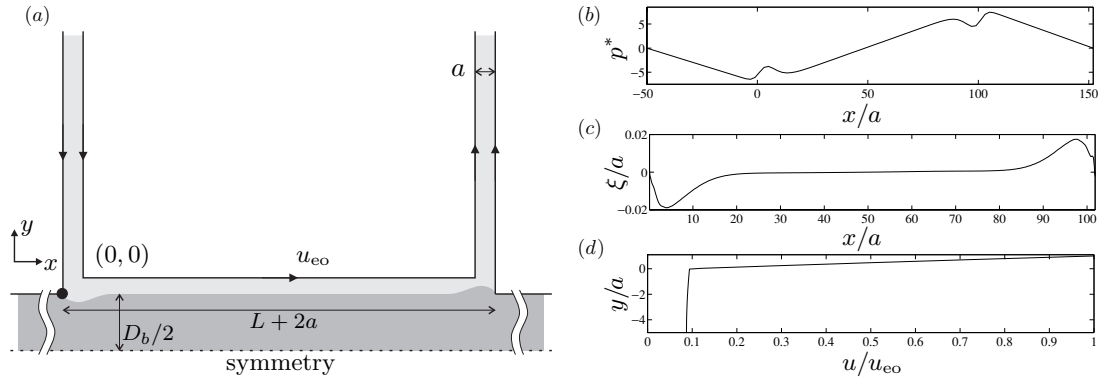

Figure 3. (*a*) The geometry used in the simulation of the immiscible case, were edges with arrows indicate an EO slip velocity $u_{eo} = 2\text{mm s}^{-1}$, (*b*) The pressure $p = p^* \mu_{cond}\, u_{eo}/a$, (*c*) the interface position ξ and (*d*) velocity profile across the channel. Viscosities are $\mu_{cond} = 1.0 \times 10^{-3}$ Pa s and $\mu_{noncond} = 300 \times \mu_{cond}$. The pressure is plotted along the symmetry axis. The deflection of interface is multiplied by a factor 100 for the purpose of visualization. The velocity profile is taken along $x = L/2 + a$.

main channel of the pump will have parabolic flow profiles. In the active part of the main channel the resulting flow is a superposition of an EO flow and an adverse pressure-driven flow, the latter resulting from the mass conservation given in equation (10). Schematic flow profiles are shown in figures 1(*b*) and 2, while a simulated one is shown in figure 3.

2.3. Optimized potential drop

A larger potential drop is needed in the main channel of the pump as compared to the valves in order to generate a higher pressure, equation (2). A single narrow valve channel has a large flow resistance but also a large electrical resistance. This means that the main potential drop would occur in the valve channels and thus not contribute to any pressure build up. The electrical resistance is inversely proportional to the area of the cross section. So, by making many short and narrow channels a low electrical resistance and high hydraulic resistance is obtained. However if the potential drop in the main channel is too large, it could cause instabilities of the two-liquid interface, see section 5.

2.4. Priming of the pump

In order for the pump to work an initial positioning of the liquid streams must be taken care of. This is termed as priming of the pump. The priming could happen in different ways depending on the viscosities, surface tensions and the surrounding fluidic network. One way of doing it would be to apply a pressure-driven flow to the side-channels q and the main channel Q simultaneously. This would generate a stream of focused nonconducting liquid along the main channel. If the driving pressures are then relaxed at the same time, the interface moves to the pinning points on the side-channels. Computer simulations or experiments may suggest other methods.

3. An example of a possible realization

A possible realization with realistic length scales of the two-liquid viscous pump is shown in figure 2. Two sets of four narrow channels are introduced from each side of the main channel as pressure valves. In figure 2 only one side with inlet/outlet valves is shown, since the device is symmetric around the center plane. Reactive ion etching systems can deliver narrow and deep channels with the aspect ratio as high as 40. So if a valve channel is 1 μm wide it can be 40 μm deep. The overall hydraulic resistance of the valves, equation (3), is 26 times larger than that of the EO section.

The Reynolds number is $Re \sim 0.01$ and in this creeping flow regime inertia can be neglected. A characteristic feature for creeping flow is that it is free of vorticity. This means that the valve channels may be positioned perpendicular to the main channel without generating any eddies. For a more detailed discussion see [11].

The Debye layer is roughly 10^4 times smaller than the total width of the main channel so we do not resolve it in the following modeling of the pump. The EO velocity appears simply as a nonzero slip velocity u_{eo} at the walls. The reduced EO flow in the valves is, therefore, realized by a reduction in the EO mobility as discussed in section 2.2.

4. Theoretical and computational analysis

We have analyzed the performance of the pump described in section 3 using computational fluid dynamics (CFD) simulations and equivalent circuit theory.

4.1. Computational fluid dynamics

The simulation effort is divided into two parts: (1) simulations with immiscible liquids, simplified geometry, free surface and velocity boundary conditions, and (2) simulations with miscible liquids, full geometry and EO mobility boundary conditions.

The problem depicted in figure 2 is simulated including the full free surface dynamics. The model is based on the FemLab 3.1 FEM solver and an in-house MatLab based free surface code [12]. The model solves the 2D Stokes equation while enforcing the full free surface stress condition including the Young–Laplace contribution to the pressure. As the problem is very complex only two side-channels are considered, in order to reduce computational time, which still ended to be of the order 24 h on a high performance computer. At the

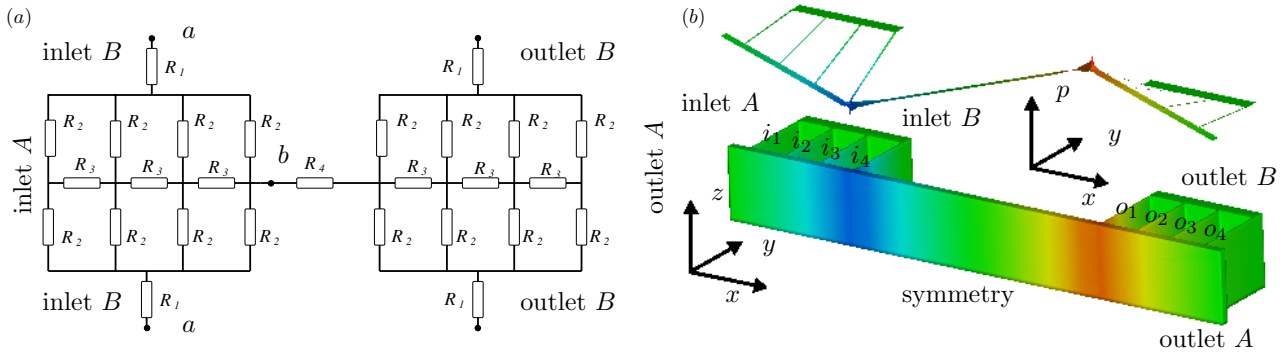

Figure 4. (*a*) The equivalent electric circuit of the two-liquid viscous EO pump. Note that the whole pump/circuit is depicted. The overall resistance is calculated as $R_{\text{total}} = 2R_{\text{ab}} + R_4$, where R_{ab} is the resistance between node point *a* and *b*. R_4 is the resistance of the EO section. (*b*) The calculated pressure distribution inside the pump obtained by numerical simulation in the miscible case with the uniform viscosity $\mu = 1 \times 10^{-3}$ Pa s. The inset floating above the pump shows how the pressure varies linearly in the main channel between the pressure valves, implying uniform flow. There is no external pressure difference, but note the pressure drop in the pressure valve region ($i_1 - i_4$) which sucks the working liquid into the main channel. Parameters: the dimensions are as in figure 2, while $\alpha_{\text{eo}}^{\text{low}} = 0.005\,\text{mm}^2\,\text{V}^{-1}\,\text{s}^{-1}$, $\alpha_{\text{eo}}^{\text{high}} = 0.05\,\text{mm}^2\,\text{V}^{-1}\,\text{s}^{-1}$, $p_{\text{in}} = p_{\text{out}} = 0$, $V = 10$ V. The peak pressure levels are $p = \pm 10$ Pa.

walls we use velocity boundary conditions to account for the electro-osmotic effects. Figure 3 depicts the simulated geometry with boundary conditions.

The insets (*a*), (*b*) and (*c*) in figure 3 show the dimensionless pressure p^* along the symmetry axis, the interface position ξ, and a velocity profile along the vertical symmetry line, respectively. From the results we see that the interface is only slightly deformed and has a thickness comparable to the inlet valve dimensions. The curved shape is a result of the pressure balance including the Young–Laplace pressure. Moreover, we notice that the slip velocity at the interface is about 10% of the wall velocity.

CFD simulations with miscible liquids were made using Coventor 2001.3. The program solves the Laplace equation for the electrical potential and the Navier–Stokes equation for the velocity field. These simulations are complementary to the more complicated free surface simulations. If the pumping liquid is chosen to be water the EO mobility along un-coated walls is typically $\alpha_{\text{eo}} = 0.05$ mm^2 V^{-1} s^{-1}. In the valve channels the walls are coated to lower the EO mobility by a factor 10. With these parameters numerical simulations yield a maximal flow rate per volt of 0.03 nL s^{-1} V^{-1} and a backpressure capacity of 3 Pa V^{-1}. The value for the flow rate is specific for the given geometry. According to equations (2) and (3) the backpressure is independent of the length of the pump but strongly dependent on the width of the main channel and the viscosities in the two liquid case. Visualization of the pressure distribution is shown in figure 4(*b*). Note the under-pressure in the region between valve i_1 and i_4. The pressure distribution from the immiscible (figure 3(*a*)) and the miscible case (figure 4(*b*)) agree qualitatively. Note, that in the miscible case the liquids will mix due to diffusion. Two time scales are involved: (1) the time it takes for the liquid to pass through the pump $T_{\text{pump}} = L/u_{\text{eo}}$, (2) and time it takes for the two miscible streams to mix $T_{\text{diff}} = D_b^2/D$, where D is the diffusion constant. The ratio $T_{\text{pump}}/T_{\text{diff}} = 1.5$ indicates that the liquids will be completely mixed downstream of the pump.

4.2. Equivalent circuit model

The aim is to establish a model that can predict the *Q*–*p* characteristic of the pump. The creeping flow regime allows us to analyze the flow by the equivalent circuit method. We only give an outline here as the detailed procedure is described in [13].

The first step is to find the effective potential drop across the EO section by analyzing the circuit in figure 4(*a*). In the miscible case with uniform conductivity the result is that 52% of the applied voltage is dropped over the EO section, R_4 in figure 4(*a*). This value represents a worst case since the main channel is full of conducting liquid leading to a lower voltage drop. In the immiscible case the analysis is complicated by the fact that the resistance R_4 is dependent on the position of the free interface, and an exact result is not obtainable due to lack of computational power. However, our simulations in the two-channel case, section 4.1, indicate that the width of the conducting layer is the same as the width of the side-channels. Since most of the electric field is inside the conducting layer, it is easy to obtain a rough estimate, and we find that 90% of the voltage is dropped over the EO section.

The next step in the equivalent circuit model procedure is to find the hydraulic resistance R_{hyd} of each of the channel segments. Since the channel cross sections are all rectangular we make use of equation (3). We then find the backpressure analogous to the treatment in section 2.2.

5. Stability analysis

The interface between the two immiscible liquids in the two-liquid viscous pump is generally prone to instabilities. Small perturbations can grow and eventually break-up the surface and disrupt the pumping operation. As sketched in figure 5 there are altogether three types of instability mechanisms at play: shear-flow, electrohydrodynamic and capillary instability. In the following we shall describe and assess the most relevant aspects of each mechanism.

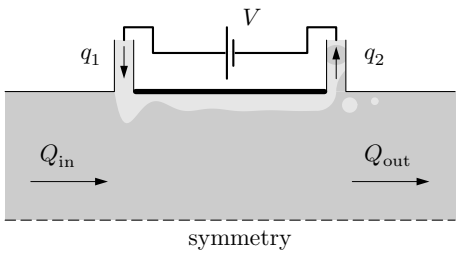

Figure 5. A schematic diagram of instabilities in the two-liquid viscous pump. Three main mechanisms of instability are at play: shear-flow and electrohydrodynamic instability are relevant in the main channel and in the outlet valve, while capillary instability plays a role below the valves where the interface curves to compensate for the induced pressures. In the case of break-up of the interphase q_1 and q_2 as well as Q_{in} and Q_{out} may differ in contrast to the case of figure 1(*b*).

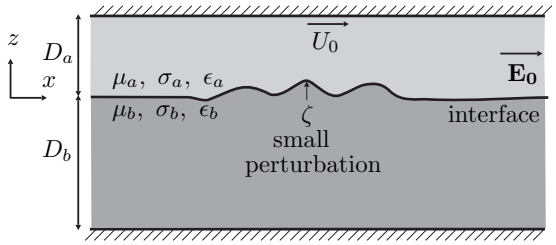

Figure 6. The simplified model with a single interface (a single 'conveyor belt') used to assess the instability regimes of our pump. Two shearing liquids are confined between two large (high aspect ratio) parallel plates in a Couette–Poiseuille flow. The liquids differ in dynamic viscosities, dielectric constants and conductivities. They are further exposed to a tangential electric field. The Debye layer is assumed negligibly thin so the driving EO velocity appears only as a boundary condition.

5.1. Approximations and methods

As long as the conducting layers are thin compared to the nonconducting region, the (in)stability modes on the two interfaces of the symmetric pump from figure 2 will be decoupled from each other. In addition, the symmetric pump can sustain larger adverse pressures known to stabilize the flow [14]. Thus, it suffices to determine the instability window of the simpler asymmetric configuration containing only one interface, i.e., a pump with only one conveyor belt. We further notice that for the high aspect ratio channels under consideration the problem is effectively reduced to two dimensions.

Perturbations of the interface are assumed to be small, and we subject the governing equations and boundary conditions to the usual hydrodynamic linear stability analysis, [15]. The unperturbed interface lies in the xy plane given by $z = 0$. Any slight disturbance of the interface is described as a displacement $z = \zeta(x, y)$. We expand all perturbed field f (velocity $\mathbf{u}$, pressure p, electric potential ϕ and vector $\mathbf{n}$ normal to the interface) in terms of the small interface position ζ

$$f = f_0 + \alpha f_1 + \alpha^2 f_2 + \cdots, \tag{14}$$

where f_0 represents the unperturbed steady-state solution, α is the perturbation strength, and f_1 is the first-order solution. Putting the perturbed variables f into the governing equations and boundary conditions, the steady-state solution cancels out, and by maintaining only terms up to linear order in α we arrive at the linearized equations which govern the perturbations. The first-order solutions are further expressed in terms of normal modes with the wave vector $\mathbf{k} = (k_x, k_y)$ and frequency $\omega_{\mathbf{k}}$

$$f_1(x, y, z, t) = \hat{f}_1(z) \exp[\mathrm{i}(k_x x + k_y y) - \mathrm{i}\omega_{\mathbf{k}} t]. \tag{15}$$

By inserting the normal modes back into the linearized equations, the problem is eventually transformed into an eigenvalue problem for the frequency $\omega_{\mathbf{k}}$, generally a complex number of the form $\omega_{\mathbf{k}} = \mathrm{Re}(\omega_{\mathbf{k}}) + \mathrm{i}\,\mathrm{Im}(\omega_{\mathbf{k}})$. It is seen from equation (15) that

$$f_1 \propto \exp[-\mathrm{i}\,\mathrm{Re}(\omega_{\mathbf{k}})t] \exp[+\mathrm{Im}(\omega_{\mathbf{k}})t]. \tag{16}$$

Therefore, an instability (exponential growth in time) is present when $\mathrm{Im}(\omega_{\mathbf{k}}) > 0$. In some cases $\omega_{\mathbf{k}}$ is real for a while before developing a positive imaginary part. In other cases the onset of instability is right at $\omega_{\mathbf{k}} = 0$. The former case is known as overstability while the latter as static instability.

5.2. Shear-flow instability

Shear-flow instability is particularly relevant in the active part of the main channel, where the liquids are exposed to mutual stresses. Microfluidic shear flows between two viscous, immiscible liquids can result in a variety of regular droplet patterns, as the shear force (constant for a given relative velocity and a fixed geometry) overcomes the cohesive surface tension force, [16].

In our case, due to the conveyor-belt action, the two liquids flow between two large parallel plates in a Couette–Poiseuille setup, figure 6. In each liquid the governing equations are the Navier–Stokes equation and the continuity equation

$$\rho_{(i)}(\partial_t \mathbf{u}_{(i)} + \mathbf{u}_{(i)} \cdot \boldsymbol{\nabla}\mathbf{u}_{(i)}) = -\boldsymbol{\nabla} p_{(i)} + \mu_{(i)} \nabla^2 \mathbf{u}_{(i)}, \tag{17}$$

$$\boldsymbol{\nabla} \cdot \mathbf{u}_{(i)} = 0, \tag{18}$$

where $i = a, b$ indicates liquid a and b, ρ is the density, p is the pressure, μ is the dynamic viscosity, and $\mathbf{u}(x, y, z) = (u, v, w)$ is the velocity field. Note that we did not include the gravitational body force as it is negligible in our microfluidic system[1].

When the linear stability analysis is performed on equations (17) and (18), we arrive at the Orr–Sommerfeld equations for two liquids, [17], and a set of eight boundary conditions. These include the no-slip velocity conditions at rigid boundaries and fairly complicated interface conditions—continuity of velocities and tangential stresses, and balance of normal stresses. The whole system is then solved for eigenfrequencies as mentioned earlier. The analytical procedure is rather involved. Here we apply the full description, found in [18–21], in the relevant limits.

An important conclusion from the analysis is that a difference between the viscosities of the two liquids cause the instability in shear flows at low Reynolds number. Once the viscosities differ, the relative thickness of the liquid layers becomes important, too.

We have estimated the onset of instability in the long-wavelength limit for the water–oil (*a–b*) system of figure 6. In figure 7 $\mathrm{Im}(\omega_{\mathbf{k}})$ is shown as a function of the viscosity ratio μ_b/μ_a. The graphs are shown for three different thickness

[1] The ratio between gravitational and capillary force in the system is the Bond number, $Bo = (\rho^{(2)} - \rho^{(1)})ga^2/\gamma$. If we consider oil and water, and $a = 10\ \mu$m is the width of the main channel in the pump, we get $Bo \sim 10^{-6}$. This allows the liquids in the pump to flow sidewise.

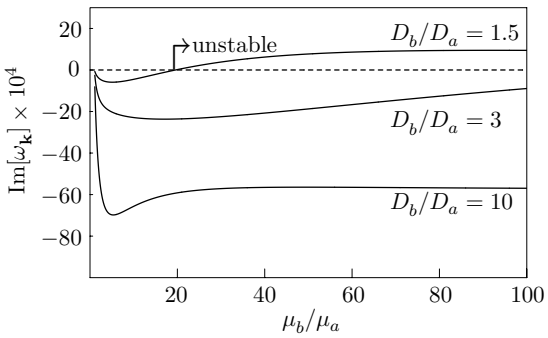

Figure 7. A shear-flow stability study of a water–oil system (liquids a and b, respectively, in figure 6). For three different values of the thickness ratio D_b/D_a the imaginary part of the frequency $\mathrm{Im}[\omega_{\mathbf{k}}]$ is plotted as a function of the viscosity ratio μ_b/μ_a for an EO velocity $u_{\mathrm{eo}} = 1\ \mathrm{mm\ s^{-1}}$, a surface tension $\gamma = 18 \times 10^{-3}\ \mathrm{N\ m^{-1}}$, and a zero counter-pressure. For $D_b/D_a = 1.5$, instability sets in for $\mu_b/\mu_a > 20$ where $\mathrm{Im}[\omega_{\mathbf{k}}] > 0$. This is an example how an increase in viscosity actually enhances instability. Increasing the oil thickness, the window of stability is increased.

ratios D_b/D_a. Keeping D_a constant, stability increases with increasing thickness ratio, while it decreases with increasing viscosity ratio, except that in the limit of very large viscosity ratios the system becomes stable again.

The above results can be used to operate the pump within a given stability window. If D_a is as thin as a few Debye lengths, the pump will practically always be stable with respect to the shear flow.

5.3. Electrohydrodynamic (EHD) instability

Another important aspect is electrohydrodynamic (EHD) instability present when liquids of different dielectric constants and conductivities are exposed to electric fields. Numerous studies of EHD instability have been published over the years, e.g. [22–27], and more recently with special attention to microfluidics [18, 19, 28].

In this brief account of EHD instability we use the formalism from [18, 25], and apply it in the relevant limits with regard to our pump. Essentially, the equations governing electric fields and charge transport in each liquid need to be added to equations (17) and (18)

$$\boldsymbol{\nabla} \cdot (\epsilon_{(i)} \mathbf{E}_{(i)}) = \rho^{\mathrm{el}}_{(i)}, \tag{19}$$

$$\boldsymbol{\nabla} \times \mathbf{E}_{(i)} = 0, \tag{20}$$

$$\boldsymbol{\nabla} \cdot \left(\sigma_{(i)} \mathbf{E}_{(i)} + \rho^{\mathrm{el}}_{(i)} \mathbf{v}_{(i)}\right) + \partial_t \rho^{\mathrm{el}}_{(i)} = 0, \tag{21}$$

where ϵ is the dielectric constant, σ is the conductivity, ρ^{el} is the free charge density and $\mathbf{E}$ is the electric field in each liquid. In equations (19)–(21) it is assumed that magnetic effects are negligible and that Ohm's law of conduction is valid. The interface boundary conditions are expanded to account for electric stresses and conservation of free charge.

There are two main effects which influence the behavior of the interface between two liquids in an electric field. First, there are polarization forces that act normally on the interface, due to a difference in the dielectric constants. And second, there are tangential shear forces resulting from the free charges that relax at the interface, due to a difference in the conductivities. Relevant in microfluidics are effects involving

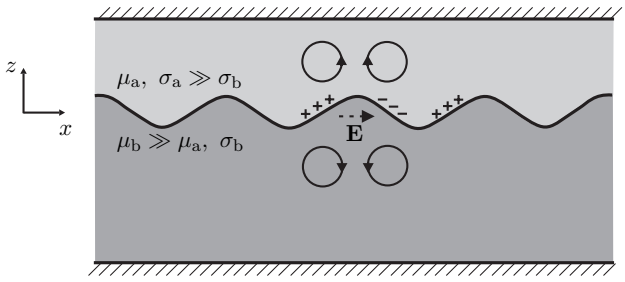

Figure 8. Overstability mechanism in the pump. A perturbation of the interface between a conducting and a nonconducting liquid results in the accumulation of free surface charge. As it screens the imposed field from the conducting region, the charge is shifted in phase with respect to the perturbation [25]. Charge motion in a tangential field induces shear stresses in the liquids above and below, which can either stabilize or further destabilize the interface. In the depicted case $\mu_b \gg \mu_a$ and $\sigma_a \gg \sigma_b \approx 0$, so the interface will be stabilized.

Debye layers, but these are out of the scope of this preliminary account.

In our pump a thin layer of conducting liquid drags a viscous nonconducting dielectric liquid. There is a huge difference in conductivities and the liquids are exposed to a tangential electric field. Therefore, the shear forces due to free charges will play the most important role, possibly causing overstability or oscillatory instability, which we now assess.

In equilibrium no current passes through the unperturbed interface and no free charges accumulate on it. However, interface perturbations cause a change in the fields which in turn attract free charges at the interface. The charges position themselves to shield out the imposed field from the high conductivity region. As the charges move under the influence of electric field, shear stresses are passed onto the liquids below and above the interface, creating fluid cells, figure 8. If the liquids have the same viscosity these effects will cancel each other, but a difference in viscosities will make these cells to further deform or possibly suppress the perturbations.

We now make a use of the general eigenvalue solution (equation (34) in [25]) applicable to our problem sketched in figure 6. In the two-liquid viscous pump the two liquids are such that the conductivities $\sigma_a \gg \sigma_b$ which results in a very short charge relaxation time $\tau = (\epsilon_a + \epsilon_b)/\sigma_a$. We are interested in the viscosity limit $\mu_a \ll \mu_b$, i.e., when the more conducting liquid is much less viscous. An involved analysis gives for the critical field that induces overstability

$$E_c^2 = -\frac{2\mu_b \sigma_a}{\epsilon_b(\epsilon_a + 3\epsilon_b)}. \tag{22}$$

The minus sign indicates that in this limit no field can induce the instability. In light of figure 8, the imparted viscous stresses, pronounced in the more viscous liquid, act to suppress the interface deformation. On the other hand, if the conducting liquid is the one with a much higher viscosity (e.g. pumping of a gas), the critical field is positive and given by

$$E_c^2 = \frac{2\mu_a \sigma_a}{\epsilon_b(\epsilon_b + 3\epsilon_a)}, \tag{23}$$

or, for $\epsilon_a \gg \epsilon_b$,

$$E_c = \left(\frac{2\mu_a \sigma_a}{3\epsilon_a \epsilon_b}\right)^{\frac{1}{2}}. \tag{24}$$

When equation (24) is evaluated for common fluids, the fields are on the order of 10^6 V m^{-1}. In the studied example (operating voltage 10 V), the electric field within the main channel is $E = 4 \times 10^4$ V m^{-1}, a much lower value.

The above results show that our viscous liquid pump is stable with respect to the EHD overstability. In the case when a more viscous, nonconducting liquid is pumped, stability is always present whereas in the case of low-viscosity dielectrics the critical fields are much higher than the operating ones. In passing we remark that the normal polarization forces also stabilize the interface when the liquid of higher conductivity has also a higher dielectric constant, which is usually the case.

5.4. Capillary instability

The pressure drop over the interface between two immiscible fluids is given by the Laplace equation

$$\Delta P = \gamma \left(\frac{1}{r_1} + \frac{1}{r_2} \right), \tag{25}$$

where γ is the surface tension while r_1 and r_2 are the principal radii of curvature. We take the width a and depth D of a valve channel to correspond to $2r_1$ and $2r_2$, respectively. In a high aspect ratio valve $a \ll D$, hence only the width a contributes to the capillary pressure.

The pressure induced below the valves in the two-liquid pump will tend to deform the interface according to equation (25), as simulated in figure 3(*c*). We now estimate under which conditions the breaking of two streams sketched in figure 5 could occur and why. For an oil–water interface $\gamma = 18 \times 10^{-3}$ N m^{-1} and a valve width of $a = 1$ μm it takes a pressure of 36 kPa to push an oil droplet through the valve opening.

The backpressure capacity of the pump is $\Delta p = 30$ Pa for 10 V using a conducting liquid. In the case of the water–oil interface the pressure increases to 9 kPa $\times\, 0.1 = 900$ Pa at 10 V due to the higher viscosity of oil ($\mu_{\text{oil}} = 300\mu_{\text{water}}$) and the reduced oil velocity, see figure 3(*d*). This value is still lower than the capillary pressure thus the interface will be stable in normal operation.

If the interphase breaks due to instabilities, e.g., in the case of lower surface tension, oil droplets may enter the outlet valve to account for the mass conservation ($q_1 \neq q_2$). Hence the pinched-off conducting droplets shown in figure 5. Similar effects of variable flow resistance on droplet break-up is demonstrated in [29]. Obviously, such behavior would eventually disrupt the pumping operation.

We conclude this section by saying that the pressure valves will prevent an immiscible liquid from entering them if the backpressure capacity of the pump is smaller than the capillary pressure associated with the valve openings.

6. Conclusion

We have presented a novel electro-osmotic pump which can be used to pump nonconducting liquids by the viscous drag of a conducting secondary liquid. In order to achieve a viable pump, the liquids must be immiscible, stability must be ensured and three main features need to be employed: a favorable under-pressure, pressure valves and an optimized potential drop.

The flow rate–pressure characteristic of the two-liquid viscous EO pump largely depends on the geometrical factors and can be significantly enhanced by advanced etching techniques. The pump design still works for miscible liquids, but here the working liquid gets mixed with the pumping liquid due to diffusion.

Numerical simulations and the equivalent circuit model of the design presented here yield a maximal flow rate per volt of 0.03 nL V^{-1} s^{-1} and a backpressure capacity per volt of 3–90 Pa V^{-1} depending on the liquids in the pump. These values are quite small and the pump is therefore suited for precise flow manipulation rather than pumping bulk volumes.

Three effects play a role with regard to the stability of the pump: (1) shear-flow instability happens only when the liquids differ in viscosities and is suppressed when the conducting-liquid layer is thin compared to the nonconducting one. (2) Electrohydrodynamic overstability is suppressed when the conducting liquid has a much smaller viscosity than the nonconducting liquid. (3) Capillary instability is suppressed by a large surface tension and by a large value of the capillary pressure stemming from a small width of the pressure valves.

Future work involves time-dependent two-phase simulations. Such work could give valuable information about priming of the pump. We are currently preparing papers containing the detailed mathematical analysis of the stability mechanisms [19, 20]. Finally a prototype should be manufactured. Because of the possibility of pumping all types of liquids in a precise and controlled manner, the described concept and design appear promising.

Acknowledgments

This work is partly supported by the Danish Technical Research Council, μTAS Frame Program Grant No. 26-00-0220.

References

[1] Laser D J and Santiago J G 2004 A review of micropumps *J. Micromech. Microeng* **14** R35–R64
[2] Takamura Y, Onoda H, Inokuchi H, Adachi S, Oki A and Horiike Y 2001 *Proc. μTAS 2001 (Monterey CA, USA, Oct.)* pp 230–2
[3] Morf W E, Guenat O T and de Rooij N F 2001 *Sensors Actuators* B **72** 266
[4] Chen C H and Santiago J G 2002 *J. Microelectromech. Syst.* **11** 672–83
[5] Yao S, Mikkelsen J C and Santiago J G 2001 *Proc. IMECE: ASME International Mechanical Engineering Congress and Exposition (New York, Nov.)*
[6] Zeng S, Chen C H, Mikkelsen J C and Santiago J G 2001 *Sensors Actuators* B **79** 107–14
[7] Alarie J P, Jacobson S C, Scott Broyles B, McKnight T E, Culbertson C T and Ramsey J M 2001 *Proc. μTAS'01 (Monterey, CA, USA, Oct.)* pp 131–2
[8] Levine S, Marriott J R and Robinson K 1974 *J. Chem. Soc. Faraday Trans.* **II** 1–11
[9] Mogensen K B, Eriksson F, Nikolajsen R P H and Kutter J P 2004 *Proc. μTAS'04 (Malmö, Sweden, Sept.)* vol 1 pp 39–41

[10] Brask A, Bruus H and Kutter J P 2004 *Proc. μTAS'04 (Malmö, Sweden, Sept.)* vol 2 pp 136–8
[11] Patankar N A and Hu H H 1998 *Anal. Chem.* **70** 1870–81
[12] Jensen M J, Garstecki P, Fuerstman M, Bruus H, Whitesides G M and Stone H A 2004 *Proc. μTAS'04 (Malmö, Sweden, Sept.)* vol 1 pp 626–8
[13] Brask A, Goranović G and Bruus H 2003 *Sensors Actuators* B **92** 127–32
[14] White F M 1991 *Viscous Fluid Flow* 2nd edn (Singapore: McGraw-Hill)
[15] Chandrasekhar S 1961 *Hydrodynamic and Hydromagnetic Stability* (Oxford: Oxford University Press)
[16] Thorsen T, Roberts R W, Arnold F H and Quake S 2001 *Phys. Rev. Lett* **86** 4163–6
[17] Drazin P G and Reid W H 1991 *Hydrodynamic Instability* (Cambridge: Cambridge University Press)
[18] Goranović G 2003 *PhD Thesis* Technical University of Denmark online at http://www.mic.dtu.dk/research/MIFTS
[19] Goranović G, Sørensen M P, Brøns M and Bruus H 2004 *Proc. μTAS'04 (Malmö, Sweden, Sept.)* vol 1 pp 617–9
[20] Goranović G, Sørensen M P, Brøns M and Bruus H 2004 in preparation
[21] Yih C-S 1967 *J. Fluid. Mech.* **27** 337–52
[22] Rayleigh Lord 1882 *Phil. Mag. Ser.* **5** 184–6
[23] Melcher J R 1963 *Field-Coupled Surface Waves: a Comparative Study of Surface-Coupled Electrohydrodynamic and Magnetohydrodynamic Waves* (Cambridge MA: MIT Press)
[24] Melcher J R and Smith C V Jr 1969 *Phys. Fluids* **12** 778–90
[25] Melcher J R and Schwarz W J Jr 1968 *Phys. Fluids* **11** 2604–16
[26] Saville D A 1997 *Annu. Rev. Fluid Mech.* **29** 27–64
[27] Mestel A J 1994 *J. Fluid Mech.* **274** 93–113
[28] Lin H, Storey B D, Oddy M H, Chen C-H and Santiago J G 2004 *Phys. Fluids* **16** 1922–35
[29] Link D R, Anna S L, Weitz D A and Stone H A 2004 *Phys. Rev. Lett.* **92** 54503

Appendix E

Paper submitted to J. Micromech. Microeng., 2005

Title
Transient pressure drops of gas bubbles passing through liquid-filled microchannel contractions: an experimental and numerical study

Authors
H. Chio, M. J. Jensen, X. Wang, H. Bruus, and D. Attinger

Reference
submitted to J. Micromech. Microeng., July 2005.

Transient pressure drops of gas bubbles passing through liquid-filled microchannel contractions: an experimental and numerical study

Henry Chio[(1)], Mads Jakob Jensen[(2)], Xiaolin Wang[(1)], Henrik Bruus[(2)], and Daniel Attinger[(1)]

[(1)]Department of Mechanical Engineering,
SUNY at Stony Brook, NY 11794-2300, USA
[(2)]MIC – Department of Micro and Nanotechnology, DTU Bldg. 345 East,
Technical University of Denmark, DK-2800 Kgs. Lyngby, Denmark

E-mail: daniel.attinger@sunysb.edu

Abstract. We present the first transient pressure measurements and high-speed visualization of gas bubbles passing through liquid-filled microchannel contractions. We have studied contractions ranging from 100 to 500 μm in glass tubes of main diameter 2 mm and compared the experimental results with the recent model of quasi-stationary bubble motion by Jensen, Goranović, and Bruus [J. Micromech. Microeng. **14**, 876 (2004)] valid for low flow rates. The influence of the wetting angle is studied by coating a tube with a hydrophobic solution. Transient pressure measurements, bubble deformations, and the influence of the bubble length on the so-called clogging pressure ΔP_c are shown to be in good agreement with the model, both in terms of maximum values and in terms of transient evolution. Some deviations from the model are also observed and possible reasons for this are investigated, such as (a) contact line pinning, (b) thin liquid film along the bubble modifying capillary pressure, and (c) viscous pressure drop in the contraction. Experiments with increasing flow rates show that two regimes govern the pressure transients of the bubbles passing the contractions: a quasi-stationary regime for low capillary number, and a viscosity-influenced regime for non-negligible capillary numbers. We propose a criterion based on a modified capillary number to discriminate between these two regimes.

Submitted to: *J. Micromech. Microeng. 28 June 2005*

PACS numbers: 47.55.Dz, 47.60.+i, 68.03.Cd

1. Introduction

In a typical microfluidic system [1], the fluid flows into channels with diameters ranging from 3 mm to 50 μm, along a path involving multiple branching and contractions. The cross-section of these channels is either round (tubing) or rectangular (due to microfabrication techniques), with some branching, e.g., in the valving part. Materials range from ceramic and stainless steel, to polymer (PTFE, Tygon, Peek) and silicon, each having different wetting properties. Bubbles may appear in microfluidic systems due to cavitation, electrochemistry, or priming (filling) of the microchannels, and they may become problematic if they get stuck in contractions, which are present in the microfluidic system due to some functionality such as valves, tree-branching, or nozzles.

The pressures needed to move a bubble through a contraction of minimum diameter d, filled with a liquid of viscosity μ and surface tension σ is related to the laminar friction and the free surface forces. In the laminar regime, the friction contribution for flow rates Q is proportional to $\mu Q \ell_{\rm con}/d^4$, where $\ell_{\rm con}$ is the contraction length, while the free surface contribution due to the Young-Laplace pressure is non-zero and proportional to σ/d as soon as the tube diameter or its wetting properties changes [2]. The resulting pressure transient may be several kPa, and if the bubbles are large enough to span across the microchannel this may block the flow. The minimal external pressure needed to drive such bubbles out of the channel is called the clogging pressure ΔP_c. In other cases, e.g., when a bubble is stuck in a corner or in a dead-flow zone, it can be extremely difficult to dislodge it, resulting in a reduction in performance or accuracy of the microfluidic device. Therefore, an entire batch of MEMS microfluidics devices can be ruined by only one problematic geometric feature. These problems were already identified a decade ago [3, 4], but were not studied in depth before the problem was picked in the recent theoretical study of Jensen, Goranović, and Bruus [5].

The goal of our work is to contribute to the solution of this important technological problem by studying bubble dynamics in a well-defined microchannel contraction. We begin by presenting the experimental setup and describe the measurement method. Then we give a short review of the theoretical and numerical model used. We move on to compare and discuss the numerical and experimental results, and finally we give some concluding remarks.

2. Capillaries and experimental setup

For the experimental part of the work different capillary glass tubes of circular cross section were used, see table 1. The tubes with contractions as shown in figure 1 were manufactured in the glass shop of Stony Brook University. The tubes have typical internal main diameters $D = 2$ mm and contraction diameter d ranging between 100 and 500 μm. In a given experiment a single capillary tube was connected via stiff polymer (FEP) connection tubes to a syringe pump and a large reservoir, as shown in figure 2.

Table 1. List of the tubes used in this work: tube ID, the main diameter D, the contraction diameter d, bubble length L, measured and simulated clogging pressure ΔP_c^m and ΔP_c^s, respectively, and the relative deviation DEV between them defined as $\mathrm{DEV} = (\Delta P_c^s - \Delta P_c^m)/\Delta P_c^m$.

ID	D [mm]	d [μm]	L [mm]	ΔP_c^m [Pa]	ΔP_c^s [Pa]	DEV
A7	1.78	490	0.6	330	420	21%
			3.1	420	500	16%
			13.8	420	500	16%
A8	1.70	264	1.1	877	790	-11%
			4.7	877	750	-17%
			12.0	877	840	-4%
A19	1.83	103	1.5	2720	2400	-13%
			3.1	2720	2410	-13%
			3.5	2720	2670	-2%
			10.0	2720	2450	-11%
A27	2.20	196	4.0	460	510	10%

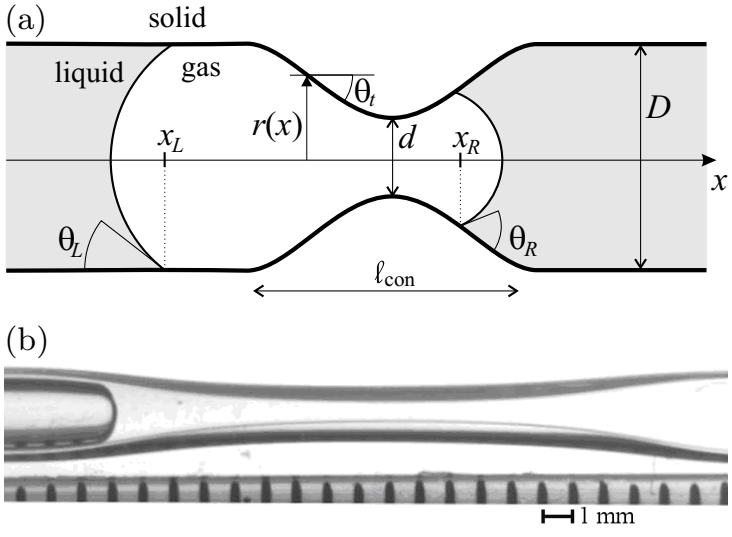

Figure 1. (a) Sketch of the gas-liquid-solid system with channel profile $r(x)$, main diameter D, contraction diameter d, left and right contact angles θ_L and θ_R, left and right contact line position x_L and x_R, length of the contraction ℓ_{con}, and local tapering angle θ_t. (b) Photograph of a gas bubble (dark gray) entering from the left into a liquid-filled (white) tube with a 490 μm contraction. The flow rate Q of the liquid is 0.33 μL/s.

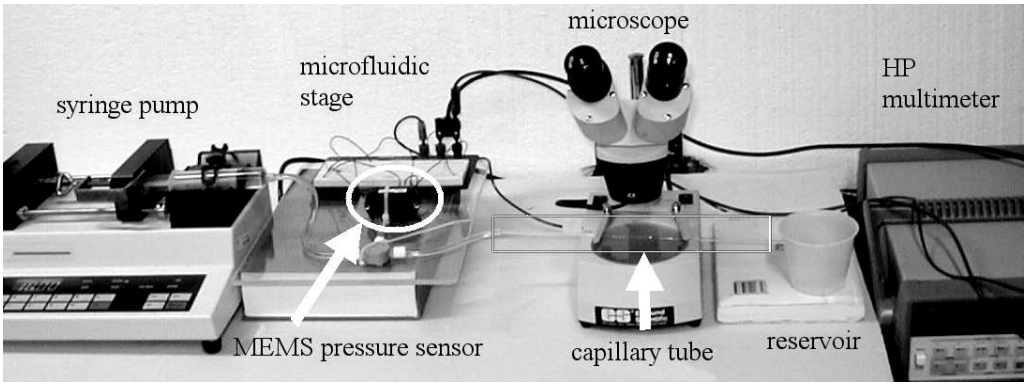

Figure 2. Measurement setup allowing for transient visualization and pressure measurement during the transport of a microbubble in a microchannel.

A single bubble was inserted in the tube and moved at steady flow rates ranging from 0.1 to 200 μL/s. Most experiments were performed at 0.33 μL/s to keep the laminar friction contribution to the pressure drops negligible. A MEMS-based piezoresistive pressure sensor (Honeywell 143PC03D) was connected through a Y-connection between the syringe pump and the tube. The pressure difference across the bubble was measured with a resolution of $\pm$20 Pa. The pressure signal was acquired with an HP multimeter and Labview, at a maximum sample rate of 100 Hz. The motion of the bubble was either observed through the stereo microscope visible in figure 2, or through a microscope objective and a Firewire high-speed camera.

While performing experiments several precautions were taken to ensure that the measurements were reproducible. The interior of the glass tubes was soaked in a solution of 5% Contrad (Fisher Scientifics) overnight and then abundantly rinsed with deionized water. No other solvents nor alcohol where put in the tubes as any residue might change surface properties, e.g., the wetting angle. The water used in the experiments was deionized with a Millipore Milli-DI purification system. The wetting angle was measured for a bubble at equilibrium and for velocities corresponding to flow rates of 17.0, 3.33 and 0.33 μL/s. The pressure sensor was calibrated with a digital pressure controller (Druck DPI 530) accurate to 0.1% full scale. The geometry of the tubes was measured from the camera pictures, and corrected for the magnification effect induced by the curved walls of the glass tube. The latter effect was tested by matching the volume injected in the tube with the experimental and numerical position of the left and right meniscus of the bubble.

3. Theory and numerics

The model for the quasi-stationary motion of a bubble in a microchannel contraction discussed by Jensen, Goranović, and Bruus [5] was implemented and adapted to the channel geometries discussed in this paper. On the basis of a microscope picture of a given tube a spline was fitted to obtain the shape $r(x)$ of the contraction, see figure 1.

This shape is in turn used to predict the pressure $\Delta P_b(x)$ across a bubble as a function of its position. A bubble is defined by its volume V_b and the value of the receding and advancing contact angles defined at the contact lines of the left and right menisci, respectively.

The contribution of the pressure change due to capillary forces (simulated by the above model) and the laminar friction pressure drop can be written as follows:

$$\begin{aligned}\Delta P_b &= P_{\text{in}} - P_{\text{out}} = \Delta P_\sigma + \Delta P_{\text{fric}} \\ &= 2\sigma\left[\frac{\cos[\theta_R - \theta_t(x_R)]}{r(x_R)} - \frac{\cos[\theta_L - \theta_t(x_L)]}{r(x_L)}\right] + \alpha\beta\frac{128\mu\ell_{\text{con}}}{\pi d^4}\,Q, \end{aligned} \tag{1}$$

where P_{in} and P_{out} are the pressure at the tube inlet and outlet, respectively. Moreover, ΔP_σ and ΔP_{fric} are the contributions to the capillary pressure change and the laminar friction pressure, respectively, θ_L and θ_R are the left and right contact angles, respectively, $\theta_t(x)$ is the local tapering angle, $r(x)$ is the tube shape, α is a factor close to unity that depends on the shape of the contraction, β is a constant between unity (for a bubble outside the contraction) and zero (for a bubble spanning the contraction), and ℓ_{con} is the length of the contraction. The measurements are made at low flow rates Q so the contribution ΔP_{fric} can therefore be neglected in the simulations. An exception to that are the measurements presented in figure 8, which specifically address the influence of increasing flow rates.

4. Results and discussion

In the following we present and discuss our results in five parts: Transient pressure and interface curvature, transient pressure and bubble breakup, clogging pressure as a function of tube diameter, influence of wetting angle, and influence of flow rate.

4.1. Transient pressure and interface curvature

In figure 3 is shown the measured and simulated pressure drop ΔP_b across the bubble, according to the definition of equation 1, as a function of the displaced liquid volume in the tube. Two peaks are seen: a positive one at $V_{\text{in}} \approx 51$ μL and a negative one at $V_{\text{in}} \approx 72$ μL. They correspond to the passage through the contraction of the left and right bubble meniscus, respectively. Before and after the two menisci have passed the contraction, the pressure difference across the bubble vanishes, because the advancing and receding wetting angles are equal at such low capillary number, and the laminar viscous contribution is negligible.

In the simulation the two peaks are symmetrical. For the first peak, the agreement between the measured and simulated pressure is good. Peak heights (within 20%), widths (5 μL) and shapes are comparable.

The magnitude of the second (negative) pressure peak is much smaller in the measurement than in the simulation. Two possible reasons for that are (1) that the rear meniscus of the bubble is flattened by interactions with impurities on the glass

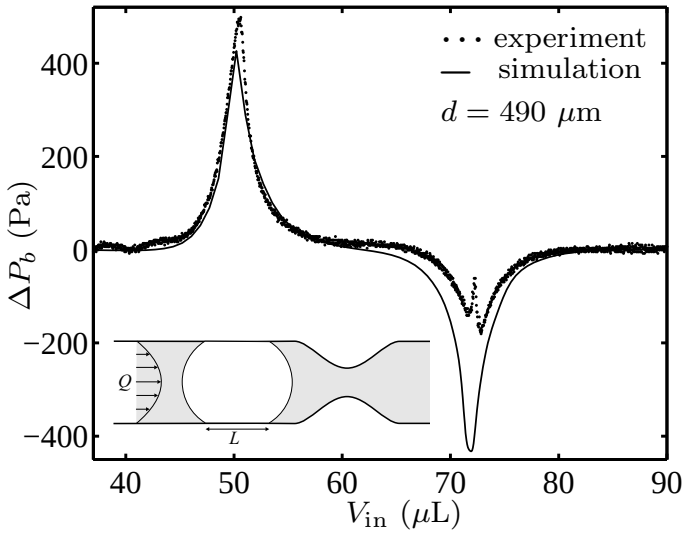

Figure 3. Direct measurements with the MEMS pressure sensor (dots) and simulation based on measured shape (full line) of the pressure across a long $L = 8$ mm bubble in tube A7 for $Q = 0.33$ μL/s as a function of displaced liquid volume $V_{\rm in} = Qt$, where t is the time. The observed values of the advancing and receding wetting angle used for the simulations are 10° and 9°, respectively. The inset indicates the bubble length L and the liquid flow rate Q.

surface, or by interactions with a film left by the front meniscus, and (2) that a thin liquid film between the bubble and the glass participates significantly in the pressure drop. Since the measured values of the advancing and receding wetting angle were relatively low (respectively 10° and 9°, without influence of the velocity), it appears that our system can be considered as hydrophilic. It is therefore worth investigating if a thin water film is formed along the bubble and interacts with the two menisci of the moving bubble. The thickness h of a film left behind a fully-wetting meniscus moving at velocity U with low capillary number $Ca = \mu U/\sigma$ in a tube of radius r, can be described by the Bretherton law [6],

$$\frac{h}{r} = Ca^{\frac{2}{3}}. \tag{2}$$

For tubes with diameters of 2.0 to 0.1 mm and flow rate 0.33 μL/s the meniscus velocity is $U = 0.1$ to 40 mm/s and $Ca = 10^{-6}$ to 5×10^{-4}. The thickness h of the water film left behind is therefore between 200 and 600 nm.

The first hypothesis, i.e., that the rear meniscus is flattened, has been tested by measuring with a high-speed camera the temporal evolution of the menisci curvature. In figure 4, the pressure calculated from the meniscus curvature (white points) is compared with the direct pressure measurement (black points). The symmetrical shape of the indirect pressure curve is a good sign that flattening of the meniscus is not responsible for the dissymmetry in the peaks of the direct pressure curve measured with the MEMS pressure sensor. However, when the tube is contaminated, we have observed flattening of the rear meniscus and a corresponding change in measured pressure. This stick-slip

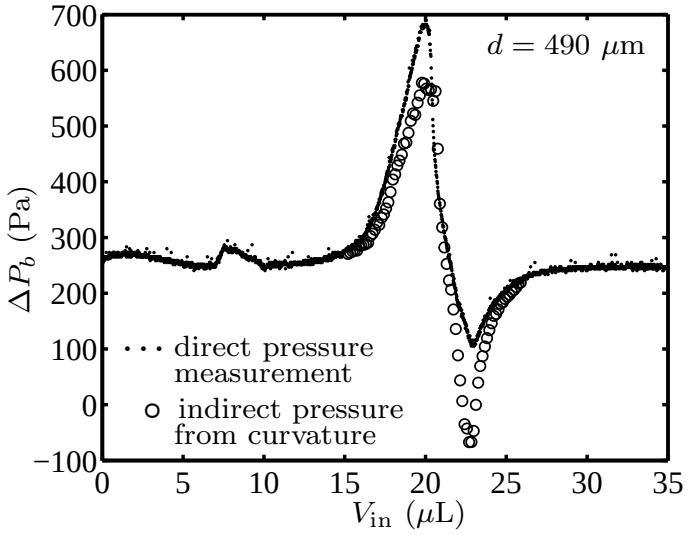

Figure 4. Direct measurements with the MEMS pressure sensor (black dots) and calculation from measured curvatures (white dots) of the pressure across a short $L = 1$ mm bubble. The tube and flow conditions are the same as in figure 3.

motion of the meniscus corresponds to a sawtooth profile of the measured pressure across the bubble.

The second hypothesis, i.e., interactions with a thin film, has been tested to some extent by observing interferences of white light with the bubble-tube contact surface. A diffraction pattern was observed and evolved to a steady pattern over a time of approximately 60 s: this transient phenomenon is likely to indicate the presence of a thin film and its dewetting. It has been shown by Redon et al. [7] that such a thin film contracts or dewets as a function of viscosity μ, surface tension σ, and contact angle θ with the approximate contraction velocity V given by

$$V = \frac{1}{120\sqrt{2}} \frac{\sigma}{\mu} \theta^3, \tag{3}$$

provided that the film thickness h is much smaller than a critical film thickness $h_c = 2\lambda_{\mathrm{cap}} \sin(q/2) = 400$ μm, where $\lambda_{\mathrm{cap}} = 2.7$ mm is the capillary length. In our case the film thickness is indeed much smaller than h_c. For the water-glass system, we obtain $V = 2$ mm/s. During the observed dewetting time of approximately 60 s, the meniscus in our experiments travels a distance between 6 mm (in the main channel) and 2400 mm (in the smallest contraction). Interactions between the dewetting film, its geometry or disjoining pressure [8], and one of the two bubble menisci are therefore very likely, and might be responsible for discrepancies between the measured and simulated pressure, as in figure 3, but these considerations are outside of the scope of this study. It must be noted that a laser fringe probing has recently been used to quantitatively monitor the liquid film thickness along a bubble in a liquid-filled capillary [9].

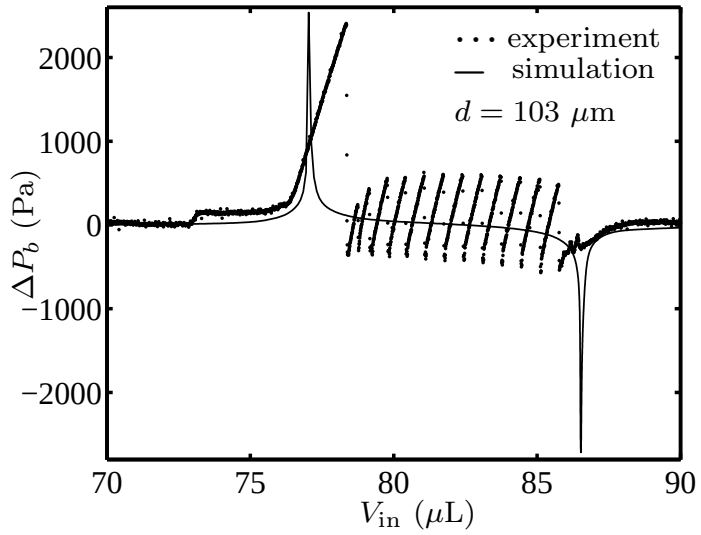

Figure 5. Measurements (dots) and simulation (full line) of the pressure drop ΔP_b across a $L = 3.1$ mm bubble in tube A19 for $Q = 0.33$ μL/s as a function of displaced liquid volume $V_{\text{in}} = Qt$. Note that this tube has the most narrow contraction ($d = 103$ μm) studied in this work.

4.2. Transient pressure and bubble breakup

Experiments have been made with a tube exhibiting a more narrow contraction (tube A19, 110 μm contraction), as shown in figure 5. The magnitude of the first pressure peak is comparable with the numerical simulation, however the shape is not in a good agreement with the simulation. Also, oscillations of the pressure occur during the entire phase where the bubble is spanning the contraction. The discrepancy in the shape of the first pressure peak can be explained by the fact that our measurement system is not infinitely stiff. We have measured that the volume of our measurement system increases by about 1 μL per kPa internal pressure. Although this deformation is negligible with respect to the overall system volume of about 12000 μL, it is enough to reduce the ascending slope of the first pressure peak observed in figure 5.

The saw-tooth pressure profile is due to instabilities occurring when the bubble passes through a long contraction with large aspect ratio: the single bubble breaks into several smaller bubbles that can merge back and separate with a given frequency. This mechanism is shown in figure 6, where the position of these sub-bubbles have been visualized with our high-speed camera at 600 fps and measured. This instability involves the creation and destruction of interfaces and induces saw-tooth perturbations in the pressure measurement. Comparison between figures 5 and 6 shows a good agreement in terms of the frequency of the perturbation. It is not known for now if the breakup is due to the elongated shape of the contraction itself or to the large diameter ratio.

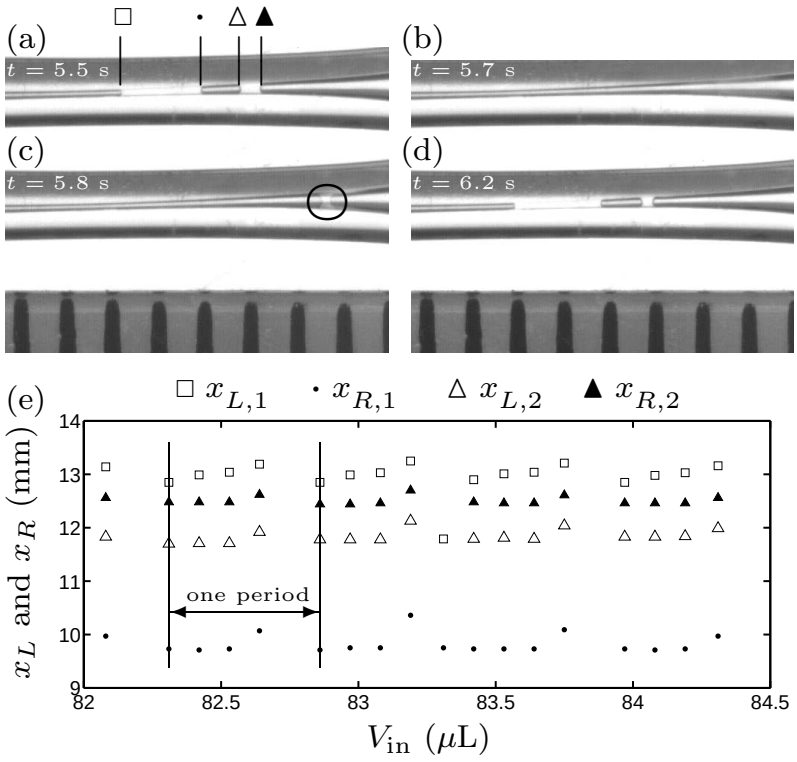

Figure 6. (a)-(d) Pictures of an $L = 1$ mm bubble advancing in tube A19 under the same flow conditions as in figure 5. The positions $x_{L,1}$, $x_{R,1}$, $x_{L,2}$, and $x_{R,2}$ of the left and right menisci are indicated on the snapshots extracted from a visualization at 600 fps. The circle in snapshot (c) at time $t = 5.8$ s shows the initiation of the instability generating the menisci. (e) The positions plotted as function of V_{in}. The vertical lines represent the start and end of a period.

4.3. Clogging pressure as a function of tube diameter

The clogging pressure ΔP_c is defined as the minimum pressure needed to push a bubble through the contraction [5]. We have measured the clogging pressure for four different micro-tubes with contractions and for different length L of the bubbles. The results are summarized in table 1.

The tubes have contraction diameters d between 103 and 490 μm, and the corresponding range of clogging pressure ΔP_c is from 2.7 to 0.3 kPa. The experimental and numerical pressure values agree within 20%. For a given contraction the amplitude of the first pressure peak is constant for bubbles larger than the contraction length. For small bubbles this is no longer true since both menisci are in the contraction when the pressure reaches its maximum value [5].

4.4. Influence of wetting angle

The influence of the wetting angle was tested by coating the inside of a tube, A27, with a hydrophobic layer of rainX and passing a $L = 4$ mm bubble through this tube. As seen in figure 7 the measured and simulated pressure drop are in agreement. The simulated

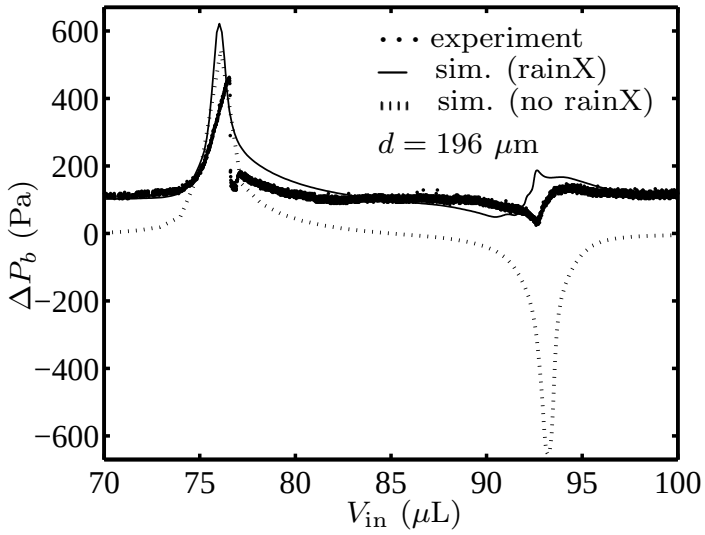

Figure 7. Measured (points) and simulated (full and dotted line) pressure drops ΔP_b across a $L = 4$ mm bubble for $Q = 0.33$ μL/s as a function of displaced liquid volume $V_{\rm in} = Qt$. The bubble moves in tube A27 covered with a hydrophobic layer of rainX, and the observed wetting angles used in the simulation are $\theta_R = 39°$ and $\theta_L = 89°$. For comparison is shown a simulation (dashed line) based on the wetting angles for the untreated (hydrophilic) tube.

curve is based on the measured wetting angles: $\theta_R = 39°$ and $\theta_L = 89°$. In both simulation and experiments the first pressure peak is much larger than the second, and the qualitative features of the first and second peak are well matched. The numerical simulation with wetting angles corresponding to a non-coated tube is also plotted for comparison, and it shows large discrepancies with the other two curves.

4.5. Influence of the liquid flow rate

A long $L = 10$ mm bubble was moved in tubes A7, A8, and A19 with contraction diameters of 490, 103 and 264 μm, respectively, at flow rates ranging from 0.1 to 160 μL/s. The maximum amplitude $|\Delta P|$ of the positive and negative pressure peaks observed as the bubble passes through each contraction are plotted in figure 8(a) as a function of the flow rate Q.

Two regimes are visible in the figure: (*i*) For flow rates smaller than a critical value, which depends on the contraction diameter, the positive and negative pressure peak amplitudes are constant, the positive peak being slightly larger than the negative one, as, e.g., in Figure 3. (*ii*) For flow rates larger than the critical value, the amplitude of the positive pressure peak decreases and ultimately vanishes, while the value of the negative pressure peak increases exponentially, without bound. This means, that in this high flow-rate regime the bubble is pushed through more easily. Further tests on two tubes with different contraction diameters explain how the transition between the two regimes occur. The first (positive) pressure peak is mostly due to the Laplace pressure, when the bubble is pushed through the contraction, as detailed in equation 1. As a first

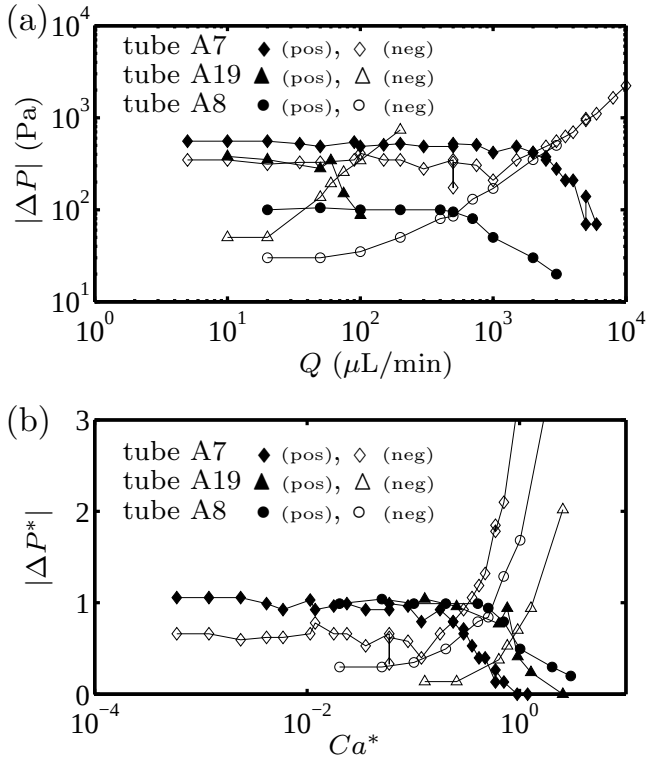

Figure 8. (a) Maximum amplitude $|\Delta P|$ of the positive and negative pressure peak observed as the bubble passes through the contraction versus flow rate Q for a long $L = 10$ mm bubble tubes A7, A8, and A19 with contraction diameters of 490, 103 and 264 μm, respectively. (b) Same data as in panel (a), but now expressed in terms of the re-scaled variables ΔP^* versus Ca^*, see equations (8) and (7). The negative pressure peak is represented by the open symbols and the positive pressure peak by the filled symbols.

approximation the Laplace pressure drop is

$$\Delta P_\sigma \approx \frac{4\sigma}{d}. \tag{4}$$

This is true for low flow rate situations, as seen, e.g., in figure 3, by the good agreement between measurements and simulation based on the quasi-stationary model. However, at higher flow rates the pressure drop ΔP_{fric} due to friction can no longer be neglected. This contribution to the total pressure drop ΔP_b is of magnitude

$$\Delta P_{\text{fric}} \approx \frac{128\mu\ell_{\text{con}}}{\pi d^4}\, Q. \tag{5}$$

The observed change in regime, where the positive pressure-peak transient vanishes, therefore occurs when $\Delta P_{\text{fric}} \approx \Delta P_\sigma$. Using this together with the expressions for the flow rate, $Q = \pi(d/2)^2 v$, and the capillary number, $Ca = \mu v/\sigma$, the transition condition can be written as

$$Ca \approx \frac{d}{8L}. \tag{6}$$

Based on this equation it is convenient now to define a re-scaled capillary number Ca^* as

$$Ca^* \equiv \frac{8L}{d}\, Ca. \tag{7}$$

In terms of the re-scaled capillary number the transition happens at $Ca^* \approx 1$. Likewise, it is convenient to introduce the re-scaled pressure drop amplitude of the pressure transient ΔP^* as

$$\Delta P^* \equiv \frac{P(Q)}{P(0)}, \tag{8}$$

i.e., the ratio between the observed amplitude of the transient pressure drop at high flow rate Q and the amplitude of the positive pressure transient at negligible flow rate $Q = 0$.

In figure 8(b) the data of panel (a) are re-plotted using the re-scaled variables ΔP^* and Ca^*. It is seen how the transition between the capillary pressure drop regime, with a large positive peak amplitude, and the viscous pressure drop regime, with a vanishing positive peak amplitude, occurs for $Ca^* \approx 1$. In other words, this criterion has practical implications: it discriminates between the case of bubbles clogging the flow through the contraction or not.

5. Conclusion

An experimental and numerical study of a bubble passing through a microchannel contraction has been performed. Transient measurements have quantified the pressure and bubble shape during its motion through the contraction. The agreement between the experiments and a numerical modeling is generally good, but some deviations have been observed and discussed. The influence of the wetting angle has been studied. High-speed visualization reveal that some departures from the simulations are due to instabilities and break-up of the bubble. Experiments varying the flow rate show that two regimes govern the pressure transients when the bubble passes the contraction: a quasi-steady regime for low capillary number, and a viscosity-influenced regime for non-negligible capillary numbers. A criterion based on a modified capillary number is proposed to discriminate between these two regimes, and it shows the existence of a critical flush velocity above which clogging by bubbles at contractions is avoided.

Acknowledgments

This work was in part supported by the US National Science Foundation (CAREER award 35405). The contractions in the glass tubes were manufactured by Rudy Schlott at Stony Brook: he passed away during our study. Despite the virulence of his illness, he mustered all his energies to continue working as a glassblower to virtually the bitter end.

References

[1] O. Geschke, H. Klank, and P. Telleman (Eds.), *Microsystem Engineering of Lab-on-a-chip devices*, Wiley-VCH (Weinheim, 2004).

[2] G. K. Batchelor, *An introduction to fluid dynamics* Cambridge University Press, (First Cambridge Math. Lib. Ed., Cambridge, 2000).

[3] P. Gravesen, J. Branebjerg, and O. Søndergård Jensen, J. Micromech. Microeng. **3**, 168 (1993).

[4] M. Elwenspoek, T. S. Kannerubj, R. Miyake, and J. H. J. Fluitman, J. Micromech. Microeng. **4**, 227 (1994).

[5] M. J. Jensen, G. Goranović, and H. Bruus, J. Micromech. Microeng. **14**, 876 (2004).

[6] F. P. Bretherton, J. Fluid Mech. **10**, 97 (1961).

[7] C. Redon, F. Brochart-Wyart, and F. Rondelez , Phys. Rev. Lett. **66**, 715 (1991).

[8] P.-G. de Gennes, F. Brochard-Wyart, and D. Quere, *Capillarity and Wetting Phenomena: Drops, Bubbles, Pearls, Waves* Springer (New York, 2003).

[9] X. S. Wang X.S. and H.-H. Qiu, Meas. Sci. Technol. **16**, 594 (2005).